Magnetic and Structural Properties of Nitrided Fe and FeTi Thin Films

by

Michael John Bonder

Joule Physics Laboratory,
School of Sciences,
University of Salford.

Submitted in partial fulfilment
of the requirements for the degree
of Doctor of Philosophy, March 2001

Contents

Figure List

Acknowledgements

In completing this thesis, I owe a huge debt of gratitude to a number of people. My supervisor, Professor Phil Grundy, who has provided me with the time and freedom to pursue ideas and grow experimentally. It is for this that I offer my gratitude. I would like to extend my thanks to the academics in the Joule Physics laboratory, especially Professor Don Lord, Dr. G.A. Jones and Dr. C.A. Faunce. The advice and conversations regarding all aspects of research have proven invaluable and will continue to influence me well into the future, thank you. Further gratitude goes to Dr. C.A. Faunce for his work on the electron microscope in acquiring the diffraction patterns and bright field images presented in this thesis. Thanks goes to Dr. N.D. Telling for whom without his assistance with deposition of samples and discussions, this thesis would not have been realized. Here I recognize the efforts of Dr. X. Zhou for his help and discussion related to instrumentation in general and specifically for tuition on the MFM. To my fellow postgraduate students, Joanne Lord, Mohammad Almasi-Kashi, Erwin, Milena Georgieva, and Nigel Mellors, who deserve mention for their help, when two hands were insufficient, their conversations on matters experimental and, of course, the camaraderie. Credit is paid to Mr. Brian Ashworth, who prepared all the electron microscopy samples considered in this thesis.

Mom and Dad…thanks for all your concern and patience in allowing me to pursue something so dear to me.

Abstract

This thesis investigates the magnetic and structural properties of Fe and $Fe_{85}Ti_{15}$ thin films nitrided using a nitrogen atom source. In this novel technique, the atom source produces an atomic nitrogen beam for which multilayer samples with bilayers of the form Fe/FeN or FeTi/FeTiN were synthesized by varying the thickness of the Fe or FeTi exposed to the nitrogen beam.

The samples studied here are all in the as-deposited state. X-Ray reflectivity confirms the presence of a multilayer structure showing sharp multilayer peaks indicative of good quality interfaces. The electron diffraction data shows a variation of nitride phases as the thickness of the Fe layer was varied. Fe_2N was present when the bilayer was 7Å thick. Increasing the bilayer thickness led to a bilayer consisting of two different nitride phases until the Fe layer was 42Å thick and the bilayer consisted of α-Fe and Fe_4N.

In contrast, when Ti was present the phase was body centred cubic for all but the thinnest bilayers considered in this thesis. The grain structure of the two systems was also quite different. The Fe/FeN grain sizes ranged from 50 to 1000Å in diameter as the bilayer was varied. In the FeTi/FeTiN sample set the grain growth was inhibited with no noticeable increase with nitriding. Despite these structural differences the magnetic character of the two series of samples were consistent. The samples ranged from non-ferromagnetic to ferromagnetic with the presence of weak perpendicular anisotropy occurring as the bilayer thickness increased. As the bilayer thickness was increased there was an asymptotic approach of the magnetization to the level of the unexposed materials. The presence of the perpendicular anisotropy was maintained for a larger parameter space. In both series the anisotropy is attributed to stress induced by the substrate. Nitriding Fe and FeTi using the aforementioned technique provides a controlled and viable way to alter the magnetic and structural properties.

Chapter 1 Introduction

The interest surrounding the iron nitrogen system goes back to the work of Jack[1] and co-workers circa 1950 and the first synthesis of $Fe_{16}N_2$. Over twenty years later, measurements by Kim[2] showed that this phase had an enhanced magnetic moment as compared to elemental Fe. Sugita et al[3] in their hallmark publication claimed that the average moment per Fe atom in single crystal $Fe_{16}N_2$ was 3.2 μ_B at room temperature and 3.5 μ_B at 4 K. These values are 45 and 59% greater than the room temperature moment of 2.2μ_B for elemental bulk Fe, respectively. Since then there has been desultory evidence for the so called giant moment of $Fe_{16}N_2$ and a stark disparity between experiment[3-14,16-20] and theoretical values[15,21]exists, with theory typically giving values of 2.4μ_B per Fe atom. Despite these problems, the race for high moment materials has continued fast and furious, driven by the magnetic recording industry. Current media are pushing the limits of flux density of the current write heads.[22,23] Further increase of areal densities will require the performance potential of $Fe_{16}N_2$ if it can live up to its promise and satisfy device requirements[22-27].

What follows in this chapter is an exposition of the current status of the iron nitride system, including the associated phases, nitriding techniques, laminated films, and FeXN alloy films, where X is a transition metal, partly in the context of device requirements.

Following that will be an overview in chapter 2 of relevant topics in magnetism, including domains, Stoner-Wohlfarth formalism, and perpendicular magnetic anisotropy. Experimental techniques and data analyses used are discussed in chapter 3. Chapter 4 will present the work associated with a series of multilayer films referred to as Fe/FeN. Chapter 5 discusses the results of a study of the FeTi/FeTiN multilayer system. Chapter 6 will summarize and pull the bulk of the work to a conclusion and, as with all scientific research the end is not yet in sight so chapter 6 also discusses prospects for further investigation.

1.1 FeN Phases

Figure 1.1 shows the phase diagram of the iron/nitrogen binary system[28]. The nitrogen is incorporated as an interstitial rather than as a compound as some of the nomenclature implies, so phases exist over a range of nitrogen percentages rather than the exact values suggested by their names. As seen, there is a progression of phase changes as the nitrogen concentration increases. With addition of an infinitesimal amount of nitrogen the material consists of pure Fe (denoted as body centred cubic (BCC) α-Fe) along with the γ'-Fe_4N phase which is face centred cubic (FCC). This combination exists with diminishing amounts of the α phase up to 20at% N when it becomes completely γ'.

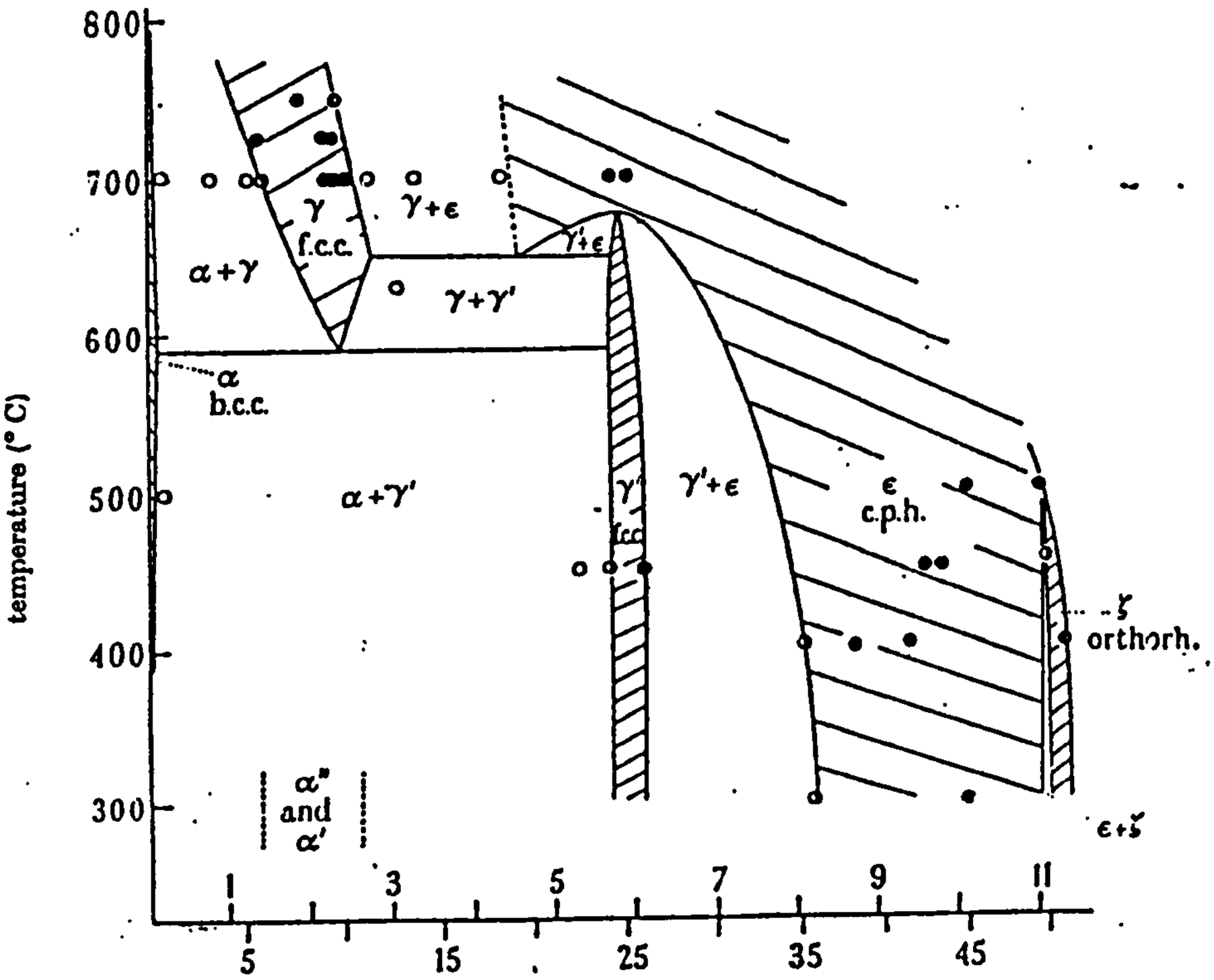

Figure 1.1) FeN phase diagram[28].

This phase persists over a short nitrogen range up from 20-21 at% N with the inclusion of the ε-Fe_3N phase depleting the γ′ component with continued increase of the N concentration up to 26 at% when it is all ε-Fe_3N. Beyond 32 at% the composition contains ζ-Fe_2N along with the ε phase. There is a small region over which the ζ phase exists at about 33 at% N.

As shown, the proposed high moment α″-$Fe_{16}N_2$ phase appears as a metastable phase at about 11 at% N at an elevated temperature in the region of 275-325°C in conjunction with the α′-Fe_8N martensite phase. The change of stoichiometry carries a crystallographic change. The corresponding transition progresses as follows: BCC for α, FCC for γ′, hexagonal close packed (HCP(labelled cph in figure 1.1)) for ε, orthorhombic for ζ, and body centred tetragonal (BCT) for the α′ and α″ phases. At higher temperatures there is a γ phase listed as well, this phase is also FCC. At this point a distinction must be made between primed and unprimed phases. The difference is due to positions of the nitrogen within the respective lattice accompanied by a degree of ordering. Shown in figure 1.2 are schematics of the aforementioned nitride phases as proposed in papers by Jack.[14, 29] The ε and ζ are base-centred hexagonal and orthorhombic respectively. From figure 1.2 it can be seen that they are very similar with respect to the Fe atom sites. In the ε phase only one of the three interstices in each of the respective planes is filled. The ζ phase unit cell consists of two base centred orthorhombic cells as proposed by Jack[29] for which nitrogen occupies three of the six interstices of the cell. The γ and γ′ phases are both FCC. It is the nitrogen ordering that distinguishes the two. The γ, or N-austenite phase, consists of a random occupation of one in ten of the cube edge and cube centred interstices by nitrogen. The γ′ phase consists of a FCC lattice with N occupying one in four of the cube centred octahedral interstices in an ordered array[14]. Again as in the prior two cases the α′ and α″ have very similar structures. Both phases are BCT with one in ten of the octahedra randomly filled in α′ and two of the 48 octahedral interstices of the α″ phase filled in an ordered array in the lattice, where the unit cell consists of eight distorted BCT cells.[1,14]

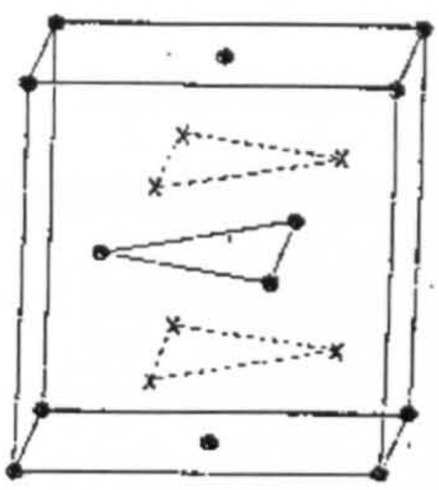

a)

3 of 6 × = N

• = Fe

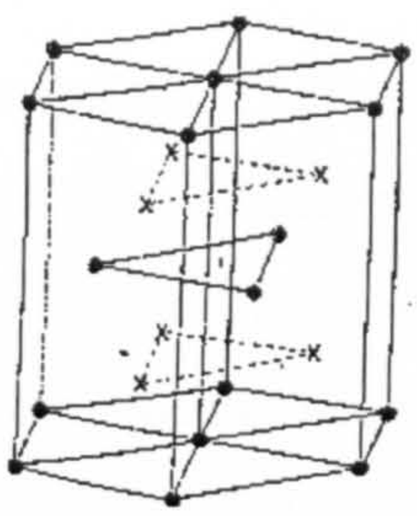

b)

2 of 6 × = N

• = Fe

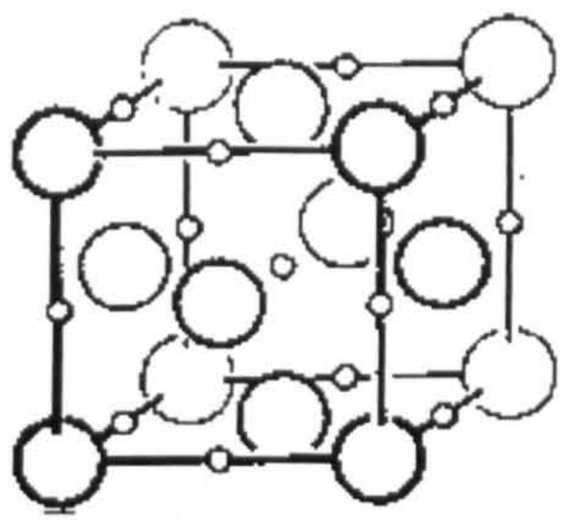

c)

1 of 10 ○ = N

○ = Fe

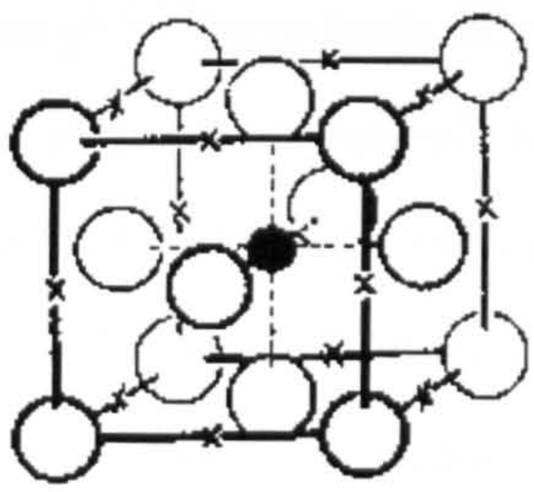

d)

● = N

○ = Fe

× = unoccupied interstice

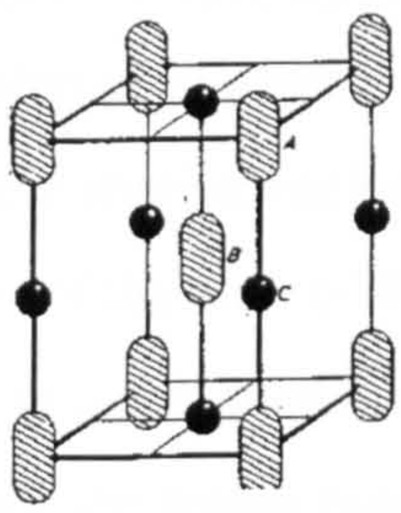

e)

2 of 16 • = N

= Fe

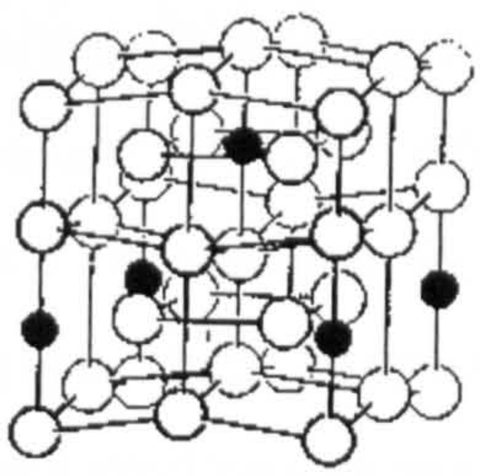

f)

2 of 48 • = N

○ = Fe

Figure 1.2) Unit cells of the FeN phases, a)ζ Fe_2N[29], b) ε Fe_3N[29], c)γ N-Austenite[14], d)γ′ Fe_4N[14], e) α'N-Martensite[14] and f) α″ $Fe_{16}N_2$[14]. In the figures the the nitrogen (N) and Iron (Fe) sites are labeled by the symbols given beneath the corresponding unit cell.

Despite the anomalous nature of the $Fe_{16}N_2$ system, it carries enormous potential when considered in the context of the magnetic recording industry. Currently write heads are reaching the limits of usefulness. Future hard drives are predicted to require values of $B_s \geq 1900$ emu/cm^3.[23] Given that projected values of the M_s of $Fe_{16}N_2$ are 2200 to 2300 emu/cm^3 there has been an increase in the amount of research into iron nitride thin films.

1.2 Nitriding techniques

Jack's original synthesis of the α″ phase consisted of low temperature tempering of Fe particles subjected to an $NH_3 + H_2$ atmosphere followed by quenching[1, 28]. Since the time of that publication several techniques have been utilized. The focus here is on thin film samples. The standard technique has been reactive sputtering[4-7, 20]. This consists of sputtering Fe in an $Ar + N_2$ atmosphere. Production of the α″ phase has been accomplished by depositing at elevated temperatures[17, 20] and on buffer layers such as Ag[8, 20] and Fe[8]. Facing target sputtering, reactive sputtering with two magnetrons facing one another has also been used[5, 7, 17]. Microwave plasma nitriding[31] and molecular beam epitaxy[3, 4, 12] have been used to grow single crystal $Fe_{16}N_2$. Ion implantation[4] of N into Fe sheet and laser ablation[41] have also been used to study the iron nitride system. A variety of substrates have been used in these studies, including InGaAs[3, 11], NaCl[4, 17], MgO[5, 7, 9] and Si[10, 20]. These techniques consist of the bulk of the research. However, in looking to possible device applications these techniques remain less than ideal. Each has required post-synthesis processing. Hence the search continues for a synthesis technique to obtain an as-deposited system containing the α″ phase. When considering the phase diagram this seems impossible. However, there are more pressing problems when considering using the high moment phase as a device. It is still debatable whether such a high moment exists or whether it can be maintained at operating temperatures. Determination of volume fraction of $Fe_{16}N_2$ within a sample and the accurate determination of the volume of a sample continue to present experimental challenges.

1.3 Laminated films

Multilayered, or laminated, FeN based structures have been of interest for possible high frequency write-head materials. When a magnetic material is subjected to a magnetic field that is switching direction at increasingly higher frequencies there is a breakdown in the ability of that material to completely switch its magnetization direction in following the field. This is attributed to a skin depth, δ, effect[30]. This phenomenon occurs in accord with Lenz' law, such that eddy currents are set up in the material that oppose the change in the

amount of magnetic flux in the material. Hence, the applied field does not penetrate throughout the whole of the sample and achieves a penetration δ as:

$$\delta = 5030\sqrt{\frac{\rho}{\mu f}}cm \qquad (1.1)$$

where ρ is the resistivity, μ is the permeability and f is the frequency of the alternating field. Consequently the whole magnetization of the material does not switch as required. This problem can be overcome by increasing the resistivity, keeping the permeability and switching frequency constant. The permeability must remain large in order to keep the switching field strength low enough for operating considerations. The skin depth problem is important for future magnetic recording applications. The rate at which data is being written to current hard drives is slowly reaching the gigahertz regime[23]. In order to optimize the flux density from the write head a high resistivity, high permeabilty material is required. In following transformer technology, laminated films have been studied. One class of samples consists of a multilayer structure with Fe nitride layers separated by a high resistance, dielectric spacer layer. Spacer layers have included Al_2O_3[35, 36] and SiO_2[35, 38, 39]. The fatal flaw in these materials is that the added material is typically not magnetic and detracts from the overall magnetization and flux density of the prospective film. Another problem still looms. The α″ phase is only stable over a small temperature range.

1.4 FeXN Alloys

The α''phase is a metastable phase that exists over a limited temperature and nitrogen content range. It has been made known at the 1999 Joint Magnetics Workshop in York that write-heads typically operate in the 250-350°C temperature range. In this temperature regime the $Fe_{16}N_2$ phase breaks down into α-Fe and Fe_4N as seen from the phase diagram in figure 1.1. Hence, the high moment would be destroyed. This is the root of the thermal stability problem; high moment or not, if the phase is not present it will not contribute to the magnetization of the write-head when required. It has been suggested[14] that addition of a small amount of another metal into the Fe would facilitate production of the α″ phase to temperatures exceeding 500°C by reducing the reactivity of N in Fe. Following this advice the magnetic materials research community have produced several

such studies, with work on FeZrN[42, 43, 45], FeTaN[46-49, 52-54], FeAlN,[44] FeRhN[41] and FeTiN[50, 51]. Each of the added metals has a different effect on the system. Addition of Zr has been used to reduce the magnetostriction of the material. Al improves the resistivity of the nitrided material. Ta and Ti have been used to control the grain structure of the systems in an effort to improve thermal stability. These materials cannot achieve the same level of saturation magnetization (M_s), as the α'' phase since the alloying dilutes the magnetization. The question remains as to what condition will maximize the magnetization of the material. Of the four aforementioned alloys only FeTiN[50] has produced M_s values above that of Fe, with values of M_s of 1900emu/cm^3 as compared to 1714 emu/cm^3 for elemental Fe. In these studies the α'' phase exists up to 800°C[51].

1.5 Multilayers

A multilayer refers to a thin film that consists of several repeats of a combination, of two different species, one atop the other, called the bilayer. Such systems include bilayers consisting of a magnetic material such as Fe and a nonmagnetic layer. The nonmagnetic layer may consist of a noble metal, a rare earth or a normal metal[92]

Magnetic multilayers have enhanced and new properties compared to bulk materials. This allows for studies of fundamental properties and potential applications. Through the use of techniques such as molecular beam epitaxy and sputtering it is possible to tailor the physical properties of the materials involved[91]. The study of the oscillatory nature of RKKY coupling is readily investigated by varying the thickness of the spacer layer. The discovery by Baibich,[93] of the giant magnetoresistance effect, utilizes multilayers with antiferromagnetic coupling between magnetic layers to set up a high resistance state. As the thickness of the magnetic layer decreases the effect of the interface becomes more important and this leads to an enhanced magnetic moment at the interface. The influence of the interface also affects the anisotropy of the material with the presence of perpendicular anisotropy, in some systems, when the magnetic layers are thin enough. Under the right growth conditions thinner layers will retain the structure of the previously deposited layer. Epitaxial growth contributes to the properties of the film. Such effects induce strain in the material altering the anisotropy of the material. The ability to alter the

properties of materials, through the use of multilayers, presents an advantage in studying the properties of magnetic materials.

1.5.1 Fe/FeN Multilayers

Previous work on samples of the multilayer genre have included studies of samples synthesized using pulsed reactive sputtering[40, 55, 58] and electron cyclotron resonance plasma nitriding[56]. These studies looked at samples with [Fe/Fe_2N] bilayers on the order of hundreds of angstroms (Å) thick[55] in the first case and layers greater than 50Å in the latter. Both experiments use N_2 as the reactive gas[55, 56]. As will be seen the bilayers are thinner here. The focus of the above studies has centred on the structural characterization of inter-diffusion of the N at the interfaces[55]and Mossbauer spectroscopy of Fe/Fe_2N multilayers with good soft magnetic properties[56]. The fabrication of Fe/FeN multilayers has shown a dependence of magnetostriction on the thicknesses of the Fe and FeN layers[58]. FeN/Fe_2N samples have been shown to consist of magnetostatically coupled layers while the equivalent FeN/SiO_2 multilayers were exchange coupled[40]. The potential for both fundamental and application driven studies into the Fe/FeN system is extensive despite the lack of work in the literature.

1.6 The Present Study

The present study utilizes a nitrogen atom source in an attempt to build upon the present knowledge concerned with the Fe-N system. A more complete description of the technique is left to chapter 3, but it suffices to say that the atom source provides an atomic beam of nitrogen at energies of about 1-2eV. The advantage lies in that the atomic form is more reactive than N_2. This highly reactive N beam is directed toward the substrate, allowing for a more controlled study of the reactivity of the nitriding of Fe. Partial motivation of this study was an attempt to produce the α'' phase. To do this a multilayer philosophy was adopted in order to produce FeN samples laminated with Fe of the form $[Fe/Fe_xN_y]_z$ where z denotes the number of bilayers. The α'' phase is BCT and the hope was that adding nitrogen to a BCC Fe lattice would be beneficial in nucleating and growing the BCT phase rather than by nitriding the Fe prior to it arriving at the substrate.

This would allow for a competition between the lattice energy and the reaction energy involved in the formation of the different nitride phases.

Chapter 2 Theory

2.1 Basic Magnetism

When a magnetic field is applied to a material it will respond in one of three ways according to the sign and magnitude of its susceptibility (χ) where[88]

$$\chi = \frac{M}{H}. \qquad (2.1)$$

M is the magnetization of the material and H is the field strength required to achieve the level of magnetization. The value of susceptibility is a measure of how a material responds to a magnetic field. For a magnetic material, the higher the χ the easier it is to align the direction of magnetization where the magnetization (M) is

$$M = \frac{1}{V}\sum_i m_i \quad , \qquad (2.2)$$

where V is the volume of the material and m_i are the moments of all the atoms in the system.

A negative χ describes a diamagnetic material. The magnetization of a diamagnet acts to counter the applied field producing a typical magnetization curve as shown in figure 2.1. Small and positive χ pertains to both a paramagnet and an antiferromagnet. The distinction between the two is the presence or absence of saturation. An antiferromagnet will eventually saturate if a high enough field is applied while a paramagnet continues as a linear function of the applied field as shown for an arbitrary field range in figure 2.2a and b.

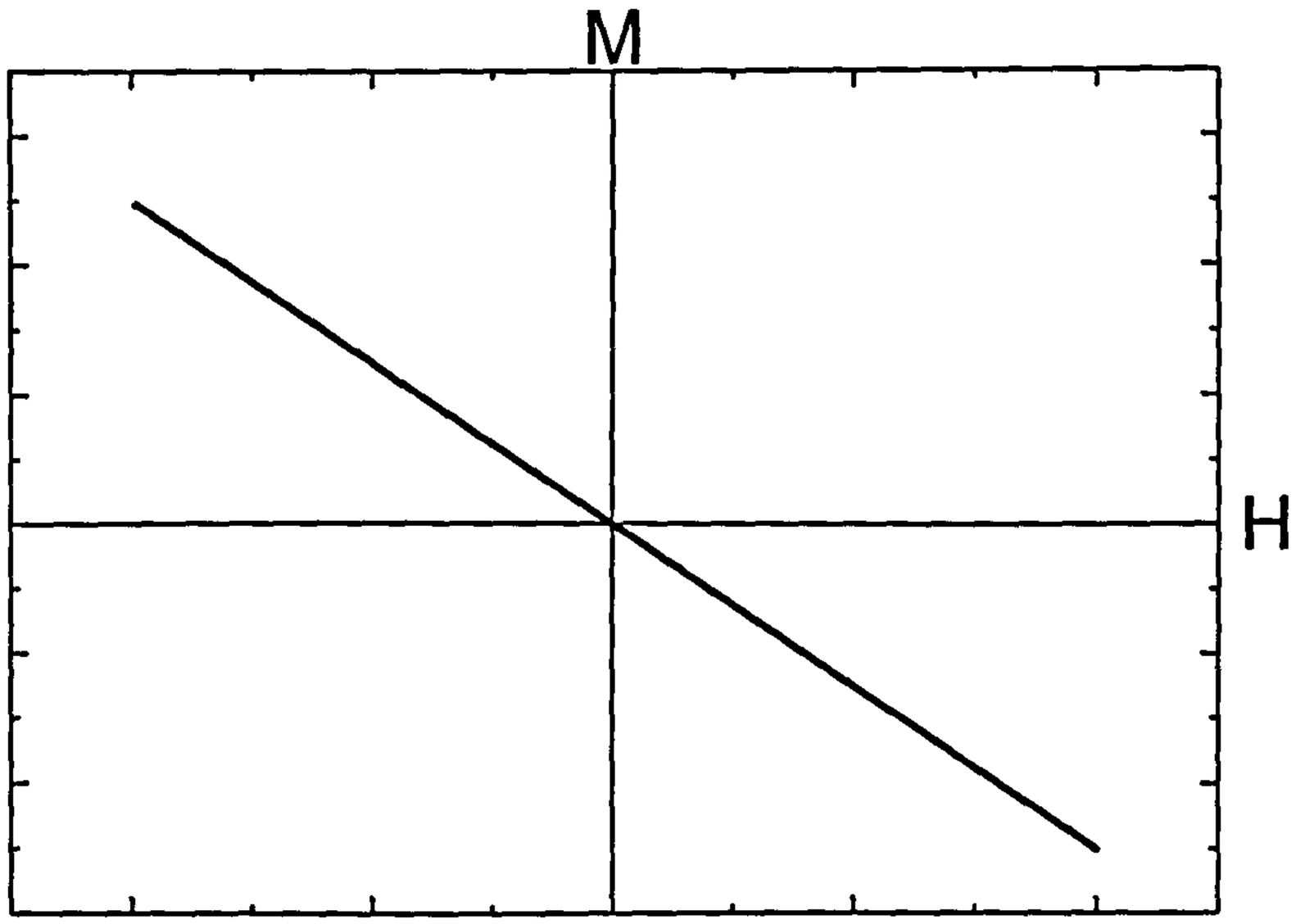

Figure2.1) Diamagnetic magnetization curve.

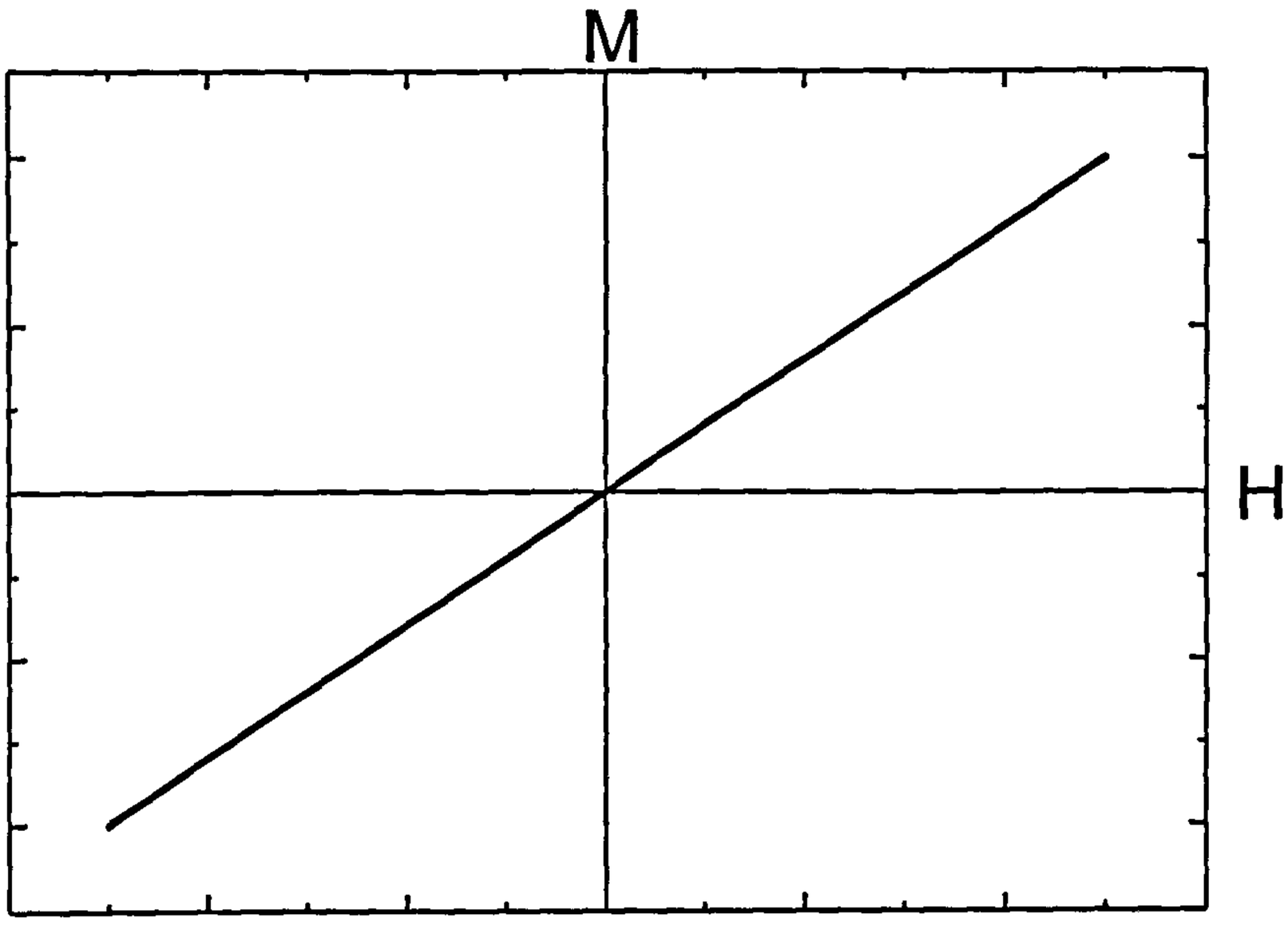

a)

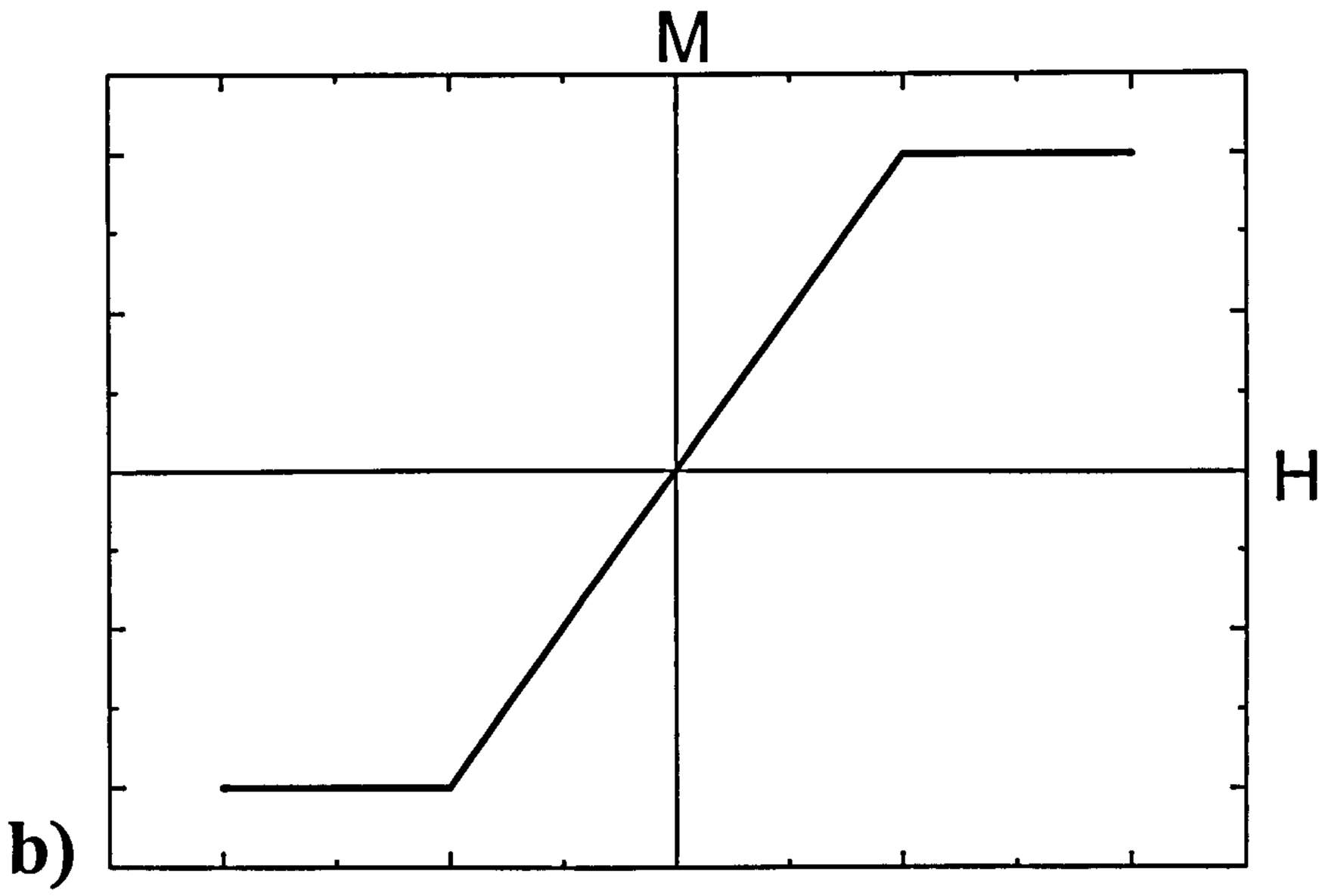

Figure 2.2) Schematic magnetization curves for a) paramagnetic and b) antiferromagnetic multilayers.

Other than the antiferromagnet, which is important in giant magnetoresistance and exchange biasing, the above are of little technological importance. A ferromagnet is a material with a large positive and variable χ. There are three elemental room temperature ferromagnets, iron, nickel, and cobalt. A ferromagnetic hysteresis loop is displayed in figure 2.3.

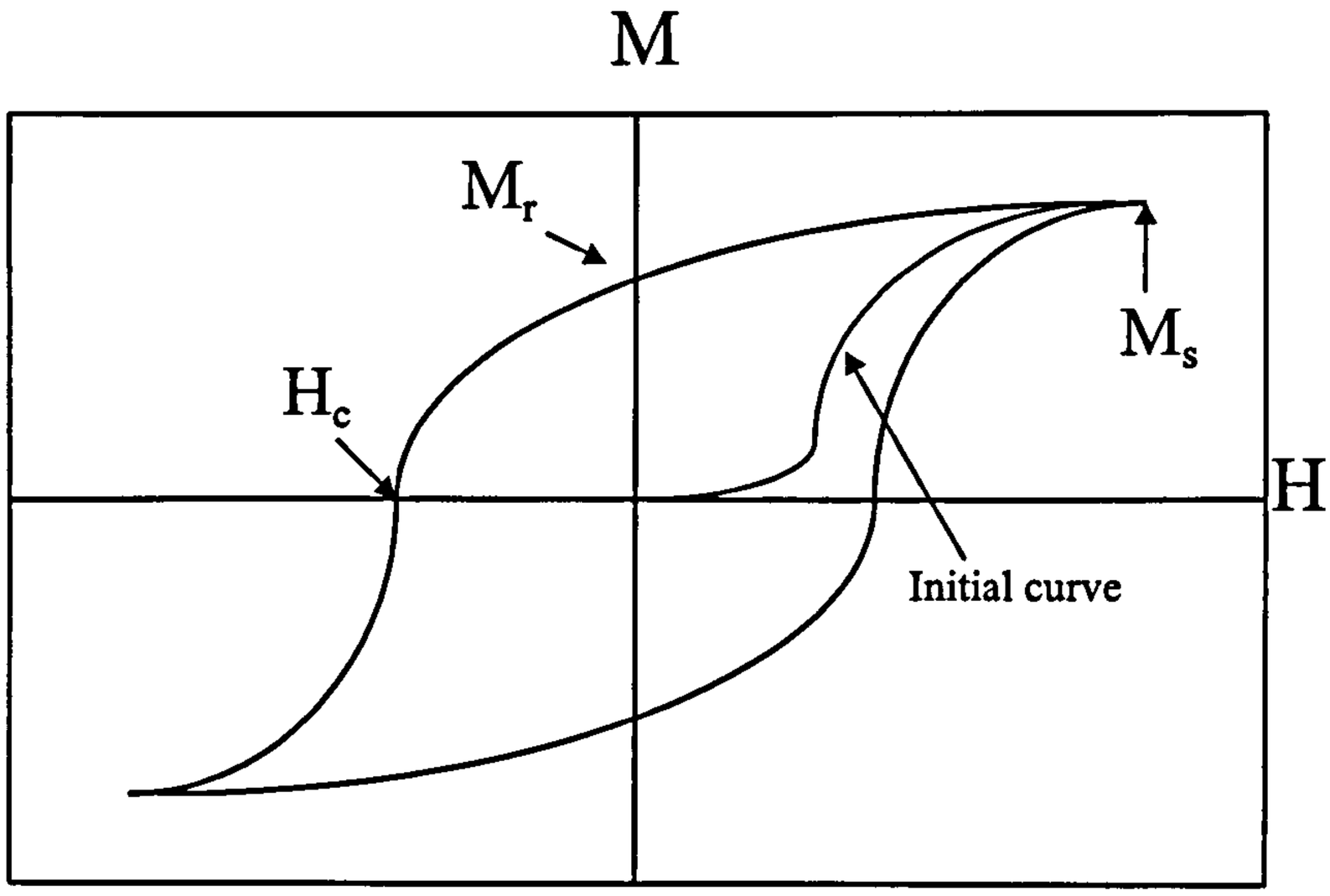

Figure 2.3) Ferromagnetic hysteresis loop with saturation magnetization, remanent magnetization and coercivity labelled.

Labelled on the figure are the quantities of interest, including the saturation magnetization (M_s), the coercivity (H_c), and the remanent magnetization (M_r). The M_s corresponds to the total moment per unit volume of a material; this is when all of the spins are aligned by an applied external field. The H_c is the reversed field required to reduce the magnetization of the material to zero. The remanent magnetization is the level of magnetization maintained by a material in the absence of a magnetic field after being saturated. The initial magnetization curve of a material gives information concerning the mechanism of how the magnetization of a material reverses. An initial curve as shown in the figure is consistent with reversal due to nucleation of reversed domains followed by domain wall motion[94]. Reversal by domain wall motion is evidence by a much steeper ascent to saturation.

2.1.1 Hysteresis

Hysteresis refers to the response of a magnetic material to an applied field that is cycled from a large positive to a large negative field and back to a large positive field. The plot of the magnetization versus the field produces a multi-valued function as shown in figure 2.3. At some high value of field, the material is said to be saturated, which refers to the state of

magnetization when all of the moments are aligned. As the field is reduced the spins remain aligned until a sufficiently large negative field is applied such that the magnetization of the material reverses direction. This magnetization reversal occurs in one of three ways, either by nucleation of reversed domains, domain wall motion, or rotation[30]. Domain wall motion results in a square hysteresis loop owing to the speed and ease of motion once the field is large enough to drive through any pinning sites, which include defects or a second phase. The applied field must also overcome anisotropy energies present. Reversal by rotation occurs via a rotation of the magnetization in following the direction of the applied field, hence the name.

2.1.2 Exchange

Ferromagnetic moments tend to align parallel to one another. This phenomenon was first explained by Weiss[30] to be due to a molecular field. This however was not sufficient in predicting the strength of the interaction. In 1928, Heisenberg[88] introduced the exchange interaction to explain ferromagnetic alignment. The interaction is purely quantum mechanical involving the interaction of electrons and the Pauli exclusion principle. As an atom is brought near enough to another atom such that they both have an unpaired outer shell, the electrons will occupy the same orbit if the spins have opposite sign. If the spins have the same sign they will not share an orbit by the exclusion principle forming separate orbits. The energy involved is given by:

$$E_{ex} = -2\sum J_{ex} S_i S_j \cos\theta\,, \qquad (2.3)$$

where E_{ex} is the exchange energy, J_{ex} the exchange integral, S_I and S_j are the spins of the two electrons being considered, and θ is the angle between the spins. When J_{ex} is positive the energy is a minimum when the spins are parallel as in ferromagnetism and when J_{ex} is negative the energy is a minimum when the spins are antiparallel as in antiferromagnetism.

2.1.3 Anisotropy

Magnetic anisotropy is concerned with the existence of preferred directions of magnetization in a magnetic material. Such anisotropy takes the form of magnetocrystalline anisotropy, shape anisotropy, stress anisotropy, interfacial and microstructural anisotropy. Magnetocrystalline anisotropy refers to the effect of the magnetic material having a specific crystal structure. The origin of this type of anisotropy is spin orbit coupling. The electron orbits are strongly coupled to the lattice. With the application of a magnetic field the field required to rotate the magnetization must overcome the spin-orbit coupling. This scenario produces an easy axis for which the field required to reverse the magnetization is less along certain directions. In the BCC Fe lattice the easy axes are in the <100> axes while the hard axes are the <111> directions. In the HCP lattice, the easy axis is the [0001] direction. The HCP system is referred to as having uniaxial anisotropy since all other crystallographic directions are hard axes.

As its name implies shape anisotropy suggests that the shape of a magnetic material requires the magnetization to orient in certain directions rather than others. For example, a bar magnet will be easier to magnetize along its long axis than the short axes. This is particularly important when considering thin films, where the aspect ratio involved is orders of magnitude smaller. The origin of shape anisotropy requires considering the magnetostatic energy of the system. Again, considering a bar magnet with north and south poles at either end of the long axis, there are stray field lines outside the magnet running from the north pole to the south pole as is commonly known. Inside the magnet there is another field set up extending from north to south poles that acts to demagnetize the material. This field is known as the demagnetizing field. The energy associated with this is:

$$E = \frac{1}{2} N_D M^2 \qquad (2.4)$$

where N_D is the demagnetizing factor, and M the magnetization. Determination of the easy axis from this proceeds by considering the first and second derivatives of the energy, knowing the demagnetizing factors of the geometry considered and the magnetization as a function of the angle of interest. The extrema for the system are determined and then the

minimum from the second derivative is found. For a prolate spheroid, the anisotropy associated with the shape anisotropy determined as prescribed is:

$$K_s = \frac{1}{2}(N_a - N_c)M^2 \qquad (2.5)$$

where N_a and N_c are the demagnetizing factors of the semi-minor and semi-major axes respectively. From this the semi-major axis is the easy axis if $N_a > N_c$.

Just as a magnetic field can alter the dimensions of a magnetic material due to magnetostriction, a stress within a material affects the preferred direction of magnetization. This stress, or magnetoelastic anisotropy, is of the form,

$$K_{st} = \frac{3}{2}\lambda_s \sigma \qquad (2.6)$$

where λ_s is the saturation magnetostriction and σ is the stress. Stress will either be compressive or tensile such that compressive stress will promote an easy axis perpendicular to the stress direction and tensile stress promotes an easy axis along the stress axis for positive values of magnetostriction.

Interfacial anisotropy becomes important when considering multilayer thin films as the layer thickness is decreased. There is an asymmetry introduced by alternately layering a magnetic material with a nonmagnetic one. The situation was first considered by Neél for single layers. In considering multilayers, the interface consists of magnetic atoms that are no longer in a homogeneous environment, in that not all the nearest neighbours are the same. This symmetry-breaking sets up a situation such that when the magnetic layer is thin enough there is a tendency for the easy axis to orient perpendicular to the plane of the layer. The anisotropy is related to the film thickness as[98]:

$$K_{eff} = K_v + 2\frac{K_s}{t_F} \qquad (2.7)$$

where K_v is the volume anisotropy, K_s is the surface anisotropy, t_F the layer thickness, and K_{eff} the effective anisotropy of the film. In addition to this interfacial roughness can produce a similar effect[99].

Deposition of a thin film may also produce anisotropy, if there is a structural feature set up such as columnar growth that produces a shape anisotropy stronger than the

previously mentioned magnetostatic phenomenon, that would make it more energetically favourable to have the magnetization align with that direction.

2.2 Magnetic Domain Formation

Weiss[30] first postulated magnetic domains. Magnetic domains form in order to minimize the energy of a magnetic system. A single domain magnet is normally not stable due to the existence of stray fields. The energy of the system is:

$$\frac{1}{8\pi}\int H^2 dv \qquad (2.8)$$

where H is the stray field and the integral is over all space. By splitting into two domains of opposite orientation as in figure 2.4a the energy of the system is approximately halved. Such splitting continues to reduce further the energy. When a domain splits into two a domain wall is formed. The region of transition between domains, schematically shown in figure 2.4b, is a Bloch wall. As can be seen the moments associated with the domain wall have a component perpendicular to the directions of magnetization of the adjacent domains. The thickness of a domain wall is given as[30]:

$$\delta = \sqrt{\frac{JS^2\pi^2}{Ka}} \qquad (2.9)$$

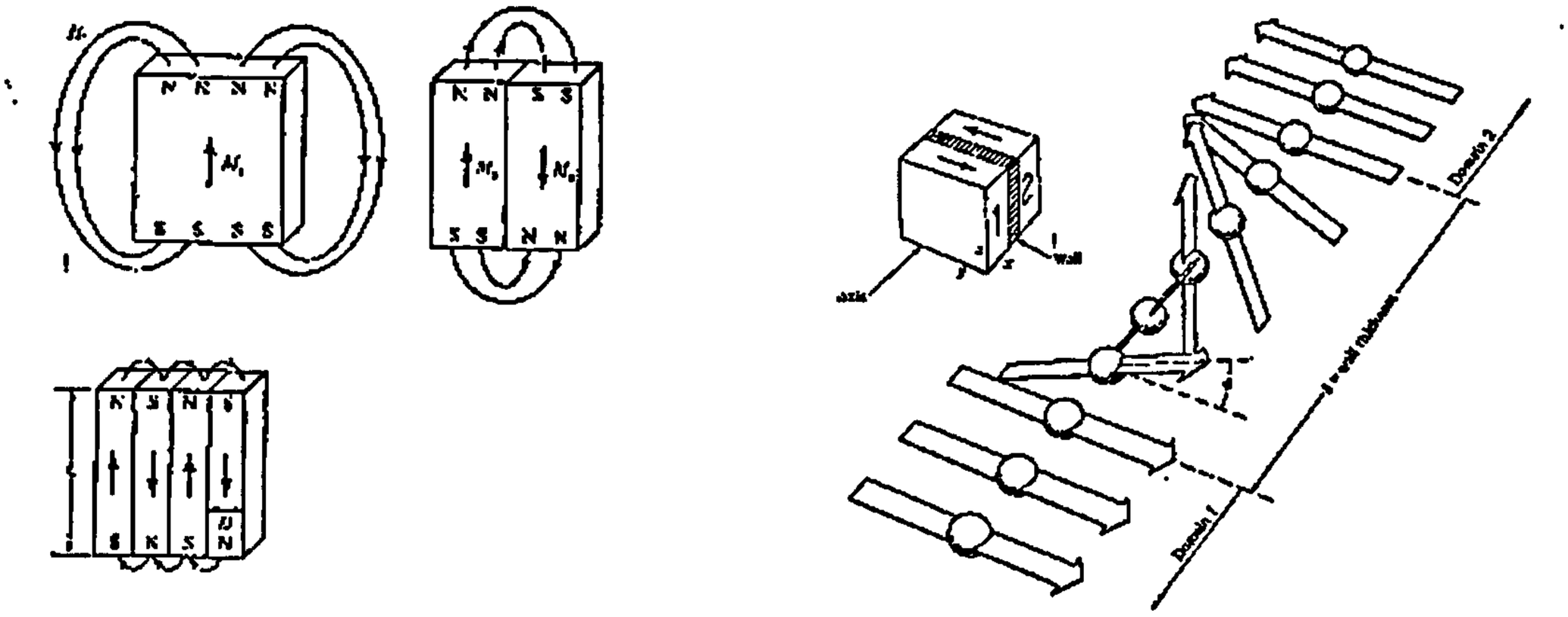

Figure 2.4) a) Schematic of single and multiple magnetic domains, b) schematic of a domain wall[30].

where δ is the domain wall thickness, J the exchange integral, S is the spin of the atom in the material being considered, K is the anisotropy of the material and a is the interatomic distance. Domain walls may consist of hundreds of atoms in order to reduce the angle between consecutive magnetic moments. Using the above equation the domain walls of Fe and Ni are approximately 120 and 290 atoms thick respectively[30]. This is because there is competition between the anisotropy energy tending to decrease the number of atoms while the exchange energy between moments tend to increase the number of atoms in the domain wall. A magnetic material will continue to split into increasing numbers of domains up to the point where further reduction in magnetostatic energy is cancelled by an increase in energy owing to domain wall formation; equilibrium is thus attained.

2.2.1 Stoner-Wohlfarth model

In 1948 E.C. Stoner and E.P. Wohlfarth devised a model of magnetization reversal for a system of single domain particles[59]. The model considered energy minimization in producing stable configurations when a magnetic field was applied at various angles to the easy axis of the particles. In doing this they made four assumptions. The particles were single domain, with uniaxial anisotropy, non-interacting and reversed magnetization by

coherent rotation. Hence for an elongated spheroid particle with easy axis along its major axis the hysteresis loop taken along the easy axis would be square. The energy relation used was:

$$E = K_u \sin^2 \vartheta - M \bullet H \qquad (2.9)$$

where K_u is the uniaxial anisotropy constant, θ the angle between the magnetization and an applied field. This produced a square hysteresis loop after considering the first and second derivatives with respect to the angle θ and considering the condition $\frac{\partial E}{\partial \vartheta} = 0$ for an extremum and $\frac{\partial^2 E}{\partial \theta^2} > 0$ for the extremum to be a minimum. This model serves as an effective guideline for magnetization reversal when the appropriate energy contributions are considered[59]. Calculations for two thin film systems are given in the appendix.

2.2.2 Stripe Domains

For thin films the magnetization usually lies in the film plane owing to the predominance of shape anisotropy. If a thin film has an easy axis perpendicular to its plane, then above a certain critical thickness, the magnetization may leave the film plane and align along the film normal. The resulting domain configuration consists of stripes as shown in cross-section in figure 2.5 and was considered first by Kittel[62].

The two configurations contain adjacent domains for which the magnetization alternates between parallel and antiparallel to the film normal. The second case in figure 2.5b also contains flux closure domains which are oriented parallel to the film plane. The magnetization configuration discussed by Kittel is now referred to as strong stripes where adjacent domains are separated by 180° walls. A second category of stripe domains was posited by Saito[70], of which a schematic is shown in figure 2.6.

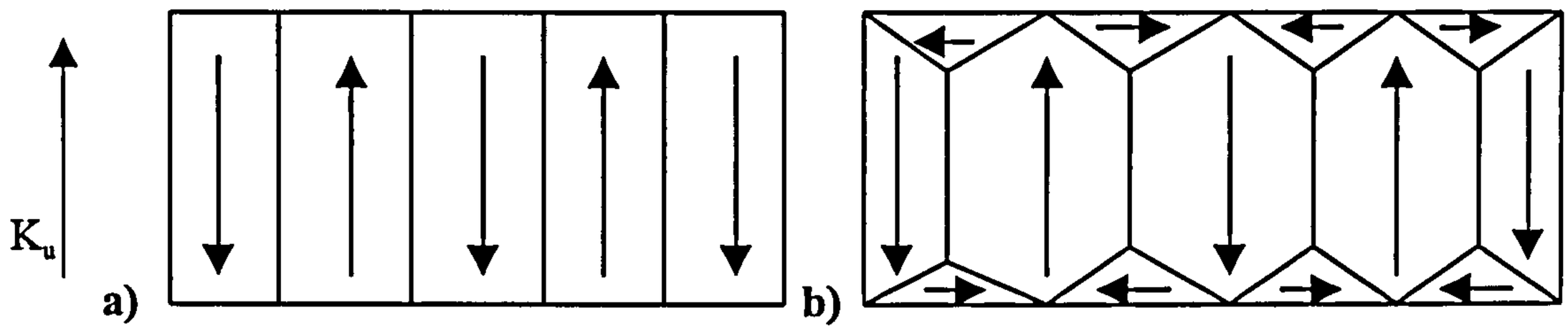

Figure 2. 5) Cross sectional schematic of stripe domain configurations proposed by Kittel[62] which assumes a perpendicular easy axis a) without closure domains, b) with closure domains. The easy axis direction is indicated by the arrow

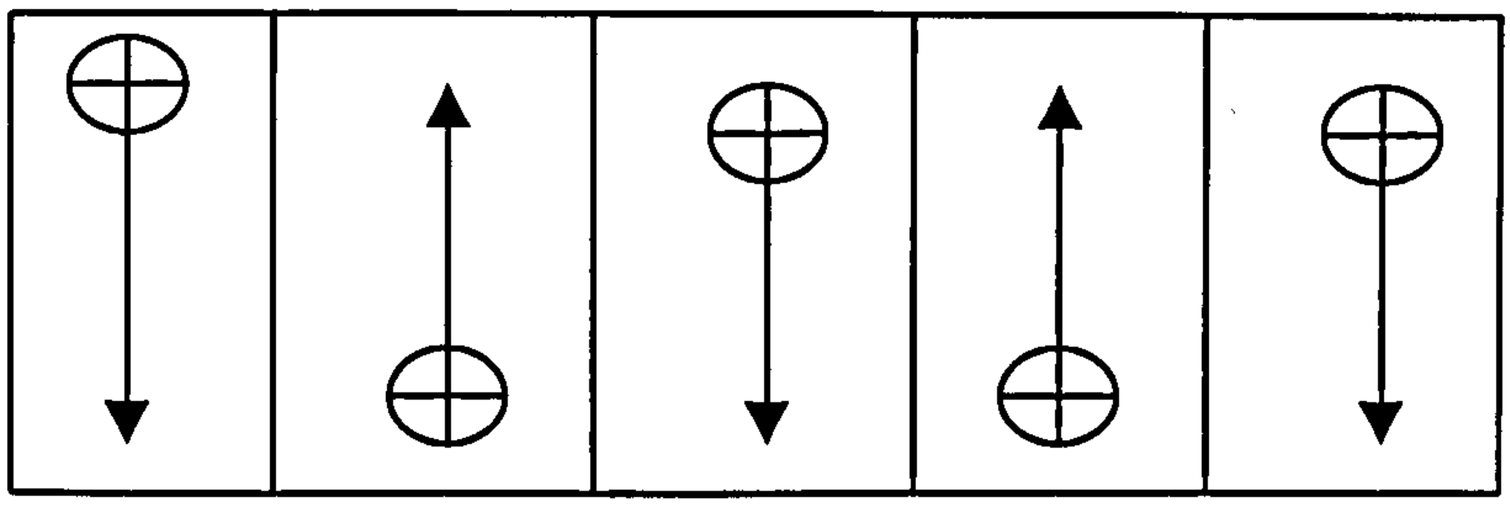

Figure2.6.) Cross sectional schematic of Saito's weak stripe model

The magnetization vectors are considered to have an in-plane component all in the same direction while the perpendicular component alternates direction with antiparallel alignment in adjacent domains such that the magnetization vector lies at a positive or negative angle θ with respect to the film plane. Hara[69] extended these stripe domain models by combining elements of both models as shown in figure 2.7.

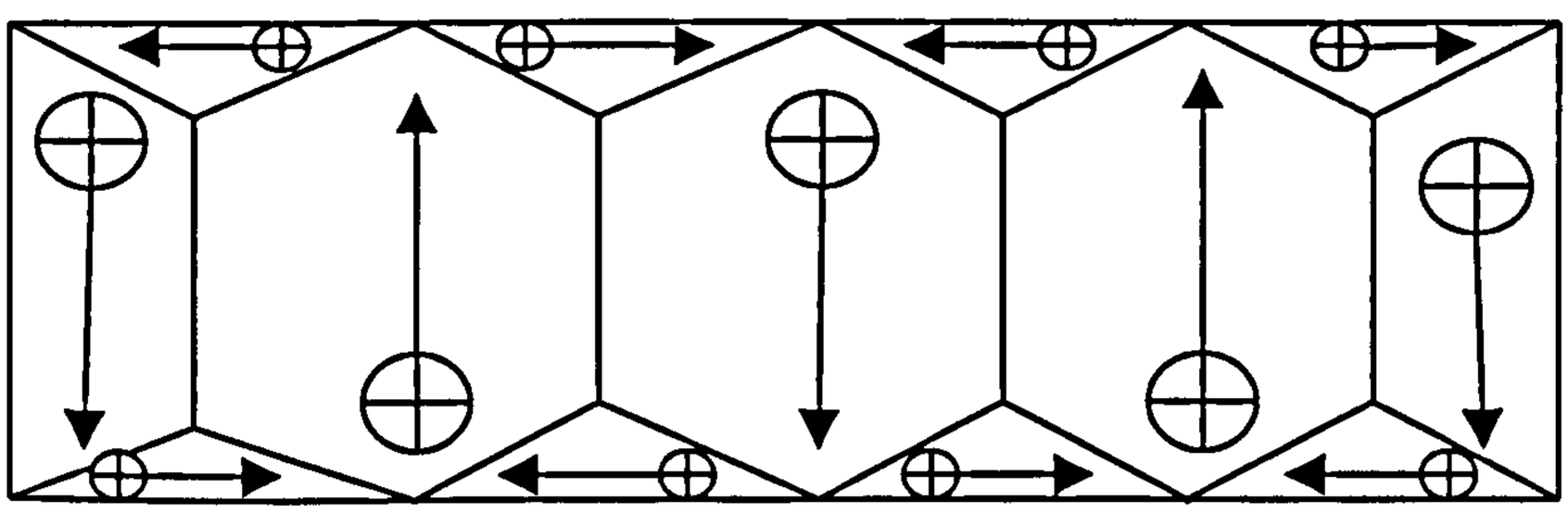

Figure 2.7.) Cross sectional schematic of Hara[69] weak stripe model.

Hara considers weak stripes having flux closure domains. This would be more energetically favourable negating the magnetostatic energy of free poles at the surface. In

discussing strong stripes, Hara considers domains to be magnetized at an angle θ with respect to the normal rather than strictly perpendicular. The strong stripe model also incorporates closure domains in reducing the energy of the system.

There are several checks in experimentally determining the presence of one or the other type of stripe domains. Hara poses the idea that if strong stripes are present the stripe domains will expand or diminish in width in the presence of an applied field along the stripe direction. For weak stripes the stripe width would remain unchanged upon application of a magnetic field. Another attribute of weak stripes as proposed by Saito is the presence of rotatable anisotropy. This refers to the idea that the stripes will rotate to align with an applied field[72, 78]. The presence of strong stripes necessitates a square hysteresis loop along the easy axis of the stripe domains in light of the Stoner-Wohlfarth model. The models of Saito and Hara predict the hysteresis loop shape of weak stripes in the region from remanence to saturation; however they do not show the entire loop.

Since they were first proposed, stripe domains have been demonstrated in thin films of NiFe[73], NiCo[66, 67, 72, 74], NiS[77], Fe/Si[71], Fe[76], and CoPt[87], CoAg[65] and Co/Pd[64] to give a few examples. Lorentz microscopy[84, 85], the Bitter method[68, 72, 86], the magneto-optical method[63], and the magnetic force microscope[76] have been used for stripe domain observation. Stripe domains of both varieties have been produced by evaporating at oblique angles inducing an oblique columnar grain structure[67] as well as in multilayers[87]. Multilayers of Fe/Co have produced the characteristic, stripe domain hysteresis loop[90]. In the Fe/Co system the presence of the weak stripe hysteresis loop is transient. As the bilayer thickness is varied the stripe domain loop first appears at a bilayer structure of (20Å Fe/20Å Co) and subsequently disappears above (50Å Fe/50Å Co).[90]

Chapter 3 Experimental

This chapter considers the various experimental techniques and data analysis methods used in preparing this thesis.

3.1 Deposition Chamber

Part of the project involved the development of a sputter deposition system used to make the samples with which this thesis is concerned. A diagram of the system is shown below in figure 3.1a.

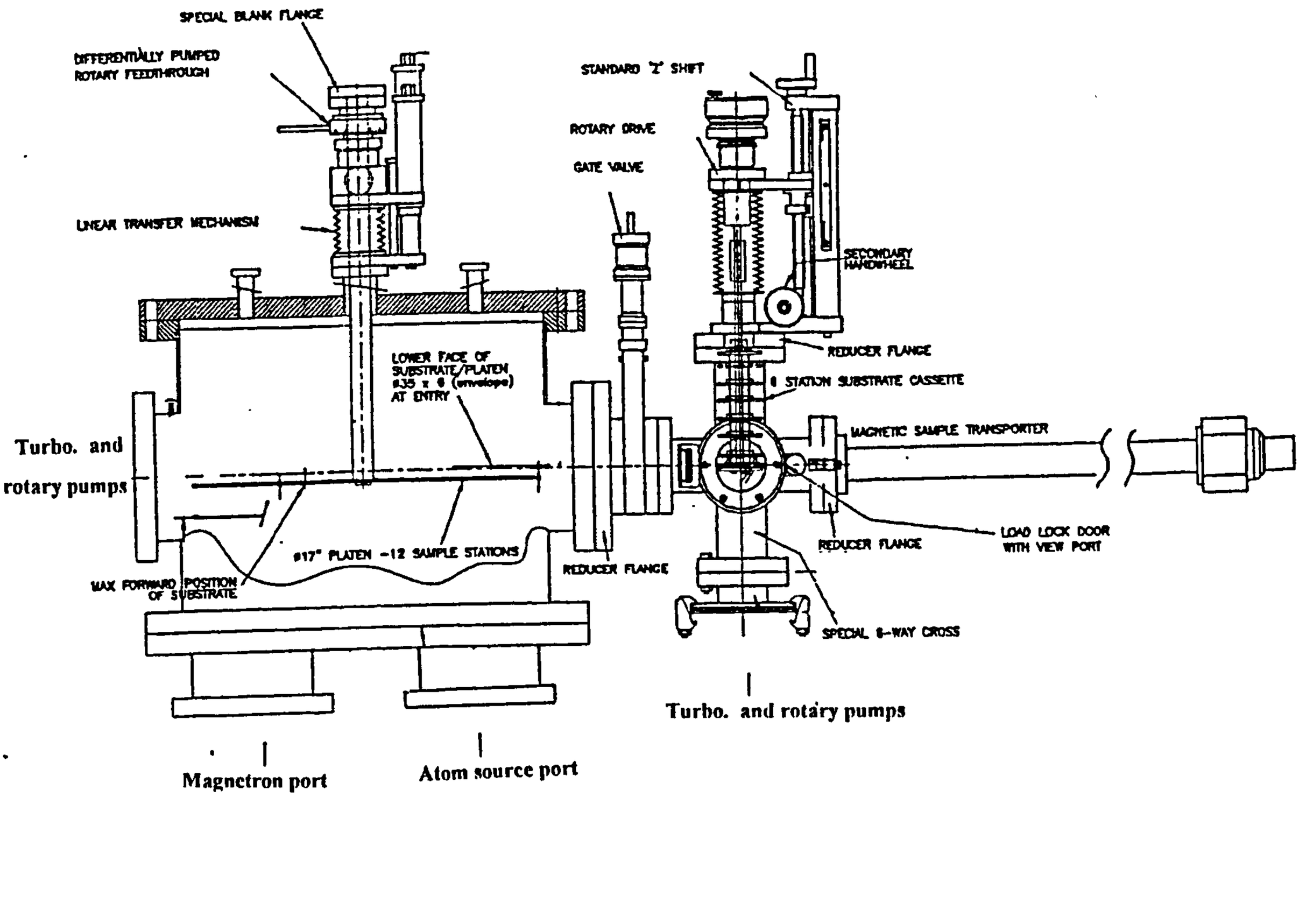

a)

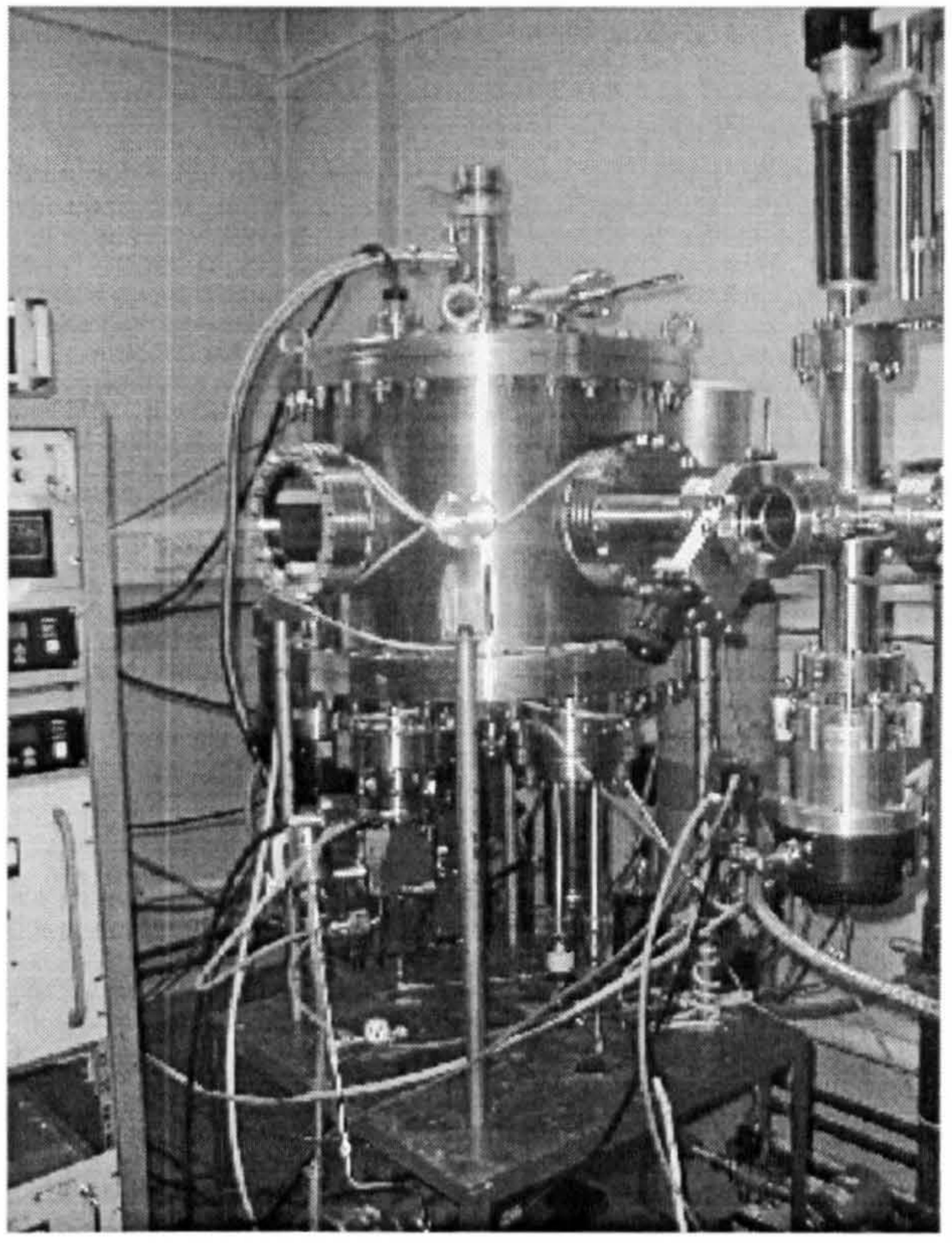

b)

Figure 3.1) a) Schematic and b) photograph of the sputter deposition chamber.

It shows the two chambers and ferro-fluidic transfer arm. Also included is the sample cartridge in the transfer chamber. As seen in 3.1b, a photograph of the system is shown, it consists of two chambers, magnetrons, an atom source, two turbo pumps, and two mechanical pumps. Not shown explicitly are two flow controllers used for the Ar and N_2 during sputtering.

As seen in the schematic diagram of the sputtering geometry in figure 3.2, the system is a "sputter up" system. Magnetrons are pointed up with substrates facing down. Though the "down" configuration is seemingly easier when considering the ergonomics of maintenance, the "up" configuration was utilized in hopes of preparing films free from defects due to flakes from the target material.

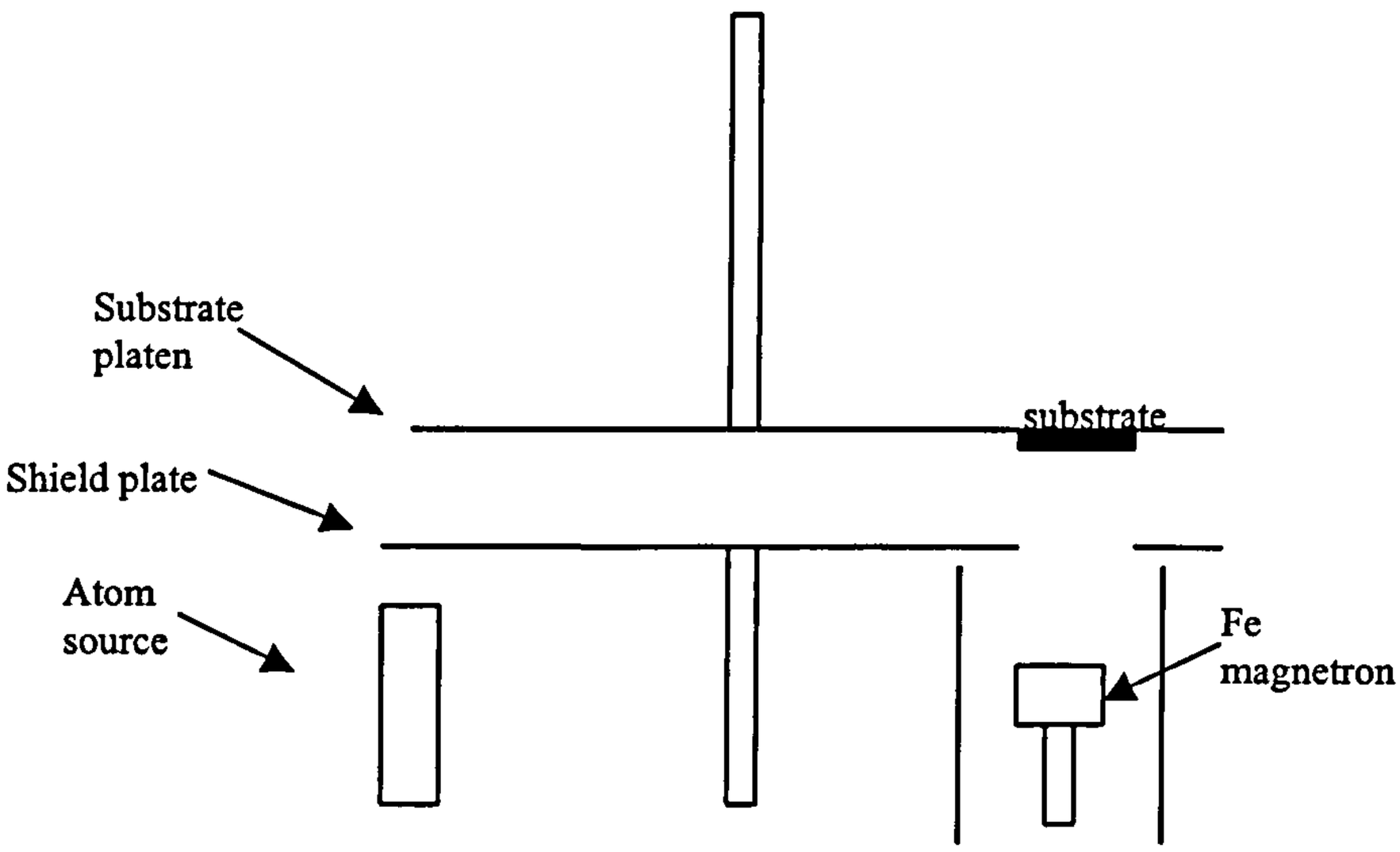

Figure3.2) Sputtering geometry used for deposition of samples.

There is a four port base plate that holds the nitrogen atom source and three dc magnetrons. Typically a shutter system is used to start and stop deposition. Here a single stainless steel plate, of radius just smaller than the chamber, with a hole at the magnetron radius is used to sequence the deposited layers. In an effort to stop cross-contamination, as well as maintain visibility through the window port, stainless steel cylinders are fitted around each of the magnetrons to a height just below the shield plate. A cold trap with a stainless steel vane system provides further reduction of contaminates within the chamber upon the addition of liquid nitrogen. The second chamber consists of a load-lock system for transfer of samples whilst the main chamber remains at vacuum. The two chambers are separated by a manual gate valve. A ferrofluidic transfer arm allows for linear transport of samples to a substrate support plate that translates vertically to lift and lower samples off the transfer arm. The main chamber is typically kept at a base pressure of about 1×10^{-8}mbar and the load-lock is pumped down to about 8×10^{-8}mbar. The load-lock can hold six substrates in its rack system and the substrate support platen in the main chamber has twelve positions for substrates.

3.1.1 Atom Source

This thesis is concerned with the nitriding of Fe using an Oxford Applied Research nitrogen atom source. Figure 3.3 shows an illustration of the apparatus.

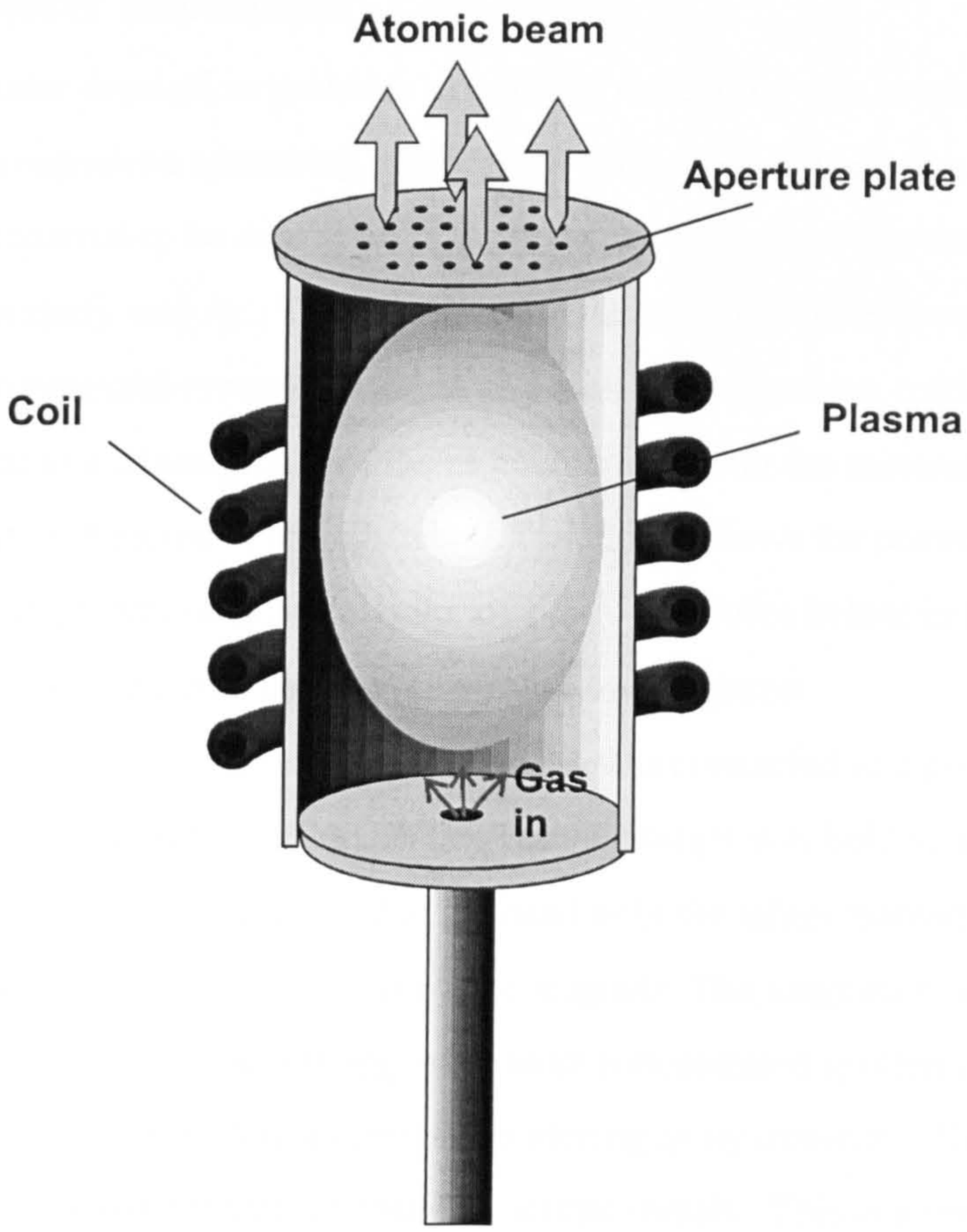

Figure 3.3) Atom source schematic.

As N_2 enters the cavity it is subjected to a RF potential difference. The rf electric field produced by this potential difference dissociates the molecule, by providing enough energy, into atomic nitrogen, which effuses through the aperture, due to a constant flow of gas through the atom source. The nitrogen is subsequently directed at the substrate. The nitrogen arrives at the substrate with thermal energy on the order of 1-2 eV. At these energies, there is no alteration of the surface owing to bombardment. Nitriding of films is

seemingly reminiscent of chemical oxidation in that the nitrogen is introduced into the deposited Fe just as when an Fe film is exposed to ambient air an oxide layer forms at the surface.

3.1.2 Sputter Deposition

Sputter deposition provides a means of depositing thin layers of material. In the case of dc magnetron sputtering, the process consists of setting up a potential difference above the material to be deposited in the presence of an inert gas atmosphere. The gas used in this study was Ar. The Ar ionizes in the potential difference and accelerates through the potential toward the target material. The argon ion collides with the target material and as a consequence of the momentum transfer the material of interest dislodges from the target directed at the substrate. Sputtering allows for controlled deposition of material with growth rates of the order of 1-5 Å/s. Shown below in figure 3.4 is a schematic of a magnetron used in the present investigation.

The target material sits on a support that is connected to a power supply that holds the target at a specified potential, in this case the target was held at about 300 volts. Above the target was a grounded shield that exposed only the target material. Below the target was a circular configuration of permanent magnets. The magnets confine the electrons above the target and define the region of most concentrated sputtering as evidenced by the sputtering "track" created as a result of sputtering away material. The track diameter is different for magnetic materials than for normal metals. This is a result of the constriction of the magnetic field lines from the permanent magnets. This phenomenon occurs as a result of the permeability, μ, of the material, where[30]

$$\mu = \frac{B}{H}. \qquad (3.1)$$

B is the flux induction in the material and H is the applied field. The larger the permeability the more the field lines are pinched inside the material as compared to outside. Hence, the sputtering track for an Fe target has a much smaller diameter and subsequently a much smaller amount of material available for deposition.

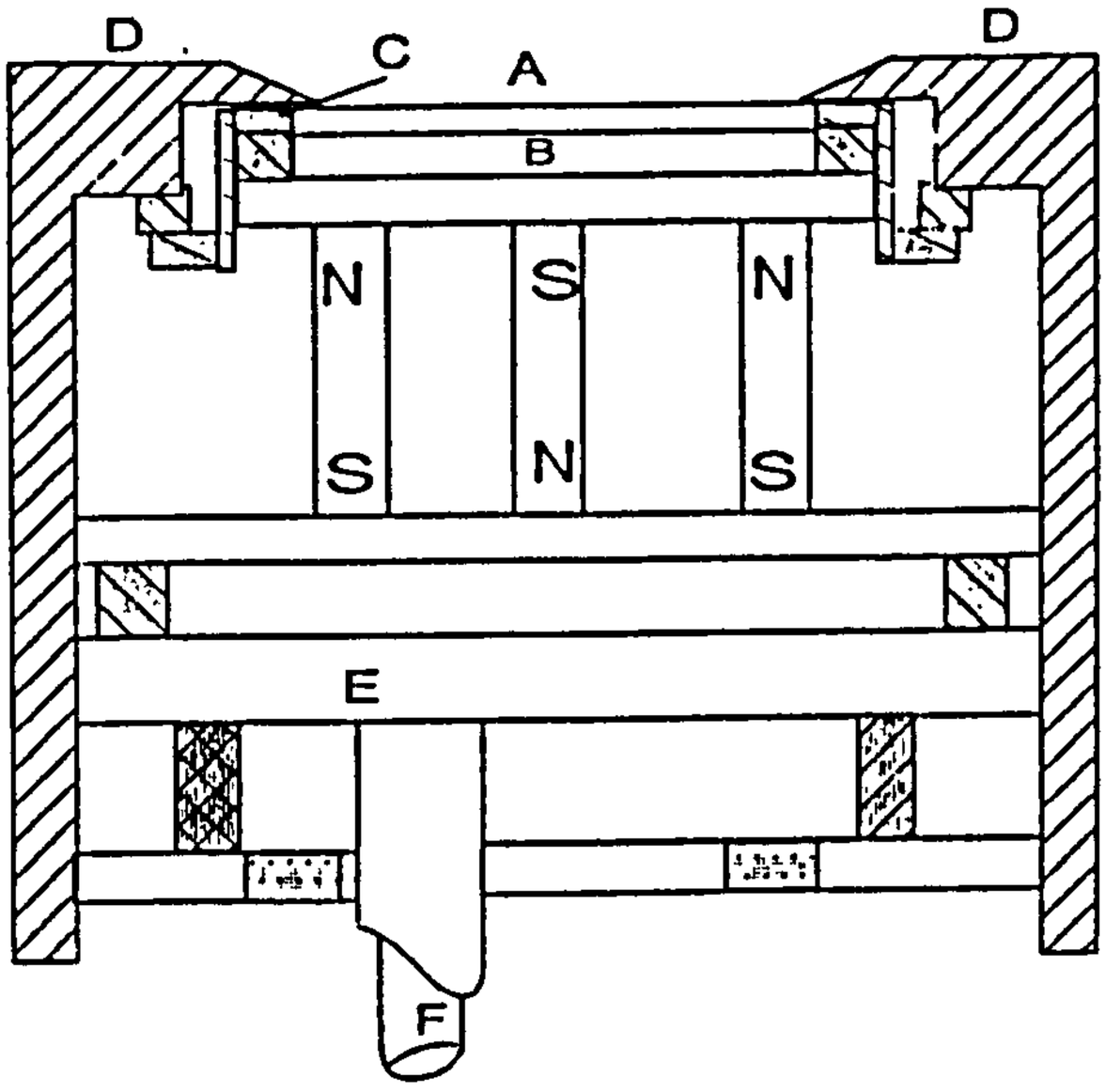

Figure 3.4) Magnetron schematic. Labelled are A) target material, B) copper cathode, C) centring ring, D) ground shield, E) electrode and magnet assembly and F) water cooling pipe.

3.1.3 Reactive Sputtering

This process is identical to the one discussed above with a partial pressure of a reactive gas added to the Ar sputtering gas. The reactive gas here was N_2. Reactive samples were varied by varying the partial pressure ratios of the two gases for which

$$R = \frac{P_{N_2}}{P_{N_2} + P_{Ar}} \qquad (3.2)$$

where R was the ratio of interest, P_{N_2} was the partial pressure of nitrogen and P_{Ar} was the partial pressure of argon in the chamber. There are three mechanisms for incorporation of nitrogen into the material of interest, one at the target, in the plasma and at the sample. At the target the N reacts with the surface forming a phase of Fe-N which would be sputtered from the surface. In the plasma any Fe could react with the N in the chamber. Further the deposited film could react with the N in chamber. These processes in tandem make for a very complex sample deposition process.

3.2 Measurement Techniques

The characterization of samples was concerned with their magnetic and structural properties. This section describes each technique and related analysis techniques used in the results sections. Structural techniques, including transmission electron microscopy (TEM) with sample preparation, X-Ray diffraction (XRD), and X-Ray reflectivity (XRR), are first dealt with, followed by the magnetometry techniques of a vibrating sample magnetometer (VSM) and a superconducting quantum interference device (SQuID). Next, a short discourse on the Magnetic Force Microscope (MFM) and Lorentz microscopy is given. This chapter closes with a treatment of sample preparation procedures including a description of sample deposition.

3.2.1 Structural Measurements

3.2.1a Transmission Electron Microscopy and Sample Preparation

Figure 3.5 shows a schematic of the TEM.

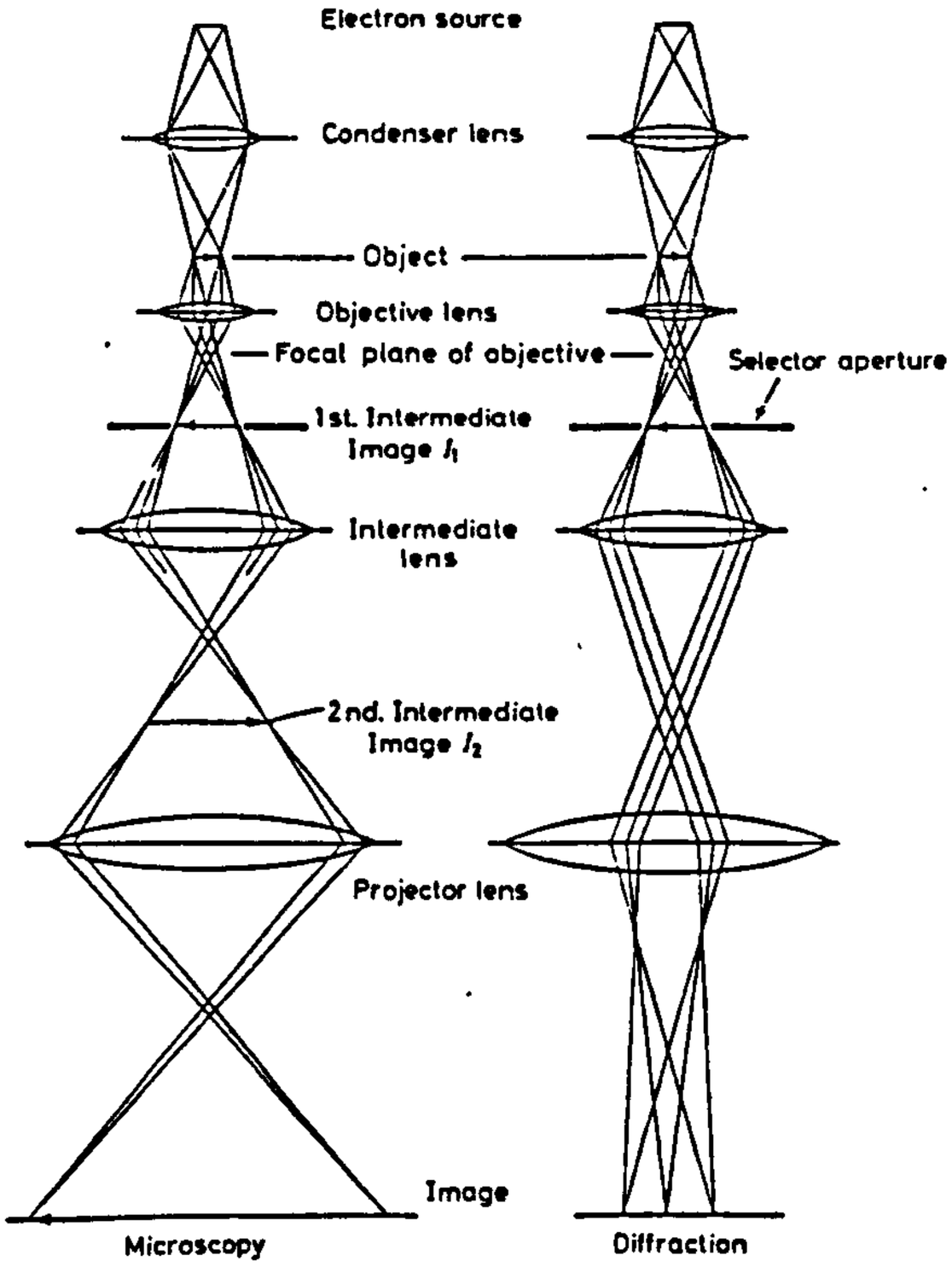

Figure 3.5) Schematic ray diagram of an electron microscope[60].

The basic microscope consists of a filament (electron source), a series of magnetic lenses, used for focusing, the objective aperture and the diffraction aperture and a viewing screen. Electrons are typically thermally emitted, accelerated to the desired energy and directed toward the specimen. Upon interaction with the specimen both elastic and inelastic scattering take place. The elastic scattering takes the form of Bragg diffraction which, in the electron microscope, produces ring patterns for random polycrystalline materials and spot patterns for single crystal materials following the formula[60],

$$D = \frac{2\lambda L}{d}, \tag{3.3}$$

where D is the diameter of a diffraction ring, λ the electron wavelength, L the distance from the sample to the photographic plate or camera length, and d is the interplanar spacing for the specified ring. From equation 3.3 the numerator is a constant for a particular diffraction pattern. This provides a method of calibrating the d-spacing of the diffraction configuration if a feature of known d-spacing is present in the pattern, such as the spots from a single crystal substrate. Hence the quantity Dd of the known pattern can be equated to the corresponding value for the pattern of interest such that:

$$\frac{D_1}{D_2} = \frac{d_2}{d_1}. \tag{3.4}$$

Bright Field (BF) images are produced with the insertion of the objective aperture into the diffraction pattern. This removes the diffracted beam contribution to the image, which consists of transmitted and inelastic scattered electrons. BF images allow for determination of grain size and microstructure.

Inserting the objective aperture and centring it on a specific diffracted ring produces a dark-field (DF) image. Contrast is produced here by the grains having the ring orientation selected by the objective aperture. This is useful when attempting to determine the relative amount of a specific phase or orientation within a sample.

All electron diffraction patterns and bright field images were acquired using 300kV electrons on a Jeol 3010 electron microscope, while the dark field images were acquired on a Jeol 200cx microscope. The d-spacings determined from electron and x-ray diffraction were compared with values from the Joint Conference of Powder Diffraction (JCPDS) data-base to determine the phases present.

TEM specimen preparation of planar samples consisted of a three-step process. The sample was secured to a metal base and cut into a disk three millimetres in diameter. The resulting disk was then secured to another base film side down. The silicon substrate was then worn away by mechanically polishing the disk using a dimpling wheel in the presence of 6 micron diamond paste. When the sample was thin enough, designated by optical transmission of light, the sample was removed from the base and prepared for the ion beam thinner. The ion beam thinner utilizes an argon ion beam, accelerated to a preset energy(≈4 keV), aimed at the disk centre. The beam sputters away the residual silicon left after mechanical polishing. The difference between the two techniques is that the polishing removes quite a bit of material while the ion thinning was a much slower process of removal of material. Each of the samples in this thesis was cooled to liquid nitrogen temperature in order to reduce any annealing effect from the ion beam as any effective annealing could alter the nitride phases present. Ion thinning proceeded until the sample was perforated. At this point the angle of the ion beam was reduced to about 10° with respect to the sample surface to finish the sample.

For cross sections two squares of material were cut in the same manner as for planar samples into rectangles as in fig 3.6a. These were then placed in a stack of virgin silicon secured to one another with resin as in figure 3.6b-c. Curing the resin consisted of subjecting the stack to a furnace at 80° Celsius for about an hour. From this stack a tube was bored out and put into a brass tube such that the sample squares were oriented in the brass tube as in figure 3.6f below.

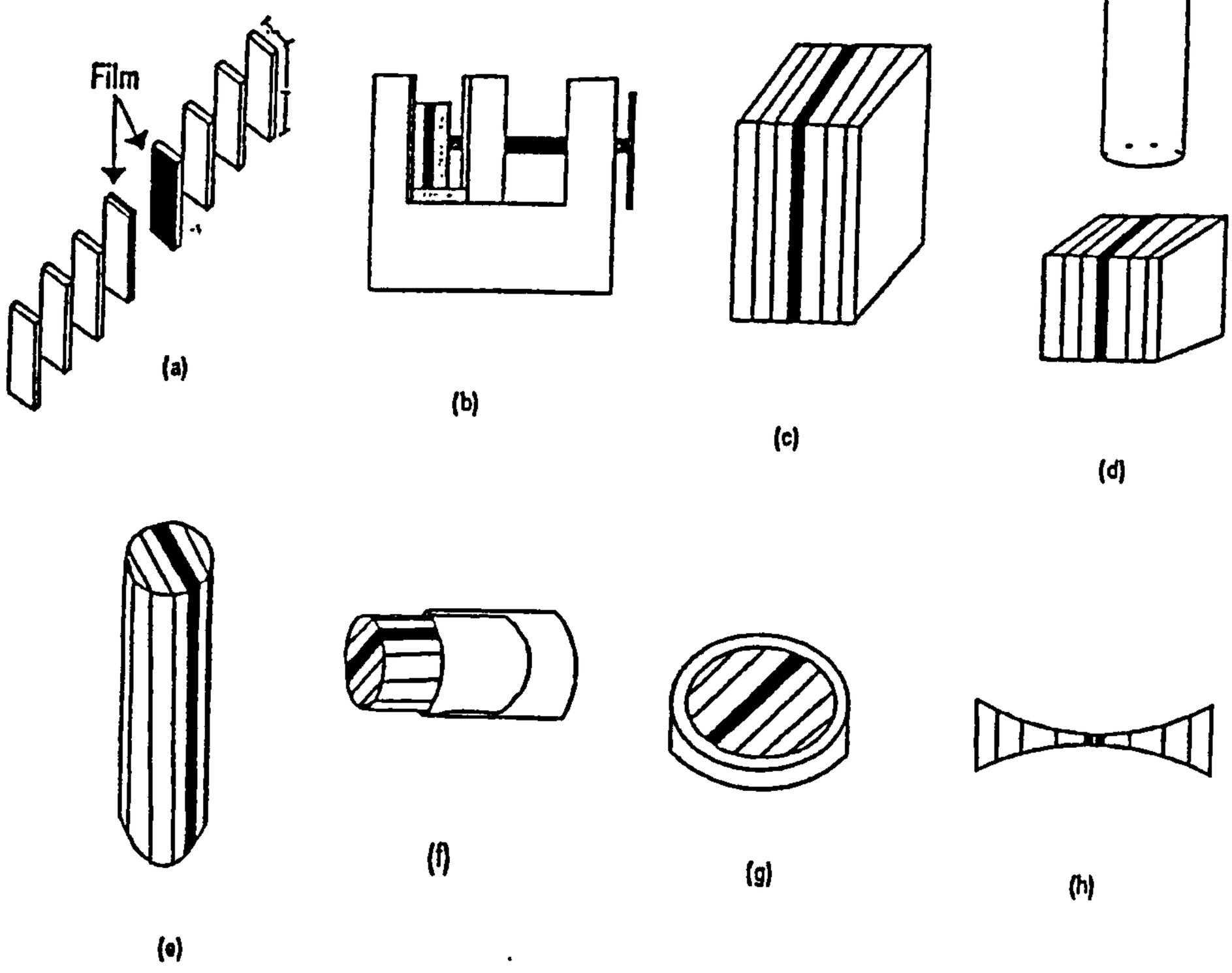

Figure 3.6) State of the sample at the different stages of cross sectional TEM preparation.

At this point a slice of the tube was cut using a diamond saw after which the protocol proceeds as in the case of planar samples. The finished specimens in both cases are of the form in figure 3.6h with a thin enough area for electrons to penetrate near the hole.

3.2.1b X-Ray Reflectivity

X-Ray Reflectivity (XRR) refers to low angle X-Ray diffraction where the x-rays are sensitive to much larger d-spacings. The diffraction of x-rays by a material consists of the constructive and destructive interference due to path differences set up by the periodic nature of a crystal lattice. This phenomenon is well known and follows the Bragg equation, given by[95]:

$$n\lambda = 2d\sin\theta \qquad (3.5)$$

n is the order of interference maxima, λ is the wavelength of the incident radiation, d is the magnitude of the layer thickness, and θ is the incident angle. For small θ the Bragg equation is sensitive to a thickness much larger than the lattice spacing and hence the Bragg condition can be satisfied by interference from the top and bottom of a layer. Shown below in figure 3.7 is a schematic diagram of the experimental set up of a typical θ-2θ scan geometry.

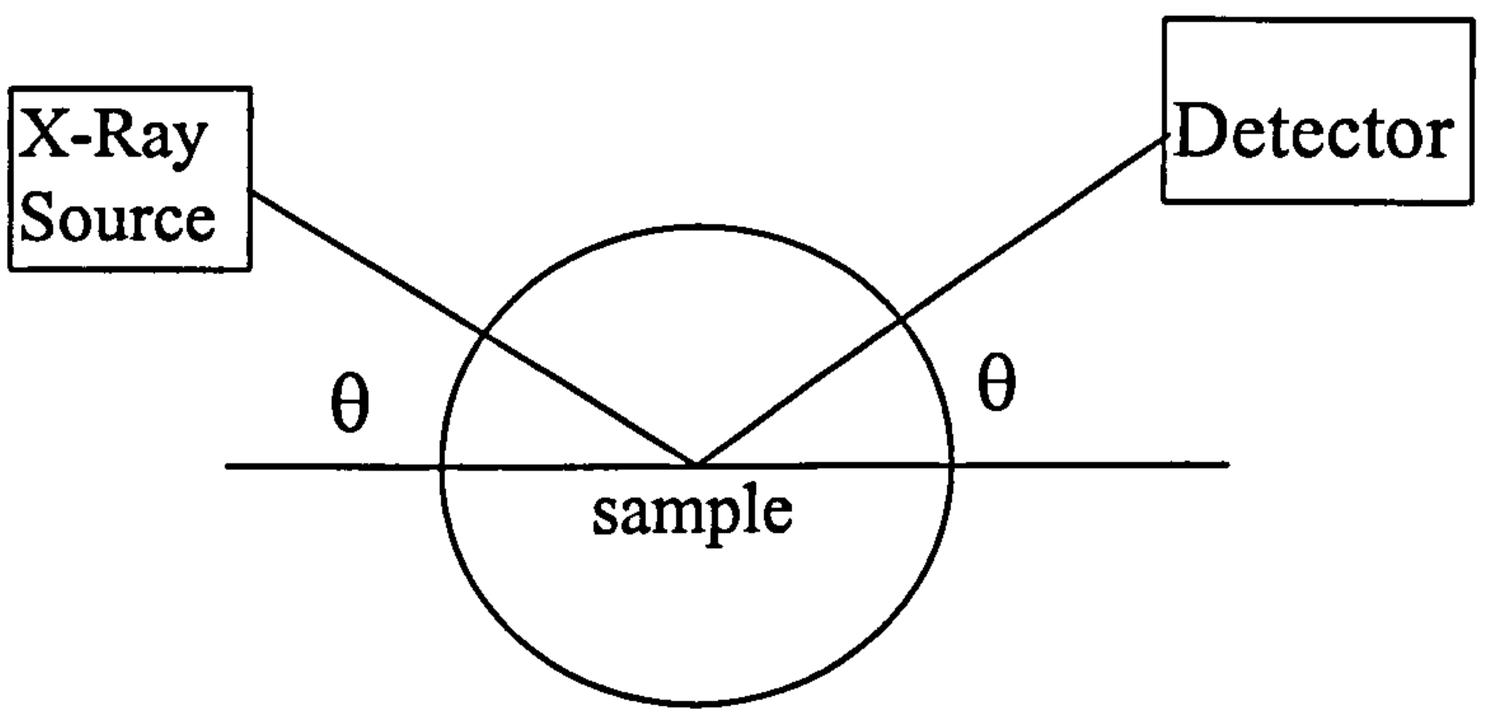

Figure 3.7) X-Ray Reflectivity measurement geometry.

For a single layer interference maxima are set up by waves reflected from the top and bottom of the layer. This produces a set of peaks referred to as Kiessig fringes. Utilizing the angular position of consecutive fringes and the Bragg equation provides a means of extracting the thickness of a thin film. An example of an XRR pattern for a single film is shown in figure 3.8 below.

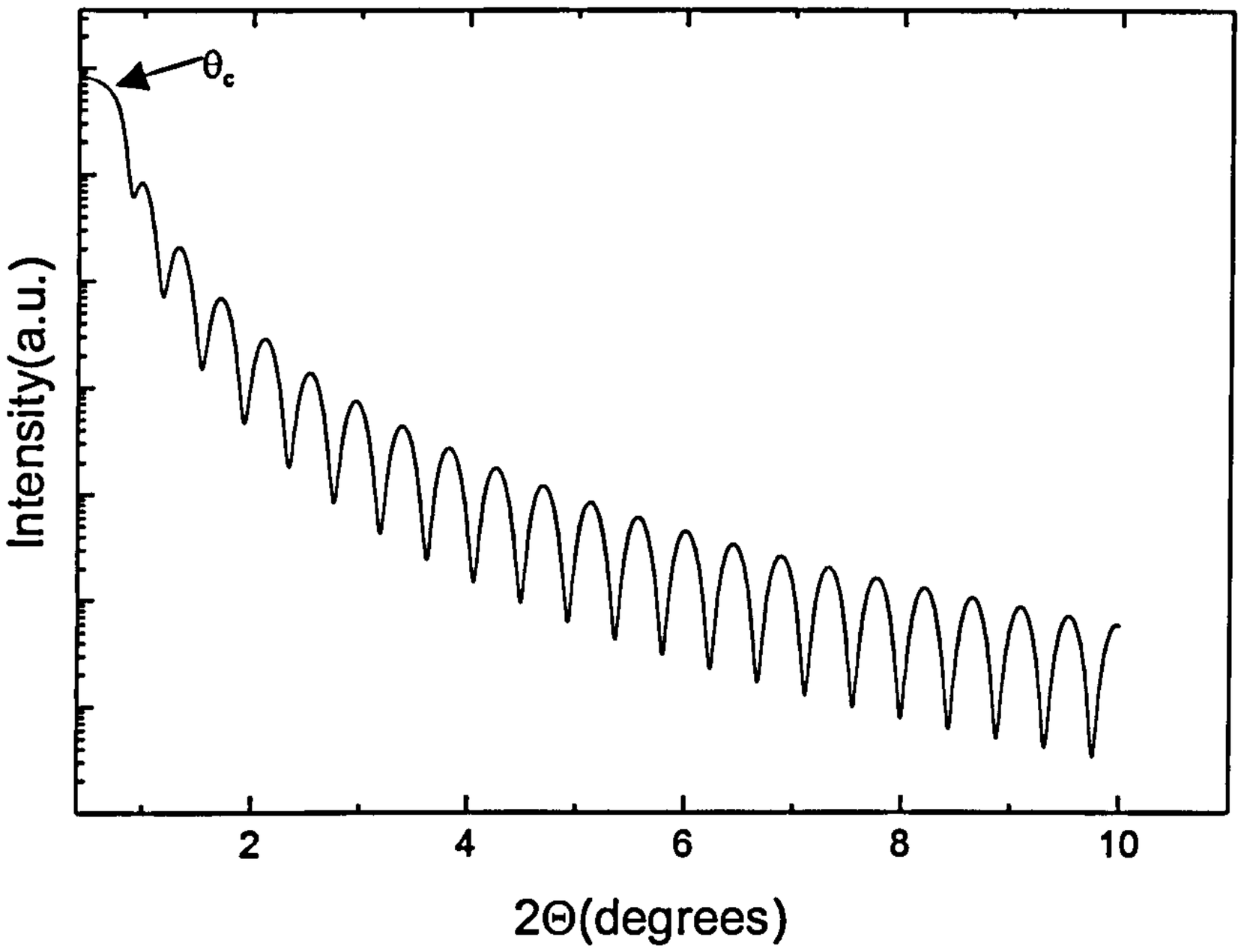

Figure 3.8) Simulated XRR spectra of a single Fe layer with no interfacial roughness.

Several features of importance should be noted from the XRR scan. From the minimum angle up to the critical edge (θ_c) the scan is flat. This is due to total external reflection of the x-rays. Each material will have a characteristic angle at which the x-rays begin to impinge below the surface, know as θ_c. Beyond this angle the intensity of the scan falls as (θ^{-4}).[96] This is due to an increasing amount of destructive interference and attenuation of the beam. Attenuation refers to the phenomenon of absorption of x-rays by a material. Hence for thick specimens the x-rays will only penetrate the sample to a maximum depth. This is also responsible for the decrease in spacing of consecutive Kiessig fringes with increasing angle. This is understood in the sense that the x-rays do not encounter as much material upon reflecting off the bottom interface at higher angles. This poses the problem that not all of the consecutive fringes give a consistent layer thickness. At higher angles there is a convergence to a consistent layer thickness. As seen in the chapters 4 and 5 this property of the XRR pattern will be used to determine the thickness of a single layer

sample. Plotting the thickness found for consecutive fringes vs. the order of the fringe difference and fitting a curve to the data determines the layer thickness.

The development of artificially engineered multilayer films produces materials with an induced periodicity. Multilayers usually consist of two materials layered one on the other, or bilayer, stacked in a periodic fashion as seen in the schematic of figure 3.9.

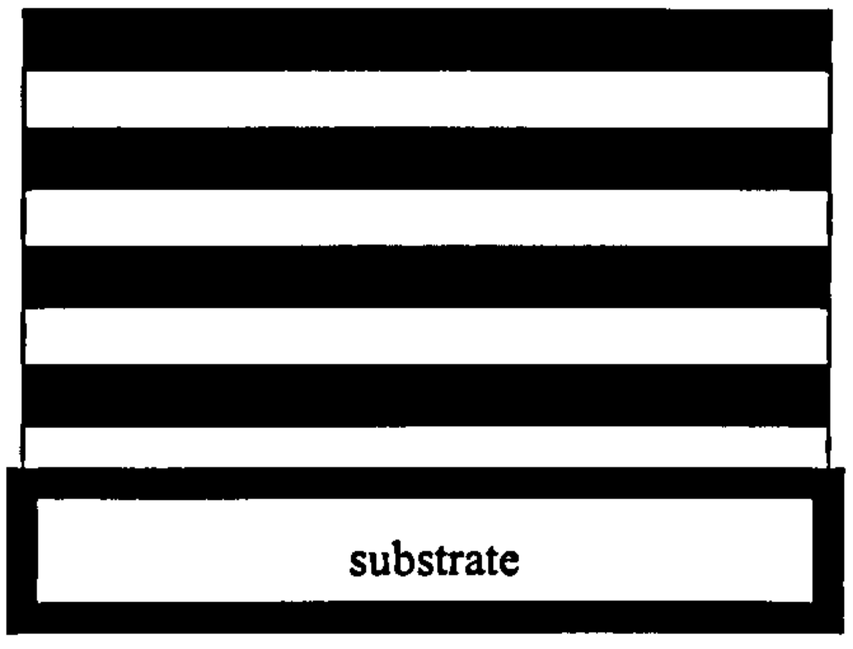

Figure 3.9) Multilayer schematic.

This superlattice structure introduces a periodicity that is elucidated by a set of peaks in the XRR pattern termed multilayer peaks. These peaks are due to constructive and destructive interference at the top and bottom interfaces of the bilayer. From these peak positions, the Bragg equation, and knowing the number of bilayers the sample thickness can be determined. For XRR patterns a correction, attributed to refraction and Snell's Law, to the multilayer peak must be considered that accounts for the critical edge position of the material such that[96],

$$\sin^2\theta = \sin^2\theta_m - \sin^2\theta_c \qquad (3.6)$$

where θ is the corrected value of the peak position, θ_m the peak position measured off the XRR pattern, and θ_c is the angle of the critical edge. Using the corrected θ in the Bragg equation will produce the bilayer thickness after some simple mathematical manipulation. The higher the angle considered here the less effect the correction will incur owing, once

again, to attenuation considerations. All x-ray reflectivity and x-ray diffraction were acquired on a Siemmens D5000 diffractometer using the reflectometry stage.

3.2.1c X-Ray Diffraction

Here again the Bragg equation is of prime importance. The object here is that the x-ray diffraction (XRD) patterns concern a regime of angles for which the x-rays are sensitive to the inter-atomic distances of a crystal lattice. The basic geometry is identical to the reflectivity scenario beyond a shift to higher angle. XRD, like electron diffraction provides a means of phase identification by determining the d-spacing using the Bragg equation.

3.2.2 Magnetic measurements

Magnetic properties of interest required measurement of hysteresis loops using a vibrating sample magnetometer (VSM), which was calibrated using magnetization values from a SQuID magnetometer. An Alternating Gradient Force Magnetometer (AGFM) was used when samples required better sensitivity. Magnetic domains were imaged using the magnetic force microscope (MFM) and Lorentz microscopy to obtain information on the magnetic microstructure.

The values of primary concern, as shown in figure 2.3, in this thesis are the saturation magnetization (M_s) and the coercivity (H_c). The former corresponds to the value of the total moment, when all magnetic moments are aligned by an applied magnetic field, divided by the volume of the measured sample.

The M_s is a measure of magnetic flux produced by a material. The larger the value of M_s a write-head has, the larger its stray field. Hence the field required for switching the magnetic domains that make up the information stored on a computer hard-drive can be larger. The value of H_c is used to separate magnetic materials into two categories. When H_c<100Oe it could be classified as a soft magnetic material. Conversely, when H_c>100Oe it is said to be a hard magnetic material. The work associated with this thesis is concerned with coercivity less than 100 Oe.

3.2.2a Vibrating Sample Magnetometer and SQuID

Originally developed by Foner[61], the vibrating sample magnetometer (VSM) is used to acquire magnetic hysteresis loops. As shown in figure 3.10 it consists of an electromagnet, a sample probe, and two sets of pick-up coils.

The sample of interest is secured to the sample probe such that the sample is centred with the set of pick-up coils. The sample is then vibrated at a frequency of 80 Hz[30] whilst the electromagnet is ramped through a specified field (H) range from positive to negative field and back again in discrete steps specified by the user and within the resolution of the magnetometer. By Faraday's law of induction, the vibrating magnetic sample sets up an emf in the pick-up coils. As the direction of magnetization of the sample changes in response to the applied field there is a varying emf set up that when plotted as a function of H produces a multi-valued function that is a hysteresis loop. Two sets of coils are required to negate the signal due to the applied field. This is accomplished by having the two sets wound in an opposite sense to one another. Hence, the signal set up in one set of coils by the applied field is subtracted from the other set and the remaining signal is due to the sample. The sample signal is produced by the horizontal stray field. The VSM provides a voltage as the output. This voltage is directly proportional to the moment. In order to determine the magnetization of samples it had to be compared with the signal strength of a standard sample of known magnetization. The M_s values used in this thesis were calibrated with a standard sample that consisted of one of the experimental samples, for which the M_s value was determined from SQuID magnetometer measurements obtained at the University of Sheffield. The moment attained was divided by the volume of the sample determined from the thickness extracted from XRR and measured dimensions of the sample. The standard sample was measured on the VSM and compared to the moment determine by the SQuID measurement. The VSM was an in-house system that was computer controlled with an optimum field step resolution of 5 Oe.

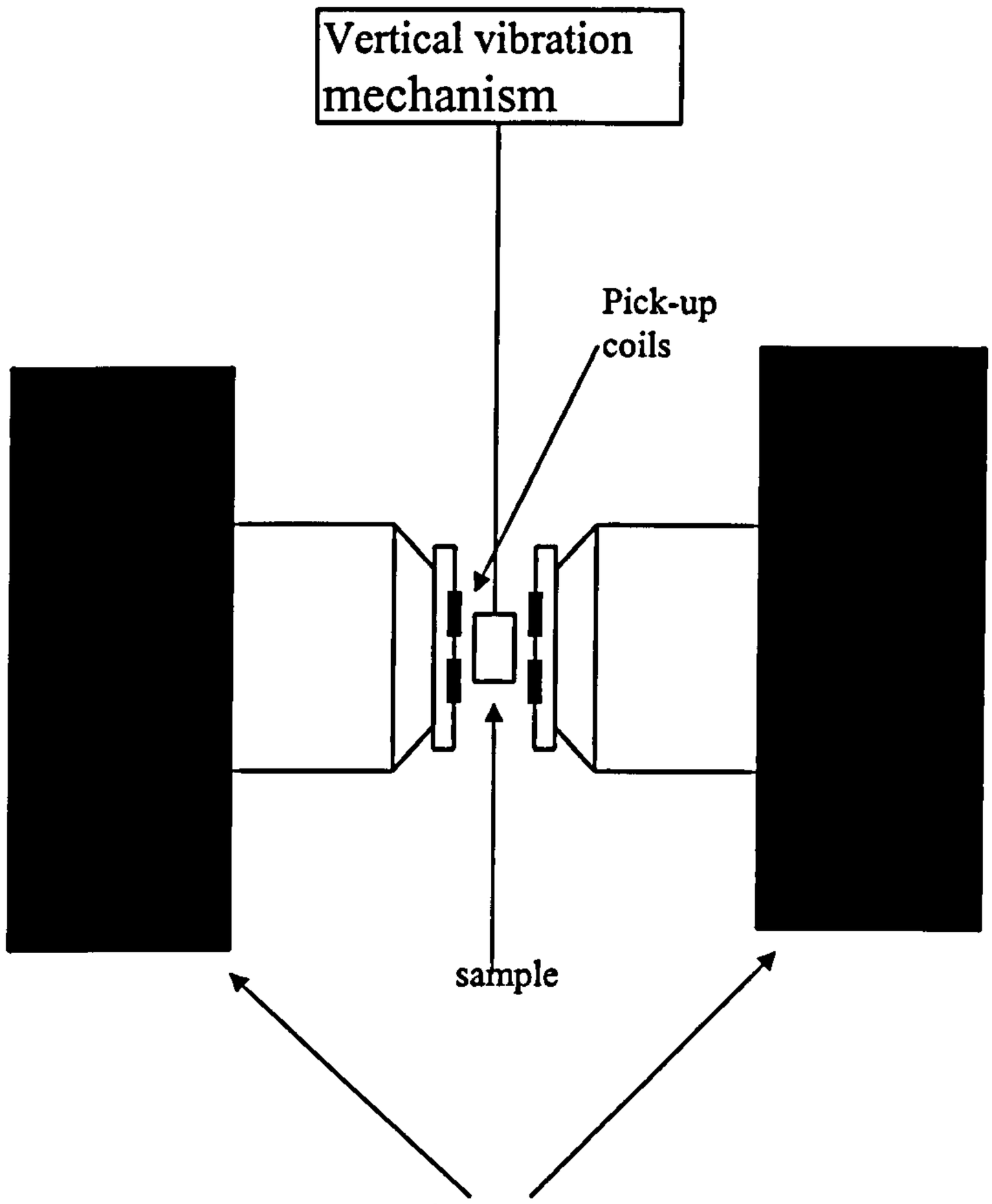

Figure 3.10) Schematic diagram of a VSM.

A Superconducting Quantum Interference Device (SQuID) is a highly sensitive magnetometer that utilizes superconducting technology to measure the magnetization of a sample. A true SQuID uses the quantum interference signal set up by Josephson junctions in a double slit geometry to enhance a signal produced by vibrating a sample through a superconducting coil. In some SQuID magnetometers there is no quantum interference set up by Josephson junctions. In this class of SquID, sensitivity is still higher than a VSM since there is no resistance loss of signal in the superconducting wires. SQuID magnetometers are capable of sensing moments down to the level of 10^{-10}emu while the best commercial VSMs quote sensitivities of 10^{-8} emu.

b. 3.2.2b Alternating Gradient Force Magnetometer (AGFM)

An Alternating Gradient Force Magnetometer provides a sensitive method of obtaining a magnetization curve. A specimen is vibrated at resonance by an oscillating magnetic field while it is stepped through the applied field of the hysteresis loop. The AGFM used in this work required mounting the sample on a glass plate on a thin quartz rod attached to the piezo-electric bimorph. The sample is subjected to a varying oscillating magnetic field gradient whilst held in a dc magnetic field strong enough to saturate the sample. Measurements are taken with the ac field gradient operating at the resonant frequency of the sample system. The piezo-electric bimorph produces a positive or negative voltage depending on the direction it is flexed. A magnetization curve is produced by measuring the voltage at specified intervals as a dc field is cycled from positive to negative fields and back, such that the field gradient applies a force on the sample where:[57]

$$F = M(H)\frac{\partial H}{\partial x} \qquad (3.7)$$

where F is the force, M(H) the magnetization at a field H and the partial derivative is the field gradient. The AGFM described here is after Flanders[57].

3.2.2c.) Magnetic Force Microscope

A Magnetic Force Microscope (MFM) utilizes a cantilever tip coated with a magnetic material that oscillates above the sample surface at a resonant frequency. Magnetized along its long axis, the tip is repelled or attracted in the field gradients above the sample surface. This deflection of the cantilever moves the cantilever off resonance corresponding to a phase shift that produces the contrast seen in an MFM image. The images produced for this thesis were taken on a Digital Instruments 3000 MFM using a commercially available CoCr coated tip.

As mentioned in chapter 1 the test for weak or strong stripe domains requires imaging the domains in the presence of a magnetic field. Shown in figure 3.11 is the sample stage used to acquire MFM images of samples in a magnetic field.

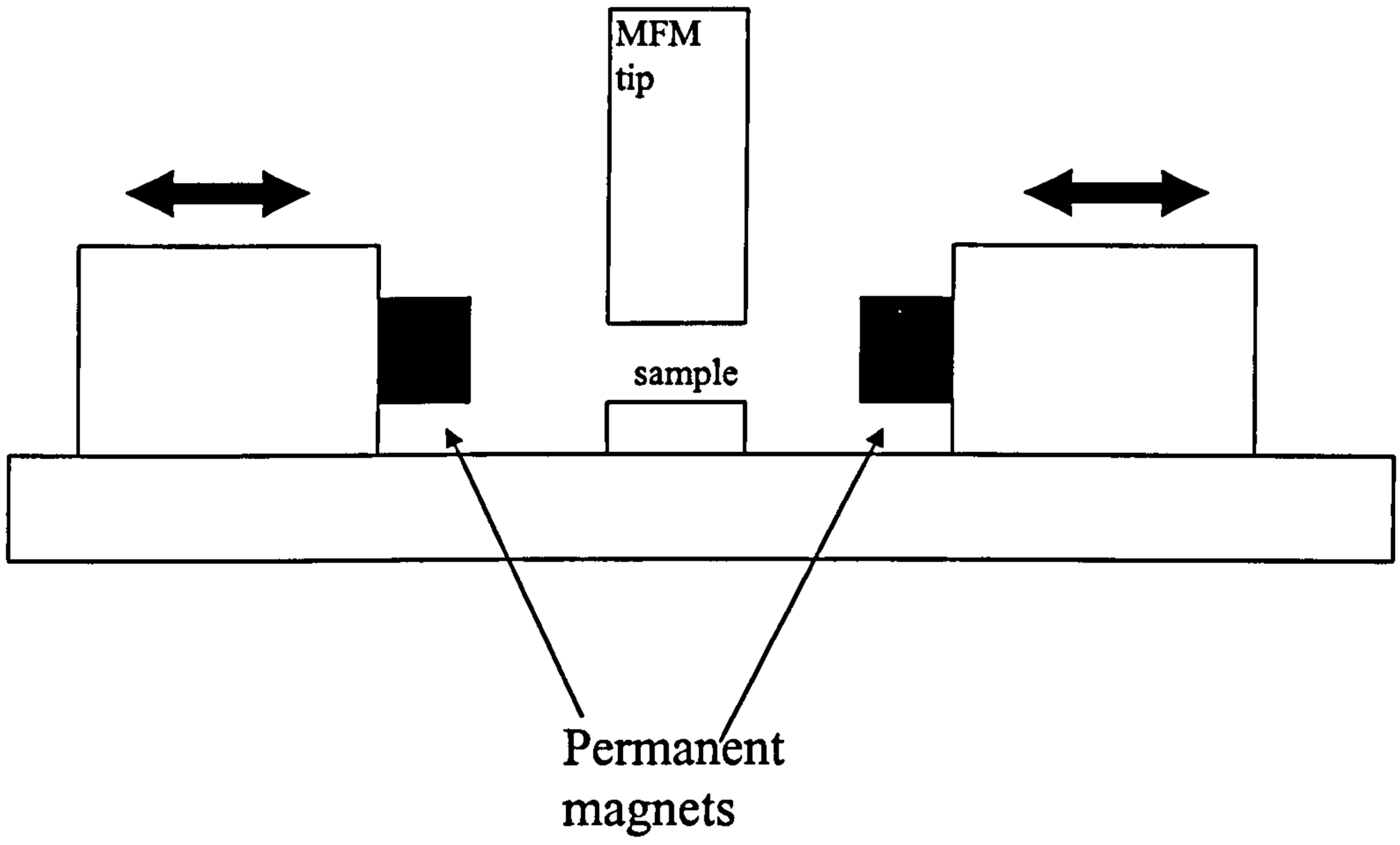

Figure 3.11) Schematic diagram of the MFM Field stage used.

The stage consisted of a brass base plate, two permanent magnets and a rotary drive motor. By applying a positive or negative voltage to the motor the two magnets could be positioned at specified distances from the sample of interest. The predetermined distances corresponded to field values between about 262 Oe at the closest point to 39 Oe. So without having to change the sample position the magnets were wound from high to low field strength positions allowing for reproducible imaging of the same sample area.

3.2.2d.) Lorentz Microscopy

Lorentz microscopy takes advantage of the Lorentz force[83],

$$F = q(\vec{v} \times \vec{B}) \qquad (3.8)$$

in the electron microscope. The deflection of electrons due to this interaction with a magnetic specimen produces domain wall contrast from interference from electrons deflected by neighbouring domains. There are two primary methods of domain observation in the TEM, the Fresnel method and the Foucault method. The Fresnel method utilizes a

defocusing of the image to produce domain wall images as schematically shown in figure 3.12.

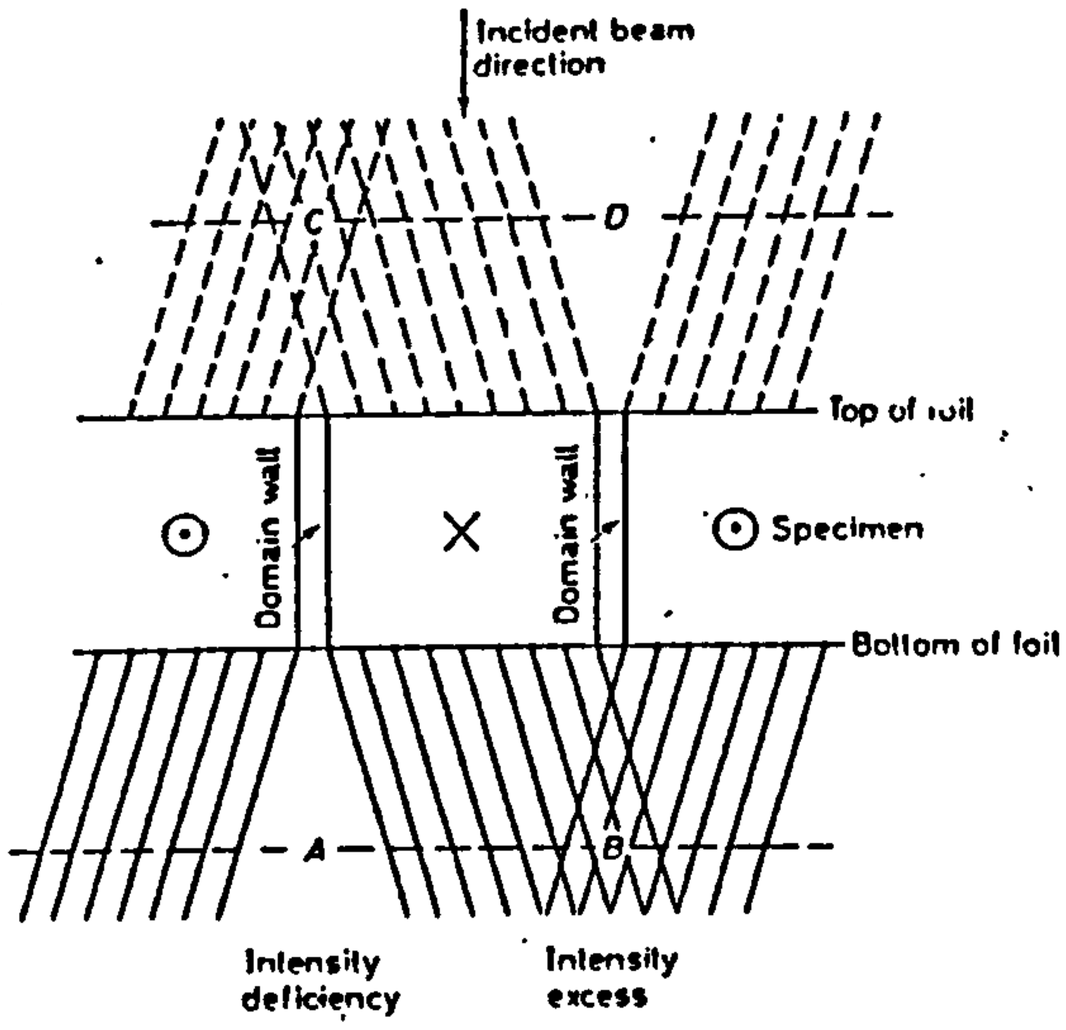

Figure 3.12) Schematic diagram of the electron paths in Fresnel imaging[60].

Foucault images utilize an in-focus image for which part of the incident, zeroeth order beam is covered by the objective aperture thus producing domain images. In this scenario the ideal situation is concerned with a through beam that has been sufficiently split by the interaction with adjacent domains. Hence one half the beam corresponds to domains magnetized in one direction while the other through beam pertains to the antiparallel aligned domains. Blocking out one of the two is analogous to the technique of producing Dark Field images. One of the advantages of the Foucault technique is that it produces an in-focus image allowing for the elucidation of the effect of inclusions or dislocations or other defects on the domain structure.

3.3 Samples

This thesis concerns itself with two sets of samples made with a combination of dc magnetron sputtering and a nitrogen atom source. Both sets incorporate a multilayer

structure obtained by alternating between the atom source and a magnetron. The samples will be discussed in terms of an effective bilayer consisting of the metal thickness deposited and the time it was subsequently exposed to nitrogen. This was necessary since the incorporation of nitrogen forms a bilayer constituent that detracts from the respective bilayer component. In the present case the materials of interest are Fe and $Fe_{80}Ti_{20}$ alloy targets. A quick look at the FeTi phase diagram as in figure3.13[61] shows this to consist of a mix of α-Fe and Fe_2Ti.

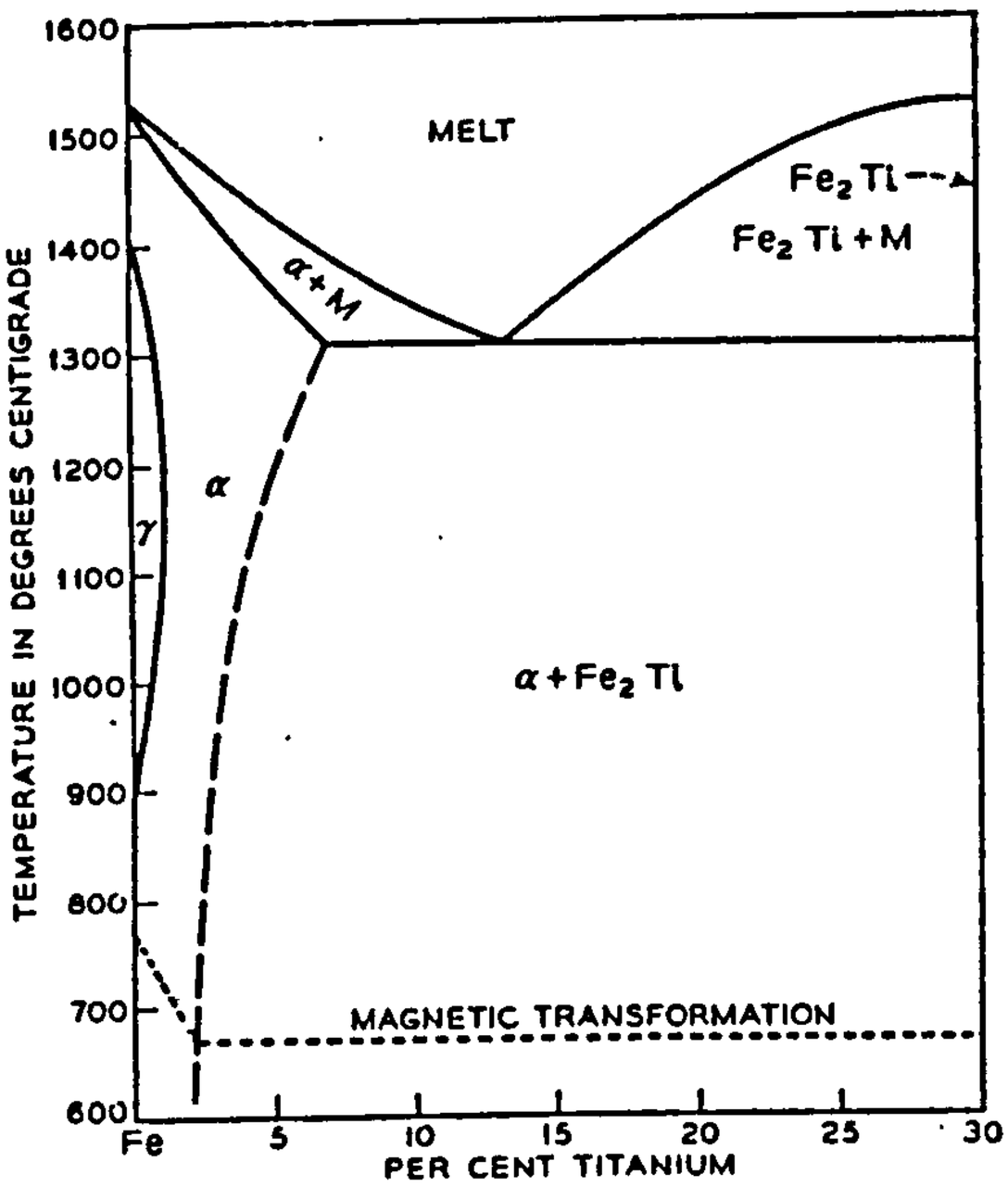

Figure 3.13) FeTi phase diagram[61].

The first set of samples as discussed in chapter 4 of this text will be referred to as the Fe/FeN sample set. This set consists of samples with Fe deposition times ranging from 10 seconds to 120 seconds. For a calibrated deposition rate of 0.7 Å/sec this nominally means that layers between 7 and 84 Å thick were exposed to the atomic nitrogen beam. Nitrogen exposure times ranged between 5-30 seconds. Samples were made up of ten or twenty such layers successively stacked. For thick bilayers, fewer bilayers were deposited such that samples remained in a thickness regime suitable for XRR measurements. Beyond about 1000 Å thick XRR becomes ineffective due to absorption effects. The thickness regime was also chosen in an effort to exploit the strain and epitaxy typical of thinner layers before there is any relaxation of the lattice to the bulk values. The above

conditions provided for samples with total thickness between 200-1000Å. Table 3.1 below lists the Fe/FeN sample conditions considered here.

Sample	Fe layer thickness(Å)	N exposure time(sec)	base pressure (mbar)	Ar pressure (1×10^{-3} mbar)	atom source RF power (watts)	number of effective bilayers	N_2 partial pressure (1×10^{-3} mbar)
V17(reactive)			$5.5*10^{-9}$	4.7			0.3
V20(reactive)			$5.5*10^{-9}$	4.4			0.6
V26(reactive)			$5.5*10^{-9}$	3.7			1.3
V66	7.0	30	$3*10^{-8}$	2.0	550	25	
V73cal	248	0	$2*10^{-8}$	2.0	550	0	
	was a single Fe film deposited with atom source running but no direct exposure to the beam.						
V74	14	30	$2.5*10^{-8}$	2.0	550	20	
V75	630	240	$2*10^{-8}$	2.0	550	1	
V76	630	120	$2.5*10^{-8}$	2.0	550	1	
V77	630	30	$2.5*10^{-8}$	2.0	550	1	
V78	630	360	$2*10^{-8}$	2.0	550	1	
V80	21	30	$2*10^{-8}$	2.0	550	20	
V81	42	5	$2*10^{-8}$	2.0	550	20	
V82	42	30	$2*10^{-8}$	2.0	550	20	
V84	420	0	$3.5*10^{-8}$	2.0			
V84	was used as calibration of new target as well as a control to compare to nitrided samples						
V85	84	30	$1.5*10^{-8}$	2.0	550	10	
V87	42	60	$1.5*10^{-8}$	2.0	550	20	

Table 3.1. Sample list for the Fe/FeN series. The atom source was run at 5×10^{-5}mbar N_2 partial pressure for all samples where relevant.

All samples were deposited with an atom source power of 550 watts and a nitrogen pressure of 5×10^{-5}mbar. Hence the changing variables are the times of N exposure and Fe thickness deposited between exposures. This effectively varies the ratio of Fe to N in the sample. Further consideration of the implications of these variables on magnetic and structural properties is left to chapter 4.

The second set of samples, referred to as FeTi/FeTiN, looks at the affect of Ti on the nitriding of Fe. Here the Fe/FeN sample set was repeated using the FeTi sputtering source. After calibration of the target the appropriate conditions were chosen such that the FeTi deposition rate was 0.8Å/s. Table 3.2 gives a list of the deposition conditions

considered. All samples were deposited onto Si (100) substrates with a native oxide layer present.

Sample	FeTi layer thickness(Å)	N exposure time(sec)	base pressure (mbar)	Ar pressure (1×10^{-3} mbar)	atom source RF power (watts)	number of effective bilayers	N_2 partial pressure (1×10^{-3} mbar)
VI1	480	0	$5.*10^{-8}$	2.0			
VI3	48	30	$2*10^{-8}$	2.0	550	20	
VI4	8.0	30	$1.5*10^{-8}$	2.0	550	20	
VI5	24	30	$1.5*10^{-8}$	2.0	550	20	
VI6	96	30	$1.5*10^{-8}$	2.0	550	10	
VI7	16	30	$1.5*10^{-8}$	2.0	550	20	
VI8	48	5	$1.5*10^{-8}$	2.0	550	20	
VI9	48	60	$1.5*10^{-8}$	2.0	550	20	
VI11(reactive	693		$1.5*10^{-8}$	2.0			0.1
VI12(reactive	455		$1.5*10^{-8}$	2.0			0.3
VI13	308		$1.5*10^{-8}$	2.0			0.7

Table 3.2. Sample list for the FeTi/FeTiN series. The atom source was run at 5×10^{-5}mbar N_2 pressure for all samples, where relevant.

There are three features that make this study unique in contributing to the knowledge base of the study of nitriding of Fe. This work uses atomic N rather than N_2 as in reactive sputtering. The bilayer thickness of the multilayer samples is much less than previously considered[55-57], and the Ti is in the alloy target rather than as chips on an Fe target[50, 51]. The first is related to the reactivity of the system. Atomic N is a free radical and hence more reactive than N_2, in considering the reaction kinetics and its affect on phase formation, the nitriding post Fe deposition takes on an air of oxidation as discussed in chapters 4 and 5. In utilizing thin bilayers it was hoped that any epitaxial growth might promote the formation of different phases of Fe nitride through stress effects between layers, along with a competition between the energy of the lattice and reaction energy between the Fe and N. Previous work on the FeTiN system has focused on the stabilization of $Fe_{16}N_2$ to temperatures in excess of 500°C[51]. This phenomenon has been

attributed to the formation of TiN clusters within the material[50, 51]. Jack[14] has suggested that addition of small amounts of a number of transition metals, including Ti, would have such an effect. Jack's impetus was not the incorporation of a second phase, but an altering of the reaction kinetics of the system. It is well known that in reactive sputtering there is a reaction of material with the reactive gas at the target surface as well as within the plasma. Hence it may be speculated that the TiN clusters are an artifact of the reactive sputtering with the Ti chips. Here this ambiguity is removed and chapter 5 discusses the results and the implications.

Chapter 4 Results-Fe/FeN

4.1 Introduction

As discussed in chapter 1 the structural and magnetic properties of Fe are very sensitive to the amount of nitrogen present. This chapter considers two sets of samples. The first includes a variation of the initial Fe layer thickness for a constant nitrogen exposure time. The Fe layer was varied from 7 to 84Å and the nitrogen exposure time was 30 seconds. The second looked at the effect of varying the nitrogen exposure time for a constant Fe layer thickness. The Fe layer thickness used was nominally 42Å while the nitrogen exposure time was varied from 5 to 60 seconds. Structural data discussed here include X-Ray reflectivity scans, TEM diffraction patterns (DPs), bright field images as well as some high angle X-Ray diffraction (XRD). The second part of the chapter considers the magnetic properties from VSM, MFM, and Lorentz microscopy measurements. The last section of this chapter gives a discussion of the results.

4.2 X-Ray Reflectivity

Figure 4.1 shows a scan of a sample for which the effective bilayer was 7Å Fe and 30 seconds nitrogen repeated 25 times.

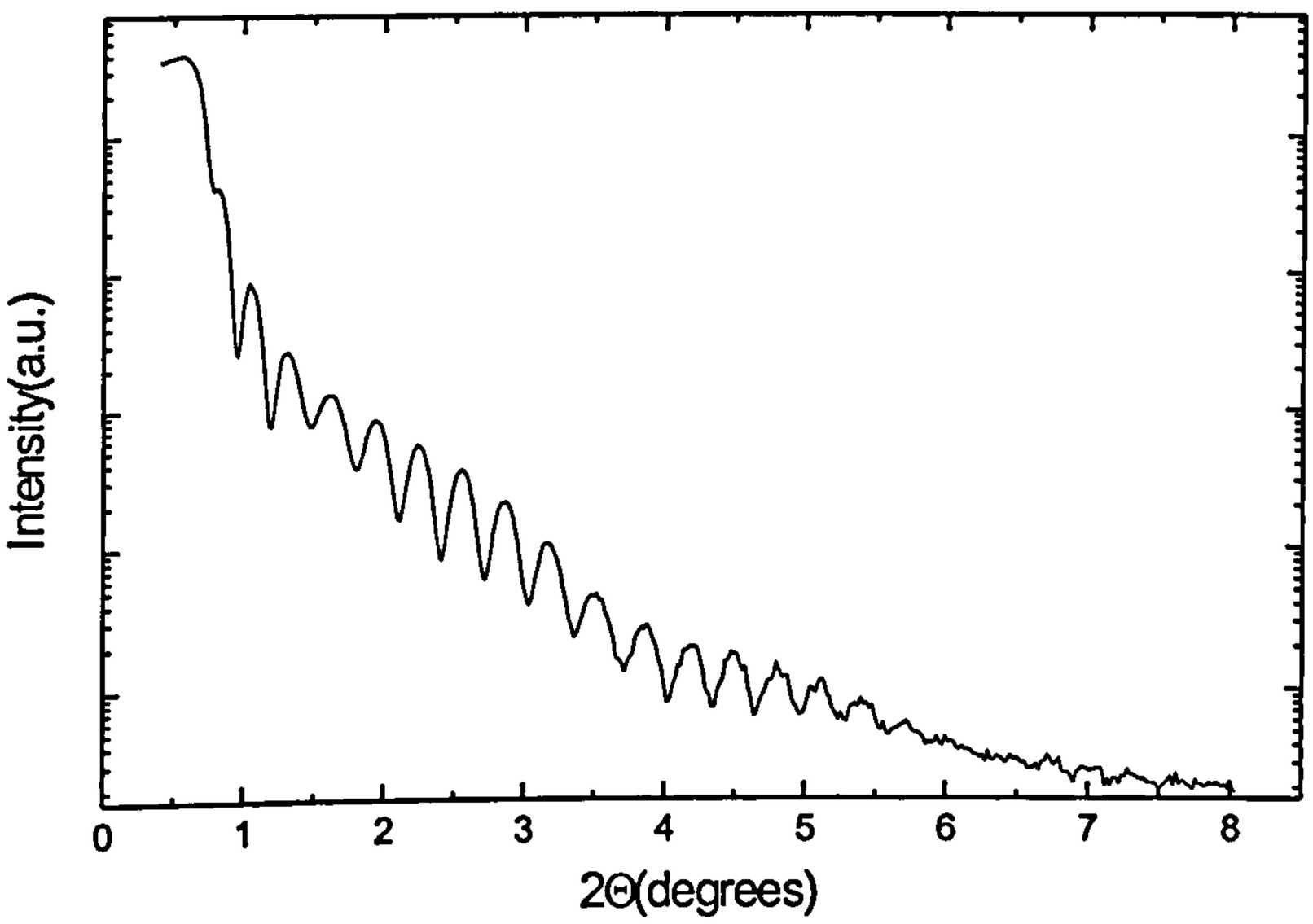

Figure 4.1) XRR scan of v66 (7Å Fe/30 sec N).

The thickness determined from the convergence of the film thickness calculated from consecutive Kiessig fringes in the scan was 270Å. Despite the deposition technique the scan is characteristic of a single layer with only a hint of a superimposed oxide layer. If the Fe layers are considered alone the total thickness of the film without nitrogen exposure for the whole of the sample would be 25×7=175Å thick. Hence the nitrogen has expanded the thickness by about 37%.

Increasing the initial Fe layer thickness in the effective bilayer to 14Å gave a reflectivity scan as shown in figure 4.2 below.

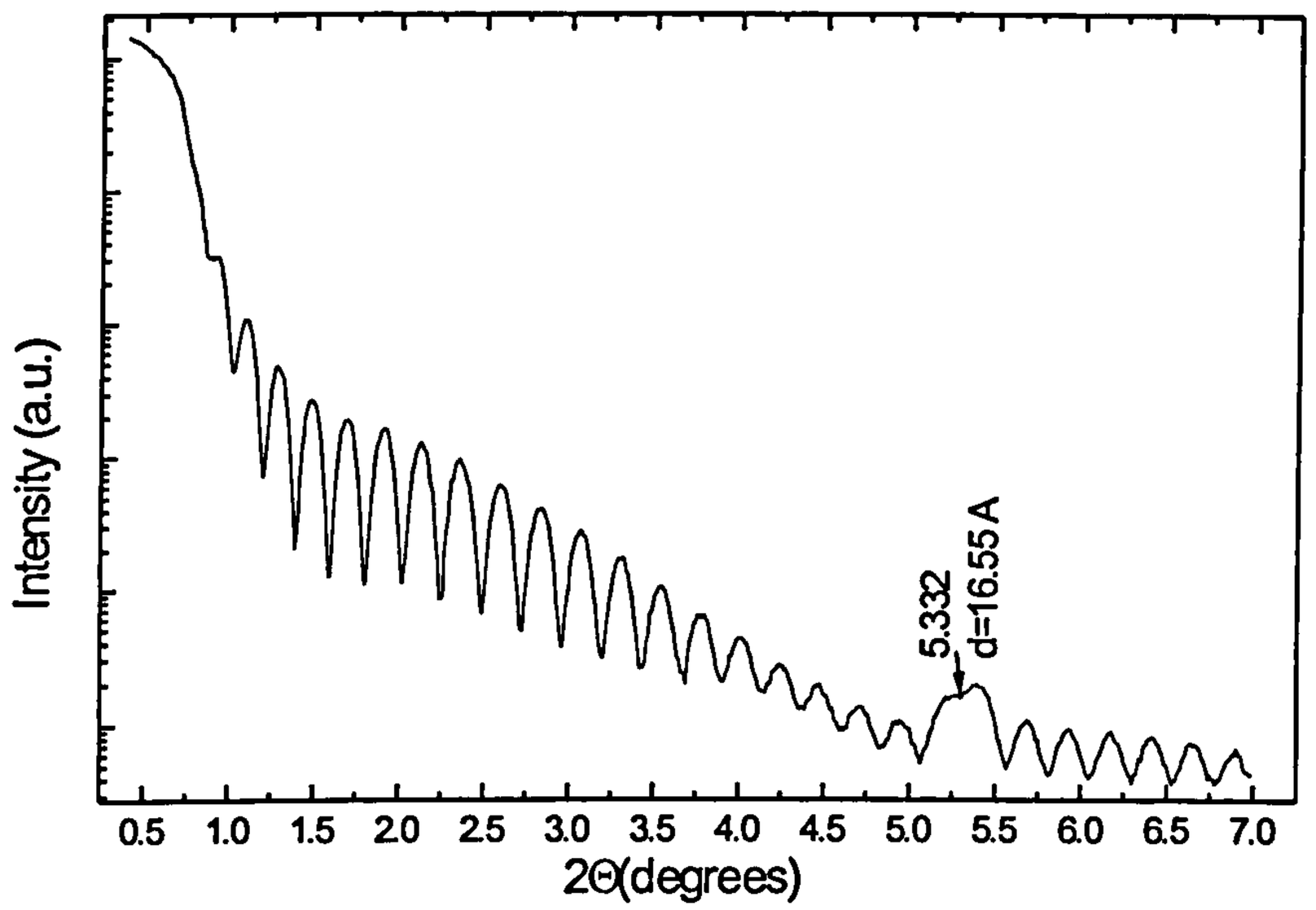

Figure 4.2) XRR of v74 (14Å Fe/30 sec N).

At 2θ=5.332° there is a multilayer peak due to constructive interference from a bilayer periodicity. Application of the $\sin^2$ correction gives a bilayer thickness of 16.6Å and a total thickness of 333Å. Here, there is a slightly more prominent oxide layer contribution to the scan as seen by the large period oscillation of the Kiessig fringes in the region of 2θ=2.5°. Considering the total thickness of the Fe layers the total thickness of the film is approximately 20×14=280Å, corresponding to an approximate expansion of 18.9%.

Figure 4.3 shows a reflectivity scan for a sample with an effective bilayer of 21Å Fe and 30 seconds nitrogen exposure.

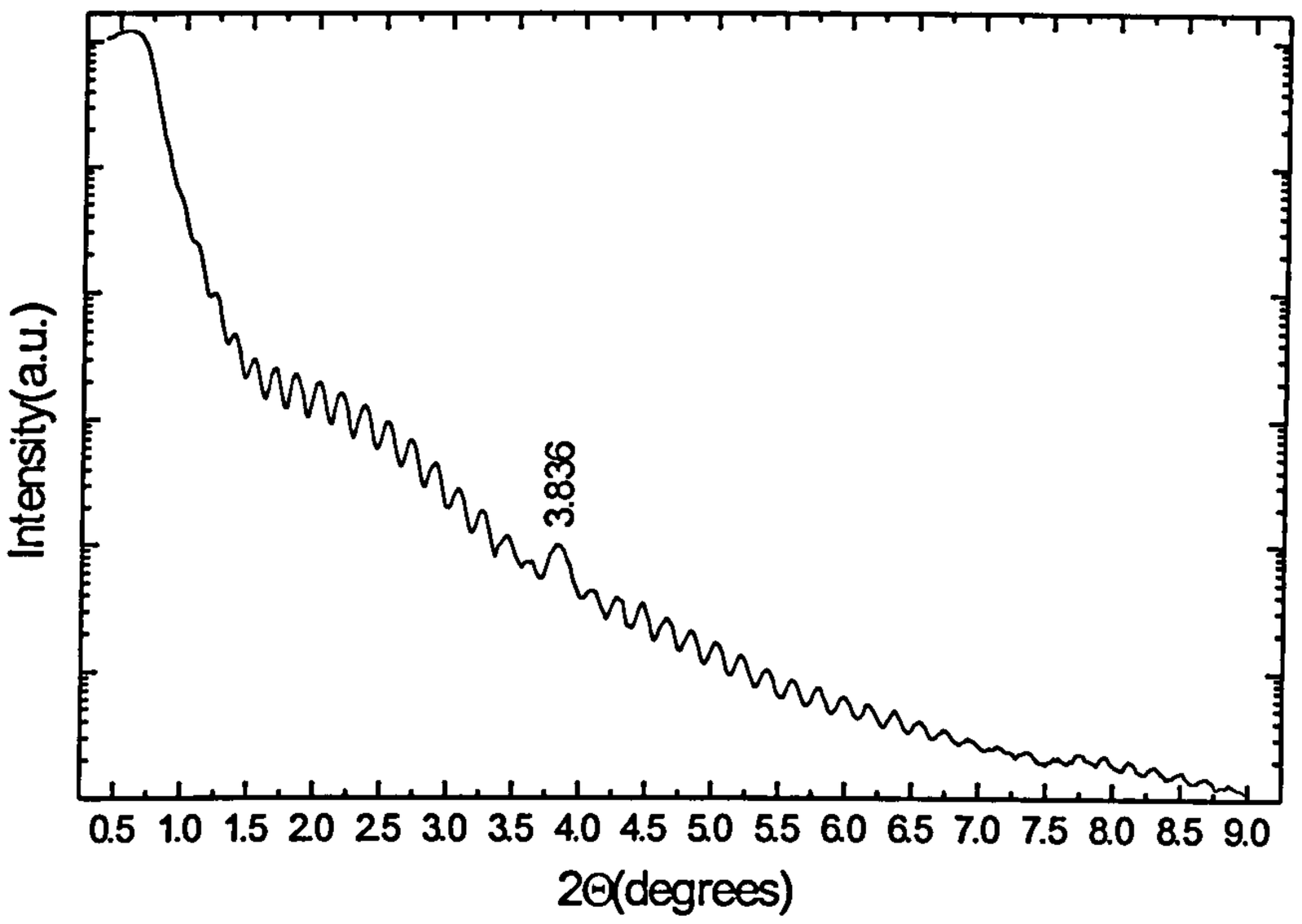

Figure 4.3) XRR of v80 (21Å Fe/ 30 sec N).

The most prominent feature in this scan is the multilayer peak at $2\theta=3.836°$. The peak is sharper and hence indicative of sharper interfaces in the multilayer. Applying the $\sin^2$ correction to this peak gives a bilayer thickness of 23.3Å and a total thickness of 467Å. As expected the bilayer thickness is increasing as evidenced by a shift of the multilayer peak to a lower angle. The Kiessig fringe intensities are significantly reduced from the levels of the previous sample. Here the effect of attenuation is evident. For thicker films fewer x-rays are reflected from the film/substrate interface. Expansion of the film here is small and approaches the error of measuring the thickness using the $\sin^2$ correction.

Further increasing the Fe layer to 42Å gave the reflectivity scan shown in figure 4.4. In figure 4.4 there are two multilayer peaks with no oxide periodicity evident. The first and second order multilayer peaks occur at $2\theta = 2.131$ and $4.025°$ respectively. The critical edge is shown at $2\theta=0.584°$. Applying the $\sin^2$ correction to the second order peak gives a bilayer thickness of 44.2Å which is a 5.5% expansion of the initial 42Å Fe layer. Here again the error involved in measuring the appropriate angles makes the

expansion negligible. The Kiessig fringes have continued to reduce in amplitude and the multilayer peaks are indicative of good quality interfaces.

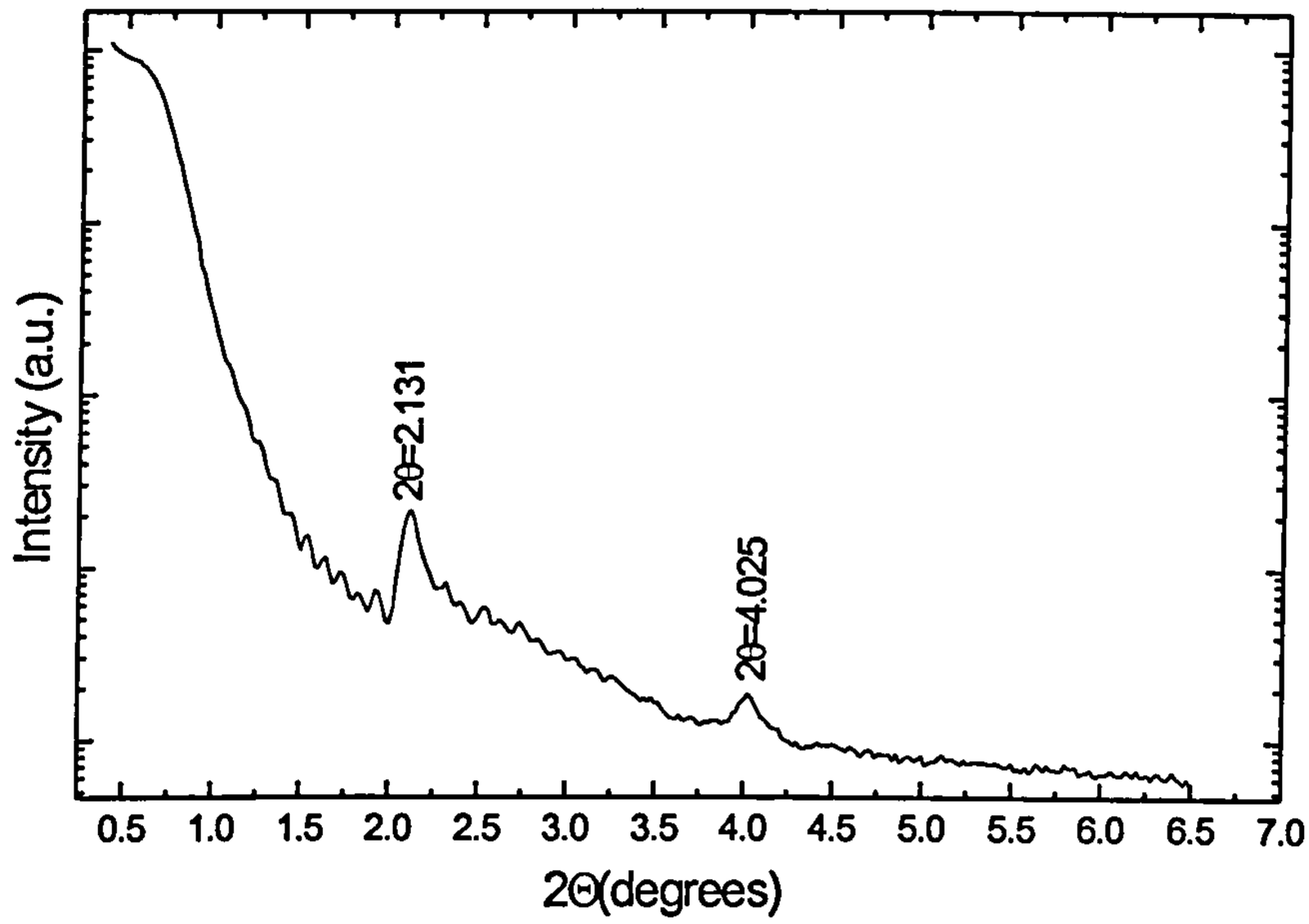

Figure 4.4) XRR of v82 (42Å Fe/ 30 sec N).

Figure 4.5 shows a reflectivity scan of a sample with an effective bilayer of 84Å Fe and 30 seconds nitrogen exposure. Three multilayer peaks are evident. The first order peak at $2\theta=1.301°$ is an intensity dip corresponding to destructive interference set up by the relative thickness of the bilayer. The second and third order peaks at $2\theta= 2.170°$ and $3.098°$ respectively are as in the previous cases due to constructive interference. Applying the $\sin^2$ correction to the third order peak amounts to a bilayer of 87.7Å and total thickness of 877Å given that this sample consists of 10 bilayer repeats.

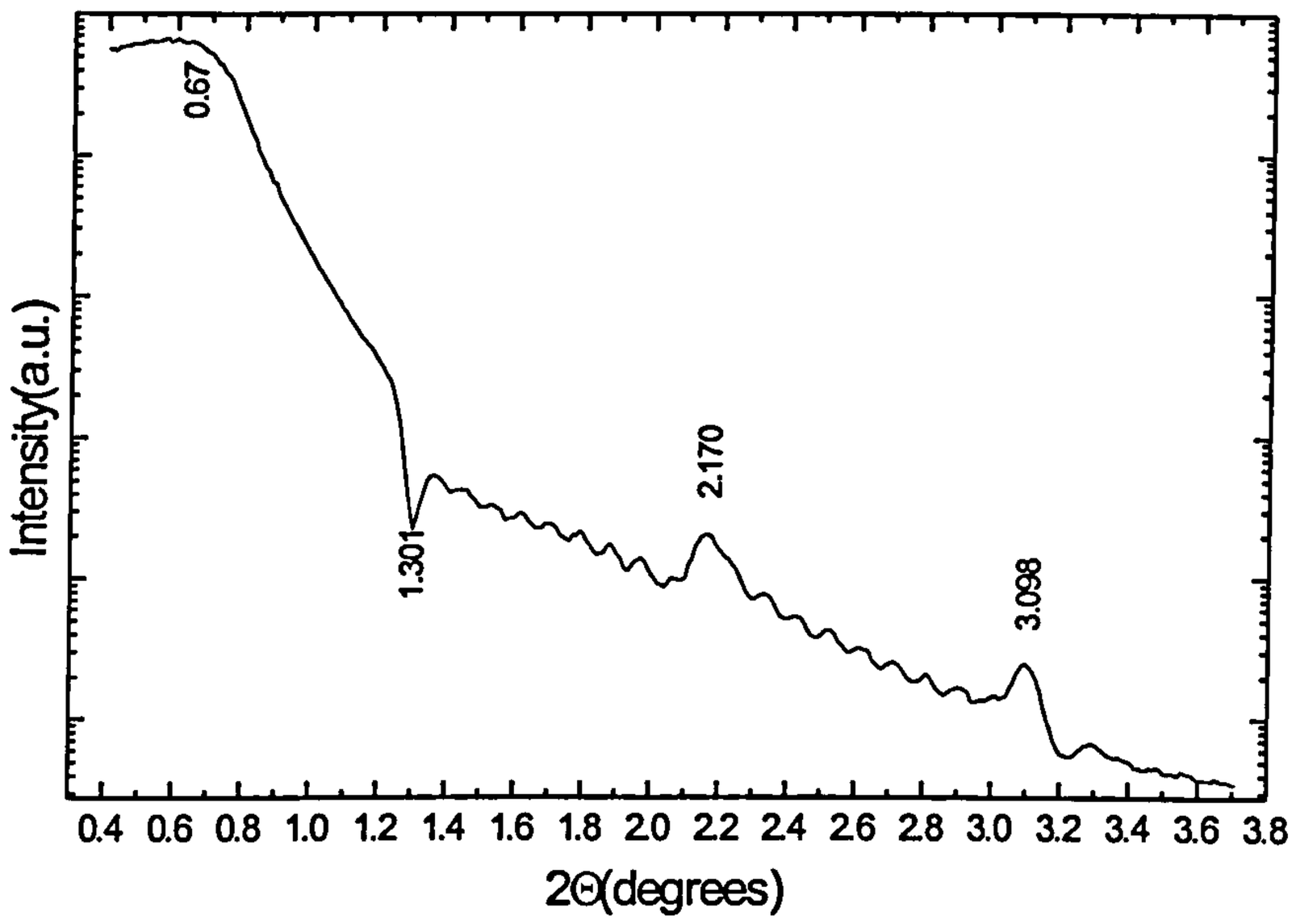

Figure 4.5) XRR of v85 (84Å Fe/ 30 sec N).

Figure 4.6 is a plot of three reflectivity scans corresponding to a variation of the nitrogen exposure time and keeping the Fe layer thickness constant at 42 Å.

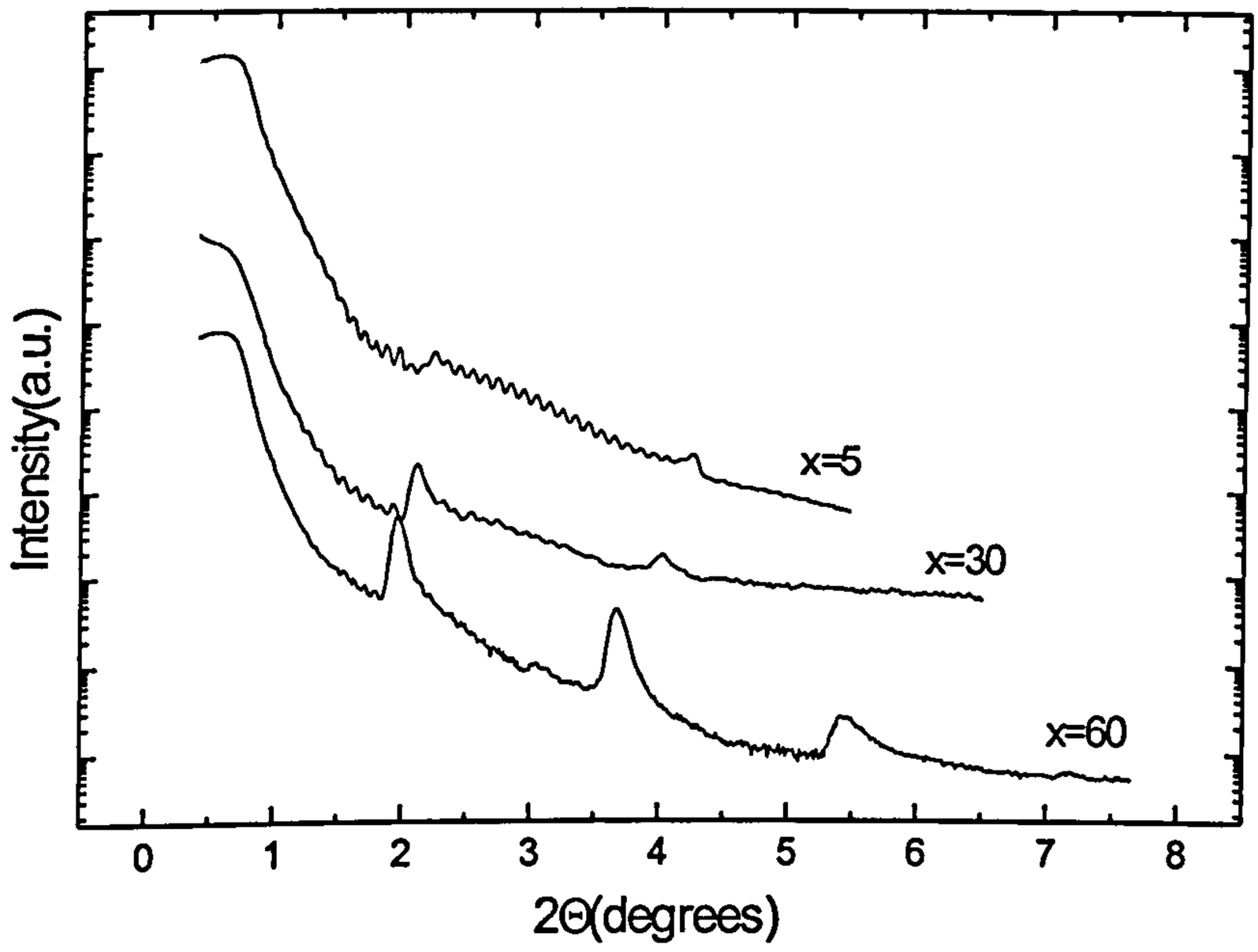

Figure 4.6) XRR of samples with 42Å Fe and X sec N, where X=5, 30, and 60.

The nitrogen exposure times denoted by x in the figure correspond to 5, 30 and 60 seconds. As when the Fe layer thickness was increased, as previously seen, there was a shift of the multilayer peaks to lower 2θ for a nitrogen exposure time of 30 seconds. Here as the nitrogen exposure time was increased there is also a shift to lower 2θ, but the amount of shift is less in going from 30 to 60 seconds nitrogen exposure than increasing from 5 to 30 seconds. There is an improvement in the interfaces with increased nitrogen content as evidenced by the sharpness and intensity of the multilayer peaks. The decreased shift of the multilayer peak due to nitrogen incorporation was further investigated. A series of thick, 900Å, single Fe layers were exposed to the nitrogen beam for x= 30, 120, 240, and 360 seconds. The reflectivity scans of these four samples are shown in figure 4.7 below.

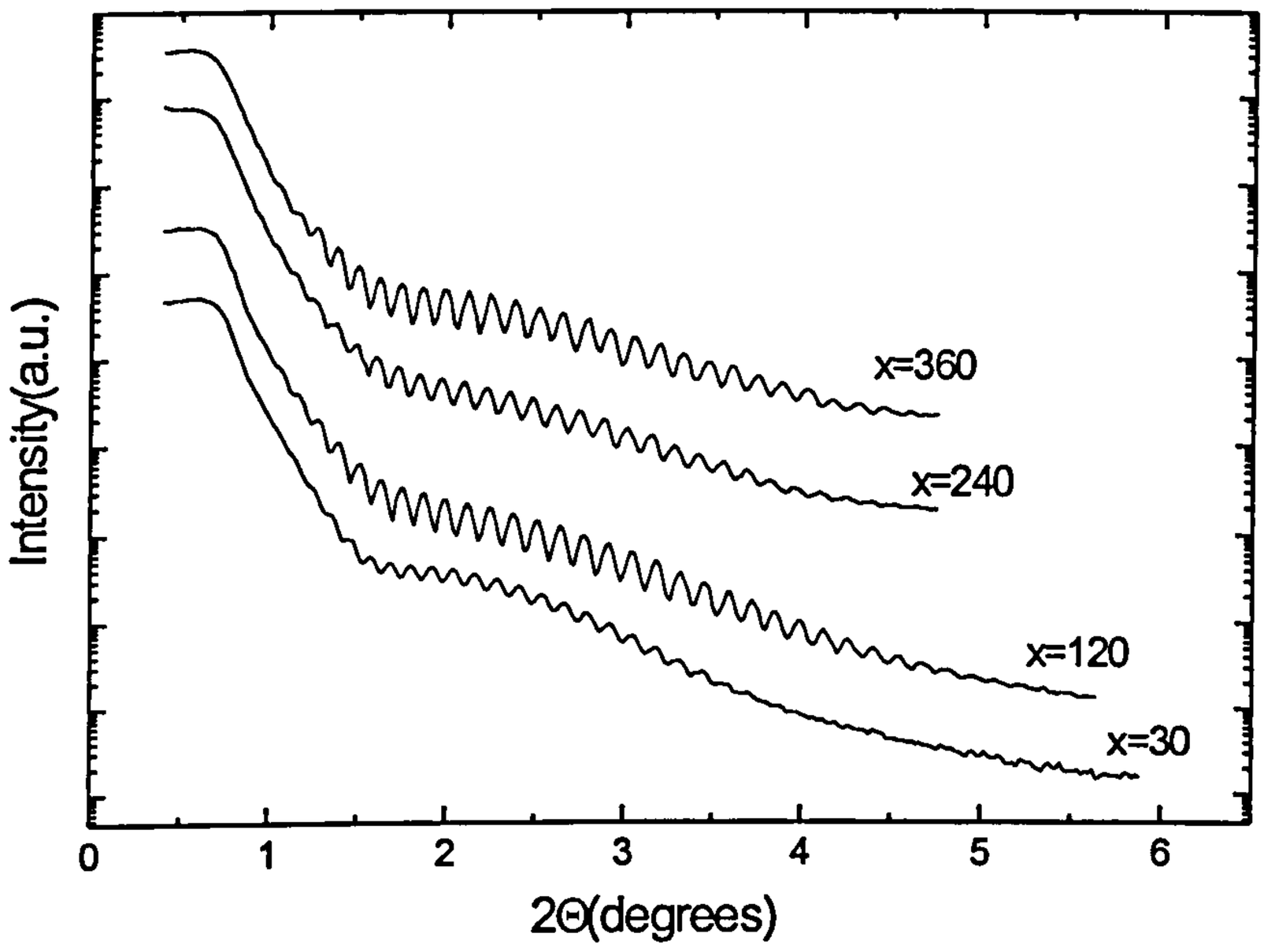

Figure 4.7) XRR of 900Å single Fe layers exposed to the nitrogen beam for x=30, 120, 240, and 360 seconds.

From this scan there is, qualitatively, no difference in the magnitude of the nitride layer thickness as seen by the similarity of the large period oscillation typical of an oxide layer but here attributed to the nitride layer. Hence the nitride layer thickness reaches a

maximum and remains constant, which is consistent with oxidation of metals in an oxygen atmosphere[80]. An example of this would be the native oxide layers on silicon wafers.

By varying the constituents of the effective bilayer it is possible to manipulate the bilayer periodicity, as when two metal species are multi-layered[81]. There is evidence of expansion of the Fe layer with thinner Fe layers showing a more definite effect. The discussed expansion is dependent on the error of angle determination so accuracy is suspect but there is qualitatively a genuine expansion despite the difficulty of obtaining a precise quantitative value. The nitriding technique is analogous to oxidation in that nitrogen only penetrates to a certain depth as shown by a constant periodicity above 30 seconds nitrogen exposure. The evidence provided above points to samples that are short period multilayers with good quality interfaces.

4.3 X-Ray Diffraction

As a first approximation, high angle x-ray diffraction (XRD) was performed on samples to determine the phases present. Figure 4.8 shows an XRD pattern from the sample with effective bilayer of 42Å Fe and 30 seconds nitrogen exposure.

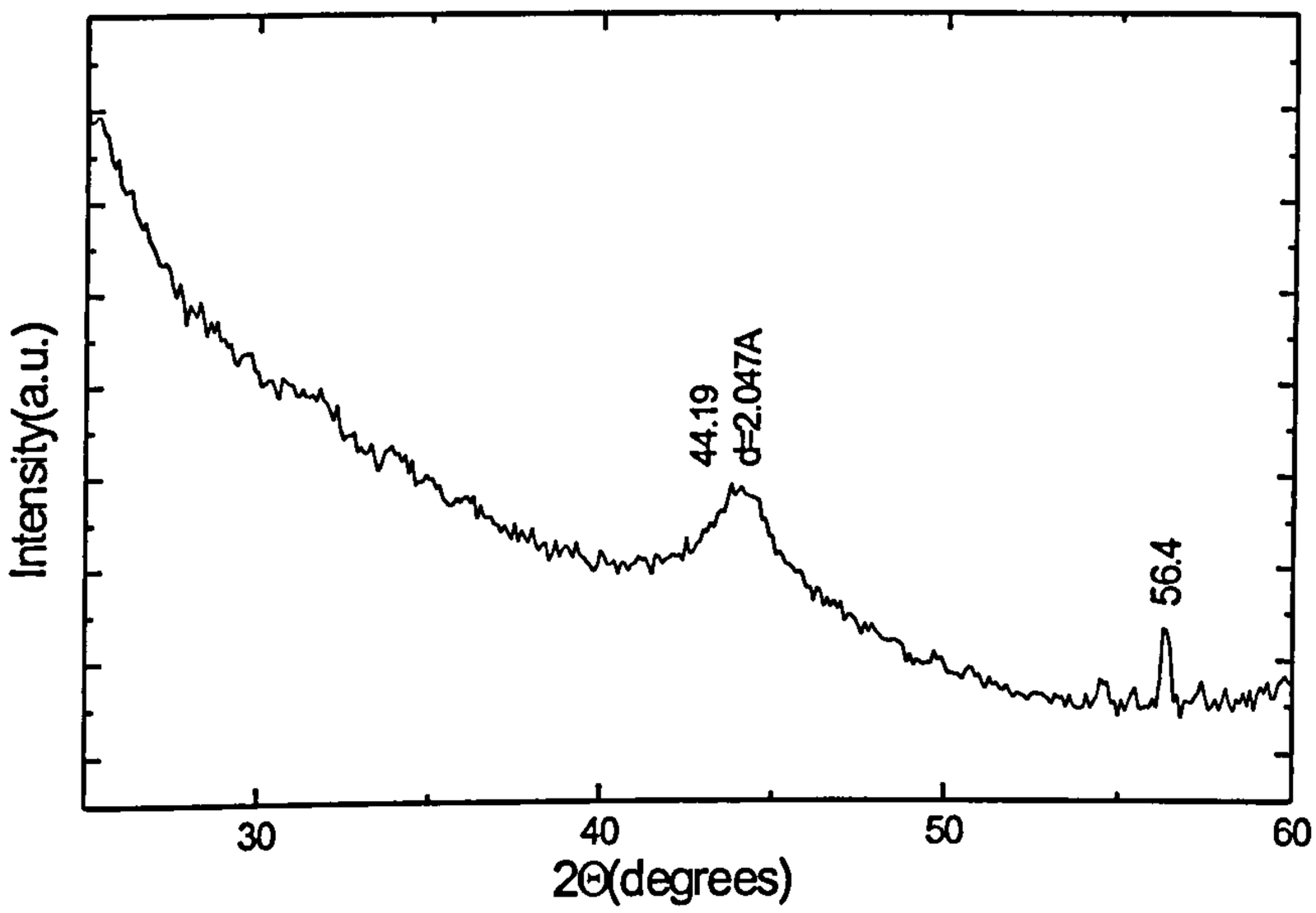

Figure 4.8) XRD pattern of v82 (42Å Fe/30 sec N).

The figure was typical of pattern from nitrided samples. There were several peaks attributed to the Si substrate including a peak at 2θ=56.4°. Although the substrate was ideally single crystal it contained some form of defect or mis-orientation giving rise to the peaks just below the main Si (400) peak at 2θ=69.2°. Sample peaks consisted of very broad amorphous-like peaks. The Fe (110) peak expected at 44.6° was shifted to lower angle by about 0.4° to a larger d-spacing, and there was a broadening of the peak. This broadening can be attributed to effects such as a reduction in grain size or stress in the sample. It was not clear here what caused the broadening. One of the concerns associated with the multilayer technique centred on whether the nitrogen incorporation was due to the direct exposure to the atom beam or to the subsequent partial pressure of nitrogen in the chamber. Figure 4.9 Shows an XRD pattern of an Fe sample deposited without directly exposing it to the atom beam but the atom source was operating during the deposition.

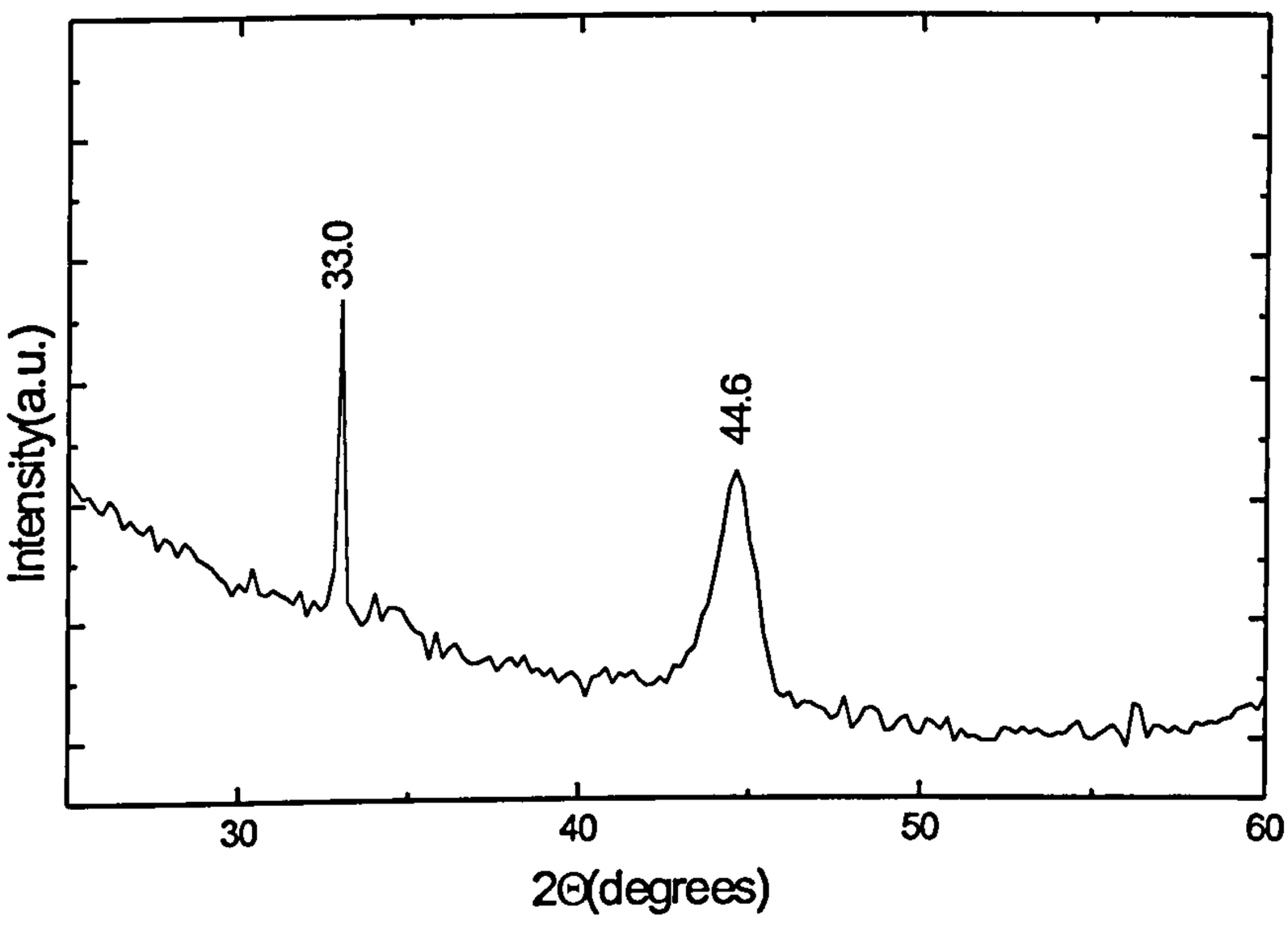

Figure 4.9) XRD pattern of Fe film deposited with atom source running.

Hence any nitriding of this sample would have occurred as a result of the partial pressure of nitrogen in the chamber. As can be seen the pattern showed no visible shift from the

expected α-Fe (110) peak at 2θ=44.6°, and the peak broadening was minimal at best. The peak at 33.0° was due to double diffraction from the Si substrate.

Any phase changes in the samples are due to direct exposure to the nitrogen atom beam. The XRD patterns were not very illuminating. Phase identification was inaccurate at best requiring a more definitive technique. Selected area diffraction in the TEM was employed.

4.4 Electron Diffraction

This section delineates the phases present in Fe/FeN samples as determined from TEM diffraction patterns (DPs). Equation 3.3 from chapter 3 has been used to calculate the d-spacings of the rings.. The Fe/FeN set of samples starts off as α-Fe as shown in figure4.10.

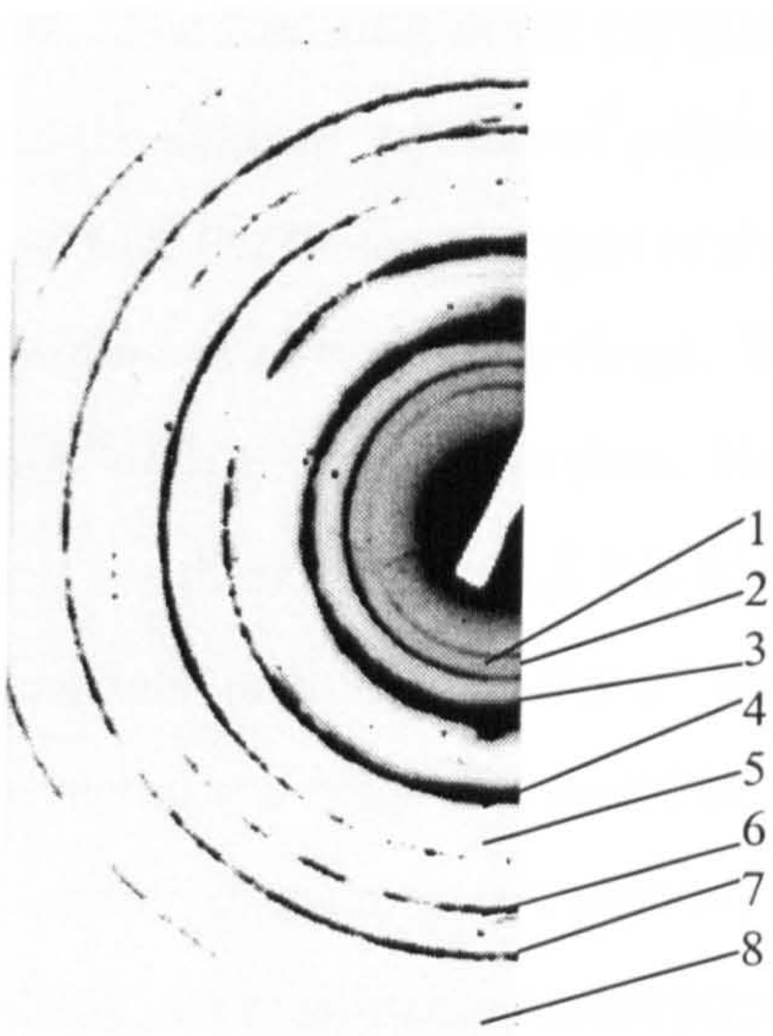

Figure 4.10) BCC diffraction pattern from an Fe film. The first two rings were indexed as oxide while the other rings corresponded to the BCC Fe 110 , 200, 211, 220, 310, and 222 rings respectively in numerical order .

Prior to nitrogen exposure all the samples ideally have a structure similar to the DP of the 500Å Fe film shown in figure 4.10. From this starting point the phases are formed by nitrogen incorporation. Figure 4.11 shows the DP for the sample with an effective bilayer of 7Å Fe and 30 seconds nitrogen exposure.

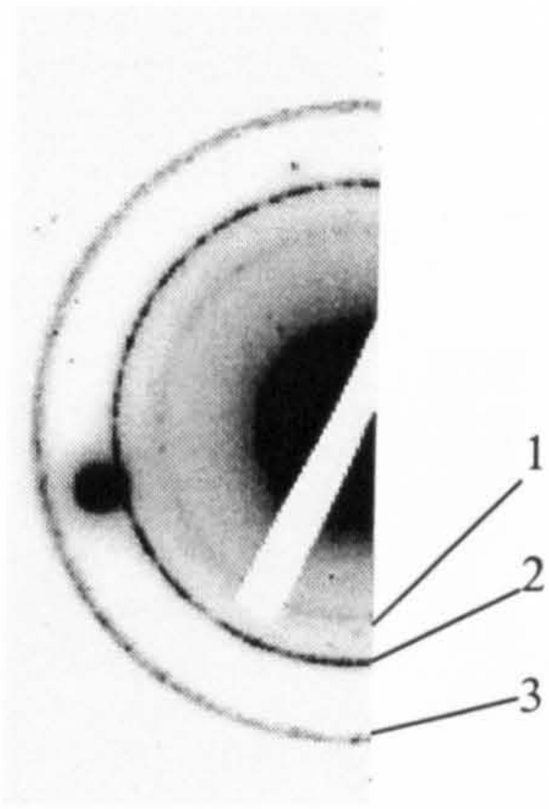

Figure 4.11) Diffraction pattern of v66 (7Å Fe/ 30 seconds N). Ring 1 is oxide, ring 2 is the Fe_2N 200 reflection and ring 3 is the 212 Fe_2N reflection. The spot is from the Si substrate.

The ring pattern shown is that from an orthorhombic material for which the calculated d-spacings fit the Fe_2N reflections. The first ring in the pattern has been identified as a surface oxide reflection. Hence the sample consists of polycrystalline Fe_2N. The DP of the sample with effective bilayer of 14Å Fe/30 sec nitrogen is shown below in figure 4.12. This pattern consisted of continuous and very spotty rings. The spotty rings are typical of diffraction patterns from samples with a larger grain size. Here the pattern is more complex and increasing the Fe layer thickness to 14Å has had a marked affect on the phase present. The inner most ring has been attributed to the α'' and oxide phases from the calculated d-spacing, while the rest of the rings that could be indexed are identified as either Fe_3N or Fe_2N given that certain d-spacings are present in both phases. Given the similarity of the two structures this is a reasonable assumption. From the reflectivity discussed in the previous section of this chapter the sample is a multilayer. In order to produce such a reflectivity scan a bilayer periodicity must exist. The oxide rings here are faint suggesting a thin surface layer. Given that the Fe_3N and Fe_2N rings overlap and the deposition configuration, it was concluded that this sample consists of a multilayer with a bilayer made up of a layer of Fe_2N and a layer of Fe_3N.

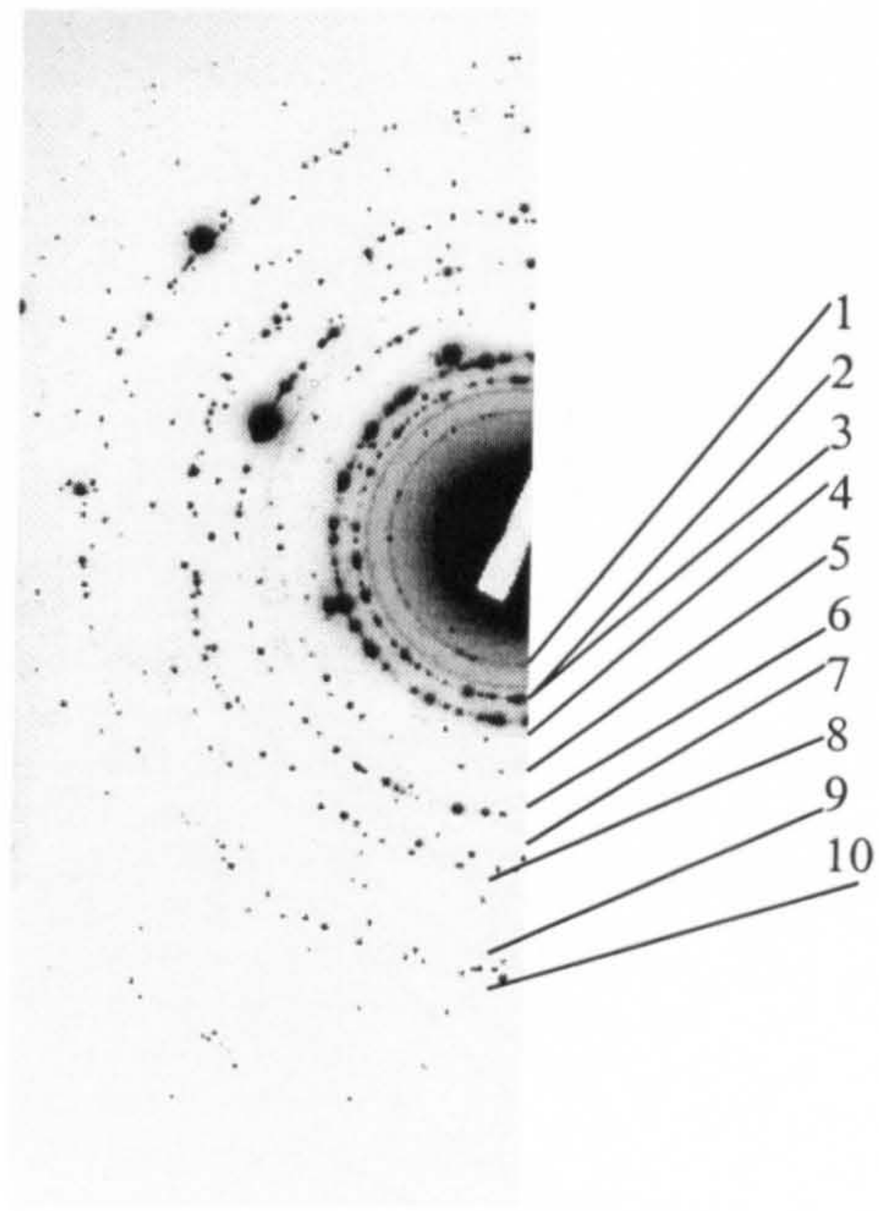

Figure 4.12) Diffraction pattern of v74 (14Å Fe/ 30 seconds N).Ring 1 is an α'' reflection, rings 2, 3 and 9 are oxide rings, rings 4, 5, 6 and 8are the Fe_3N, 100, 002, 101 and 102 reflections, rings 7 and 10 are the 301 and 131 Fe_2N reflections, ring 8 is the Fe_3N 102 reflection,

Further increasing the Fe layer to 21Å gave the DP shown in figure 4.13. Again the DP is spotty as indicative of large grains. This sample was indexed as a combination of Fe_3N and Fe_4N. The inner most rings were attributed to Fe oxide. Reflectivity of this sample showed a multilayer peak and hence it was determined that this sample consisted of a multilayer of Fe_3N and Fe_4N.

Figure 4.14 shows the DP of the sample with a 42Å, Fe layer. This pattern consists of several interesting features.

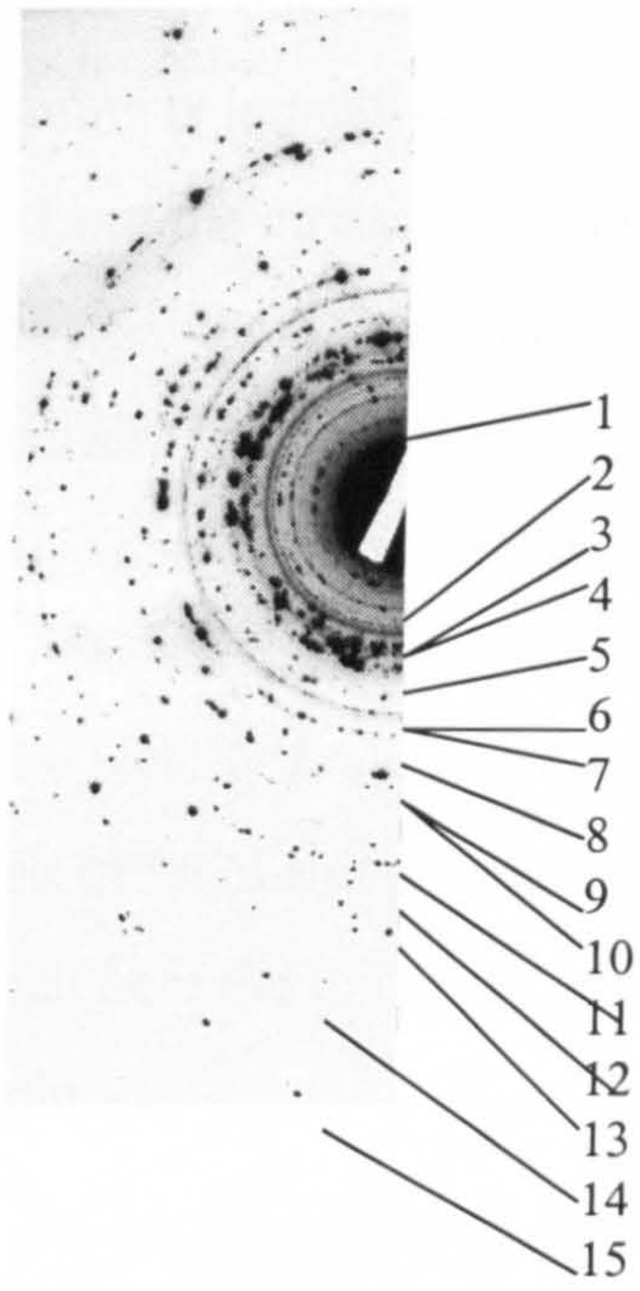

Figure 4.13) Diffraction pattern of v80 (21Å Fe/30 seconds N). Rings 2, 4, 5 and 11 were indexed as oxide reflections. Rings 6, 7, 10, 13, and 15 were the Fe_3N 002, 101, 102, 103, and 201 reflections. Rings, 1, 3, and 8 are the Fe_4N 111, 110, and 200 reflections. Rings 12 and 14 can be either of the two phases and ring 9 remains unidentifiable.

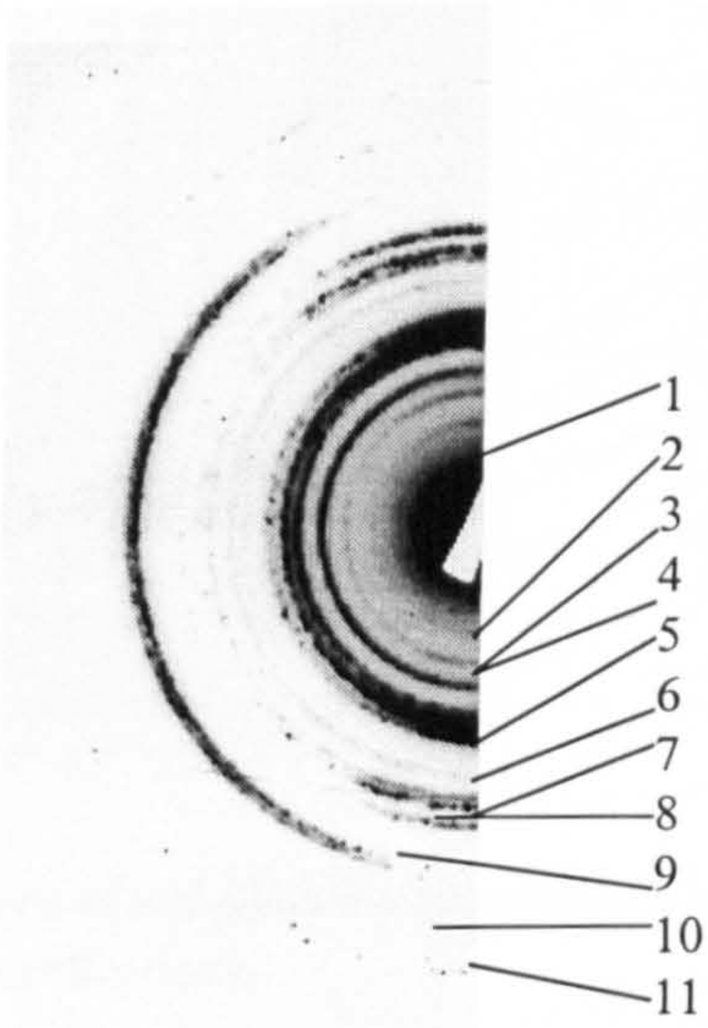

Figure 4.14) Diffraction pattern of v82 (42Å Fe/30 seconds N). Rings 1, 2, 3, 7, and 8 are oxide rings, rings 4, 6, and 10 are Fe_4N rings and rings 5, 9 and 11 are α Fe rings.

The rings in this pattern are not spotty but sharp and continuous in all but a few cases where the ring is arced. The arcing is indicative of texture. If a sample contains texture the DP will arc as it is tilted away from the diffracting condition of the textured grains. It suffices to say here that this sample indexed to a multilayer of Fe_4N and α-Fe, given the sharp multilayer peaks in the corresponding reflectivity scan. This sample marks a critical change from the previous ones. There was residual α-Fe left in the sample. The nitrogen penetrates less than 42Å.

Further increasing the Fe layer to 84Å gave the DP shown in figure 4.15. Here again the sample consisted of Fe_4N and α-Fe. The Fe reflections are more intense in this sample owing to the fact that here the thickness of the α-Fe layer is increased as compared to the previous sample.

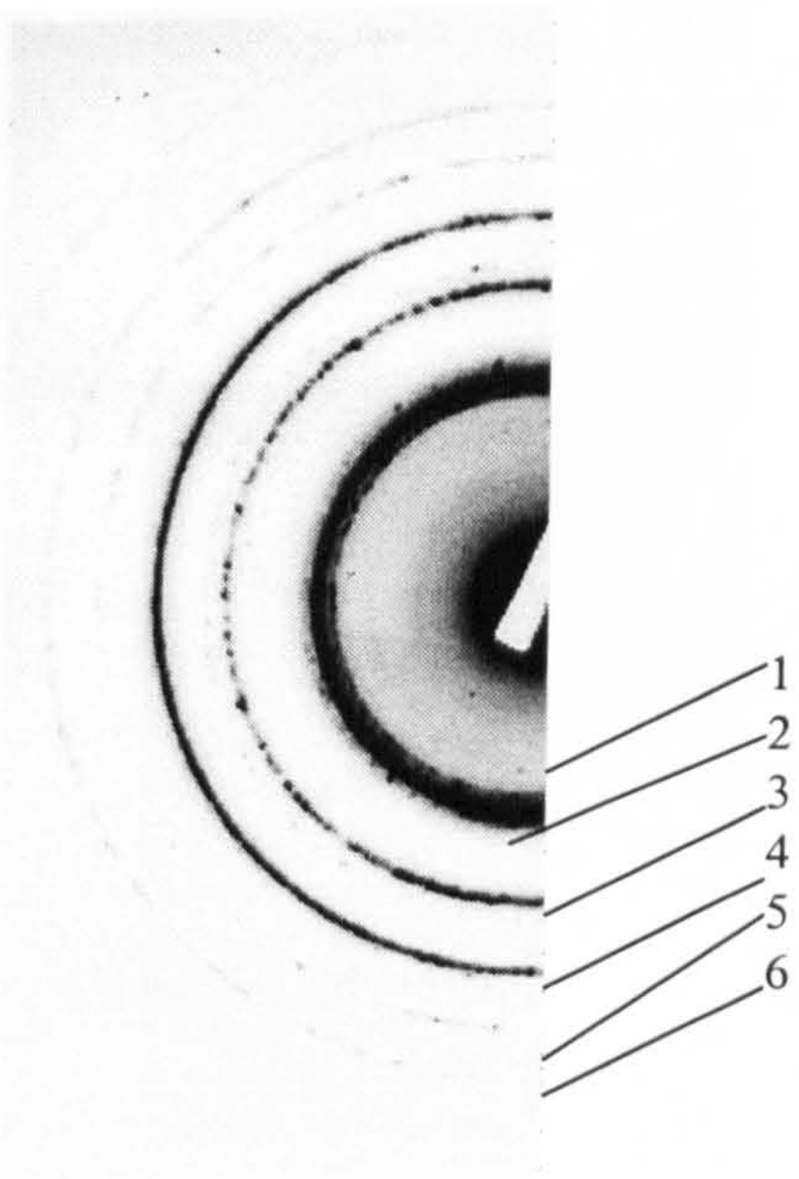

Figure 4.15) Diffraction pattern of v85 (84Å Fe/30 seconds N). Rings 1, 3, and 5 are Fe_4N reflections and rings 2, 4, and 6 are α Fe reflections.

When these DPs are considered with respect to the FeN phase diagram the phase transitions detailed here are logical. By increasing the Fe layer thickness the relative amount of nitrogen in the sample is decreased. Since the phase is dependent on the

nitrogen content the appropriate phases are present. The fact that bilayer constituents of two different FeN phases were set up is understandable in terms of a concentration gradient. As the nitrogen is introduced it penetrates to a depth somewhat less than 42Å. If the initial Fe layer thickness is less than the maximum depth the layer nitrides completely, otherwise there is α-Fe left. Just as in the phase diagram the initial nitride phase formed was Fe_4N. Further nitrogen exposure does not penetrate deeper but forms a higher nitrogen concentration layer for which under the right conditions a concentration gradient is set up as evidenced by a bilayer consisting of two different nitride phases. This process continues until the layer is saturated under the appropriate condition, for which in the case discussed above the result was Fe_2N.

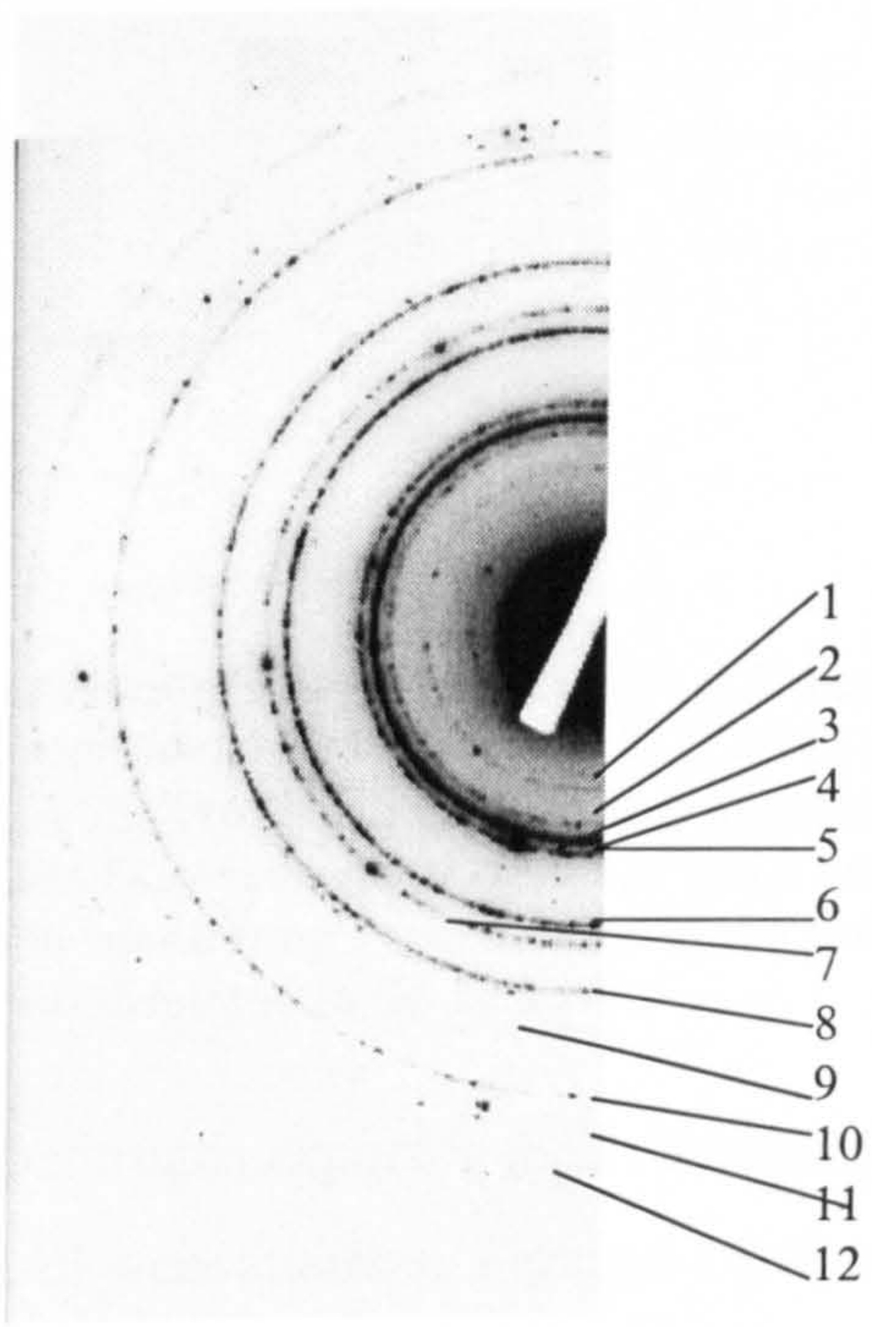

a)

Figure 4.16a

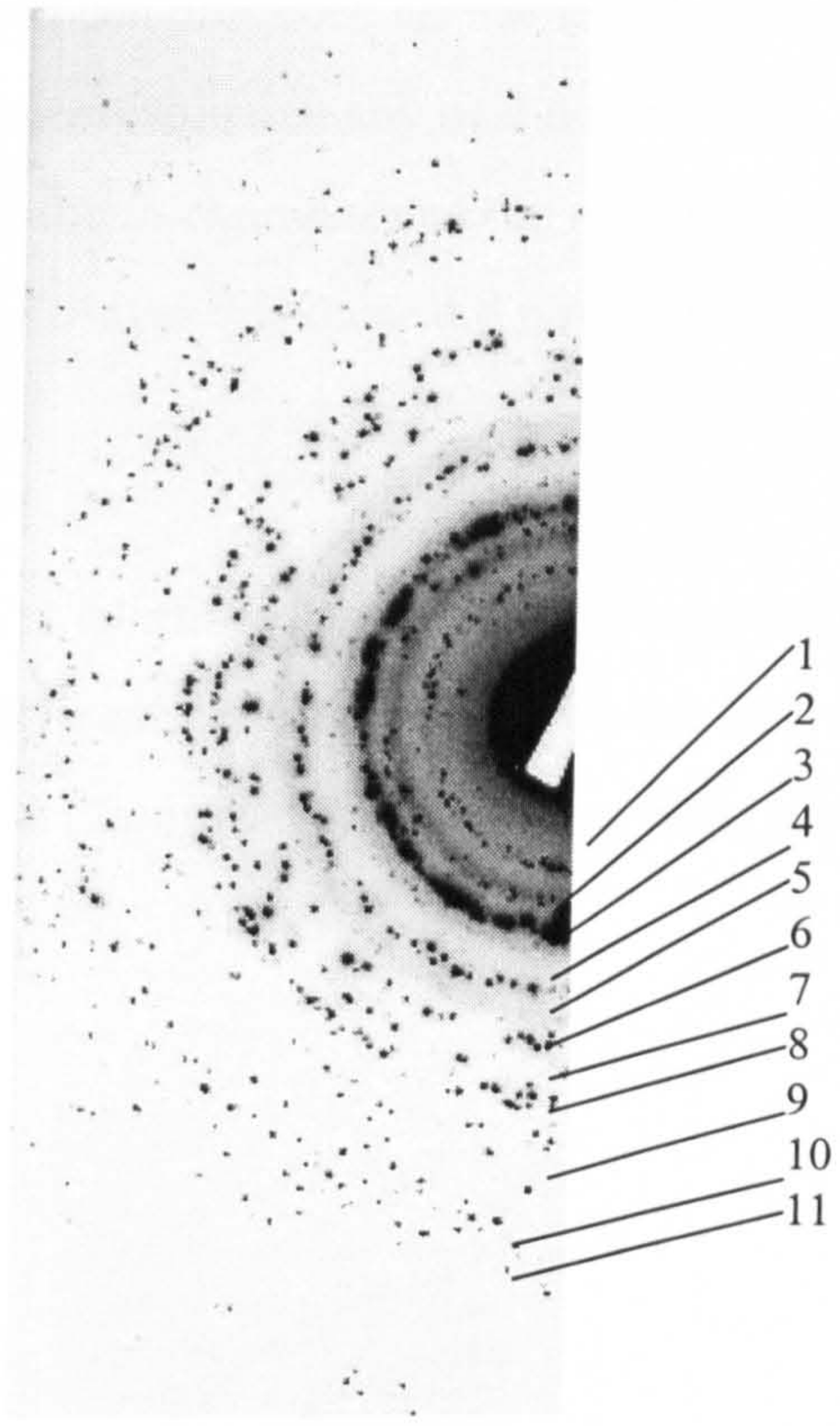

b)

Figure 4.16) Diffraction patterns of samples with 42Å Fe and N= a) 5 seconds and b) 60 seconds. In (a), rings 1, 2, 3, 5, 6, 8, 10, 11, and 12 correspond to the 100, 110, 111, 200, 210, 220, 311, 321, and 400 Fe_4N reflections, rings 4, 7, and 9 are the 110, 200, and 211 α Fe reflections. In (b), rings 3, 5, 7, 10and 11 are the 100, 101, 102, 110, and 103 Fe_3N reflections, rings 2, 6 and 8 are oxide reflections. Rings 4 and 9 are the 002, and 131 Fe_2N reflections. Ring 1 was indexed as the 110 α'' reflection. The 30 second nitrogen exposure sample was displayed in figure 4.14.

When a variation of the nitrogen exposure for a constant Fe layer thickness was considered the DPs in figure 4.16 were attained. Figure 4.16 shows samples with an effective bilayer of 42Å Fe and a) 5 and b) 60 seconds nitrogen. The 5 second nitrogen sample was identified as a combination of Fe_4N and α-Fe. This sample is a multilayer as shown previously and hence the bilayer consisted of a layer of Fe_4N and an α-Fe layer. Further nitrogen exposure to 30 seconds gave the DP in figure 4.14 above. Exposing to nitrogen for 60 seconds produced a multilayer with a bilayer of Fe_3N and Fe_2N as determined from the DP in figure 4.16b. The two variables considered here produce the same effect. The phase of FeN can be tailored by varying one or the other. Multilayer and

single layer films have been produced here where the appropriate thickness and exposure time are used. It is conceivable that any of the four stable phases can be produced as a single film throughout the thickness given the right effective bilayer. As was shown, further increasing the Fe layer thickness did not constitute a further phase change.

In comparison to films made via the atom source the samples made by reactive sputtering are much different. Figure 4.17 shows the DPs of reactively sputtered samples. The samples in figure 4.17a-c were deposited in a N:Ar partial pressure ratio of 6, 12 and 26%, respectively.

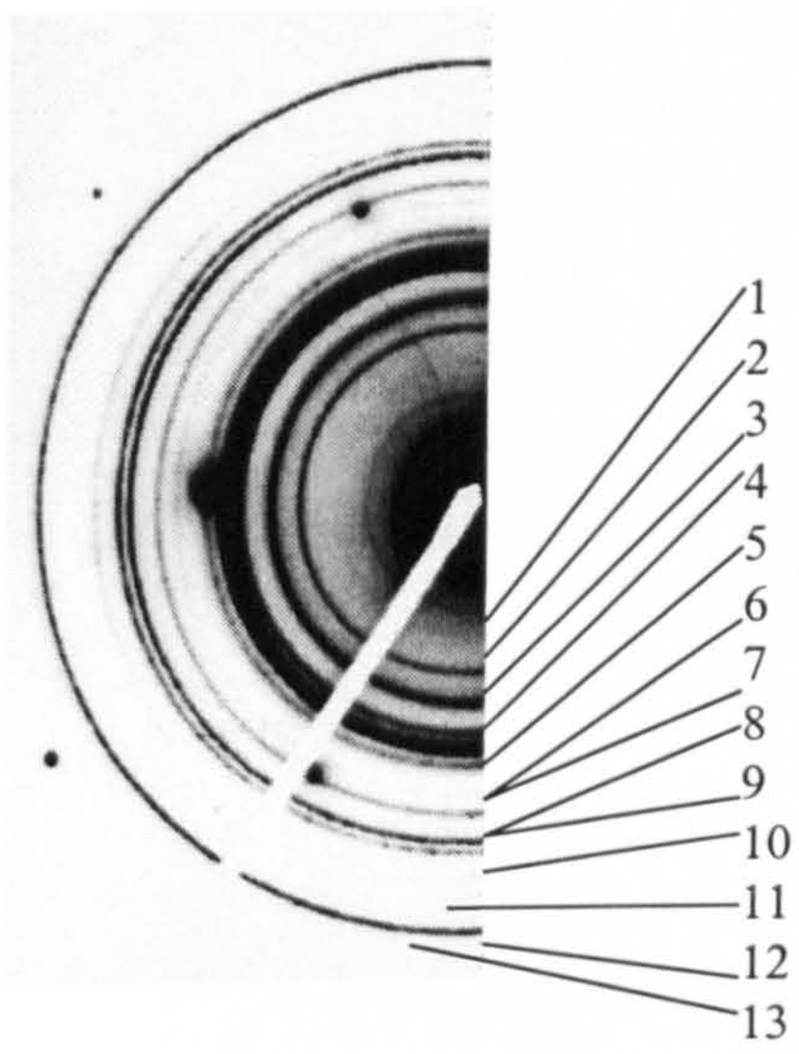

a)

Figure 4.17a.

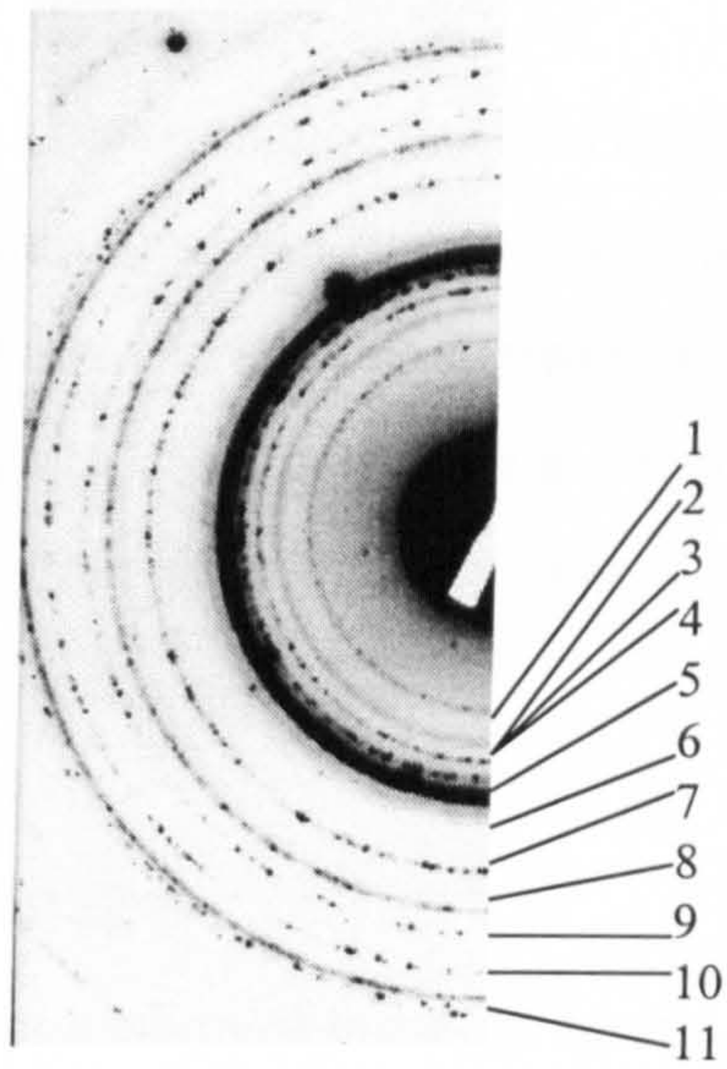

b)

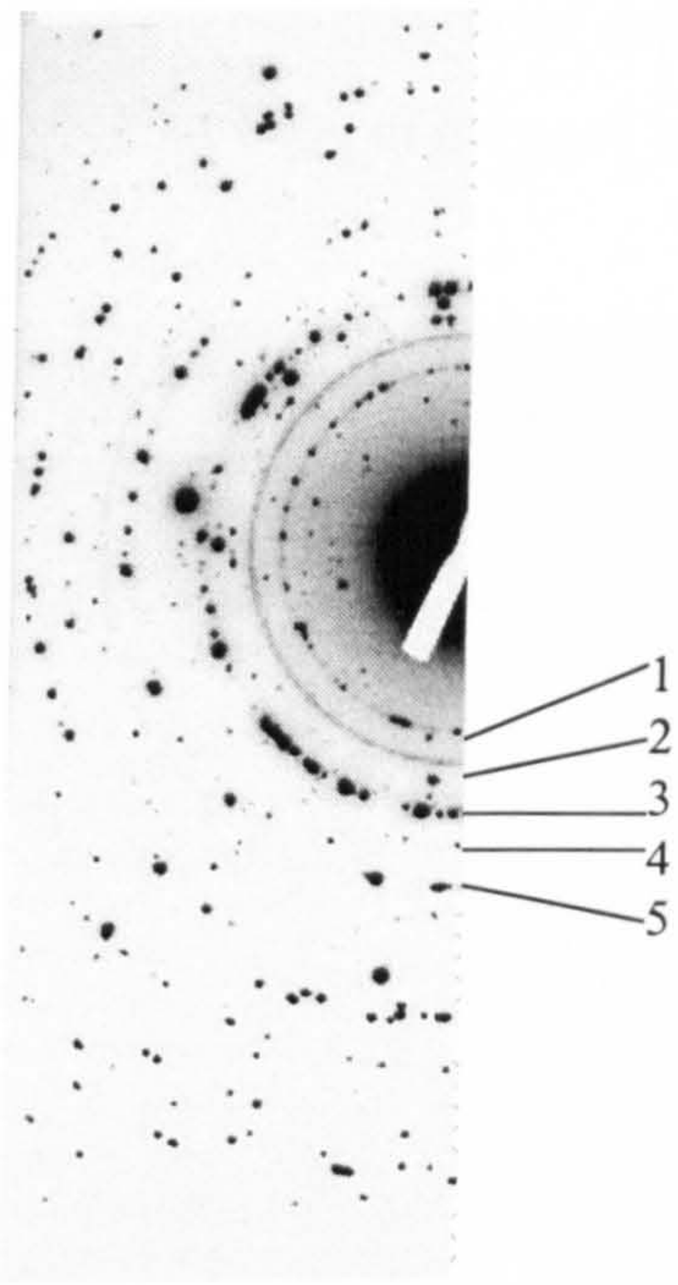

c)

Figure 4.17) Diffraction patterns of reactive samples with partial pressure ratios of a) 6%, b) 12%, and c) 26%. In a), rings 3,, 4, 9 and 12 are oxide reflections, ring 8 is the 200 Fe_4N reflection, ring 6 is the 100 Fe_3N reflection, rings 7, 10, and 13 are the 121, 301, 103 Fe_2N reflections, ring11 was indexed as the α'' 004reflection and rings 1 and 2 remain unidentified. In b), rings 2, 5, 7 and 9 are attributed to oxide reflections, rings 3, 4, 6, 8, and 11 are the 210, 002, 212, 400, and 423 Fe_2N reflections, respectively. Ring 10 was attributed to the α'' 105 reflection and ring 1 remains unidentified. In c), rings 1, 2, and 5 are attributed to oxide reflections and rings 3 and 4 are the 211 and 311 Fe_2N reflections.

The sample is a single layer as expected and multi-phase as in figure 4.17a, whereas in the atom source samples the layers are single phase. Increasing the nitrogen pressure in

reactive sputtering promoted a phase change that was again multi-phase though less so than the previous sample as shown in figure 4.17b. Increasing the nitrogen partial pressure further gave a single film of Fe_2N and Fe_3N as shown in figure 4.17c as the rings for both phases coincide but one cannot be absolutely certain. Hence the atom source provides a more controllable means of nitride phase production as was shown by the reflectivity and electron diffraction patterns.

4.5 Bright Field TEM Images

This section discusses the effect of the atom source nitriding on the grain structure of the Fe/FeN samples. The variation of the microstructure due to nitrogen exposure is dependent on the microstructure of the initial Fe layer deposited. Figure 4.18 shows a BF image from a typical Fe film deposited without nitrogen exposure.

Figure 4.18) Bright field image of a single Fe film without exposure to N.

The grains are about 100Å in diameter with regions of texture. When clusters of small crystallites exist within grains there is coherent diffraction if the crystallites have the same orientation. This gives rise to regions of dark contrast owing to destructive interference. This is the case as seen in figure 4.18 which is consistent with the arcing of the diffraction pattern in figure 4.10.

For the sample with an effective bilayer of 84Å Fe and 30 seconds nitrogen exposure the BF image in figure 4.19 was obtained.

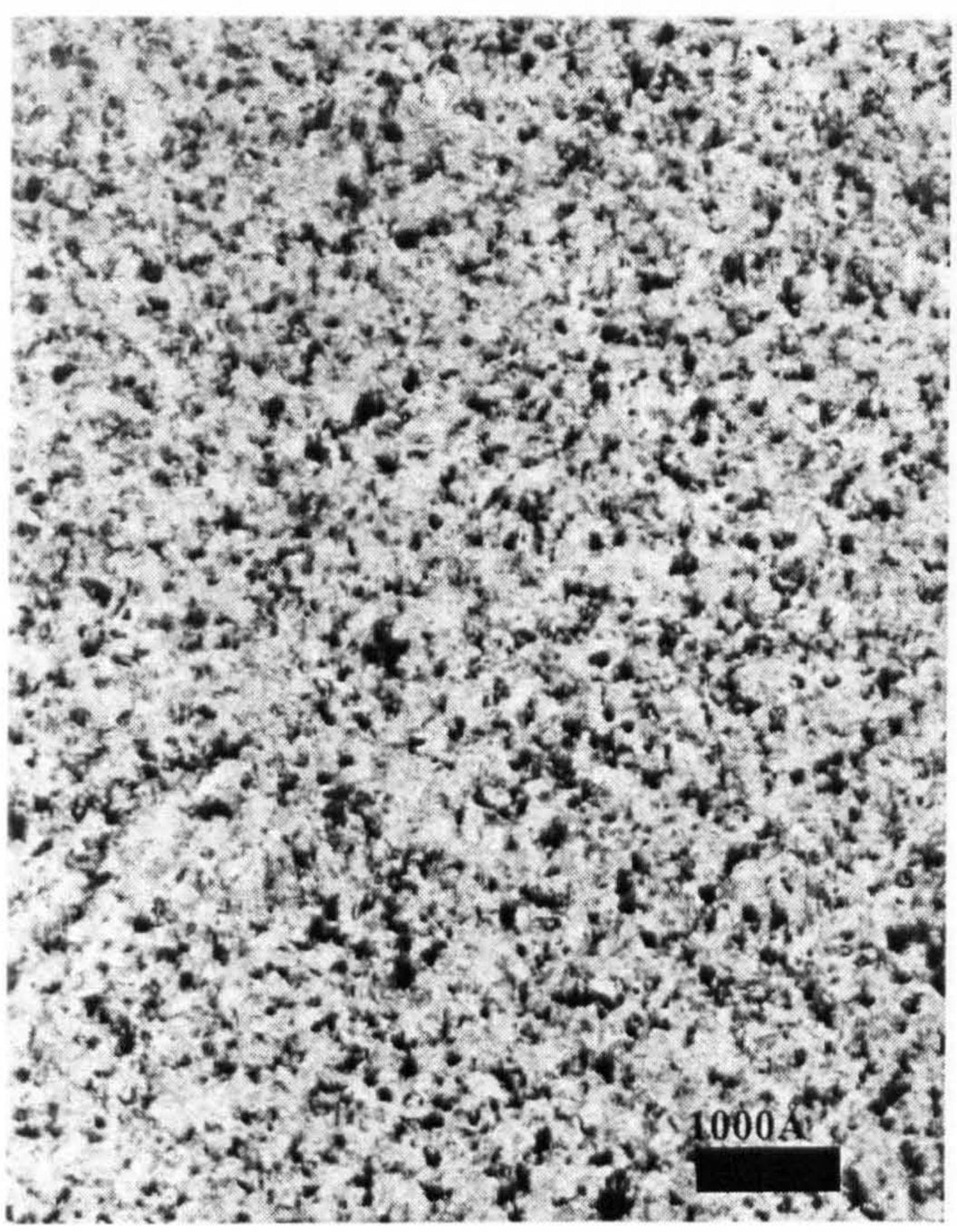

Figure 4.19) Bright field image of v85(84Å Fe/ 30 seconds N).

The grains are approximately 100Å in diameter as the grains are about one tenth of the scale line that represents 1000Å. The grain structure here is more homogeneous than the previous image. The nitrogen has apparently randomized the grain structure. Decreasing the initial Fe layer to 42Å gave the BF image shown in figure 4.20.

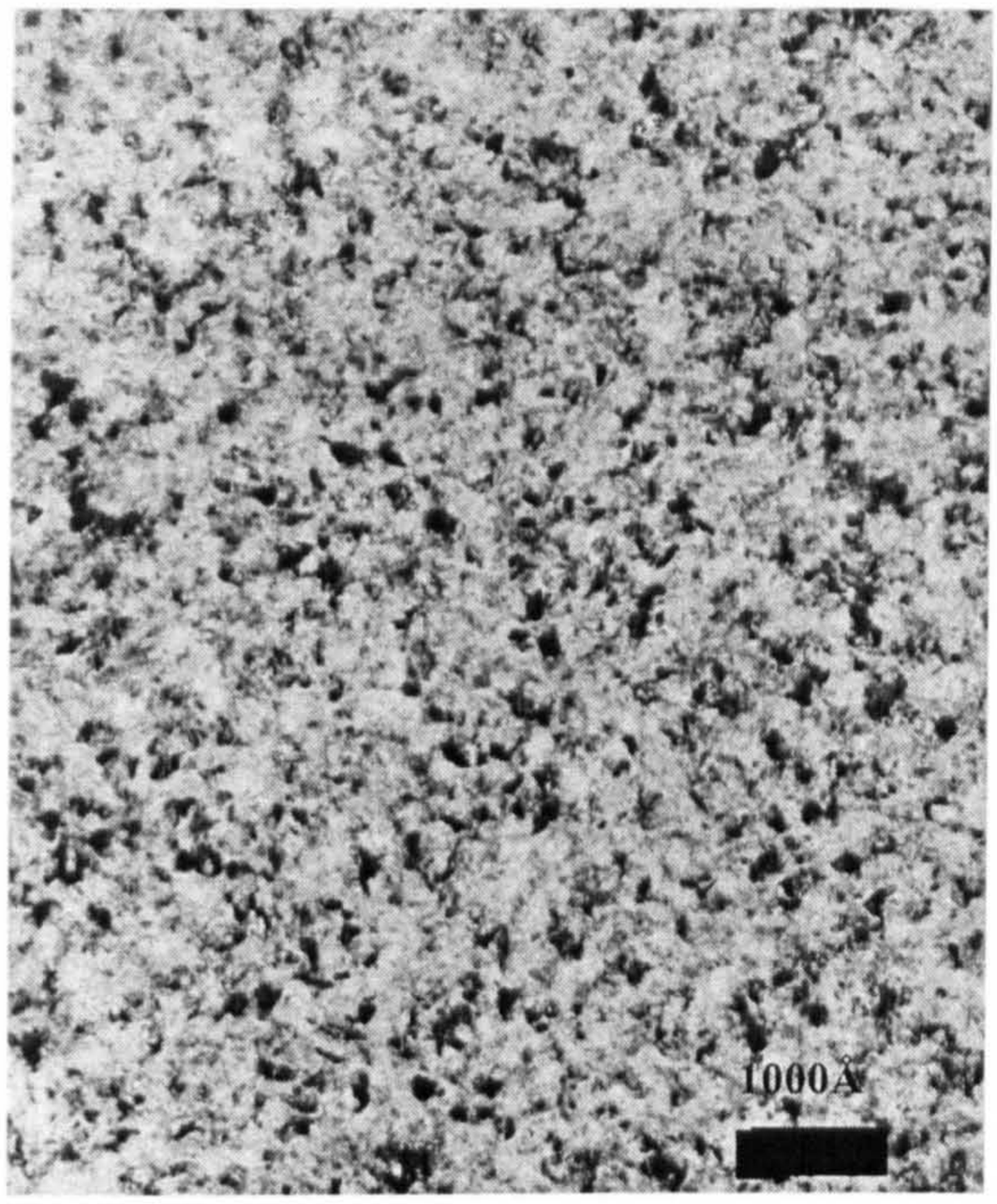

Figure 4.20) Bright field image of v82 (42Å Fe/ 30 seconds N).

There is no noticeable difference in the grain structure as compared to figure 4.19. Both of the previous two images consisted of samples that contained residual α-Fe. Only the thickness of the α-Fe layer is decreasing. The addition of nitrogen does not appear to have caused any grain growth when the samples with Fe_4N and Fe are compared to the unexposed Fe layer from figure 4.18. The initial effect has been to disturb the initial texture of the Fe.

The BF image of the sample upon further reducing the initial α-Fe layer to 21Å is shown in figure 4.21.

Figure 4.21) Bright field image of v80(21Å Fe/30 seconds N).

There is a marked contrast between this sample and the sample in figure 4.20. The grain structure has increased considerably in size. Grains are on the order of 1000Å. There is evidence of crystallographic stacking faults, as at the x in the image, and grain boundaries are less distinct. Remembering that this sample is a multilayer of Fe_3N and Fe_4N, the effects of nitrogen incorporation has destroyed the original Fe microstructure. Figure 4.22 shows the effect of reduced initial α-Fe layer to 14Å.

Figure 4.22) Bright field image of v74(14Å Fe/30 seconds N).

Just as in figure 4.21 the grain structure is on the order of 1000Å. However, the grain boundaries are well defined and there is no evidence of striations. Striations tend to be a result of stacking faults. The previous sample consisted of Fe_3N and Fe_4N. The two images seem to imply that the phase transformation occurs via an increase of stacking faults in going from FCC to HCP. These two phases only differ in their stacking sequence so the stacking fault scenario is plausible and consistent with the microstructure since there was no evidence of the FCC phase in the sample in figure 4.22. The grain structure of the 7Å α-Fe layer sample is shown in figure 4.23. It is reminiscent of the thicker bilayer samples with grain sizes on the order of 50Å.

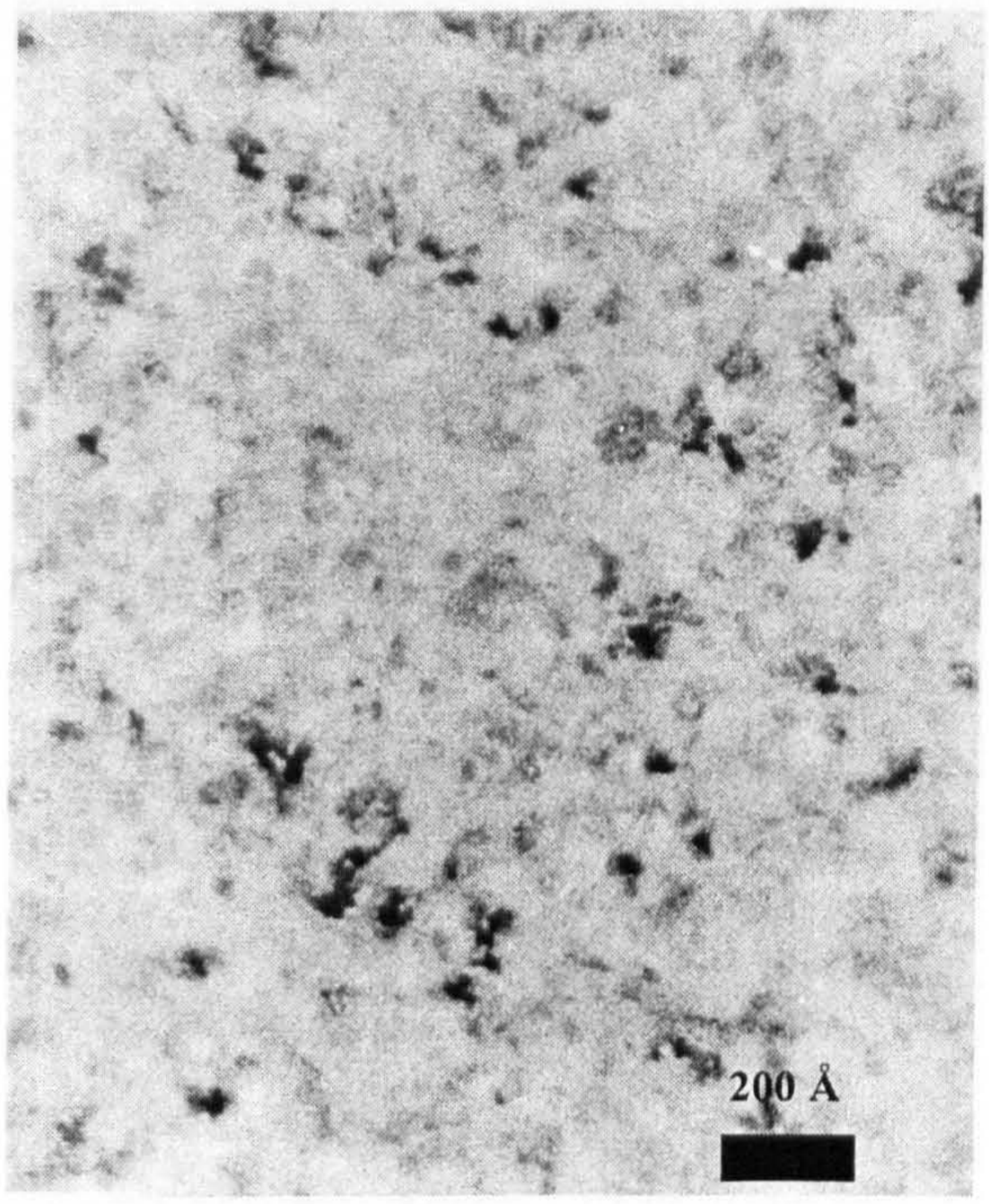

Figure 4.23) Bright field image of v66 (7Å Fe/30 seconds N).

The grains are approximately half the size of the initial α-Fe grains or 50Å. The grains are about a twentieth of the size of those in figure 4.22. The sample in figure 4.22 consisted of a multilayer of Fe_3N and Fe_2N. Given that the sample in figure 4.23 is solely Fe_2N one might attribute the large grain sizes to the presence of Fe_3N in the samples displayed in figures 4.21 and 4.22. There could be less grain growth in the atom source sample with only Fe_2N due to a lack of available material given that the sample is thinner than the 14Å Fe layer sample.

Figure 4.24 shows the BF images for the series of three films for which the effective bilayers consisted of the same initial Fe layer thickness but for which the nitrogen exposure time was varied.

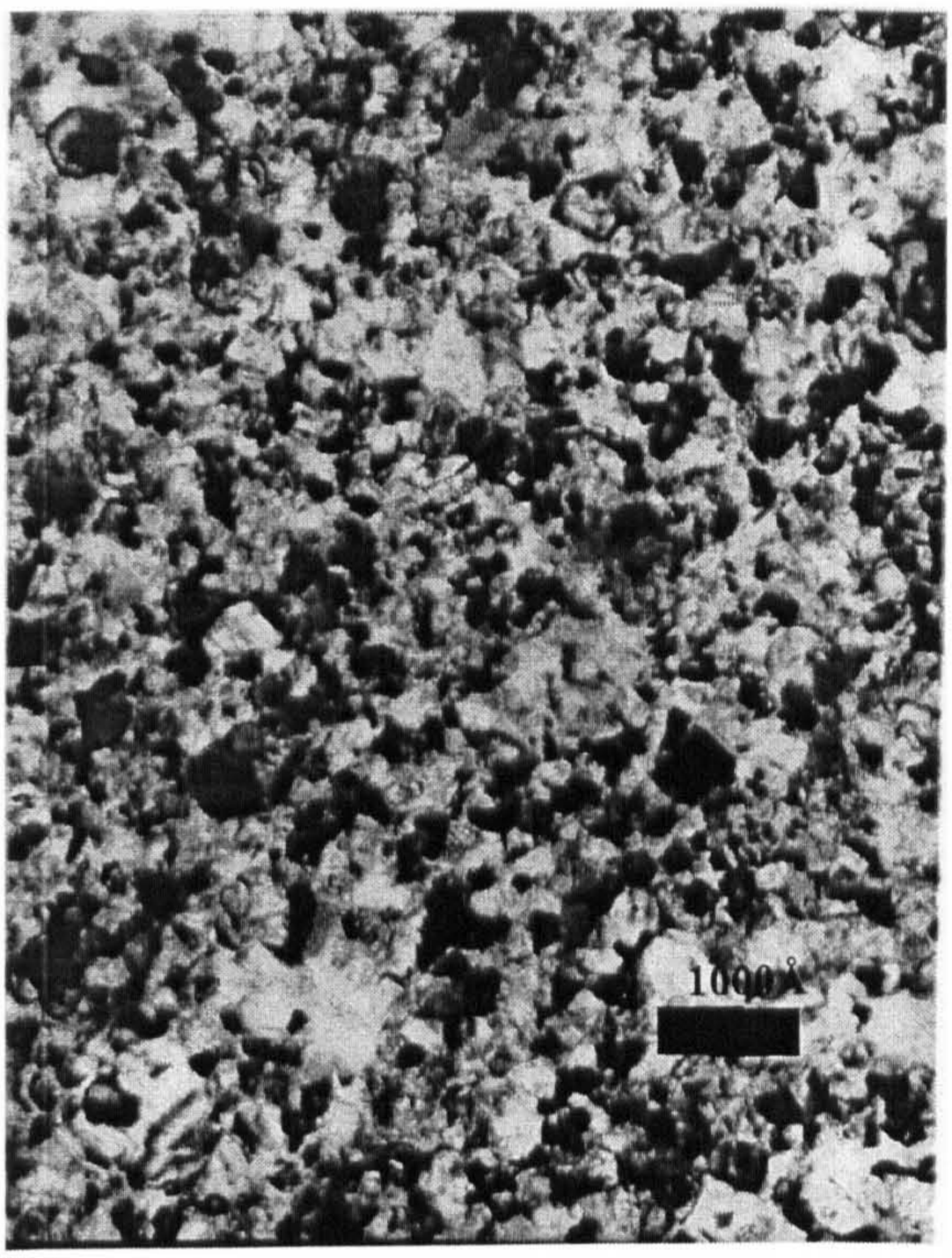

a)

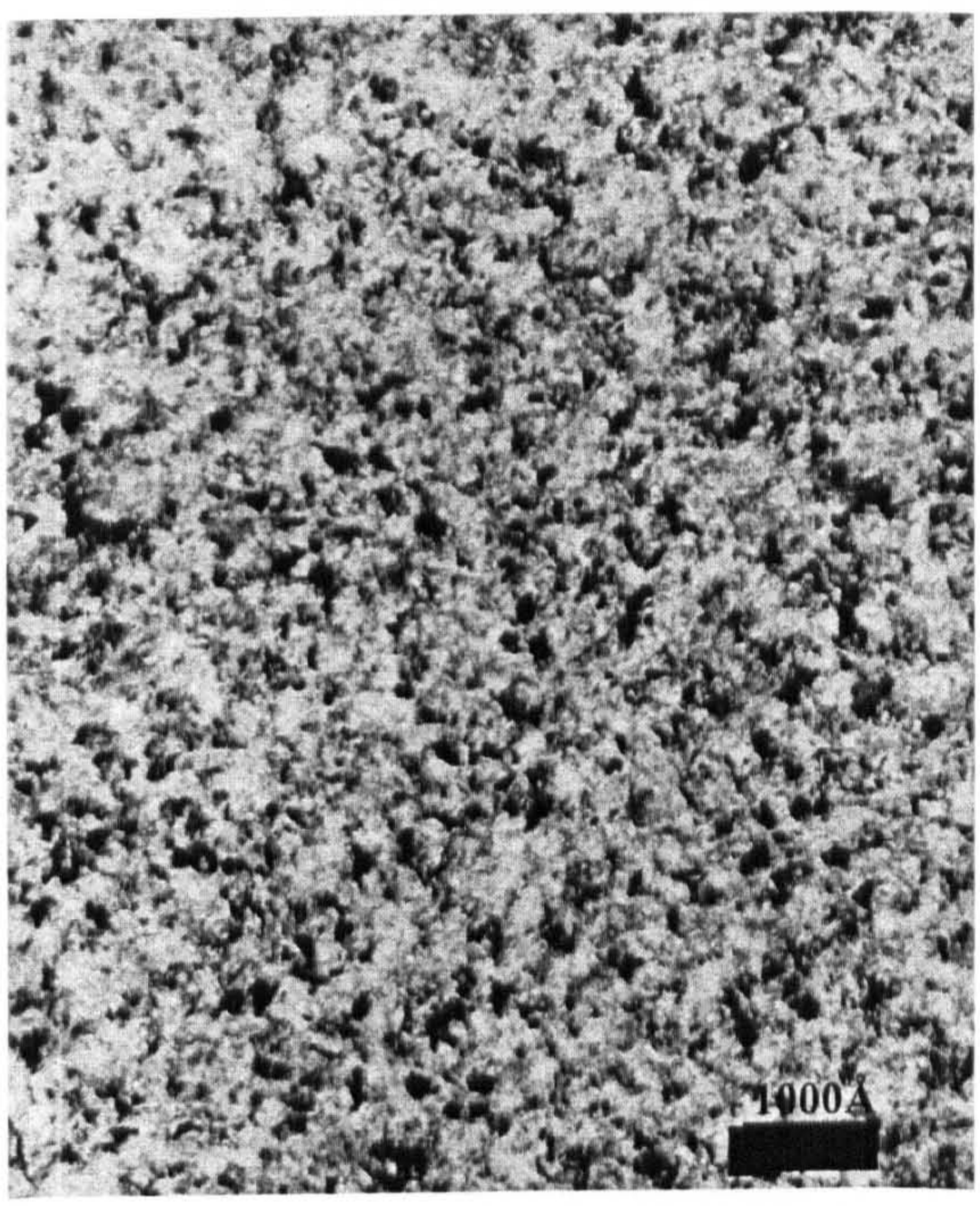

b)

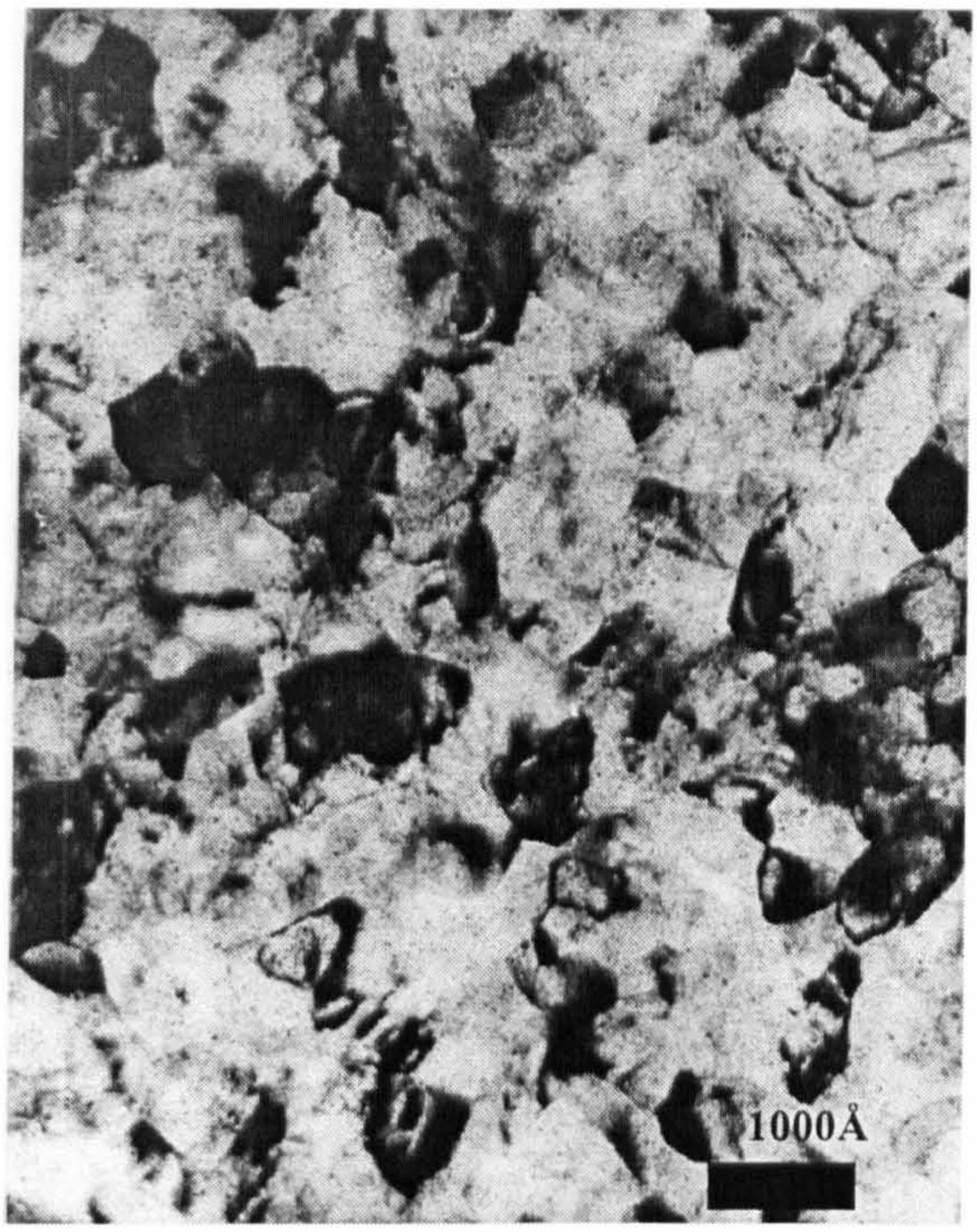

c)

Figure 4.24) Bright field images of samples for which the Fe layer was 42Å and the nitrogen exposure time varied. The exposure times for the samples were a) 5 seconds, b) 30 seconds and c) 60 seconds.

As shown the grain sizes do not vary much for the 5 and 30 second nitrogen exposure times. These are both multilayers of Fe_4N and α-Fe. However when exposed for 60 seconds the grain sizes are considerably larger. This was consistent with the effect seen for the reduction of the initial Fe layers. The sample in figure 4.24c was shown to be a multilayer of Fe_2N and Fe_3N. Despite the similar grain sizes the grain boundaries are much less distinct than in the sample with effective bilayer of 14Å Fe 30 seconds nitrogen exposure which was also shown to be a multilayer of Fe_2N and Fe_3N. It appears that the large grain is a result of the presence of Fe_3N.

The BF images of the reactively sputtered samples are shown in figure 3.25a-c.

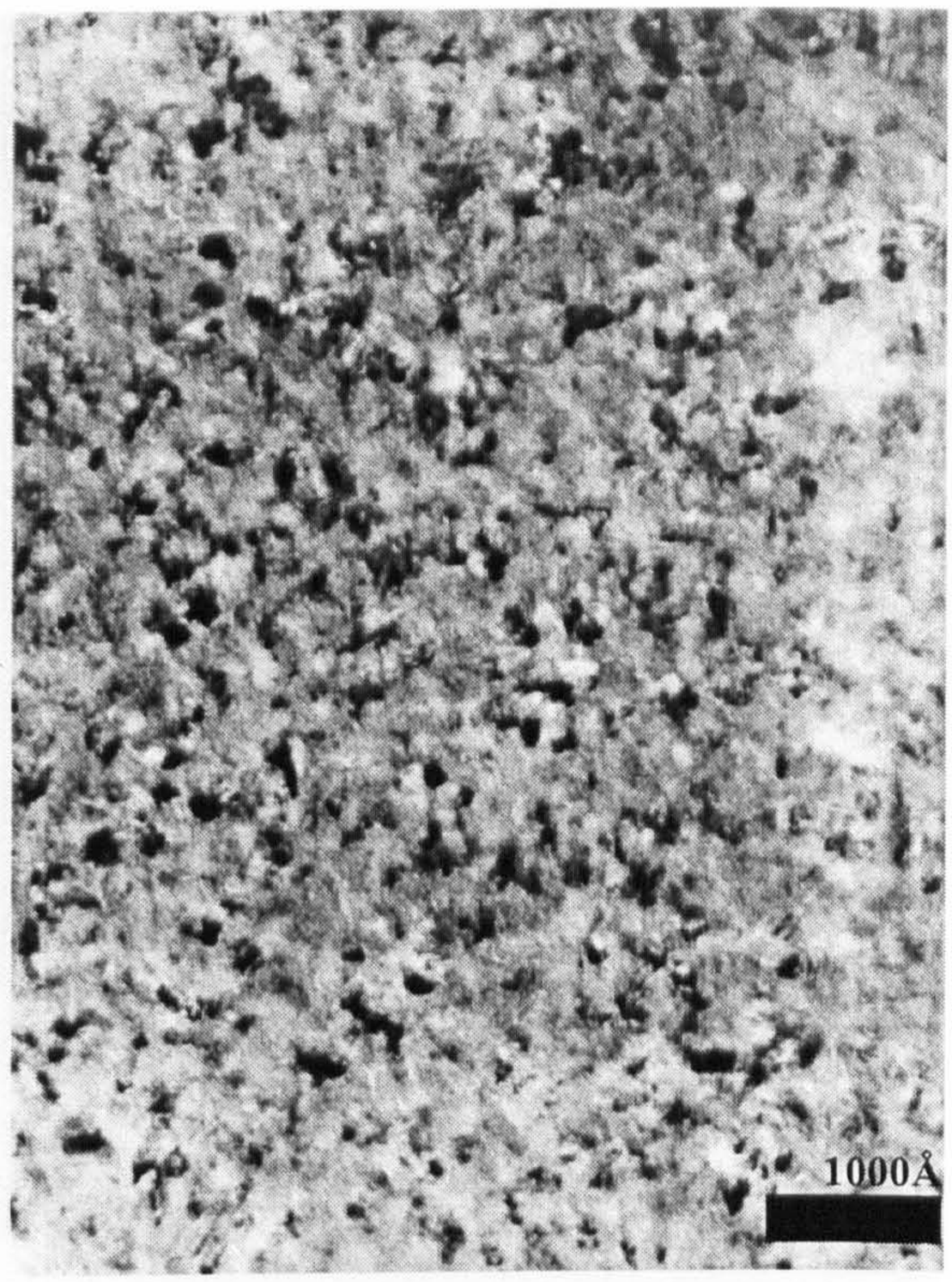

a)

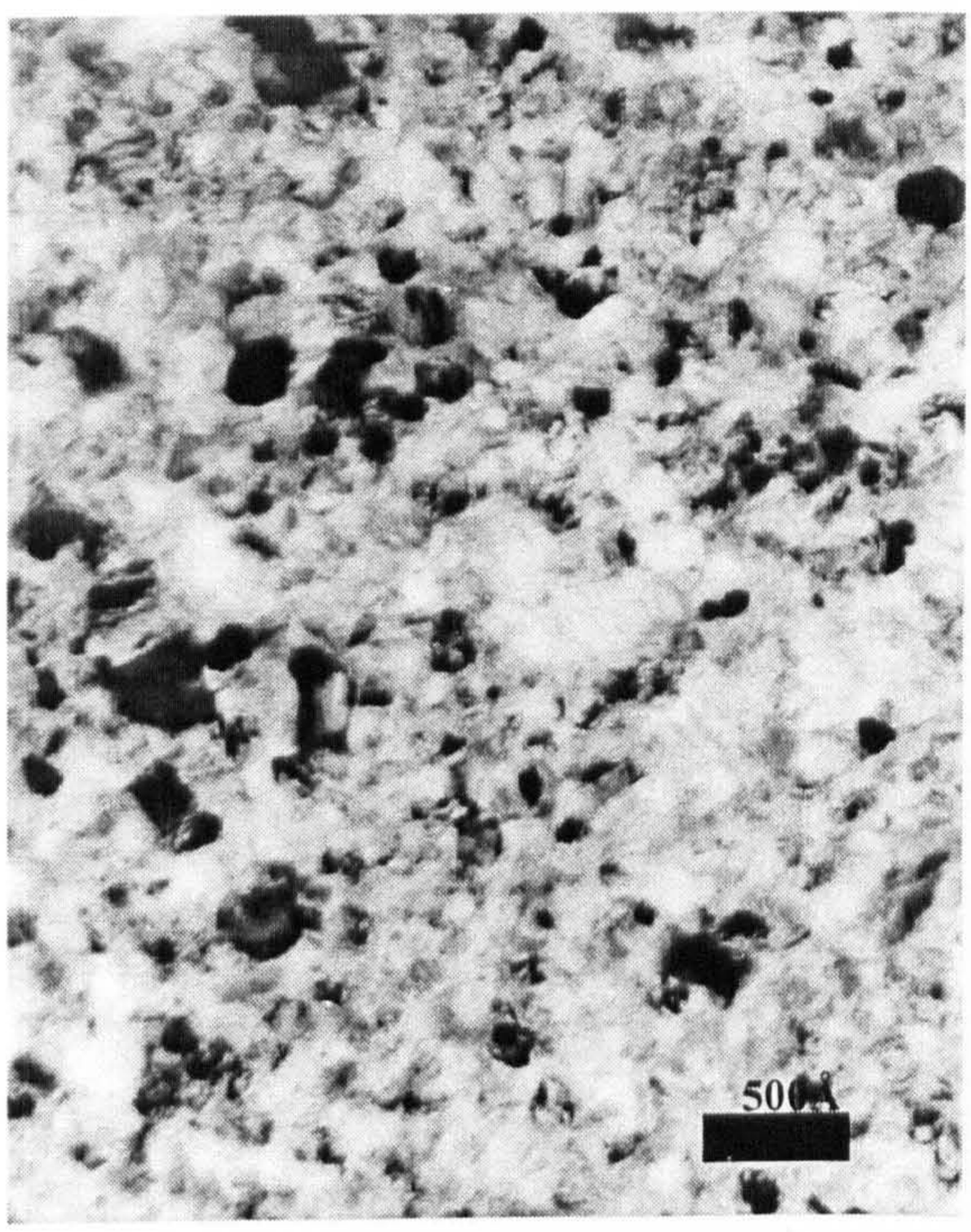

b)

c)

Figure 4.25) Bright field images of reactive FeN samples deposited using partial pressure ratios of a) 6% b) 12% and c) 26%.

The progression of grain sizes is similar to the atom source samples. Large grain sizes are an indication of a reduction of stress in a material and so it seems that the presence of similar phases when comparing the two different nitriding techniques there would appear to be less stress in the films with increased amounts of nitrogen.

4.6 Magnetic Properties

4.6.1 Hysteresis loops

It is worth remembering here that the magnetization values from the VSM were normalized with respect to a sample measured on a SQuID magnetometer.

The hysteresis loop of a 426Å thick Fe film is shown in figure 4.26. The loop was very square with a coercivity of 35 Oe and saturation magnetization of 1552 emu/cm^3,

where bulk Fe has a magnetization of 1714 emu/cm^3. This is the benchmark for which all subsequent samples will be considered in order to understand what is happening in these multilayers.

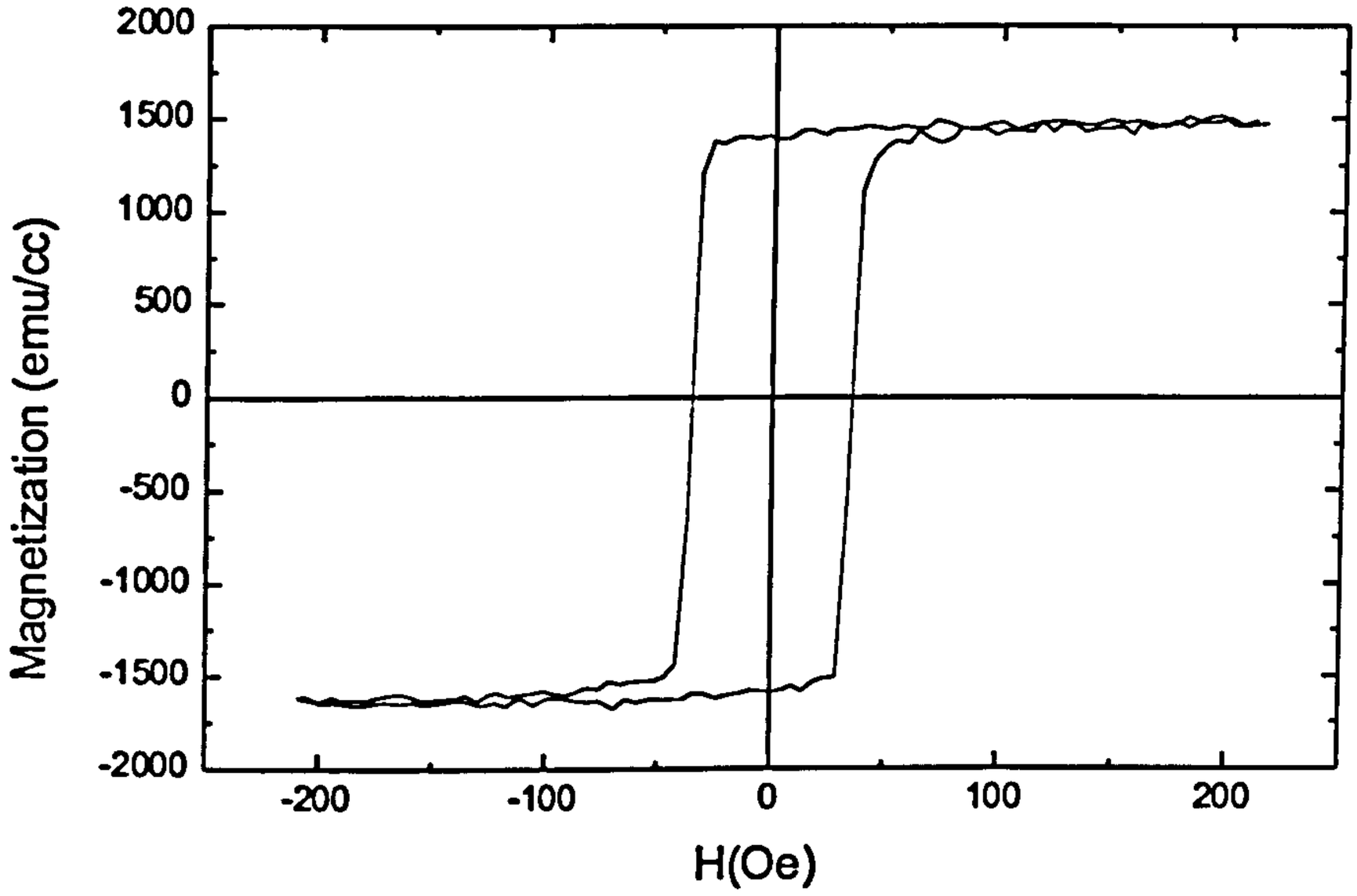

Figure 4.26) VSM hysteresis loop of an Fe thin film.

Figure 4.27a through 4.27e show the hysteresis loops for the effective bilayers Fe=7, 14, 21, 42 and 84Å and nitrogen exposure of 30 seconds.

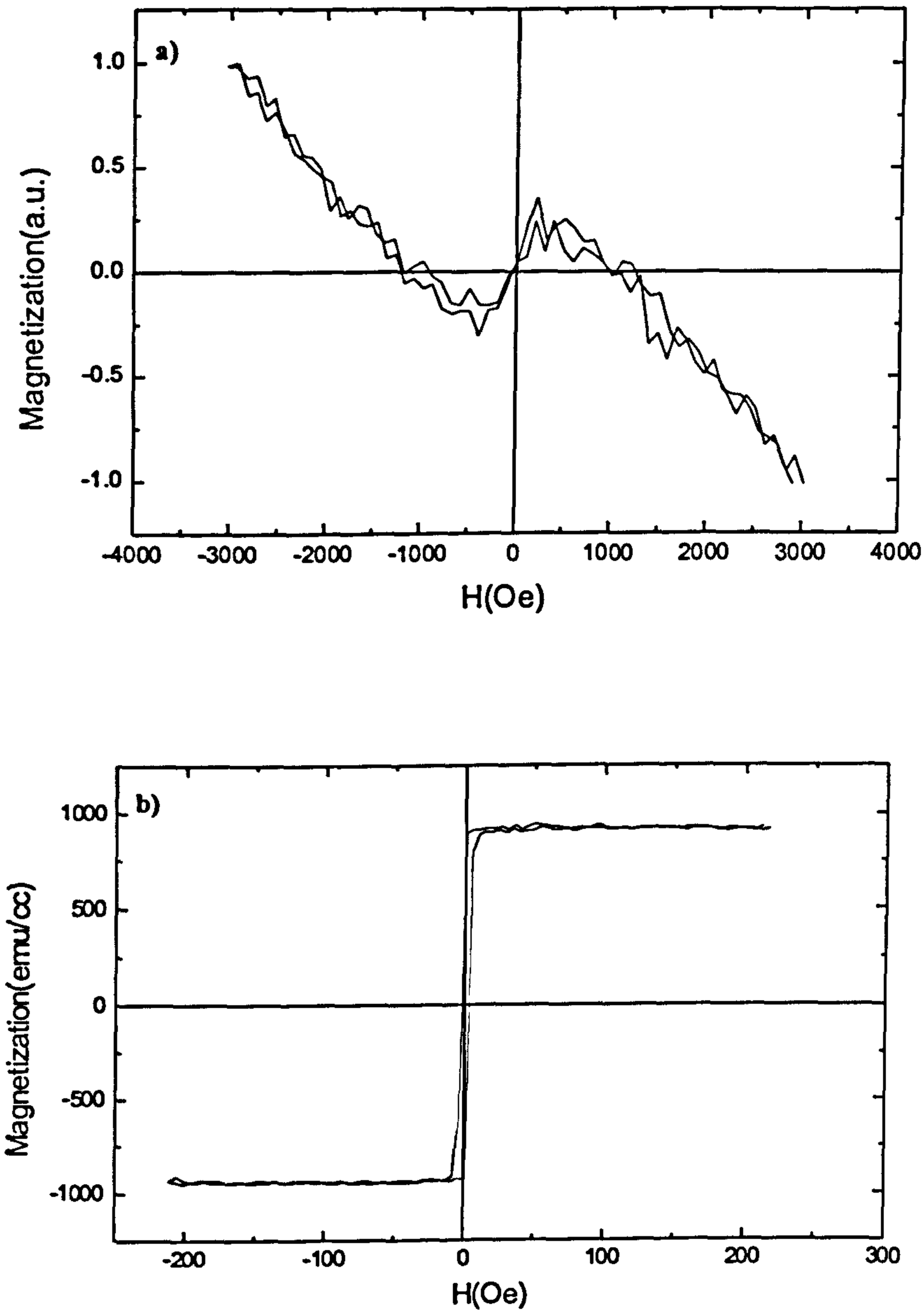

Figure 4.27a) and b).

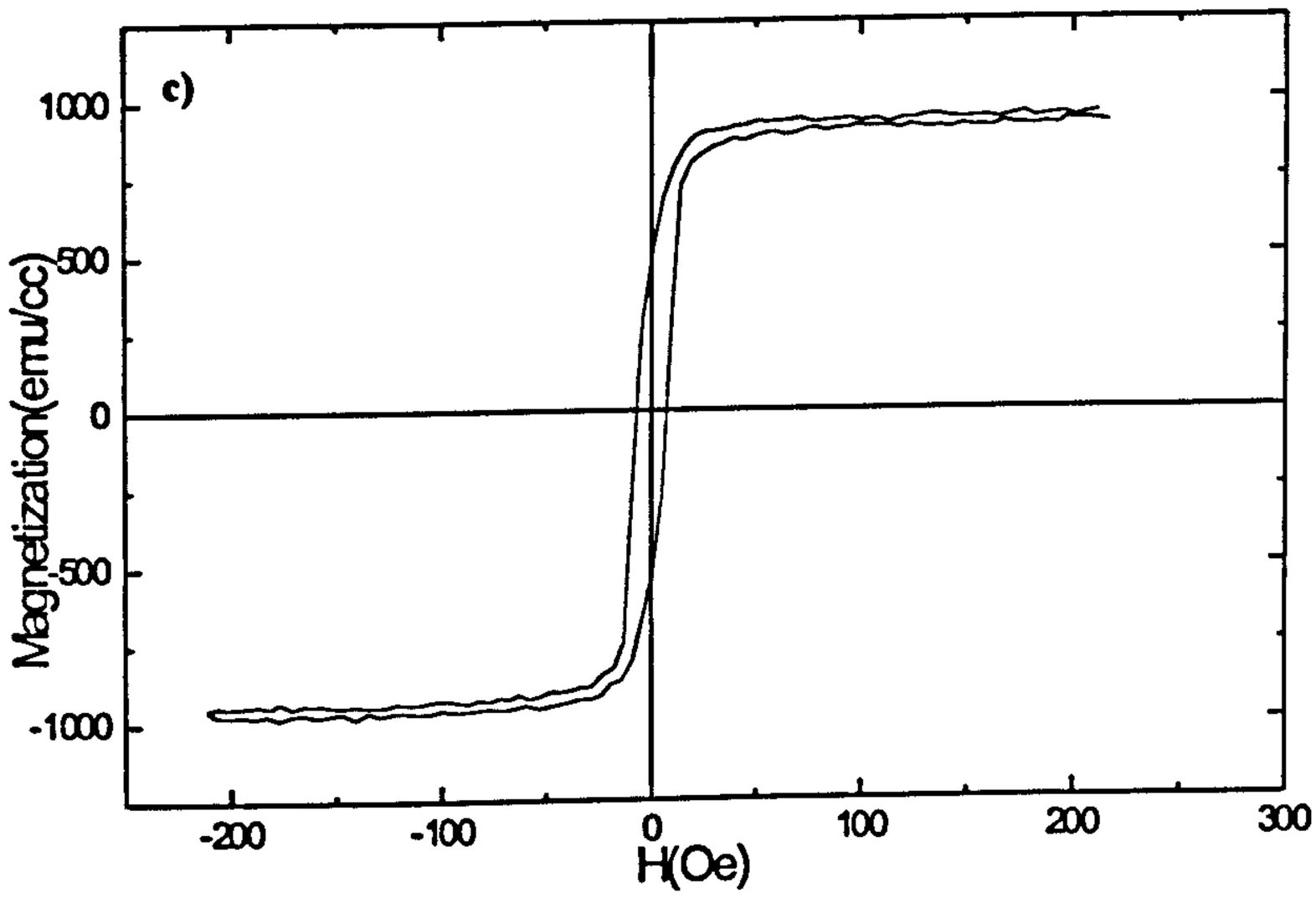

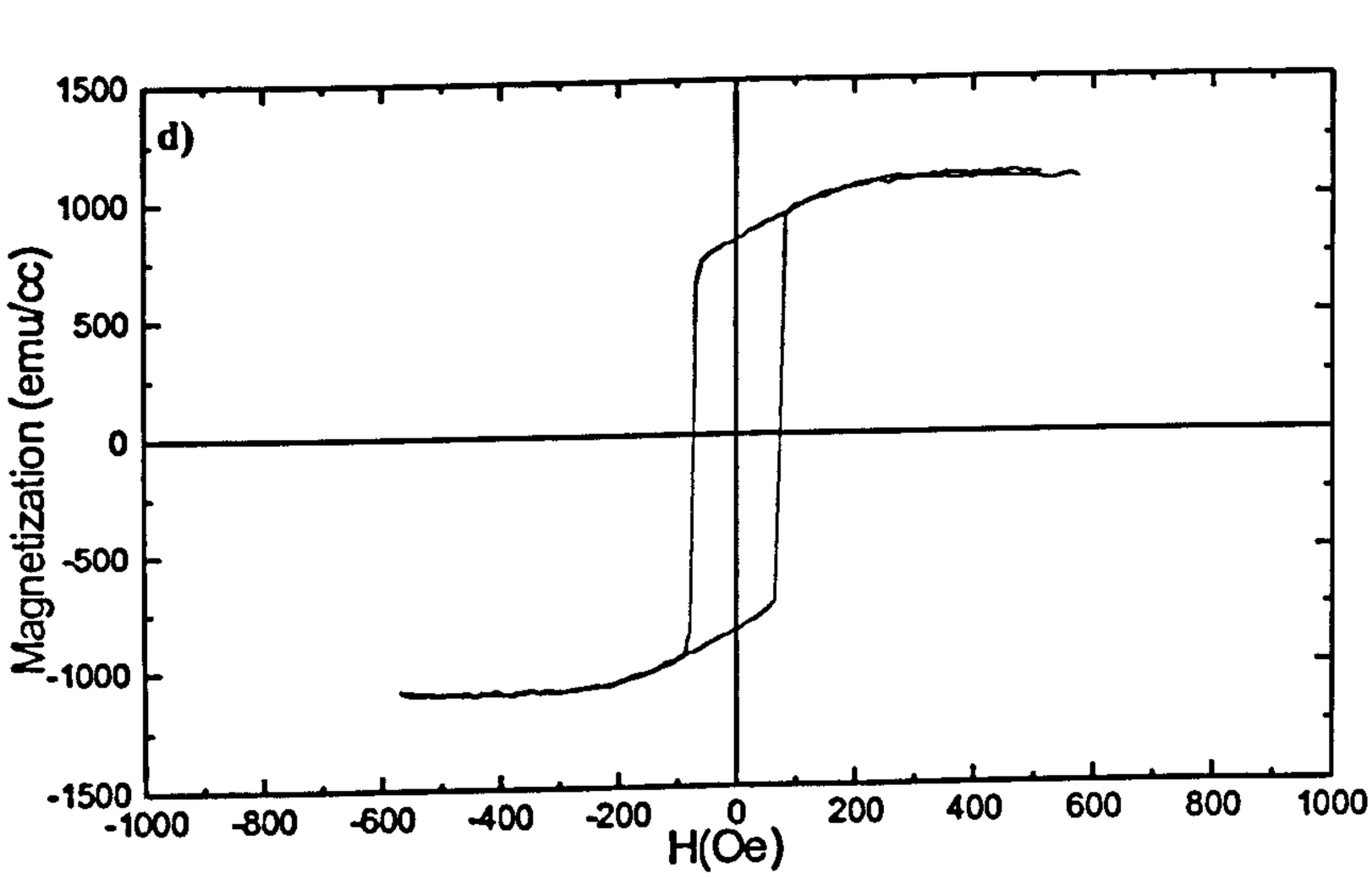

Figure 4.27c) and d).

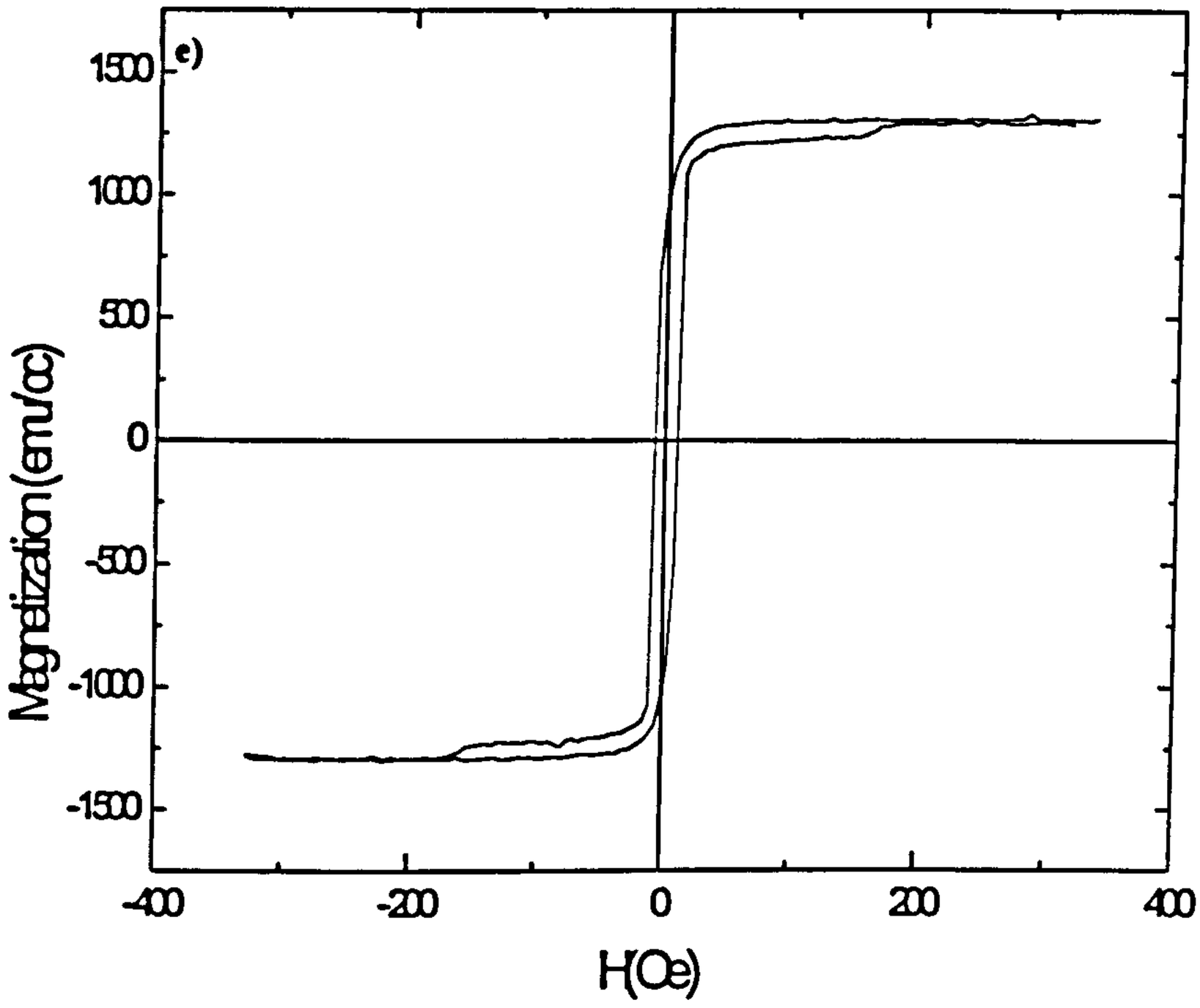

Figure 4.27) Hysteresis loops of samples with effective bilayers of a) 7Å Fe, b) 14Å Fe, c) 21Å Fe, d) 42Å Fe and e) 84Å Fe, each with 30 seconds N exposure. All but a) were acquired on the VSM while a) was acquired on the AGFM.

For the sample made up of 7Å thick Fe layers the magnetic response appears paramagnetic or ferromagnetic as shown in figure 4.27a. The magnetization curve was taken on an AGFM since it was more sensitive to smaller amounts of magnetic material. The signal from the Fe_2N consisted of the straight line with positive slope in the region of low field. As the field was increased the signal was dominated by the silicon substrate giving a diamagnetic contribution to the curve at high fields with its negative susceptibility. For the 14Å Fe layer sample, the hysteresis is ferromagnetic as seen in 4.27b. The loop is very soft with a coercivity of about 2 Oe. The saturation magnetization was calculated to be 925 emu/cm^3 from SQuID and reflectivity measurements. Further increasing the Fe layer to 21Å gave the hysteresis loop in figure 4.27c. Again the loop is ferromagnetic having an increased coercivity of 67 Oe and a saturation magnetization of

957 emu/cm^3. This loop came from the sample with a bilayer consisting of Fe_3N and Fe_4N. The region just below saturation is markedly different as well. The loop shows evidence of magnetization reversal due to rotation instead of domain wall motion as evidenced by the rounded feature. The loop is also slightly slanted indicative of magnetization out of the plane. The sample with effective bilayer consisting of 42Å Fe, in figure 4.27d, showed a very different response from the previous ones. The loop is characteristic of weak stripe domains[67, 69, 70].

Further increasing the Fe layer in the effective bilayer destroys the perpendicular anisotropy as shown in figure 4.27e for which the bilayer consists of Fe_4N and α-Fe where the α-Fe layer is thicker here than in the sample that had a stripe domain loop. The loop in figure 4.27e is very square indicative of uniaxial in-plane anisotropy. Present in the figure is also a rounded approach to saturation and a second switching field at about 200 Oe. Here again the loop reverses magnetization via rotation. The second switching field is indicative of the bilayer constituents switching separately in a decoupled fashion. This occurred in samples v81 and v85, where the bilayer contained bilayers of relatively less Fe_4N than in v82.

Figure 4.28 shows the hysteresis loops for which the nitrogen exposure time was varied.

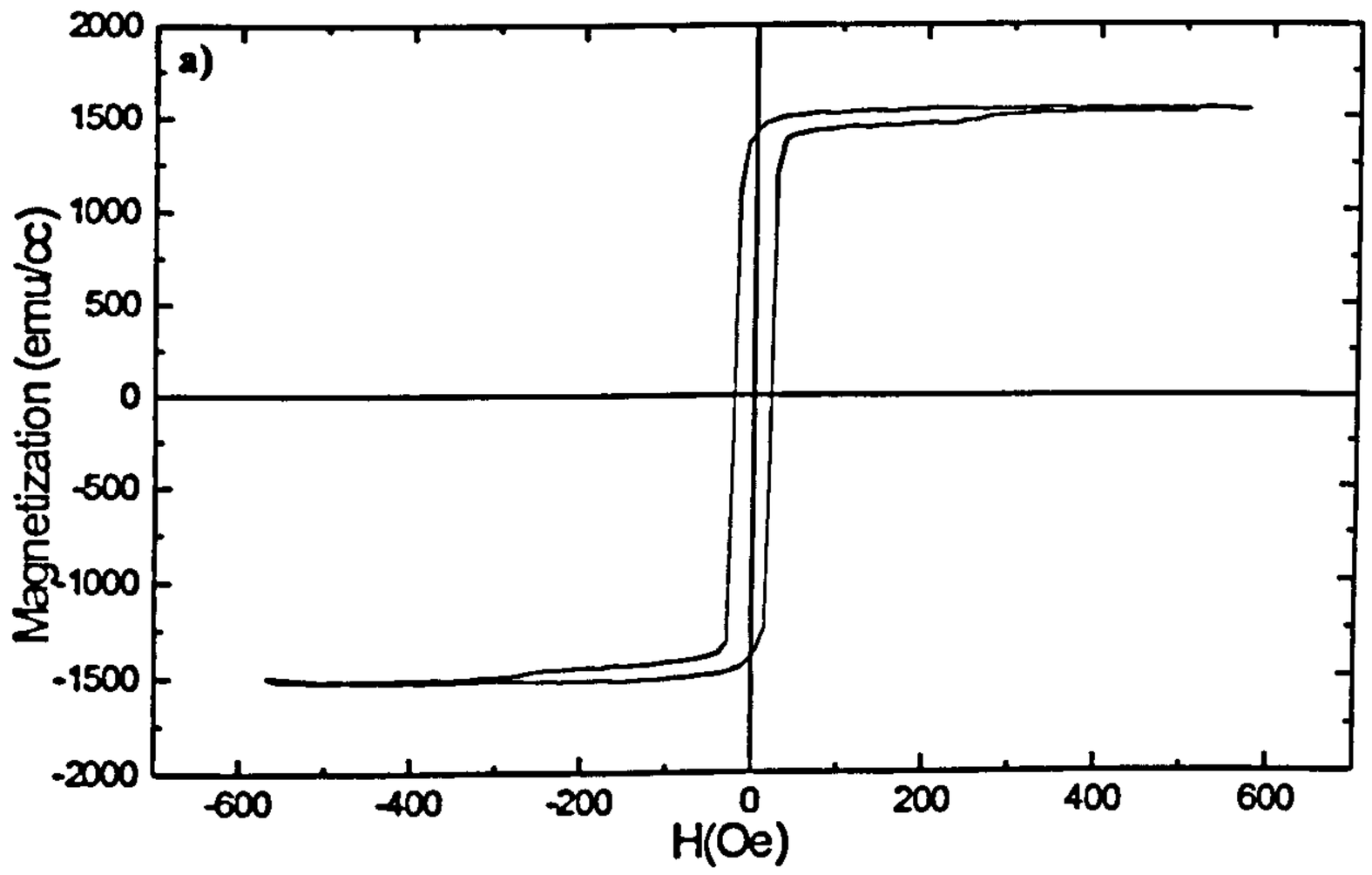

Figure 4.28a).

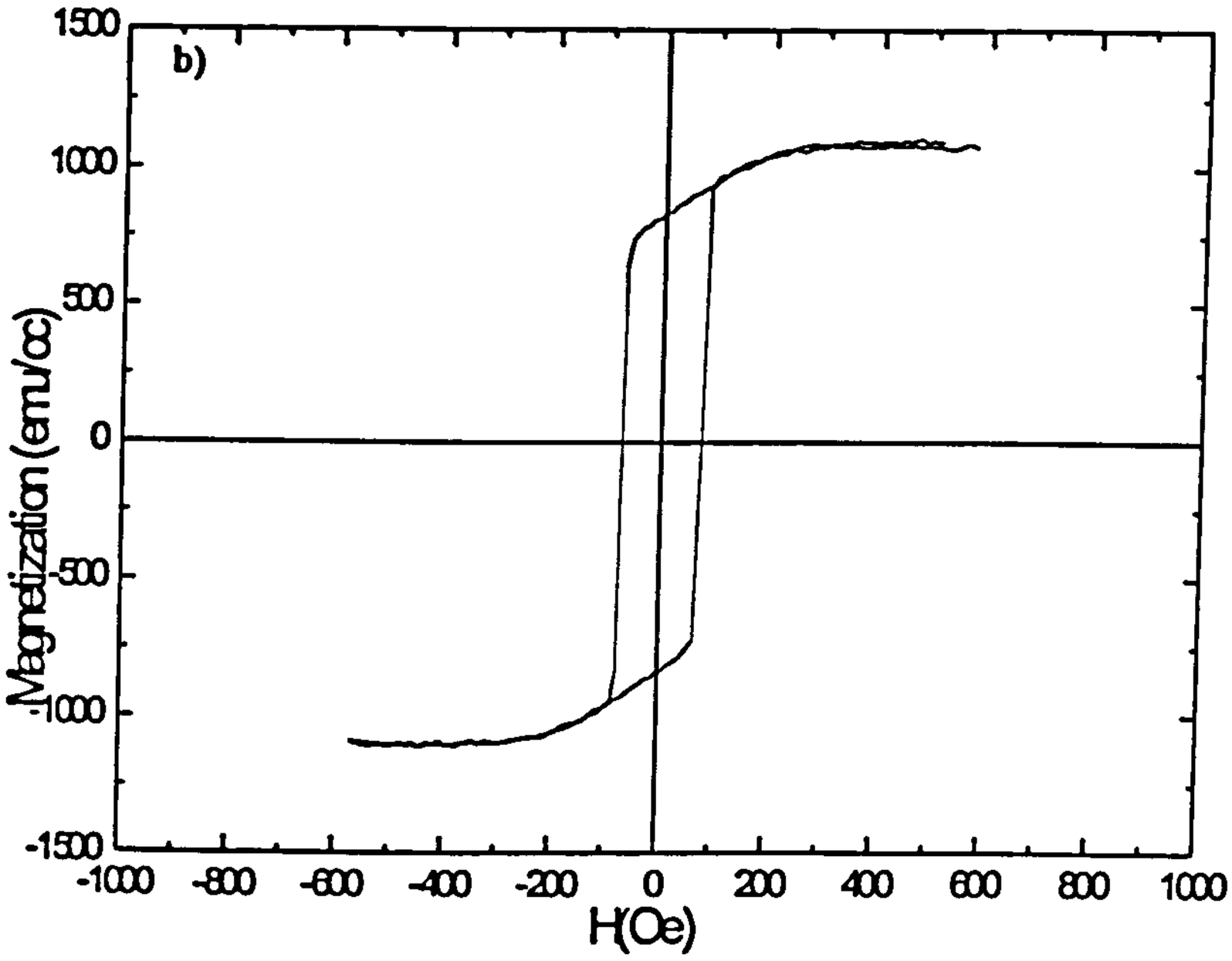

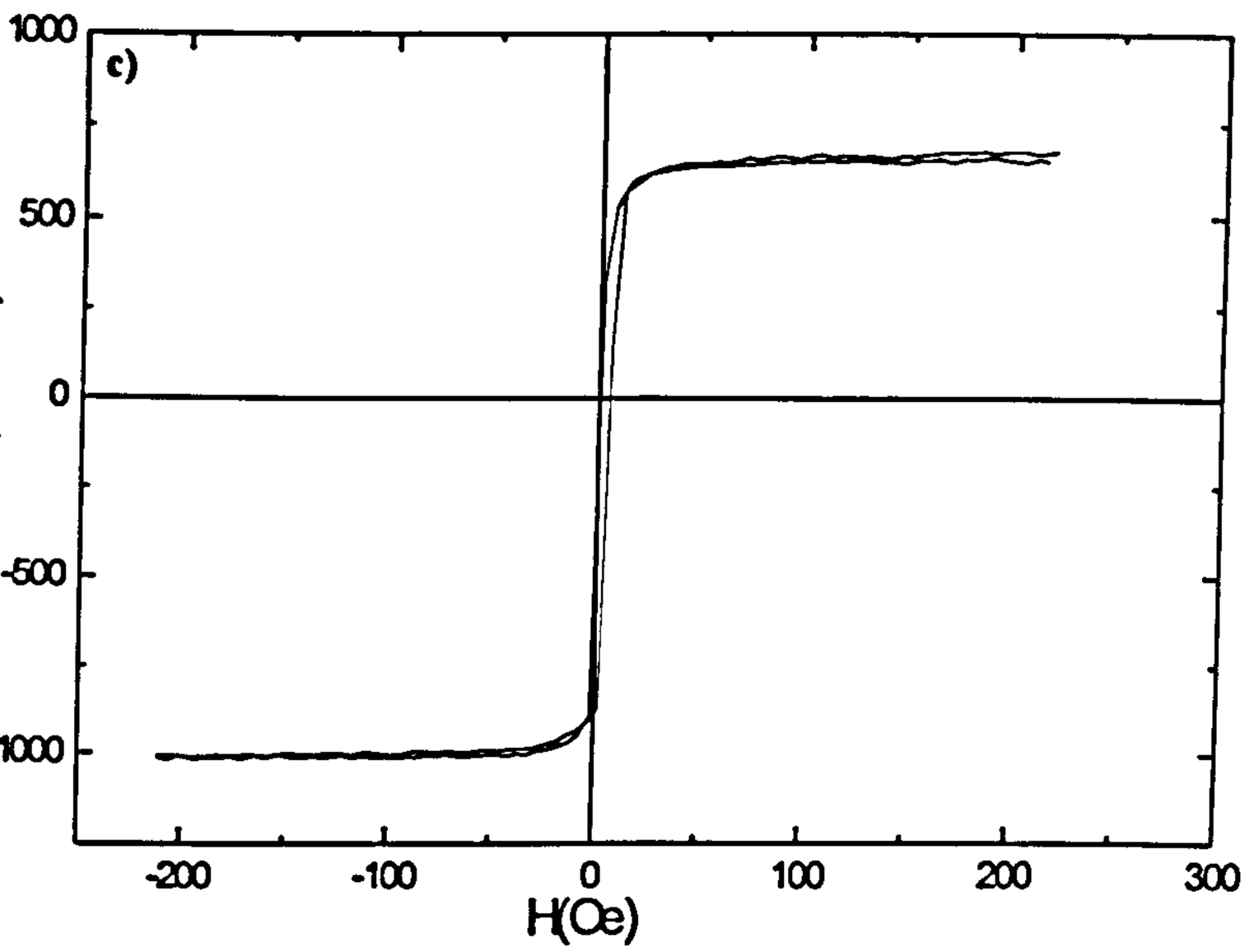

Figure 4.28) VSM hysteresis loops of samples with a 42Å Fe layer and the nitrogen exposure times of a) 5 seconds, b) 30 seconds, and c) 60 seconds.

The loops correspond to effective bilayers of 42Å Fe and 5, 30, and 60 seconds nitrogen exposure respectively. For the shortest nitrogen exposure, figure 4.31a, (5 seconds or the thinnest nitride layer), there is a second switching field consistent with the constant nitride layer thickness but a thicker α-Fe layer. The coercivity was 21 Oe and the M_s was 1520 emu/cm^3. From this it is considered that the sample consists of mostly α-Fe as the M_s deviates only slightly from the value of M_s for a single Fe layer. Increasing the nitrogen exposure time gave the loop in figure 3.30b, which showed a reduced M_s of 1098 emu/cm^3 and a coercivity of 74 Oe. As previously mentioned the loop points to a stripe domain pattern of weak stripe domains. Further increasing the nitrogen exposure further reduced the M_s to 837 emu/cm^3. The pertinent loop in figure 4.31c is also one of the softest of the sample set considered here with a coercivity of 3 Oe. The combination of Fe_3N and Fe_2N as in this sample and the sample with effective bilayer of 14Å Fe 30 seconds nitrogen exposure are consistently very soft. As will be shown in chapter 5, there is a correlation between the M_s and the relative nitrogen content, with an asymptotic approach to the level of α-Fe. This is reasonable if one considers that there is charge transfer from the nitrogen to the Fe atoms thus reducing the number of unpaired electrons responsible for the total moment.

All the samples considered here have been magnetically soft (i.e. the coercivity is less than 100 Oe) in varying degree depending on the phases present. When Fe_3N is present the films are much softer while the presence of Fe_4N seems to increase the coercivity. The introduction of N via the atom source and multilayer system has been effective in altering the magnetic properties in a consistent manner within this sample set. Further effort is required to reduce the nitrogen content of films and more clearly understand its role in producing the aforementioned characteristics including the switch in the magnetization reversal mode and the apparent perpendicular anisotropy.

4.6.2 MFM

As mention above in the section on hysteresis the sample with an effective bilayer of 42Å Fe and 30 seconds nitrogen exposure had a loop characteristic of a material with

stripe domains. The MFM image shown in figure 4.29 is of that sample.

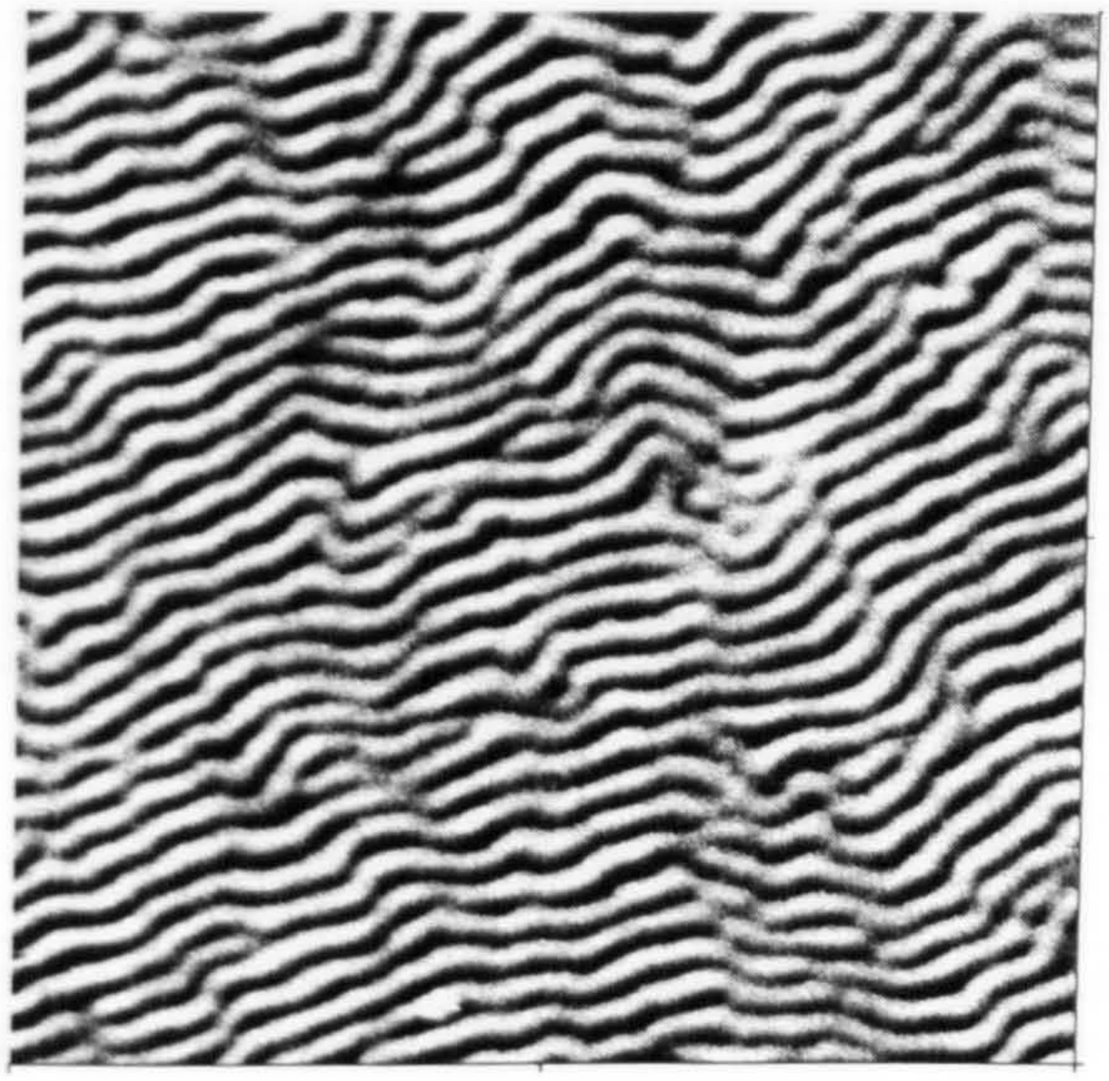

Figure 4.29) 5*5μm² MFM image of v82(42Å Fe/30 seconds N) in the remanent state.

The stripes are continuous across the image with a noticeable change in intensity of the stripes in a regular pattern along the stripes. This phenomenon is indicative of weak stripes where the magnetization vectors are pointing in the same direction when one considers the in-plane direction but there is an oscillation of the perpendicular component giving rise to the stripes.

The stripe domain pattern here is stabilized by the substrate. A possible mechanism for this might be compressive stress induced by being constrained by the substrate. Preparing the sample for electron microscopy destroyed the perpendicular anisotropy, possibly relieving any stress. Figure 4.30 shows two MFM images of the stripe domain sample after undergoing the TEM sample preparation protocol as detailed in chapter 3.

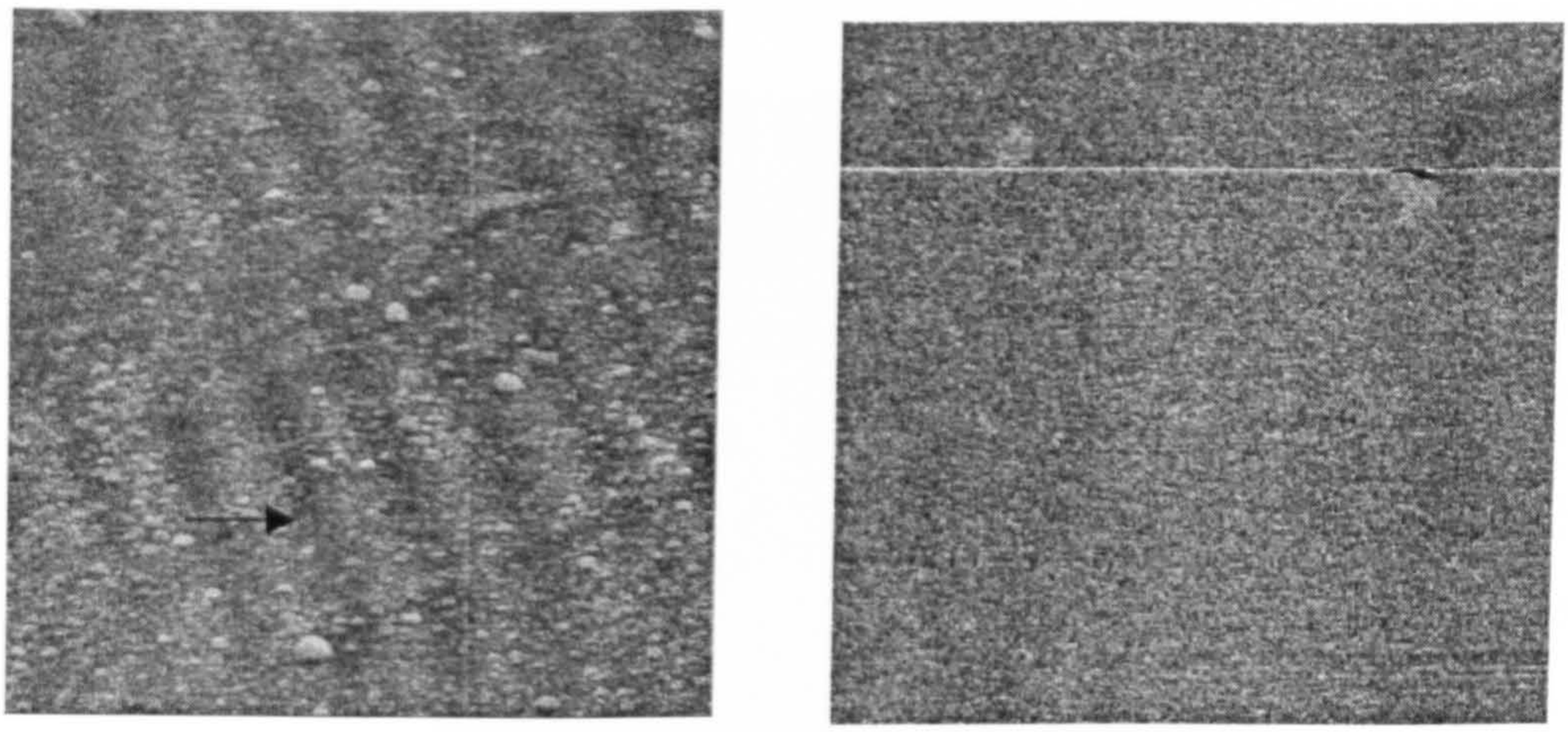

a) b)

Figure 4.30) 10×10 μm² MFM Images taken from TEM specimen of v82 (42Å Fe/30 seconds N). The images were taken at a) the outer edge of the specimen and b) the region near the hole of the specimen.

Figure 4.30b is an image from the thinnest region of the TEM sample. It does not show stripe domains. Figure 4.30a is an image from the outer portion of the sample where there was still substrate present. There are still stripe domains, however their intensity was quite diminished as compared to figure 4.29. The width of the stripes here has seemingly increased significantly. This is a bit suspect, but the contrast was considered real due to there being a phase shift of the contrast, labelled by the arrow in figure 4.30a, which is typical of images where the tip magnetization switches owing to the interaction with the sample. Hence, the thinning process destroyed the perpendicular anisotropy. The stripe domain width is about 1000Å in figure 4.29. This is on the same order as the sample thickness, in agreement with the model of Saito[70]. For the sample that showed a slanted loop in figure 4.27c the MFM image showed no contrast as in figure 4.31. Given that the MFM detects stray fields perpendicular to the film plane it will only effectively see domain walls for in-plane easy axis samples.

Figure 4.31 showed no evidence of domain walls, within the 5 by 5 μm² area. Either the domains are larger than the scan area or tip-sample interactions have switched

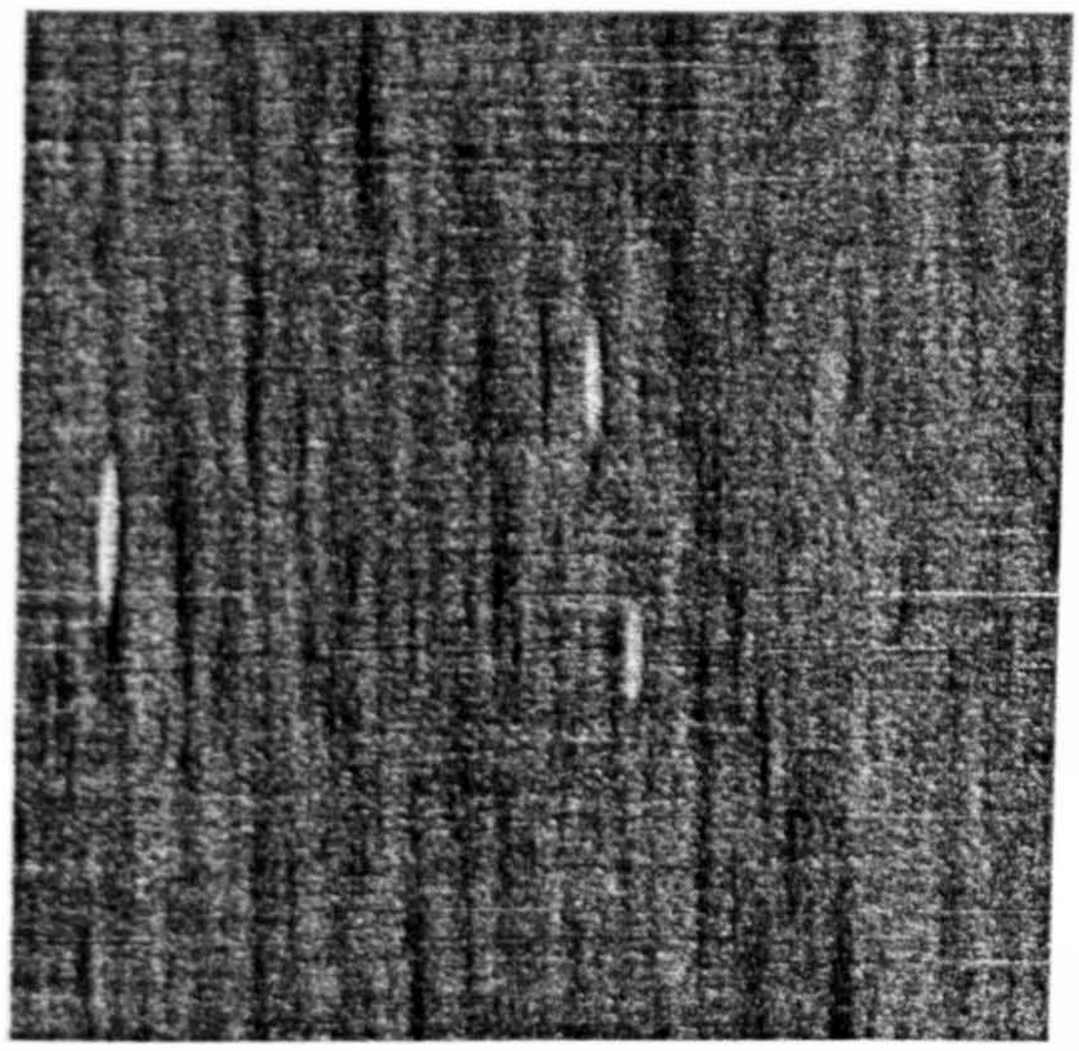

Figure 4.31) 5×5μm² MFM image of v80 (21Å Fe/30 seconds N).

the magnetization of the sample. For the soft films here this has been a major consideration, for if the field from the tip is strong enough to switch the sample a "true" picture of the magnetic domain structure may not be realized.

4.6.2a Variable field experiment

As mentioned in chapter 2 the test to determine the presence of either strong or weak stripes is to image the domains looking for any change in domain widths and any rotation of the stripes when a field is applied at an angle to the stripes. Figure 4.32 shows the results of varying the field from about the saturation field to a remanent state and imaging the same area for the sample with the effective bilayer of 42Å Fe 30 seconds nitrogen exposure.

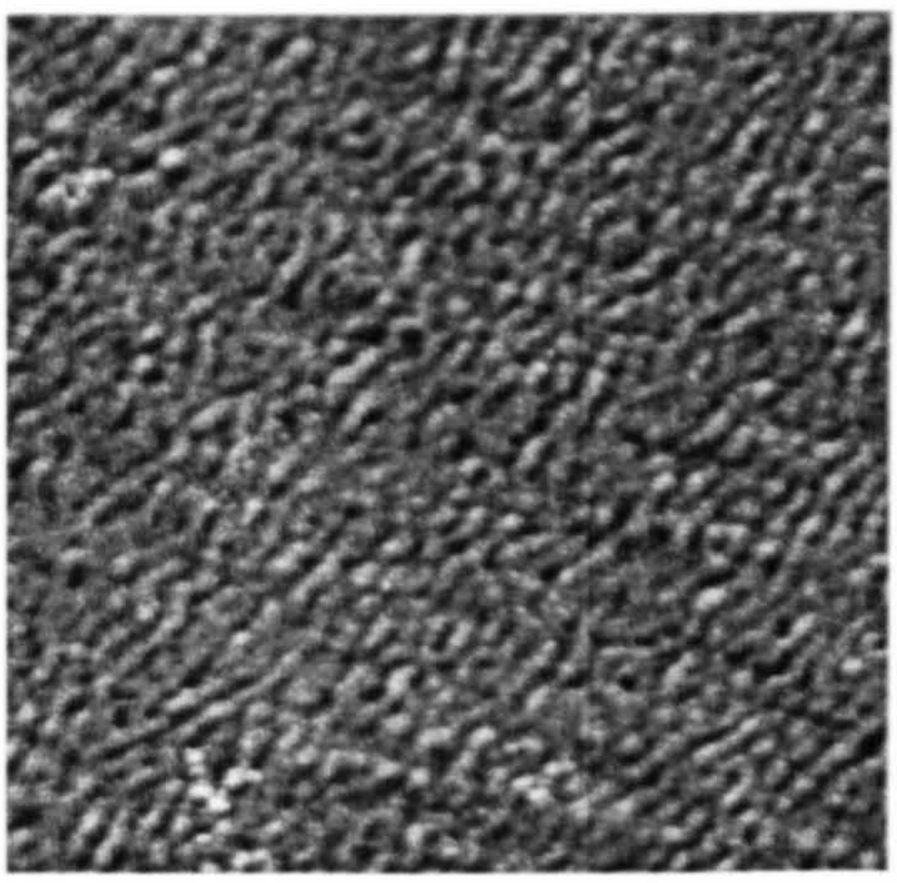

a)

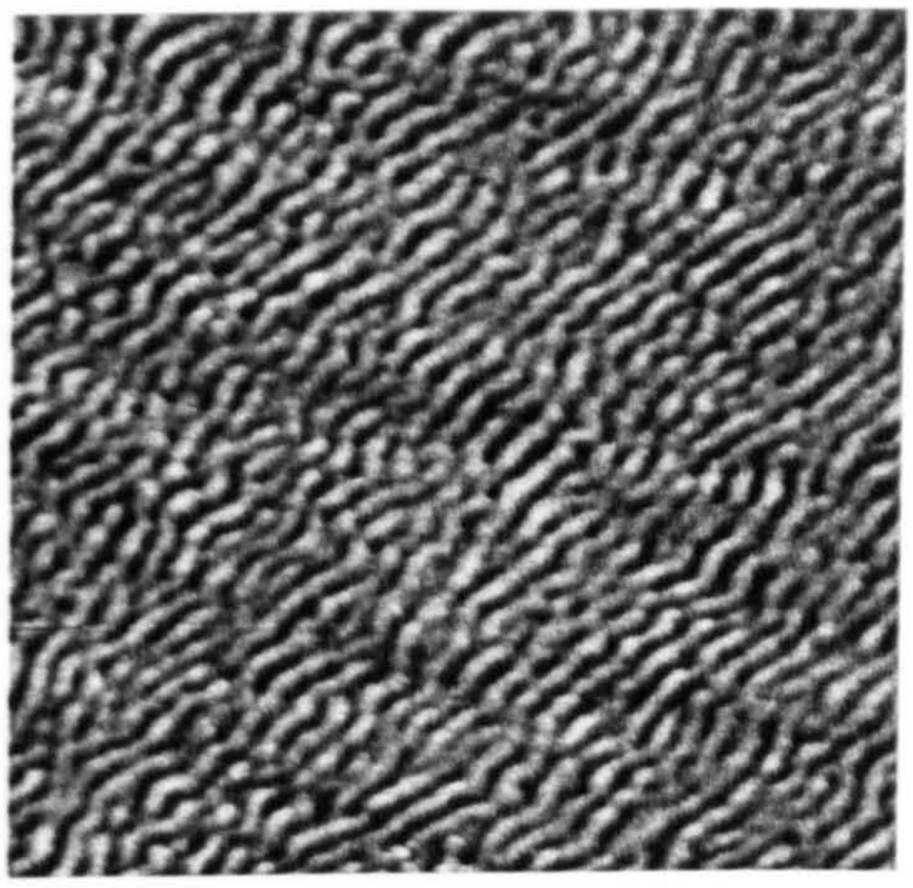

b)

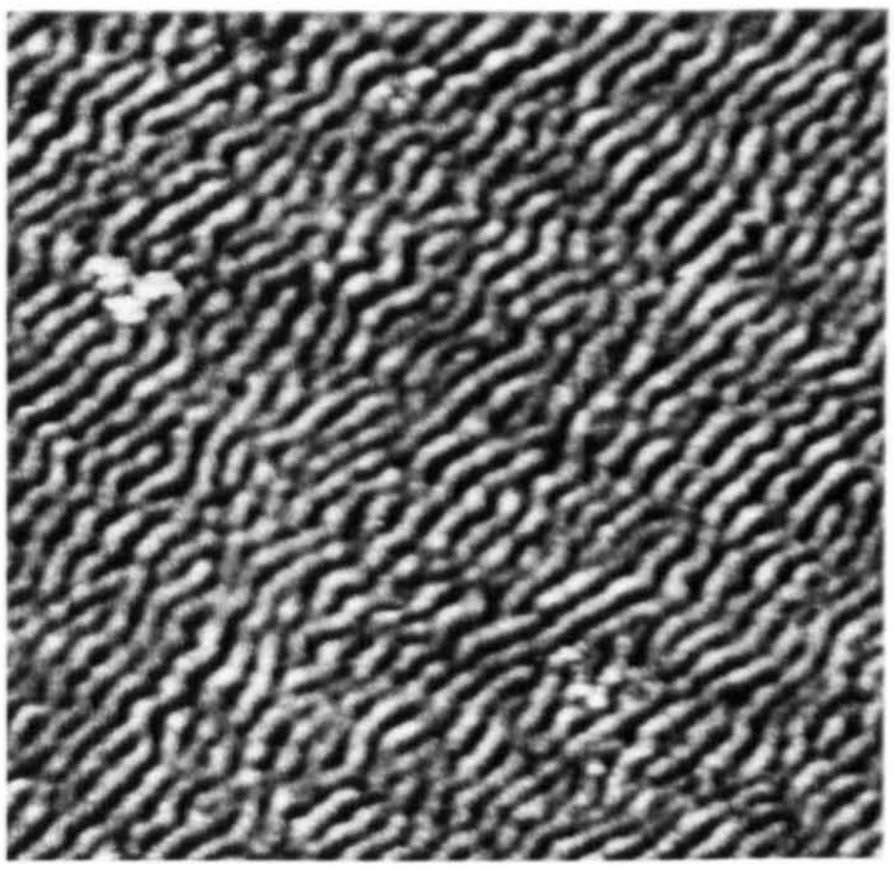

c)

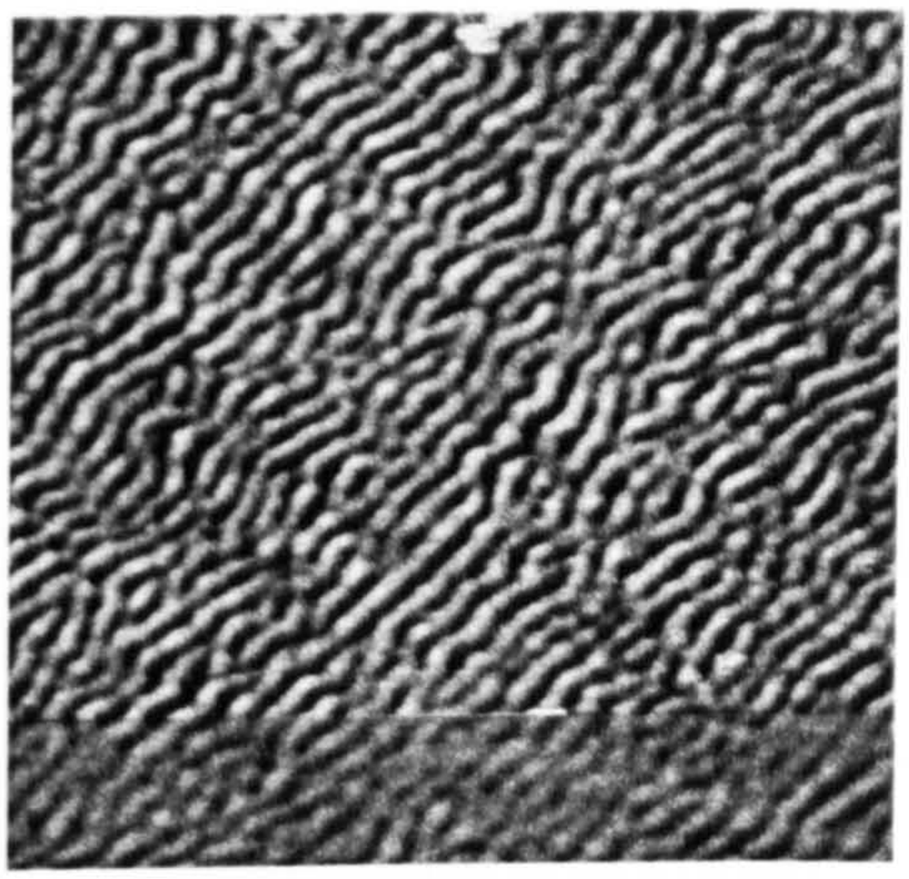

d)

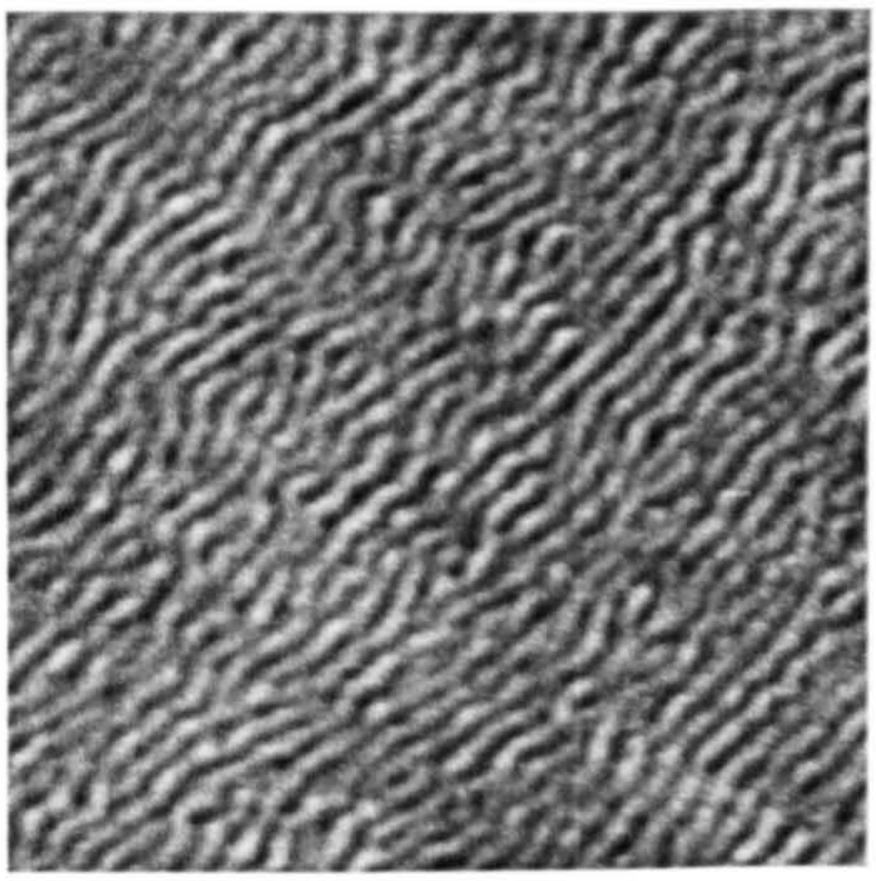

e)

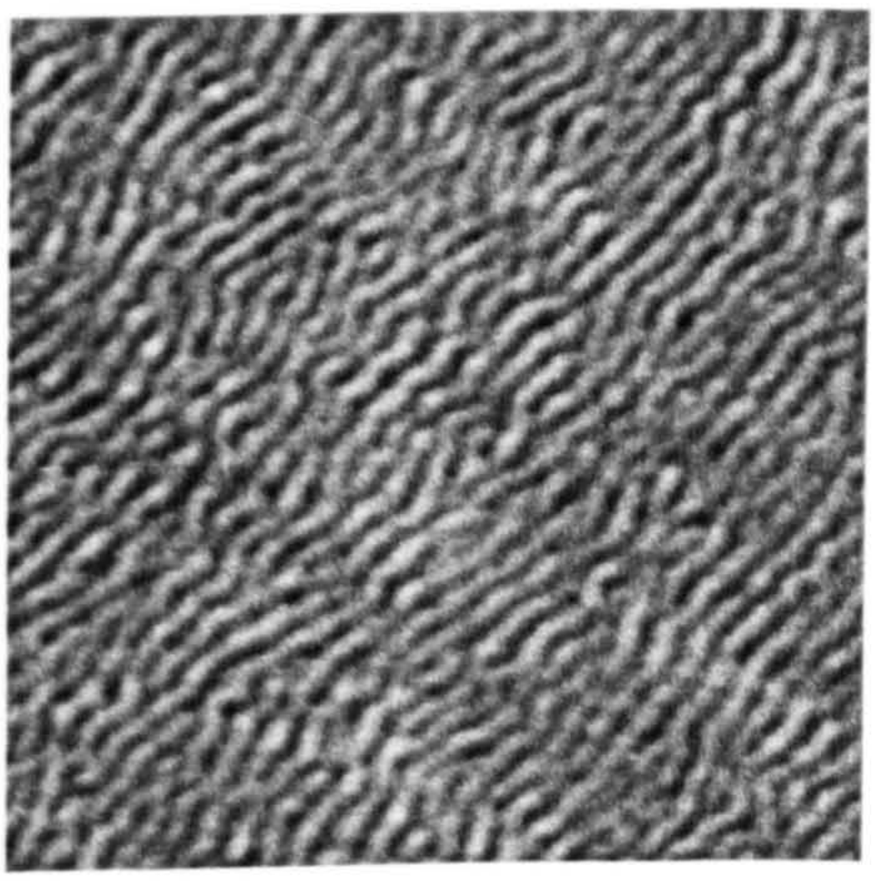

f)

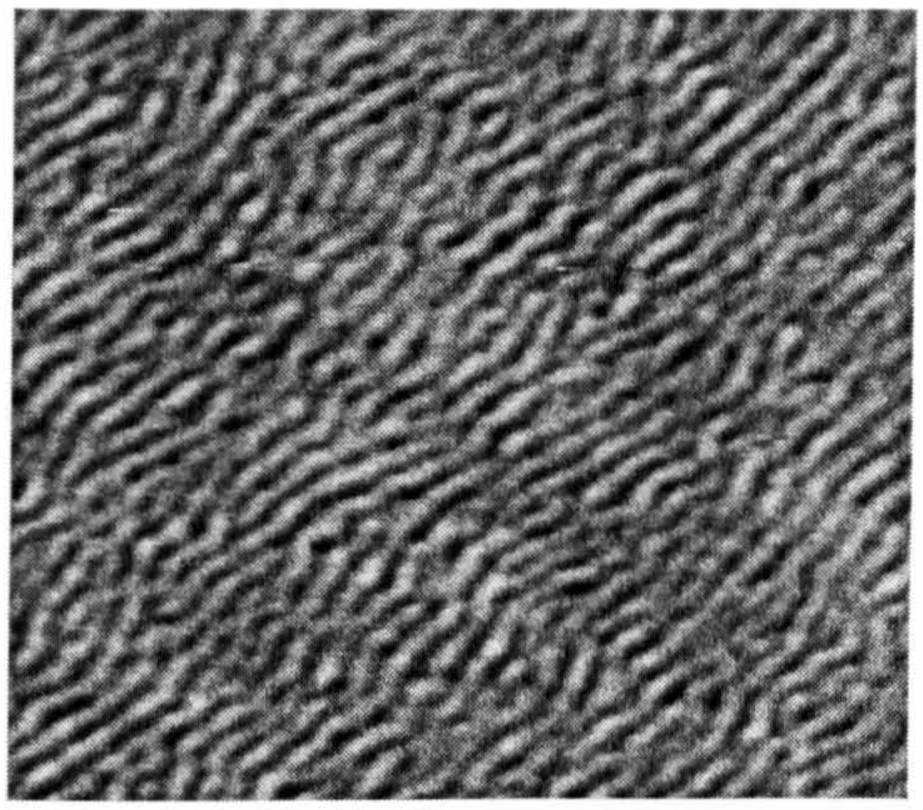

g)

Figure 4.32) 5×5μm² MFM images of v82 (42Å Fe/30 seconds N) taken in the presence of an applied field of a) 262 Oe, b) 123 Oe, c) 85 Oe, d) 71 Oe, e) 57 Oe, f) 46 Oe and g) 39 Oe. The direction of the applied field was along the direction of the stripes.

The largest field applied to the sample does not seem to have saturated the sample completely owing to the presence of a weak contrast in the image despite the fact that the saturation field is less than about 200 Oe as was shown in figure 4.27d. The presence of weak contrast was attributed to an inhomogeneous field of the permanent magnets across the sample. Reducing the field strength brought about a stripe domain pattern for which the stripes are aligned with the applied field. The intensity of the stripes increased as the field strength was reduced as seen in figure 4.32, but the domain widths remain of constant width. Once the image taken at the minimum field strength was completed a field perpendicular to the original field was applied. As seen in figure 4.33 the stripes have rotated by about 45 degrees.

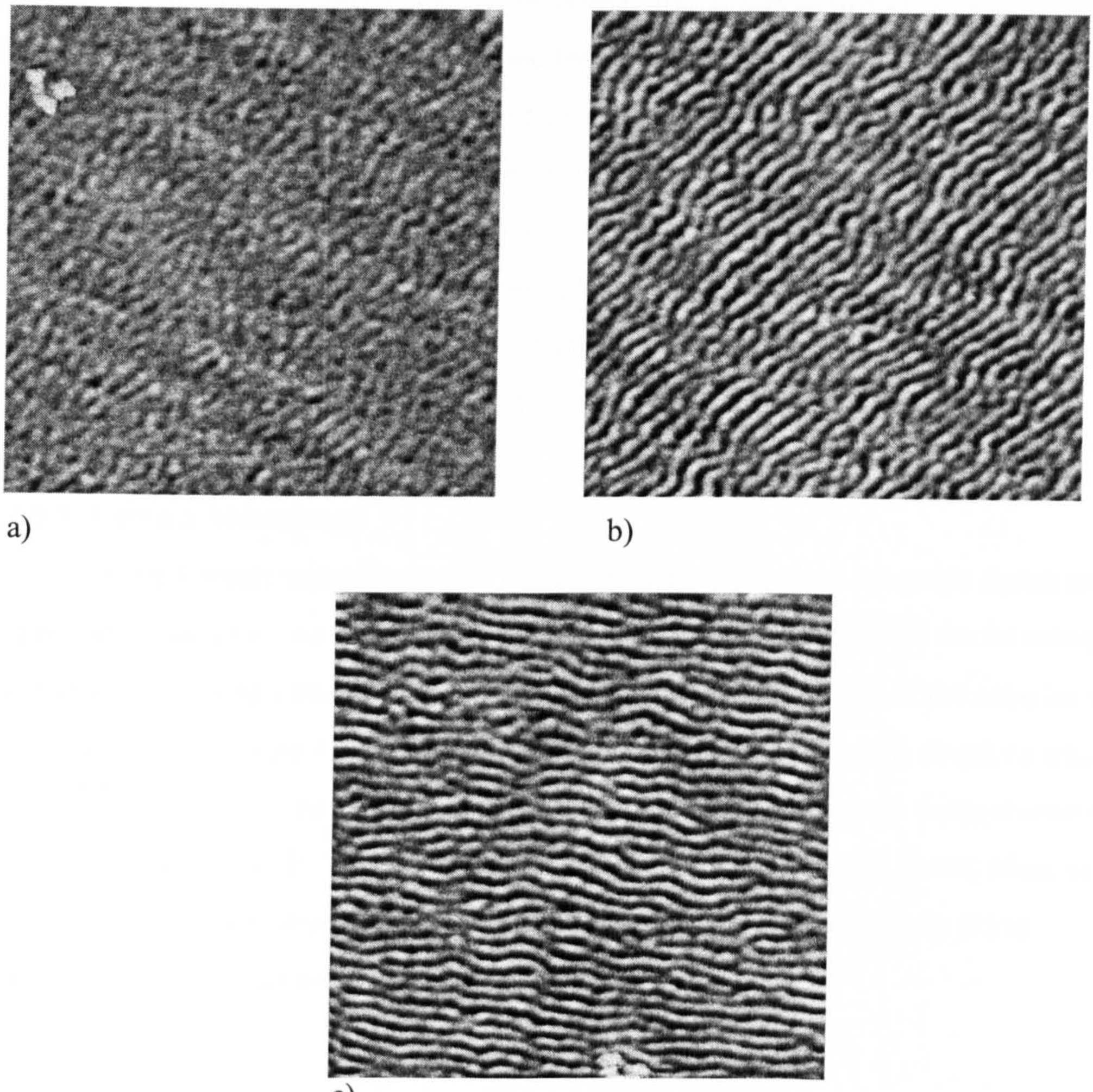

Figure 4.33) 5×5μm² MFM images of v82(42Å Fe/30 seconds N) taken in presence of an applied field of a)262 Oe, b) 39 Oe along the direction of the stripe domains and c) a 200 Oe field brought toward the sample at 90° to the initial field and then removed.

Rotation by 90 degrees did not occur, this may be due to the presence of the original field. In an effort to be consistent, the same area was imaged each time. The original field could

not be removed without removing the sample from the experimental set up when looking at the rotated field. Regardless of this, the stripes do rotate. The stripes in images 4.32a through g showed no obvious signs of becoming wider or narrower, so from this the stripes were shown to consist of weak stripes of the type Saito proposed. If there were closure domains the stripes would not be present due to the geometry of the MFM measurements. As the field was reduced there was evidence of the domains meandering as seen by the wavy nature of the domain pattern. Here the magnetization of the domains is at angles to one another determined to be on the order of 140-160 degrees using the DI software associated with the MFM. There was also a noticeable variation in the intensity in certain regions. This phenomenon would seem to take the form of a variation in the angle of the weak stripes considered by Saito. Hence, the stripe domain pattern is much more complex than the model proposed by Saito, but of the same general form.

4.6.3 Lorentz Microscopy

Here Lorentz microscopy was used in an effort to look at the stripe domains in the appropriate samples. As was mentioned earlier in the section on MFM the thinning process for TEM specimens destroyed the perpendicular anisotropy of the samples with stripe domains. Figure 4.34 below shows a Lorentz image of in-plane domains situated in the thinnest region of the sample. Displayed in the image are domain walls characteristic of in-plane domains. In a different region of the sample, figure 4.35 shows what, at first glance, might be construed as stripe domains near the edge of the sample if the magnification was not considered.

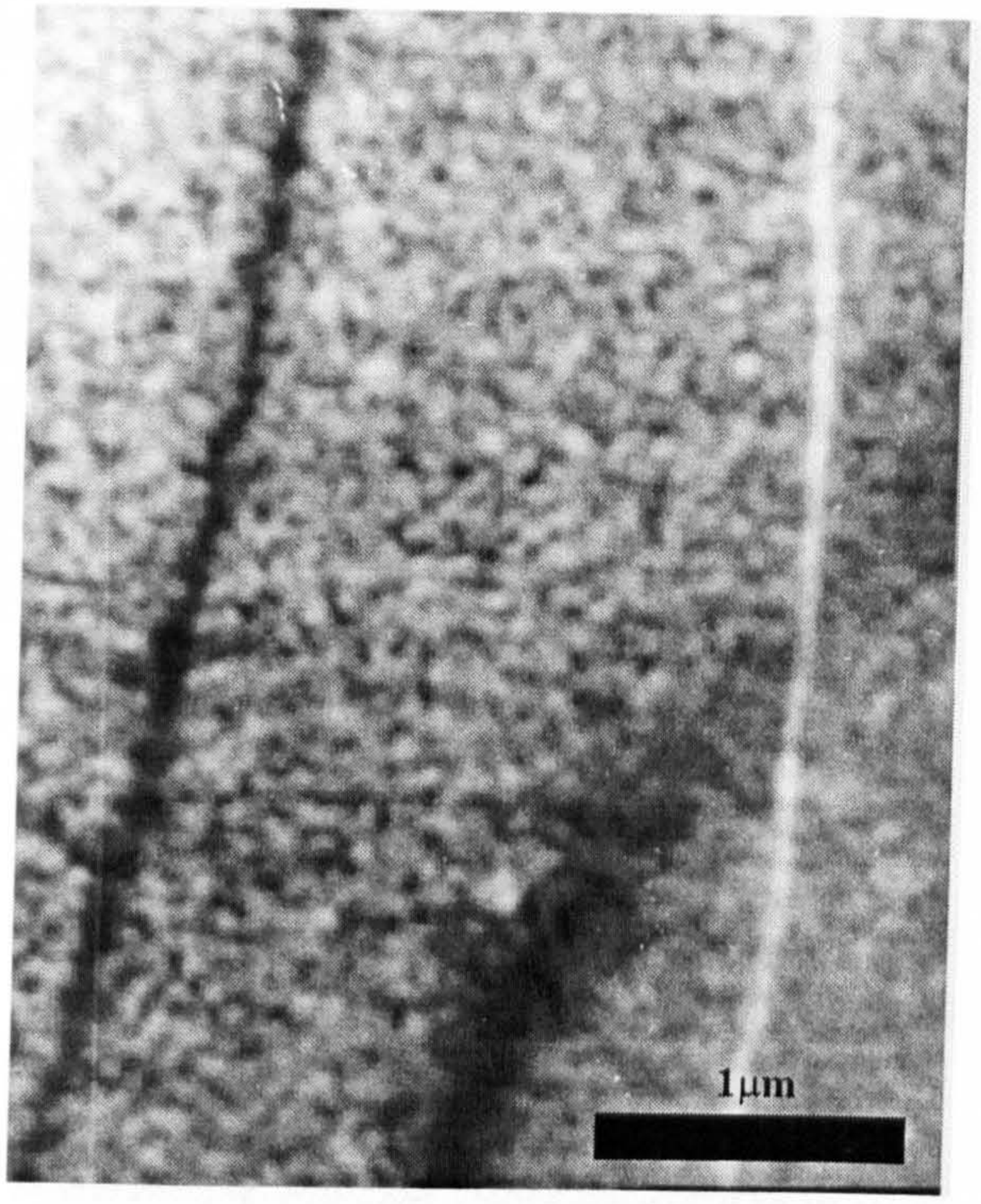

Figure 4.34) Lorentz microscopy Fresnel image of v82 (42Å Fe/30 seconds N) from a region showing only in-plane domain walls.

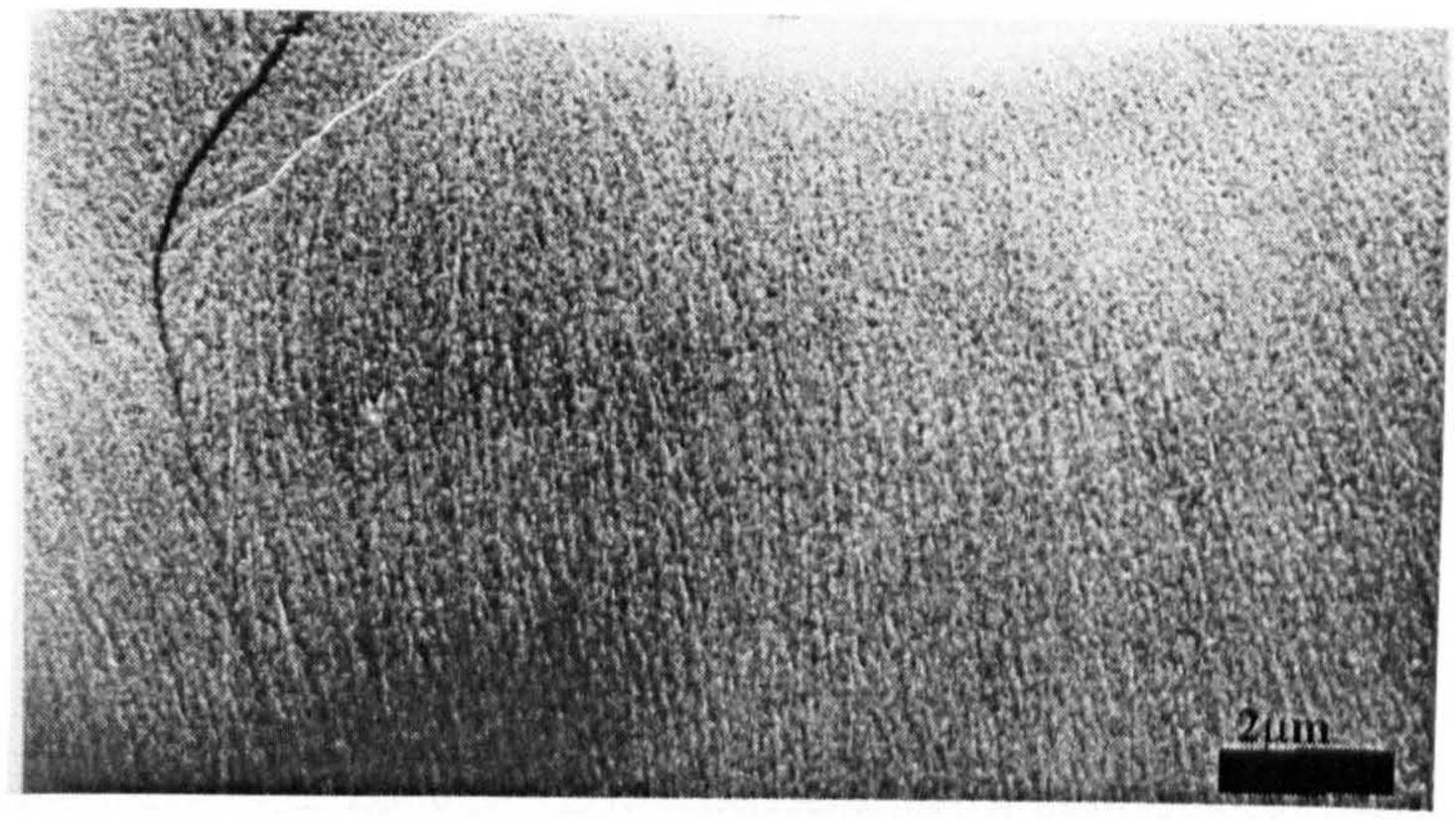

Figure 4.35) Lorentz Fresnel image of v82 (42Å Fe/30 seconds N) of a region showing strong ripple.

In the image a centimetre represents two micrometres. The top of the micrograph shows the beginning of the central hole of the thinned sample. Since the number of vertical line-like contrast in the same area on the MFM image was far less, it was recognized that the contrast here was from intense ripple, or local deviation of magnetization from the direction of the overall magnetization of the domain. The sample with an 84Å Fe layer showed a very square hysteresis loop indicative of uniaxial anisotropy. Figure 4.36 shows a Lorentz image with no ripple evident.

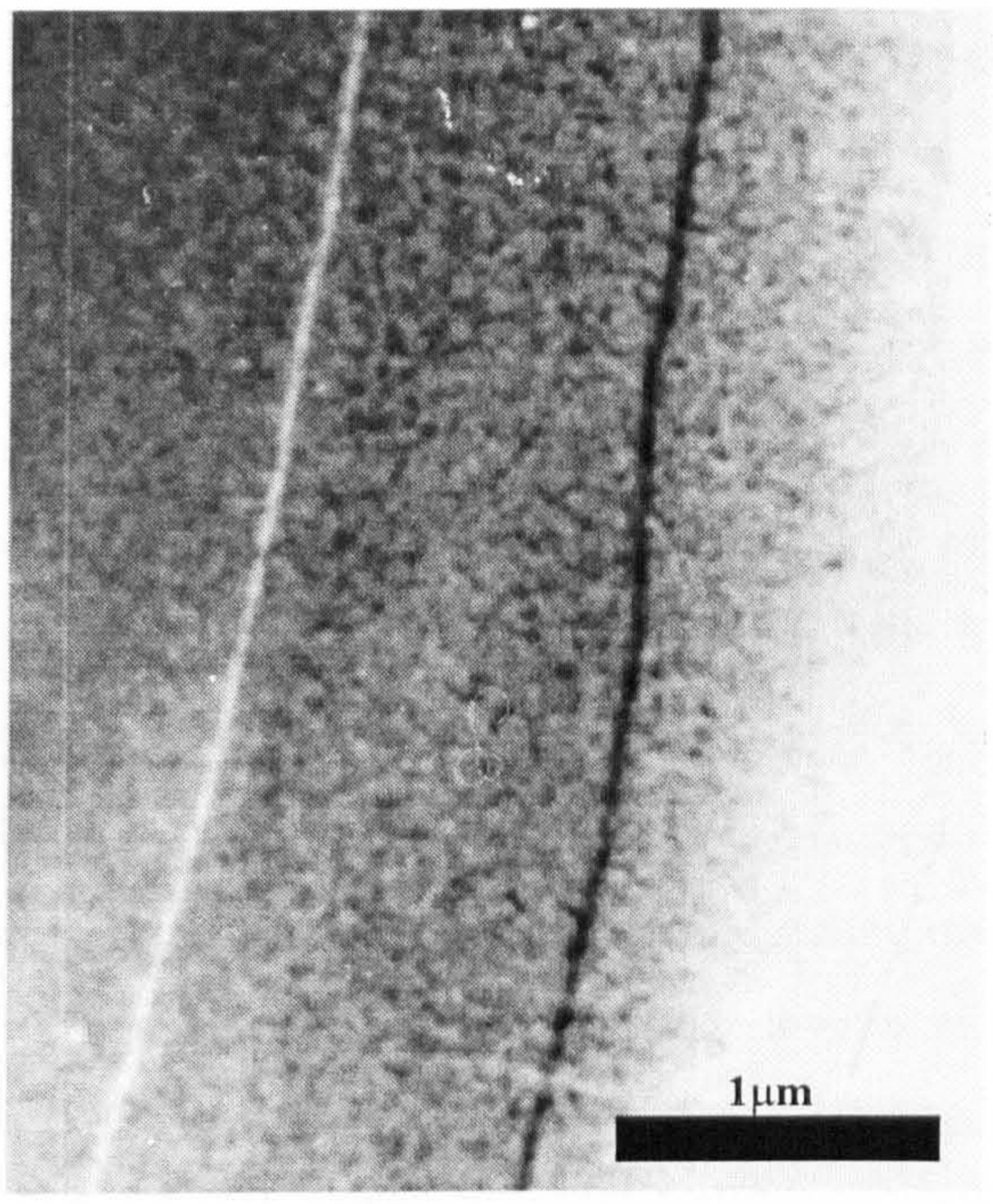

Figure 4.36) Lorentz Fresnel image of v85 (84Å Fe/30 seconds N).

Lorentz microscopy has provided a means of looking at the domain structure that was complementary to the MFM. The MFM is sensitive primarily to perpendicular magnetization while Lorentz microscopy is sensitive to in-plane magnetic structure.

4.7 Discussion

Two main topics require discussion here, the nitriding of Fe using the atom source and the magnetic anisotropy of the samples with Fe_4N.

The structural data displayed above has shed light onto the process of nitrogen incorporation when using a nitrogen atomic beam in the formation of multilayers. As described in chapter 3 a layer of Fe was sputter-deposited and then exposed to the nitrogen beam for a specified time. The XRR results in this chapter point to a multilayer structure. As the Fe layer was reduced the nitriding progressed such that a Fe_4N layer formed reaching a maximum depth. With continued nitrogen beam exposure a layer of Fe_3N formed above a reducing Fe_4N layer until it was completely Fe_3N. Continued nitriding brought the formation of an Fe_2N layer which depleted the Fe_3N until the layer was completely Fe_2N as in the sample with an effective bilayer of 7Å Fe.

One of the curious aspects of the three samples with Fe_4N was the variation of the magnetic response. The 21Å Fe sample was very soft, reversed magnetization by rotation, and showed a slanted hysteresis loop but only in-plane magnetic features in the MFM. The 42Å sample was magnetically harder, reversed by rotation, and showed weak stripe domains. The 84Å Fe layer sample reverted to a very soft material with a second switching field, reversed magnetization via rotation, and strong uniaxial in-plane anisotropy. The 21Å Fe layer sample showed much larger grain sizes which points to the soft, magnetic behaviour as it is well known that coercivity decreases with increased grain size[30]. The 42 and 84Å Fe layer samples showed very similar grain structures and contained the same nitride phase. The difference here in terms of deposition parameters is that the 84Å Fe layer sample would have a thicker Fe layer having the same eventual nitride layer thickness in light of the proposed growth mechanism. Yet the thinner bilayer sample contains stripe domains and the other has strong in-plane uniaxial anisotropy. This perpendicular anisotropy may be a result of microstructural anisotropy. A cross sectional TEM micrograph is shown in figure 4.37.

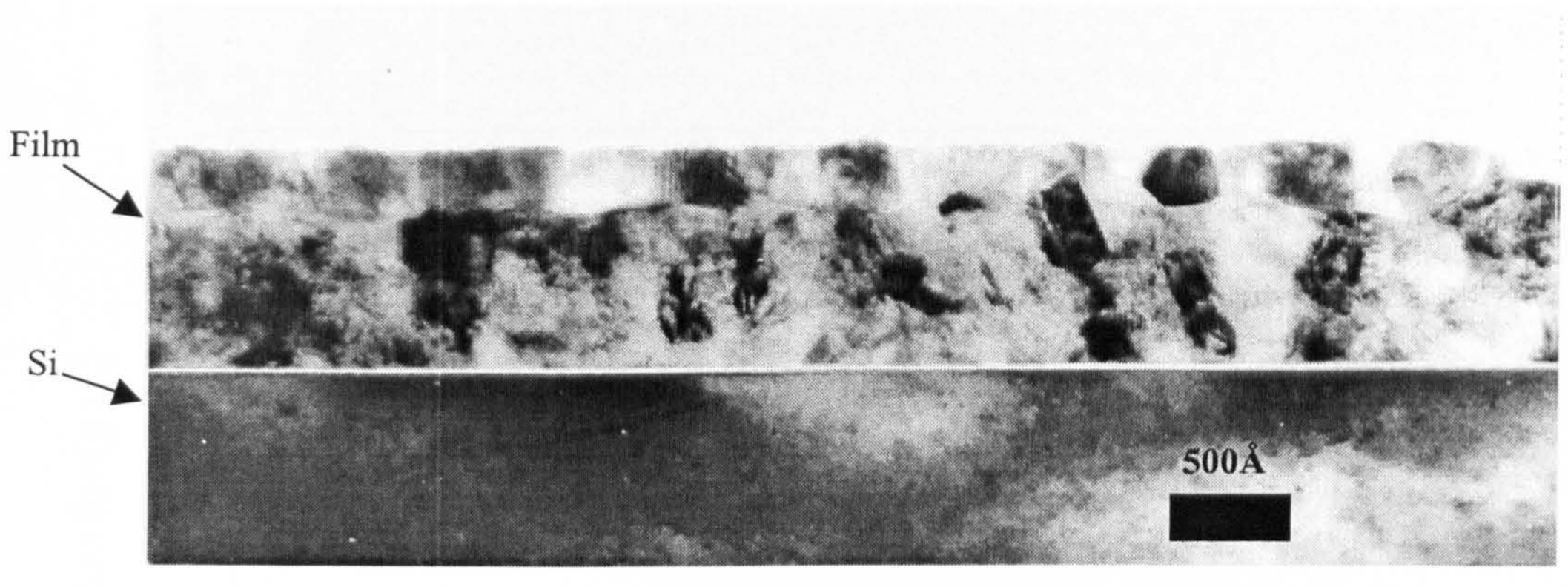

Figure 4.37) Cross-sectional TEM image of v82(42Å Fe/30 seconds N).

The image shows a grain structure normal to the film that is not continuous. There are stacks of grains on top of one another. Why such a situation exists is still not clear but points to stress in the film and the cause of the perpendicular magnetic anisotropy.

Several models have been proposed for explaining the loop shape as previously discussed in section 2.3.2. There is a simpler alternative that reproduces the required loop but is an over simplification of the situation. If one considers a Stoner-Wohlfarth calculation of a hysteresis loop for a single domain film with easy axis in the film plane and applies a magnetic field initially along the same direction, the loop in figure 4.38 is produced. The analytical calculations have been left to the appendix.

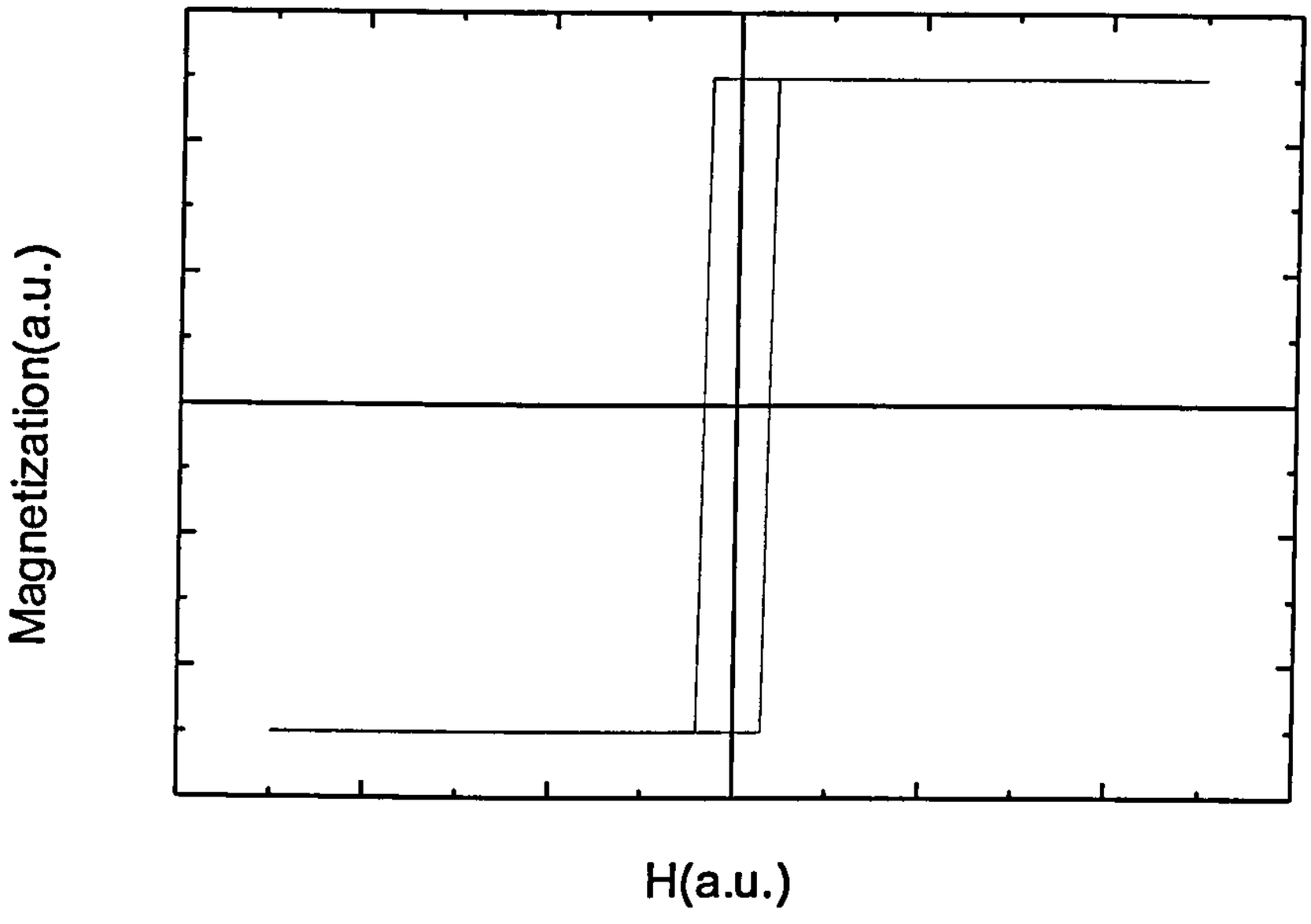

Figure 4.38) Schematic of a calculated Stoner-Wohlfarth loop for in-plane easy axis and applied field along the same direction.

A single film with easy axis perpendicular to the film plane and applied field along the in-plane direction gives a calculated loop as shown in figure 4.39.

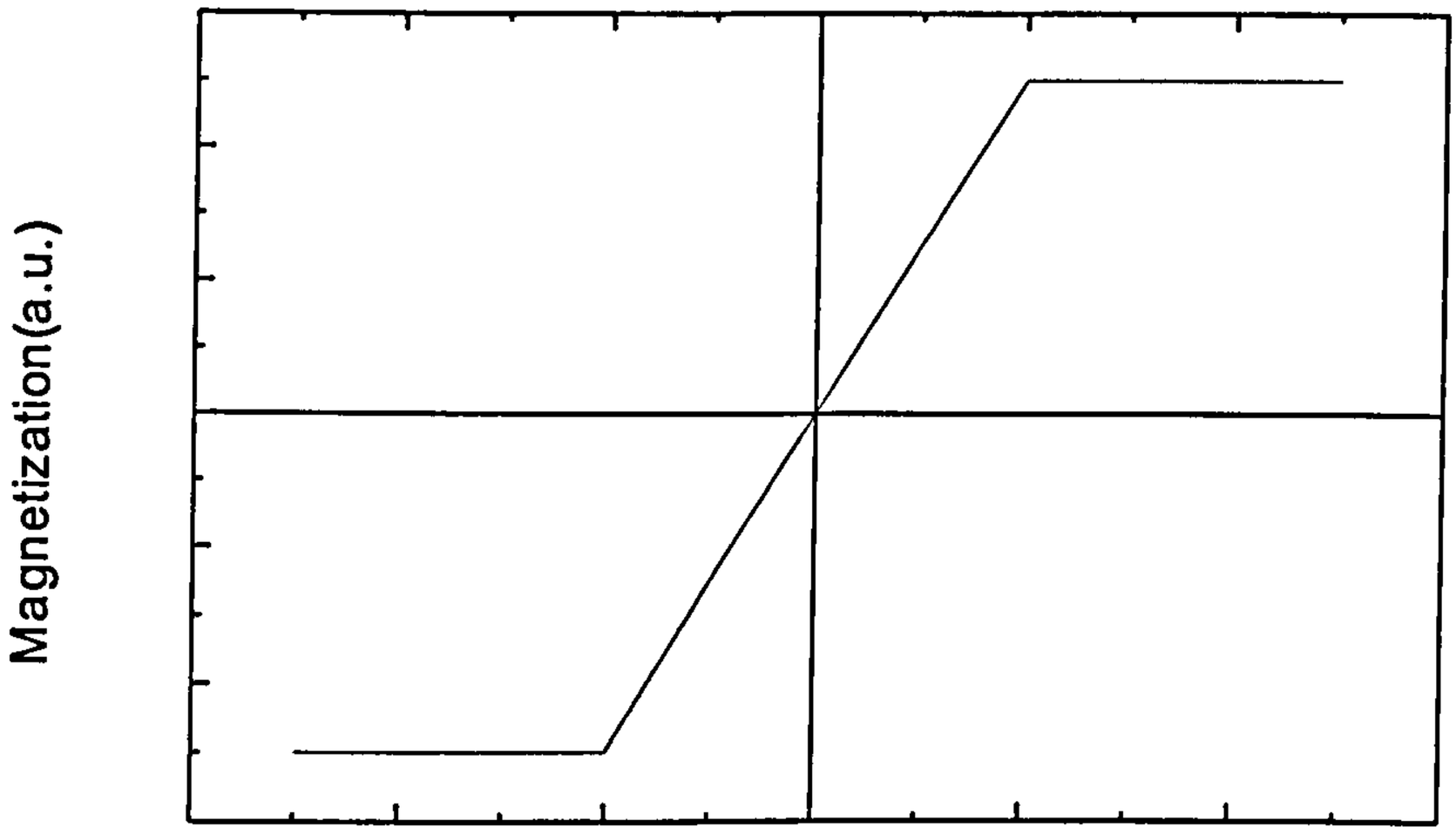

Figure 4.39) Schematic of a calculated Stoner –Wohlfarth loop for normal easy axis with field in the film plane.

Now for a bilayer consisting of two non-interacting, Stoner-Wohlfarth type films the loop will be the superposition of the loops shown in figure 4.38 and 4.39. The result is shown below in figure 4.40.

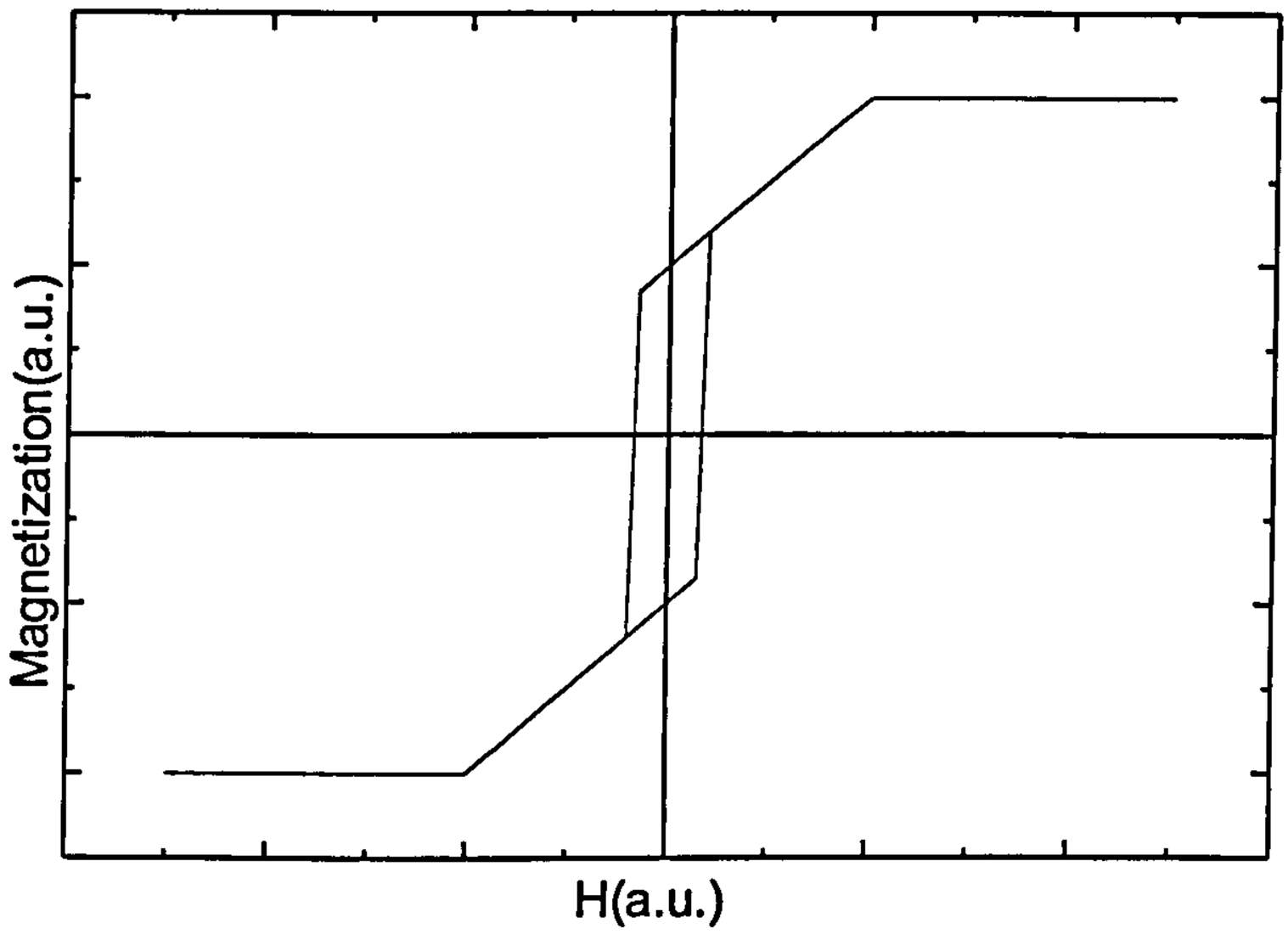

Figure 4.40) schematic of hysteresis loop for a bilayer system for which the easy axes are in the film plane and normal to the plane with the applied field in the plane of the film obtained by adding the two individual loops together..

Although the Stoner-Wohlfarth calculation neglects any possible exchange interaction in the samples considered in this thesis it has reproduced the loop shape quite nicely. A further extension and refinement of this calculation should prove fruitful.

Chapter 5 Results-FeTi/FeTiN

This chapter considers data concerning multilayer samples with an effective bilayer of an FeTi alloy exposed to an atomic nitrogen beam for specified thickness and time respectively. The aim here was to investigate the affect of the addition of Ti on the magnetic and structural properties of FeN. Previous studies have utilized Ti chips on an Fe target[50], while here an alloy target of 80 at% Fe and 20 at% Ti was used. It was subsequently determined by elemental analysis from energy dispersive x-ray micro-analysis measurements that the FeTi alloy deposited contained only 15 at% Ti and balance Fe.

5.1 XRR

XRR was used to investigate the layered structure of the samples. Figure 5.1 shows the reflectivity scan of an FeTi layer deposited without nitrogen exposure.

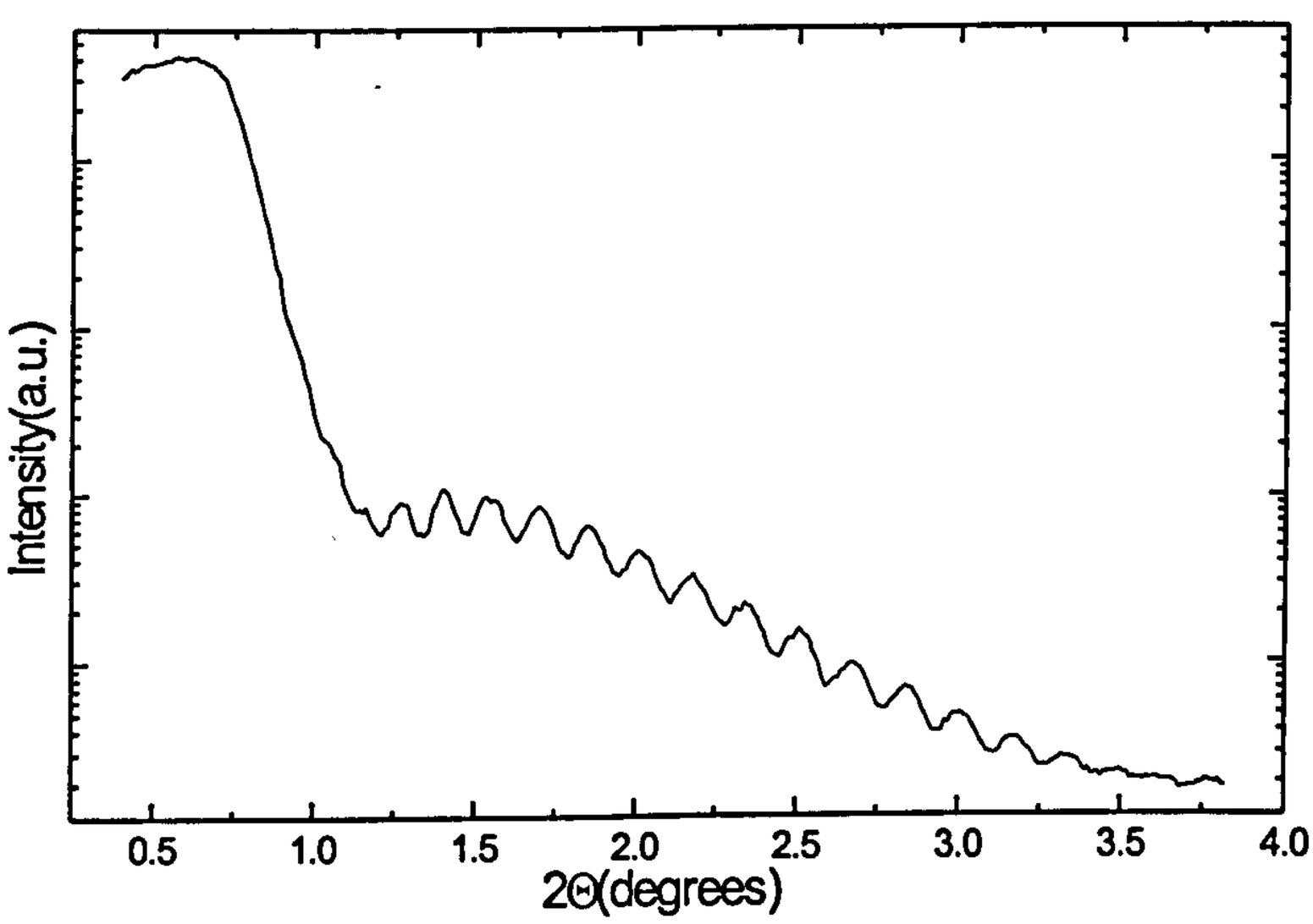

Figure 5.1) XRR of vI1 (FeTi alloy film).

As expected the sample consisted of a single layer as evidenced by the absence of multilayer peaks. A visible surface oxide layer contribution, as a result of removing the films from vacuum, to the scan was present as seen from the broad oscillation superimposed on the Kiessig fringes from about 2θ=1.0 to 2.5°.

The effect of varying the initial FeTi layer thickness while keeping the nitrogen exposure constant on the layered structures is shown in figure 5.2 for samples with effective bilayers of 8, 16, 24, 48, and 96 Å with 30 seconds nitrogen exposure.

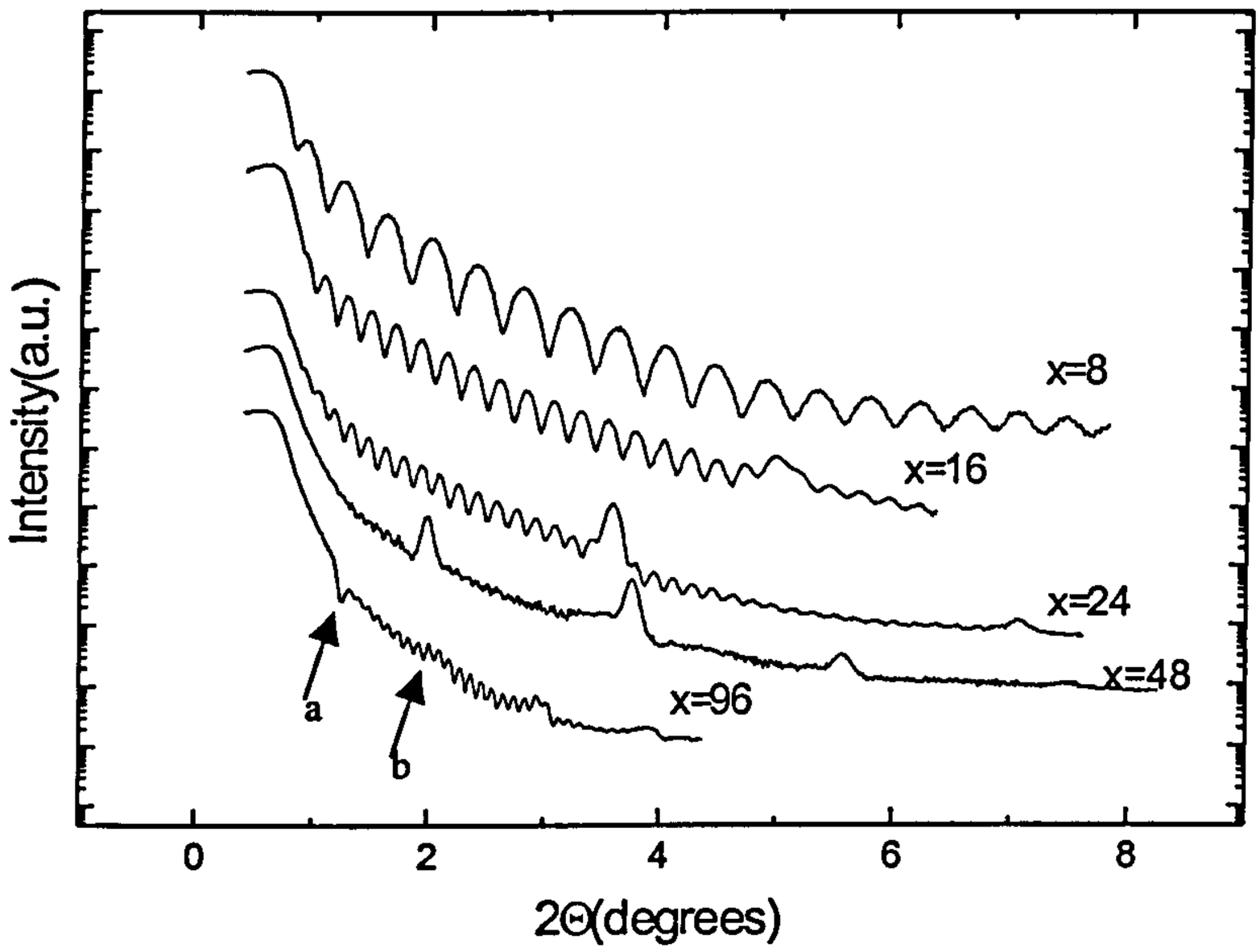

Figure 5.2) XRR for FeTi/FeTiN samples for which the FeTi thickness varied as x in the figure and the N exposure time was 30 seconds.

As in the case of the Fe/FeN samples the thinnest initial layer produced a XRR scan reminiscent of a single layer. When compared to the scan in figure 5.1 there was a distinct difference. The oxide periodicity was not evident. Here nitrogen exposure seems to have passivated the FeTi. Again there is evidence for significant expansion of the layer along the film normal as the calculated FeTi total thickness was 160 Å and the film thickness from convergence of thickness calculations from consecutive Kiessig fringes gave a thickness of 309Å. Increasing the FeTi initial layer to 16Å, the reflectivity gave the scan

shown in figure 5.2 labelled x=16. Just as in the Fe/FeN case an increase in the effective bilayer has produced a sample showing a multilayer peak. The $\sin^2$ correction to the peak gave a bilayer thickness(for 20 bilayers) of 17.8Å and a total thickness of 356Å. Increasing the effective bilayer to 24Å FeTi 30 seconds nitrogen the reflectivity shows a first order multilayer peak that was shifted to lower angle as shown in figure 5.2. The scan consisted of two multilayer peaks. Application of the $\sin^2$ correction to the second order peak gave a bilayer periodicity of 25.2Å and a total thickness of 503Å. Any expansion here was considered to be an estimate owing to uncertainty in determination of peak and critical edge positions.

Figure 5.2 shows the reflectivity for the sample with a 48Å initial FeTi layer. The scan shows four orders of multilayer peaks. The peaks are sharp and quite intense indicative of sharp and good quality interfaces. A bilayer periodicity of 47.8Å and total thickness of 956Å were obtained from a $\sin^2$ correction to the third order peak at $2\theta=5.576°$. The sample with a 96Å initial FeTi layer shows four orders of multilayer peaks in figure 5.2 such that the first and second order peaks are due to destructive interference as indicated by the intensity dip and peak suppression, indicated by points a and b, respectively. Here, as in the 48Å sample, the Kiessig fringes are weak due to attenuation of the beam. There was also no visible evidence of the presence of an oxide layer with the scan following the θ^{-4} decay of the intensity beyond the critical edge.

The effect of varying the nitrogen exposure is shown in figure 5.3a. Here it suffices to point out that with increased nitrogen exposure there was an increase in bilayer periodicity as indicated by the shift of the first order multilayer peaks to lower angle in samples for which the nitrogen exposure is less than 30 seconds. Beyond 30 seconds there was no marked shift as was the case for the Fe/FeN samples. Any further shift was not visible and any measured shift was ascribed to error in determining peak position. So, as in the Fe/FeN samples, the nitrogen seems to penetrate to a maximum depth.

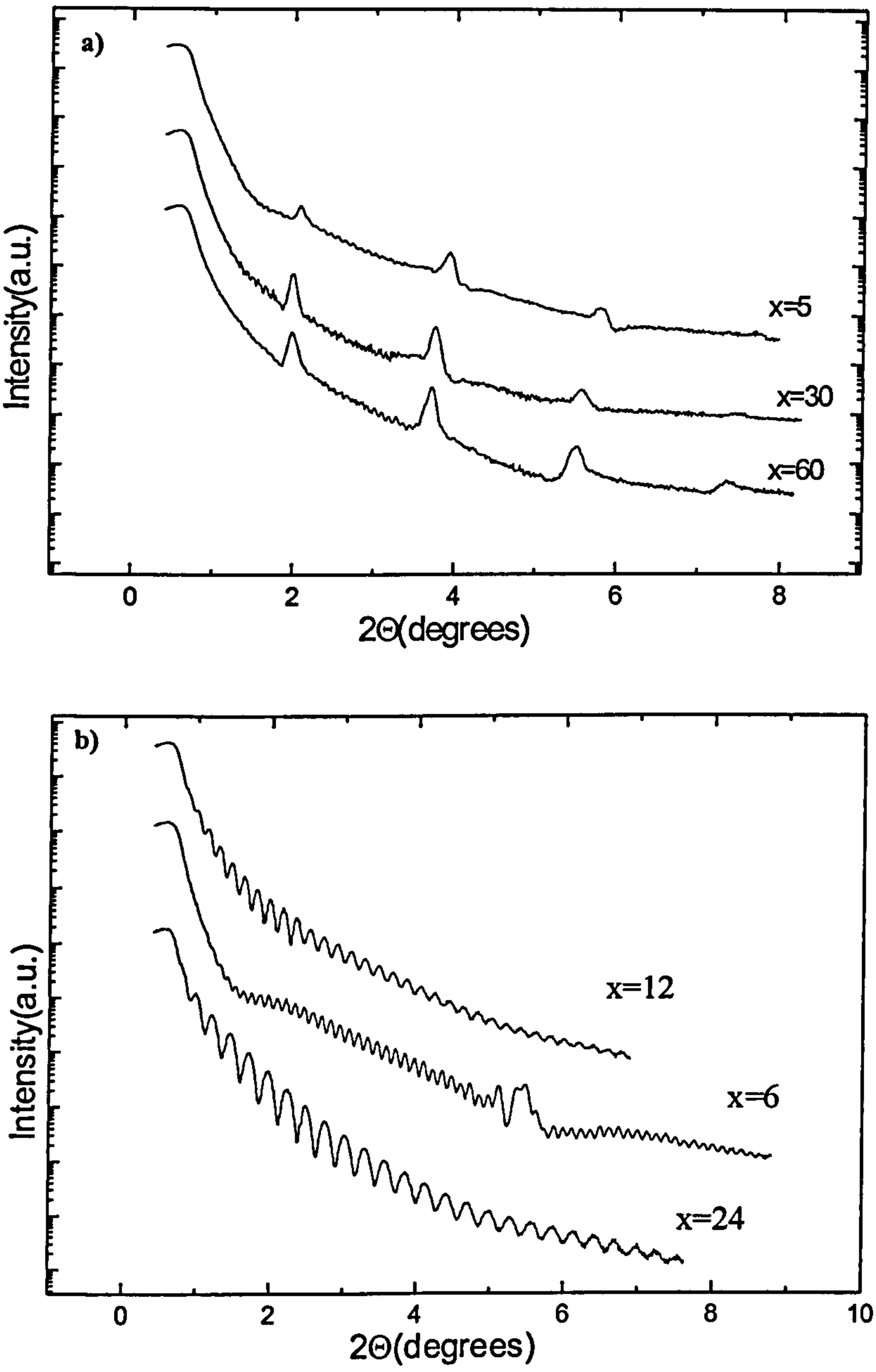

Figure 5.3) XRR scans of a) FeTi/FeTiN samples with FeTi layer thickness of 48Å and x seconds N and b) FeTiN reactively sputtered films with partial pressure ratios of x=6, 12 and 24%.

Three samples were deposited using reactive sputtering, for the same amount of time, where only the nitrogen partial pressure was varied. The reflectivity scans are shown in figure 5.3b. An analysis of the Kiessig fringes gave a thickness of 693, 455, and 308Å for partial pressure ratios x=6, 12, and 24% respectively. The thickness values decrease for increasing nitrogen partial pressure. This phenomenon was attributed to target poisoning. As the nitrogen in the chamber reacts with the target material the deposition rate of the material changes. The samples here were deposited consecutively under the same conditions, only increasing the nitrogen partial pressure, and for the same duration, hence the deposition rate must be changing due to increased nitrogen partial pressure ratio. The sample deposited with the lowest nitrogen partial pressure shown in figure 5.3b shows evidence of an oxide layer as evidenced by the hump between 2θ=1.5 and 4.5°. The features at 2θ=5.123 and 5.423° in figure 5.3c are anomalous. They look like multilayer peaks, but by the nature of the deposition the film must be a single layer. The origin of these peaks has not yet been identified.

From the data shown above the atom source deposition technique has produced multilayers with good quality interfaces with no oxide layer.

5.2 Electron Diffraction

The solubility of Ti in Fe is 3 at% at room temperature. By adding 15 at% Ti to Fe, the alloy will consist of $Fe_{97}Ti_3$ and Fe_2Ti. One would expect an increase in the lattice parameter of the material. Figure 5.4 shows the electron diffraction pattern of the FeTi alloy, reflecting the nature of the material prior to exposure to nitrogen. As can be seen by inspection the alloy was BCC. Upon measurement of the d-spacings it was determined that the alloy had a lattice parameter of 2.9Å. Elemental Fe has a lattice parameter of 2.866Å, hence the addition of 15 at% Ti produced a substitutional alloy with a 1% lattice expansion compared to elemental Fe. The pattern shows evidence of a degree of ordering compared to a random polycrystalline material indicated by the arcing of the rings. The pattern is very similar to the pattern obtained for the single Fe film.

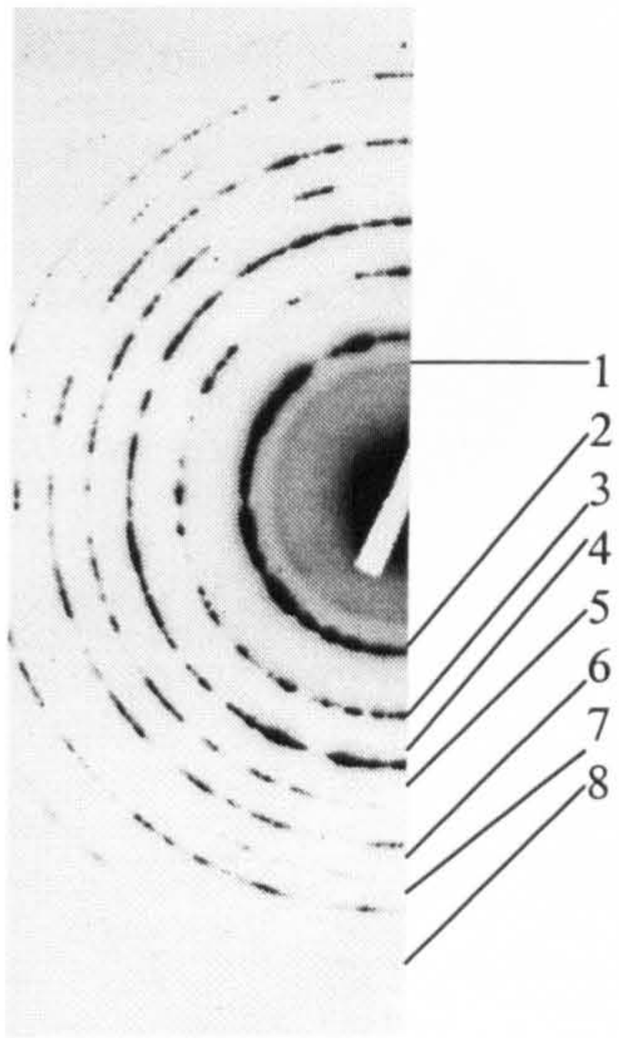

Figure 5.4) vi1(FeTi alloy without N exposure) diffraction pattern. The rings are as follows in numerical order: oxide, 110, 200, 211, 220, 310, 222, 321, 400, 330 and 420 BCC reflections

Figure 5.5a-e shows the progression of the phases of the FeTi as the initial layer exposed to nitrogen for 30 seconds was decreased from 96 to 8Å.

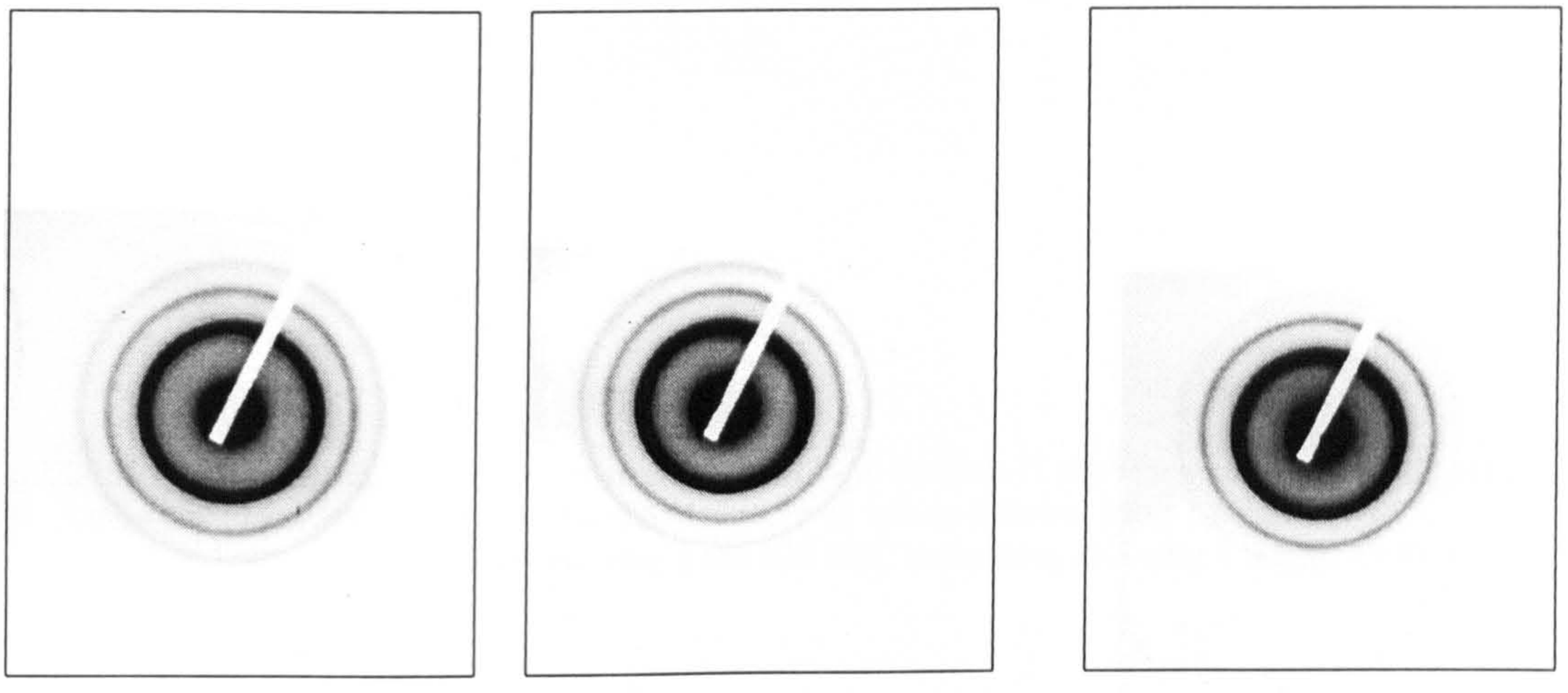

a) b) c)

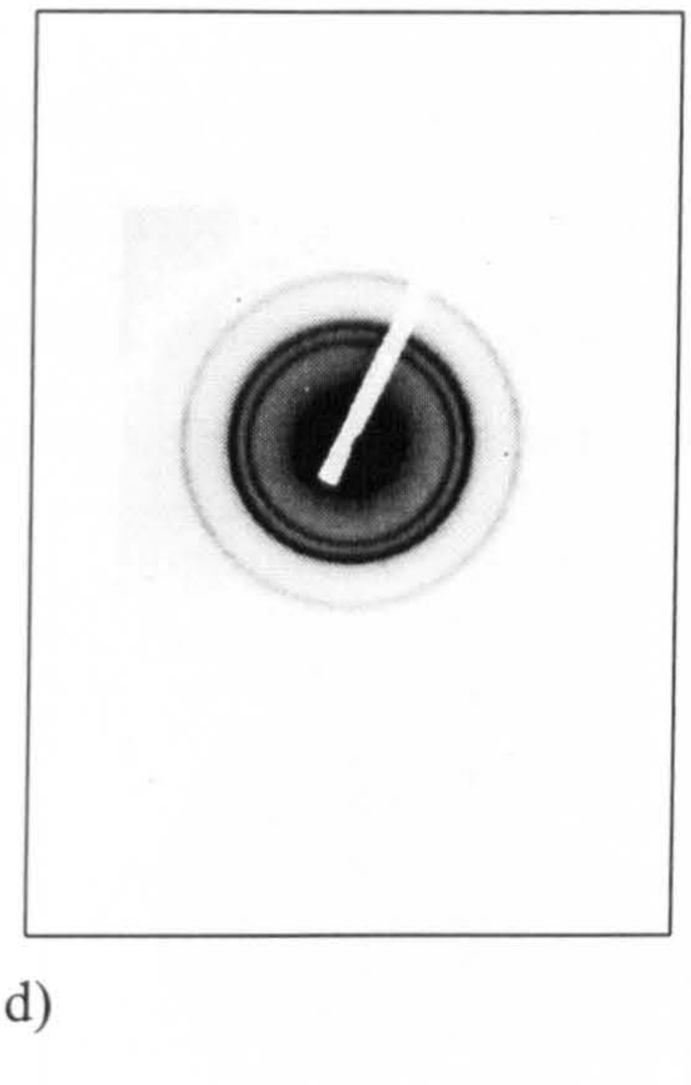

d)

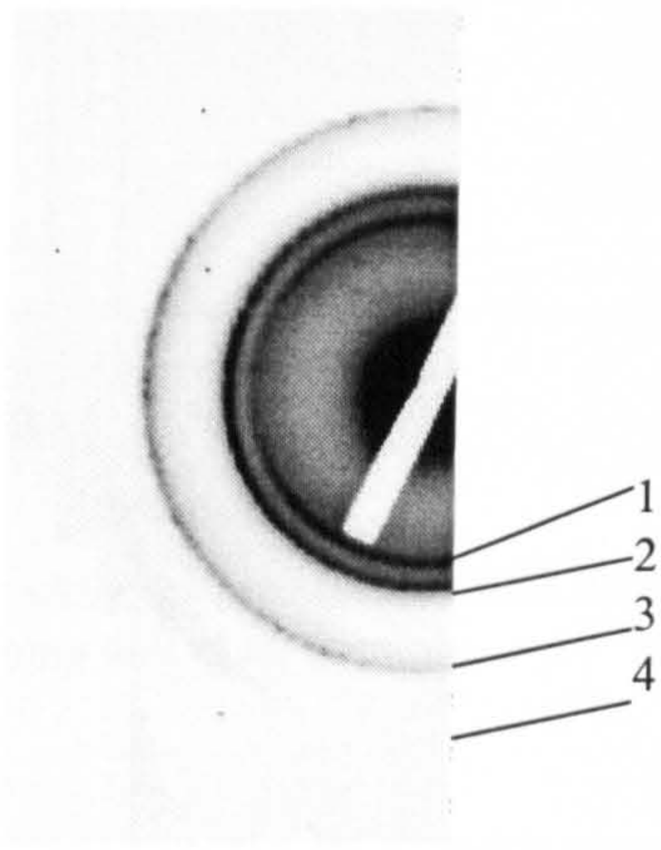

e)

Figure 5.5) Electron diffraction patterns of samples with 30 seconds N exposure and FeTi thickness of a) 96 Å, b) 48Å, c) 24Å, d) 16Å and e) 8Å. The labels in e) are as follows: Ring 1 is the 111 FCC reflection, ring 2 the 200 FCC reflection, ring 3 the 220 FCC reflection, and ring 4 is the 311 FCC reflection.

The phase changes, that were prevalent in the Fe/FeN system, are absent in the samples with Ti. Apart from the presence of an FCC pattern for the two thinnest initial FeTi thicknesses, the system is BCC, showing characteristic multilayer peaks. The sample with effective bilayer of 8Å FeTi and 30 seconds nitrogen exposure was indexed to be FCC with

a lattice parameter of 4.2Å, which was commensurate with a TiN lattice parameter of 4.24Å. As can be seen the sample with 16Å FeTi is also FCC.

For samples consisting of an effective bilayer with 48Å FeTi and nitrogen exposure times of 5, 30 and 60 seconds the same effect was seen as shown in figure 5.6.

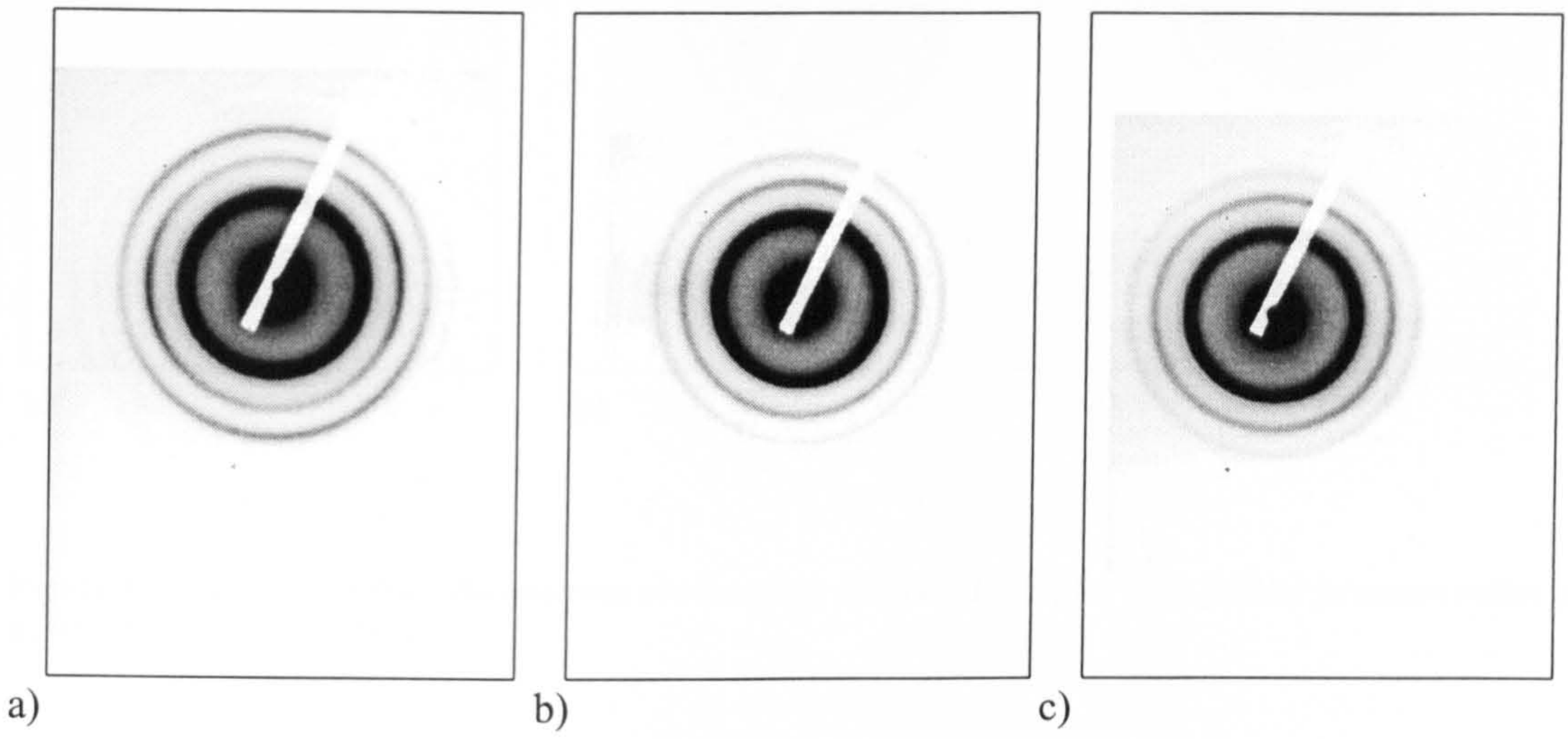

Figure 5.6) Electron diffraction patterns for samples with 48Å FeTi layer thickness and N exposure times of a) 5 seconds, b) 30 seconds and c) 60 seconds.

The diffraction patterns are consistently BCC with some arcing in figure 5.6a, expected to be residual from the initial deposited layer. The FeTi layer thicknesses are not significantly different from the Fe/FeN sample set. The Ti here seems to be frustrating the phase change so that obvious non-BCC phases are not formed.

When the reactive sputtered samples were considered the same basic trend was present. Figure 5.7a-c shows the diffraction patterns of single layer FeTiN samples deposited in N_2:Ar partial pressure ratios of 6, 12 and 26%.

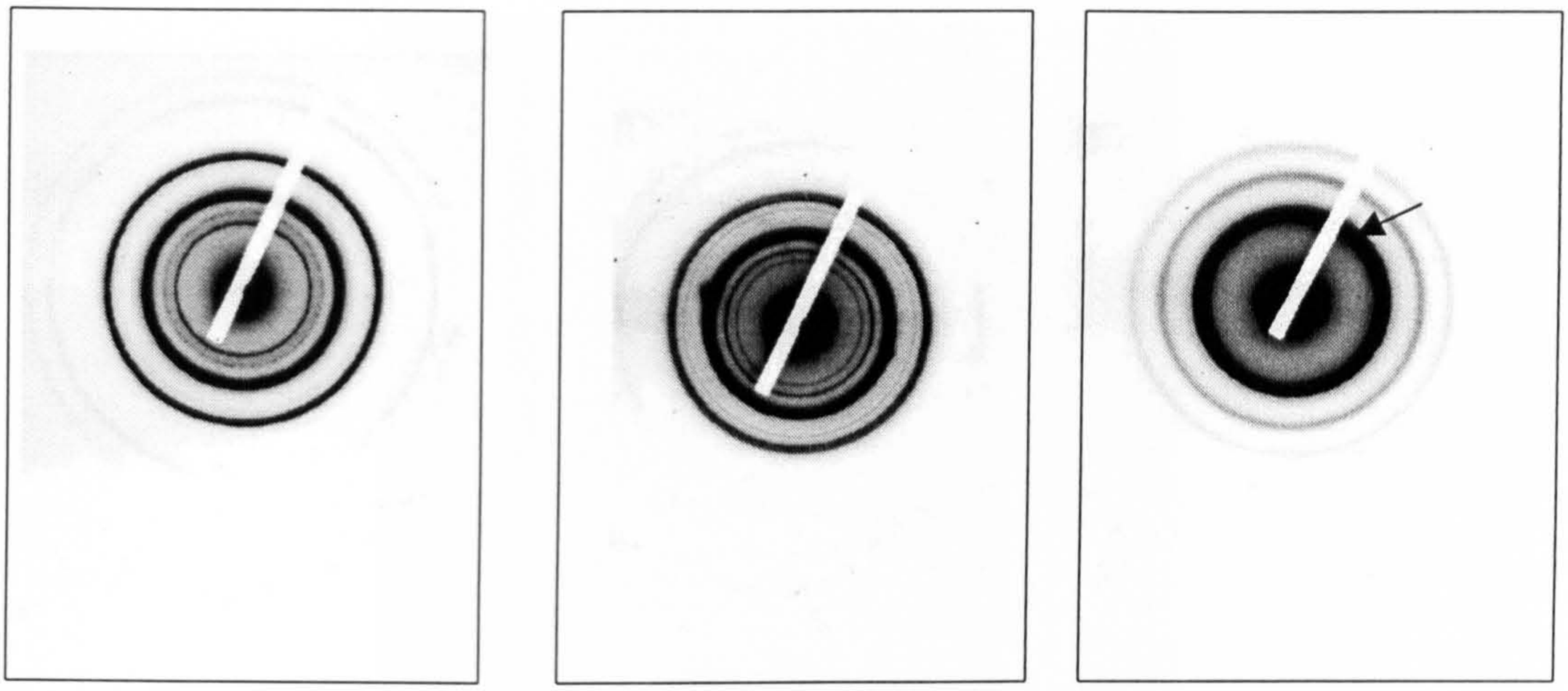

a) b) c)

Figure 5.7) Electron diffraction patterns of reactively sputtered samples with partial pressure ratios of a) 6%, b) 12% and c) 26%.

As can be seen the lowest nitrogen percentage produced a sample with a BCC structure, with a weak FCC component. The other two patterns in figure5.7 are both FCC with a weak BCC component in figure 5.7b. Hidden in the brightest ring (marked by an arrow) in figure 5.7c is a second ring that identifies the pattern more definitively as FCC. Consistent with the FeN reactively sputtered samples the material is multi-phase.

5.3 Bright Field TEM Images

This section considers the grain structure of the samples. Figure 5.8 shows the x100k magnification bright field image of the FeTi alloy not subjected to nitrogen exposure.

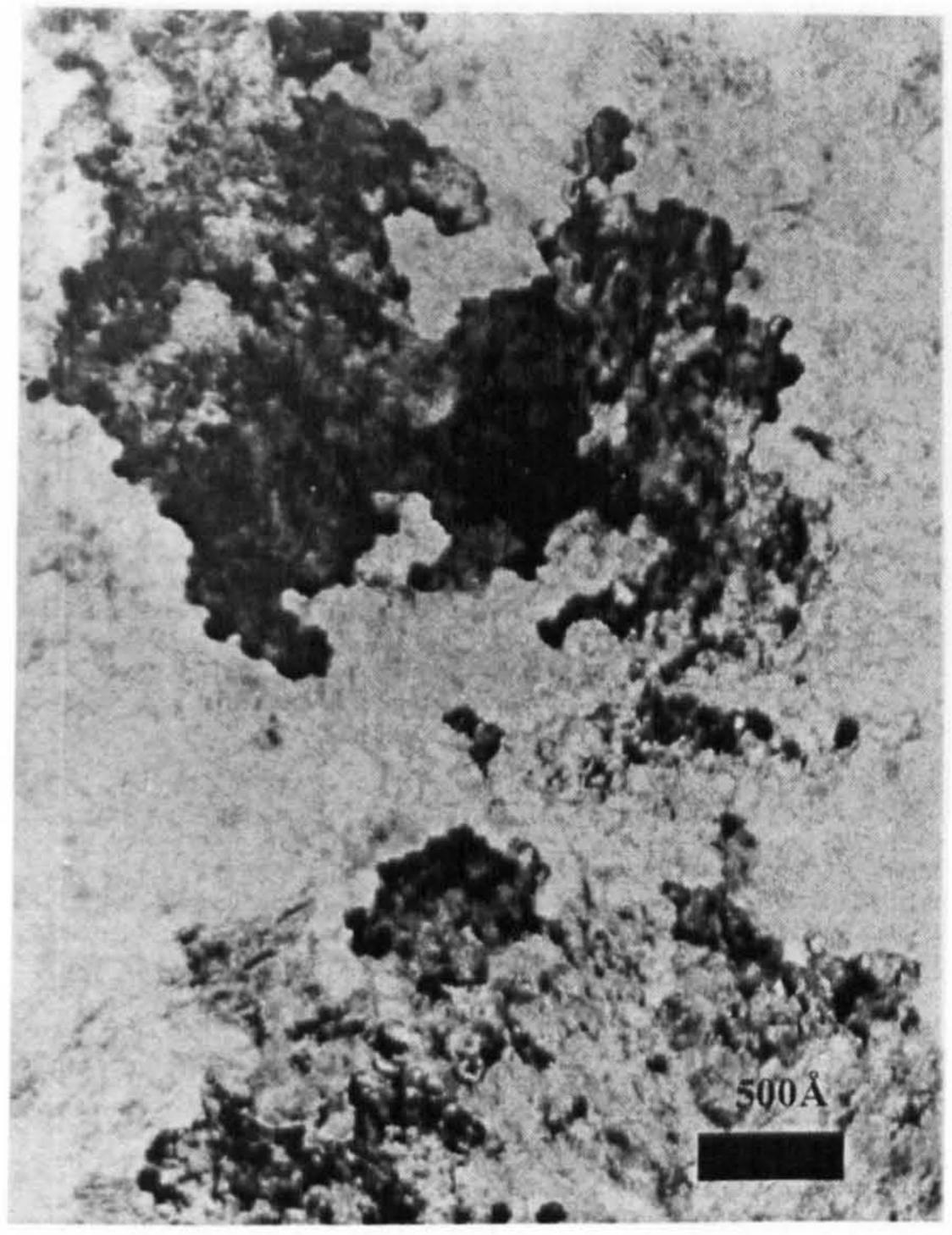

Figure 5.8) Bright field image of FeTi alloy without N exposure.

The image consisted of clusters of small crystallites, about 100Å in diameter, that were slightly oriented as seen from the larger regions of dark contrast. This analysis was consistent with the presence of arcing in the DP. Hence the material that was exposed to nitrogen started as a fine grained, slightly textured material. Upon nitrogen exposure the BF images in figure 5.9 were obtained for effective bilayers with diminishing FeTi initial thickness and constant nitrogen exposure time of 30 seconds.

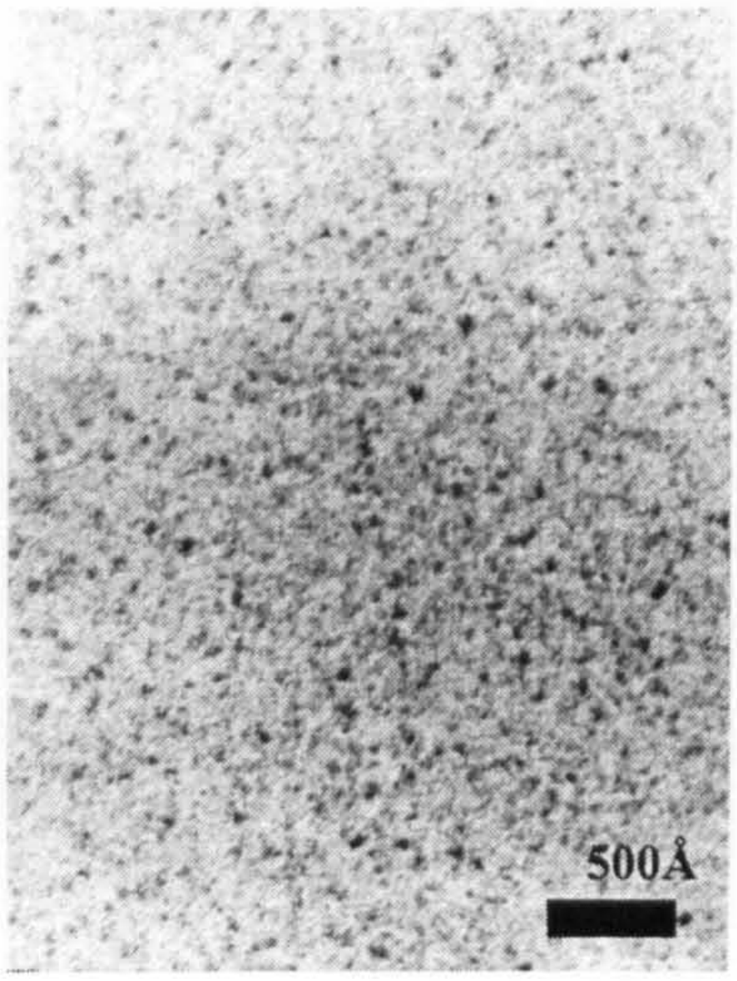

a)

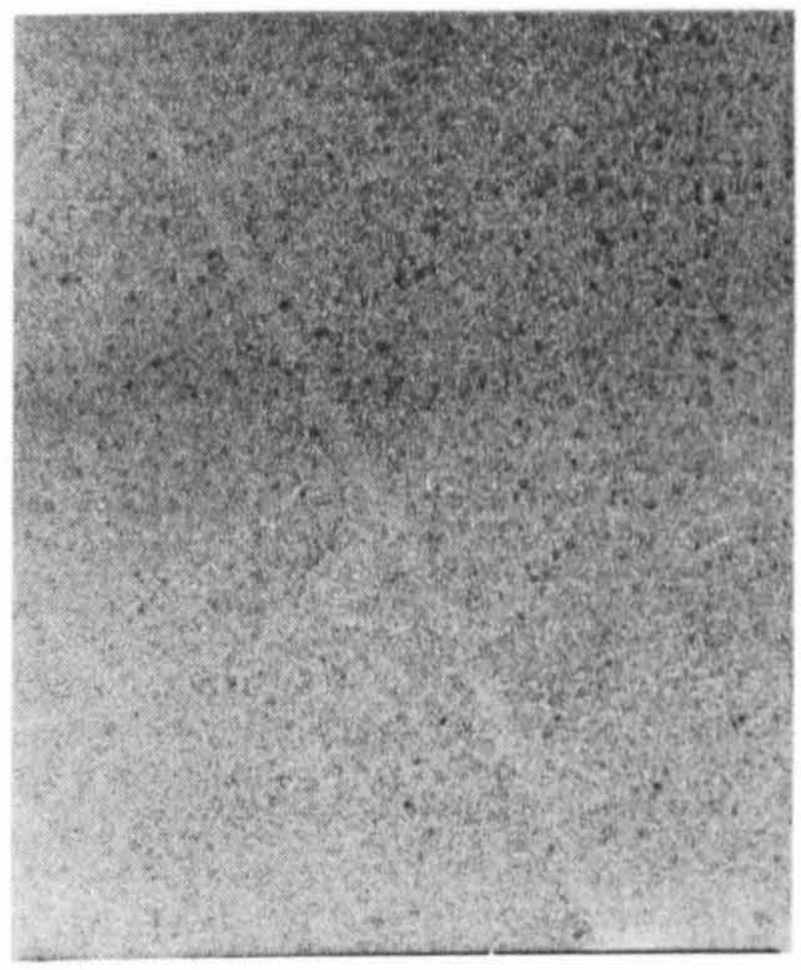

b)

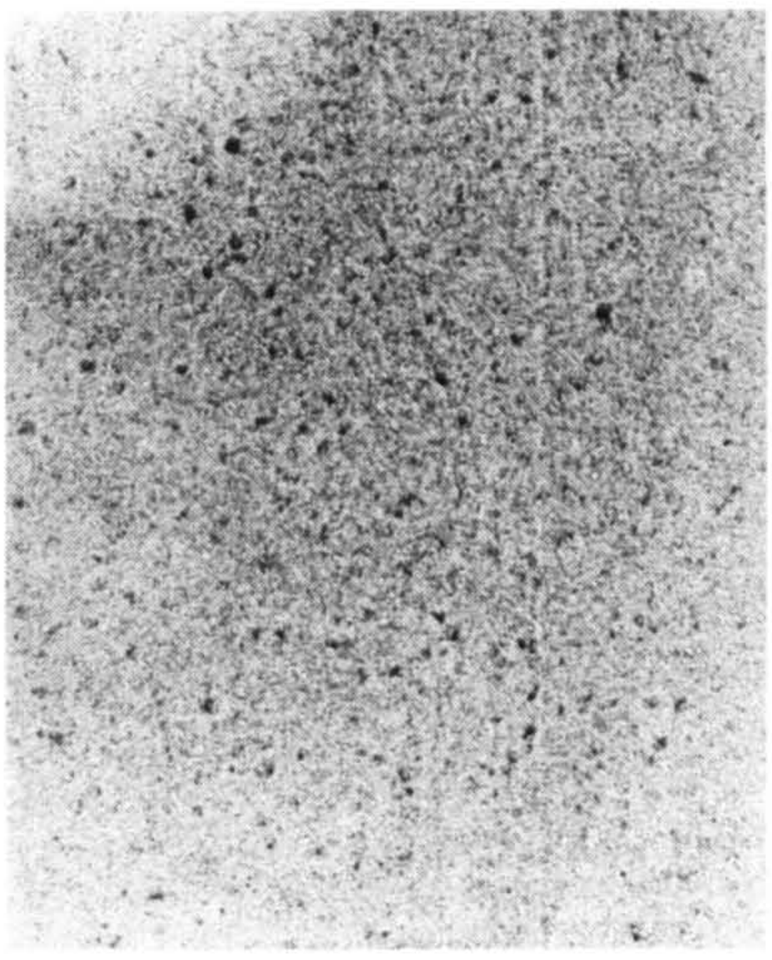

c)

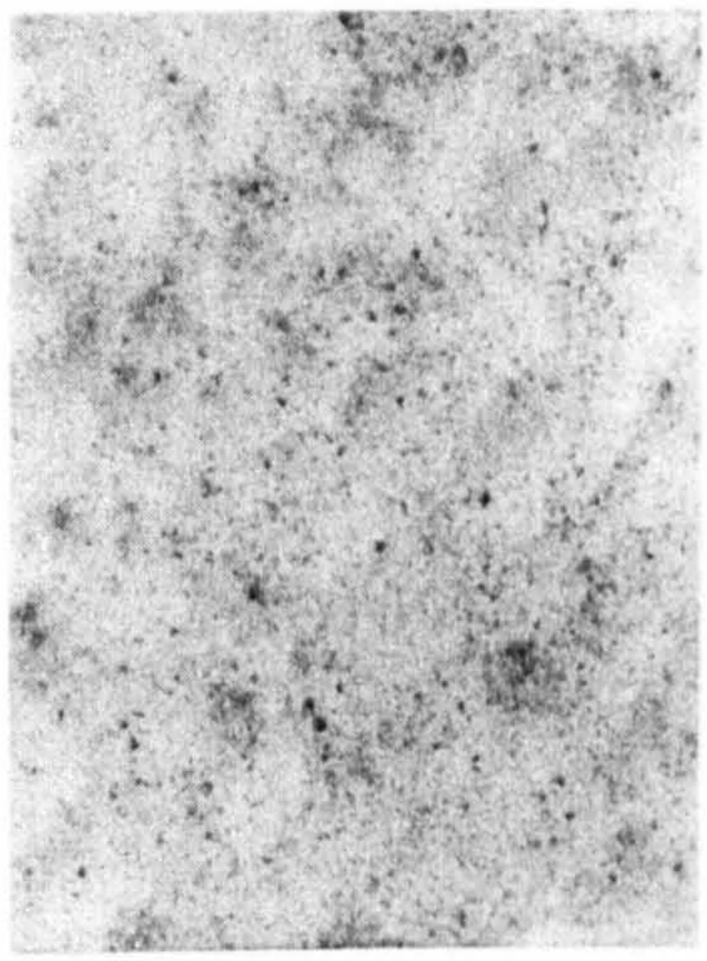

d)

Figure 5.9a-d)

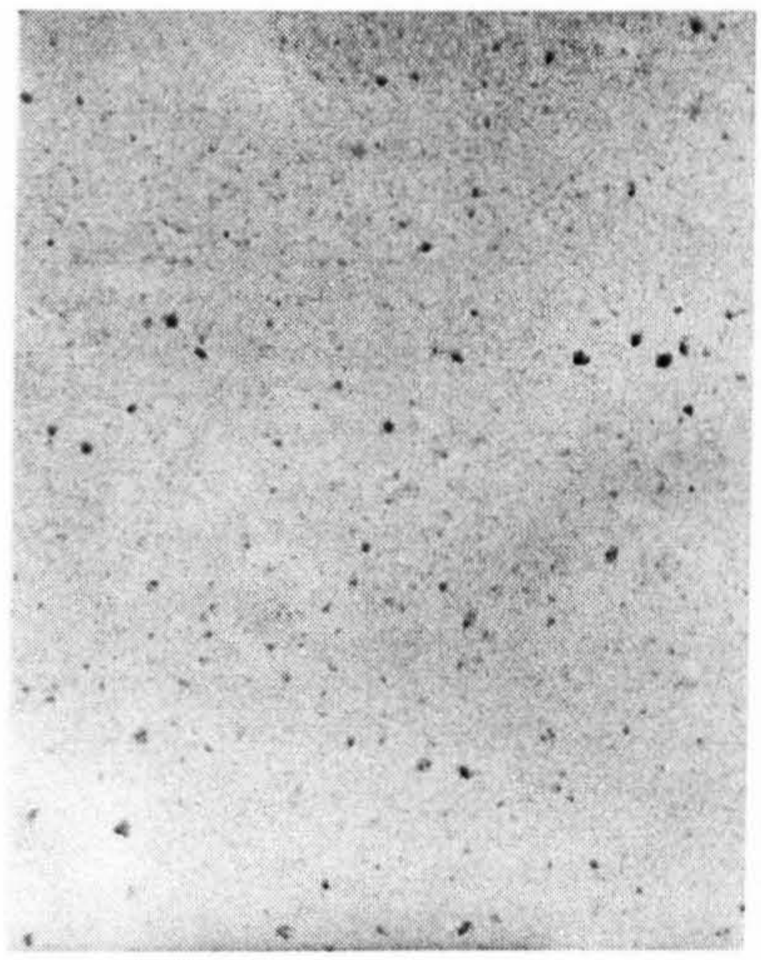

e)

Figure 5.9) Bright field images of FeTi/FeTiN samples with N exposure times of 30 seconds and FeTi layer thickness of a) 96Å, b) 48Å, c) 24Å, d) 16Å and e) 8Å. The scale in a) represents 500 Å and applies to each of the images in the figure.

The images are very fine grained as in the unexposed sample. There was little variation in grain size with reducing the initial FeTi layer thickness on nitriding, but there was no degree of ordering as was present in the pre-exposed FeTi layer. This phenomenon is in stark contrast to the grain growth of the Fe/FeN sample set.

When the nitrogen exposure was varied in the effective bilayer the BF images obtained are as shown in figure 5.10.

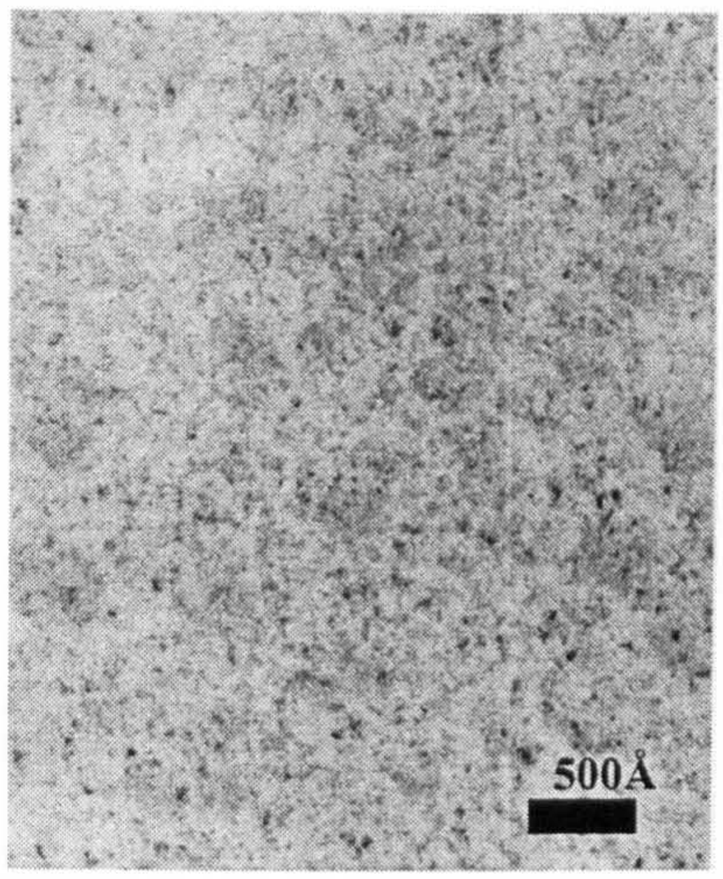

a)

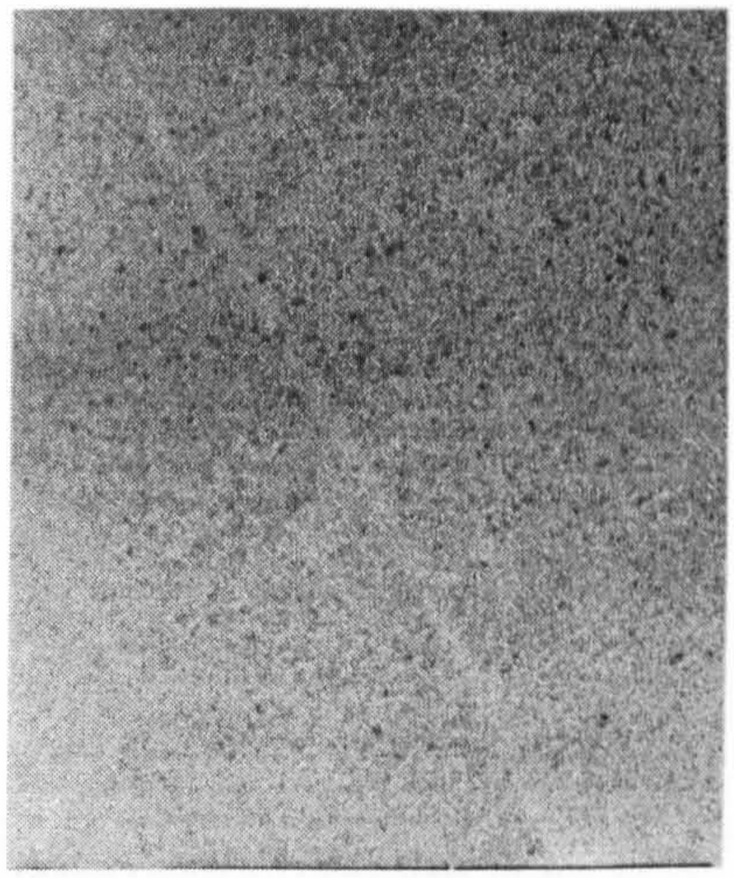

b)

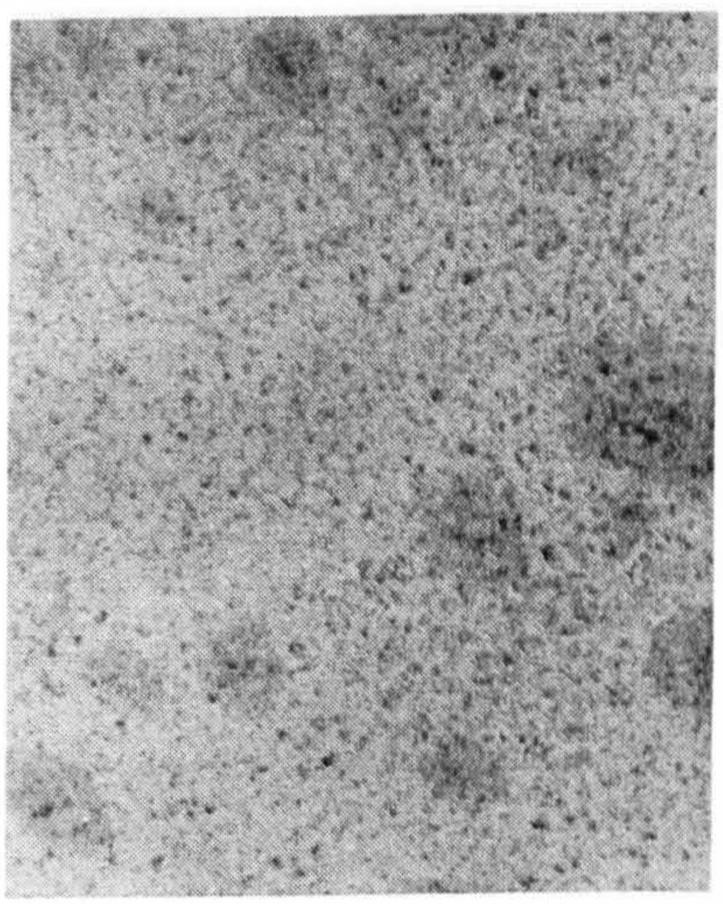

c)

Figure 5.10) Bright field images of samples with 48Å FeTi layers and N exposure times of a) 5 seconds, b) 30 seconds and c) 60 seconds.

As for the variation of the thickness of the FeTi initial layer the grain structure of the material did not visibly vary much as the nitrogen exposure time was varied.

Figure 5.11a-c shows the BF images for the reactive sputtered samples for comparison.

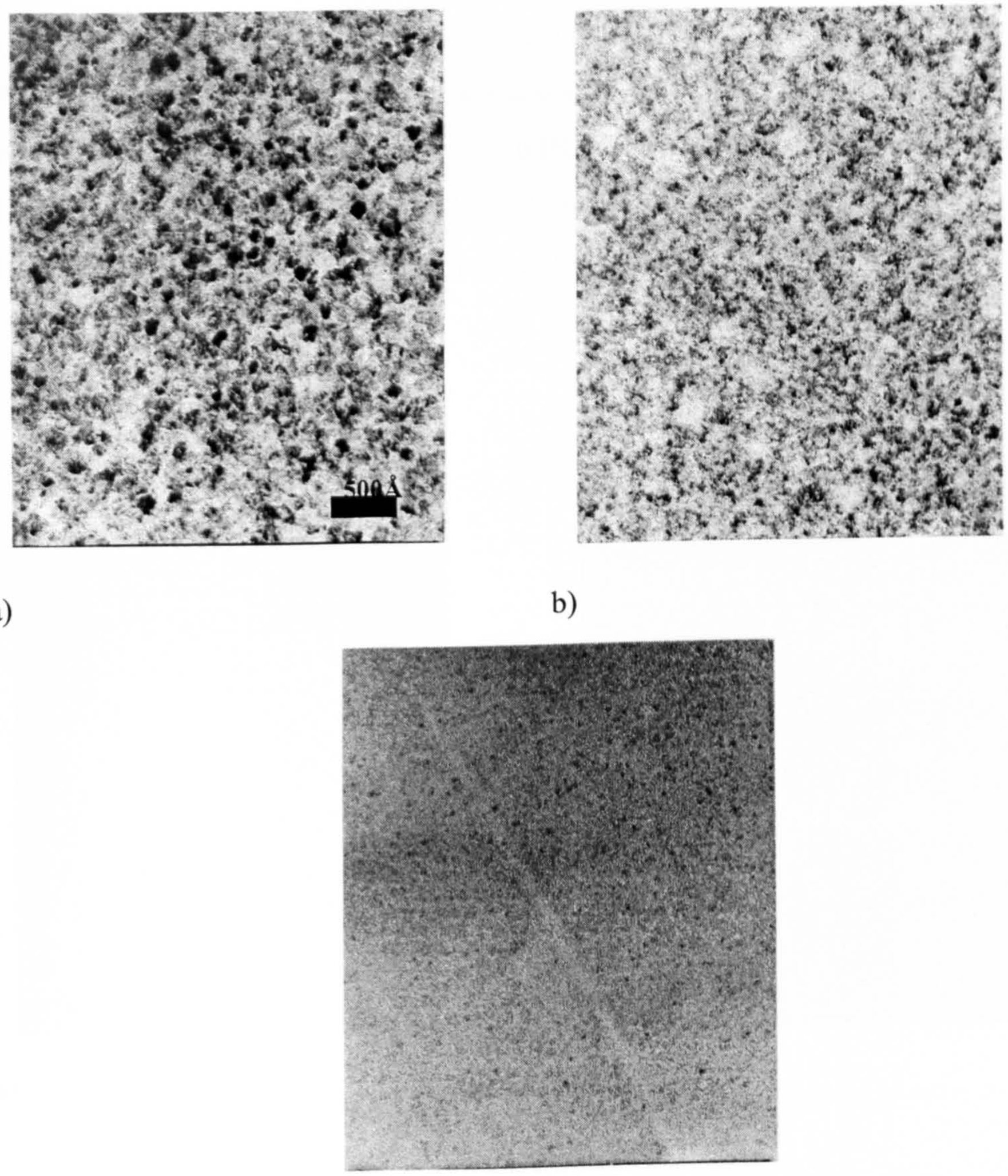

a) b)

c)

Figure 5.11) Bright field images of FeTiN reactively sputtered samples with partial pressure ratios of a) 6%, b) 12% and c) 26%.

When compared with the FeN reactively sputtered samples there was significantly less grain growth in the FeTi/FeTiN samples consistent with the atom source nitriding. From this it seems that the Ti has restricted grain growth on nitriding, producing a nanocrystalline structure just as when Ti is added to Cr[100].

5.3.1 Dark Field TEM images

As the diffraction patterns have shown the samples were either BCC or FCC. The FCC ring pattern contains rings that are also in the BCC ring pattern. The question arose whether the FCC samples also contained a BCC phase. This was examined using dark field images. Figure 5.12 shows dark field images from the inner, figure 5.13a, and outer, figure 5.12b, rings of the diffraction pattern in figure 5.5e.

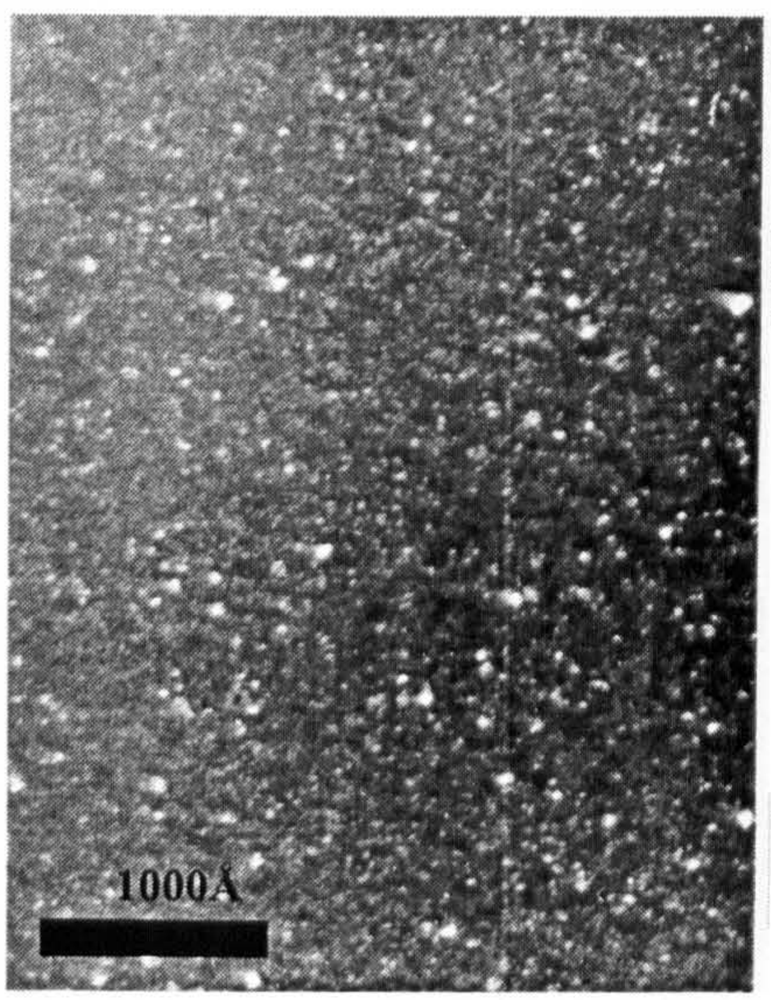

a)

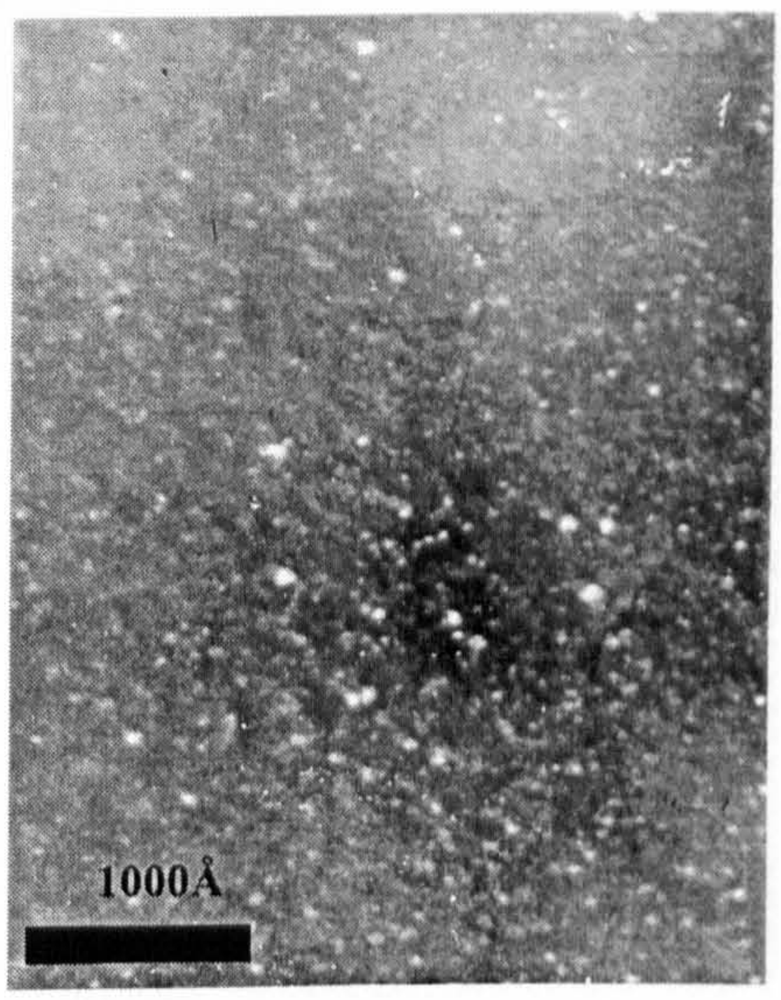

b)

Figure 5.12a and b)

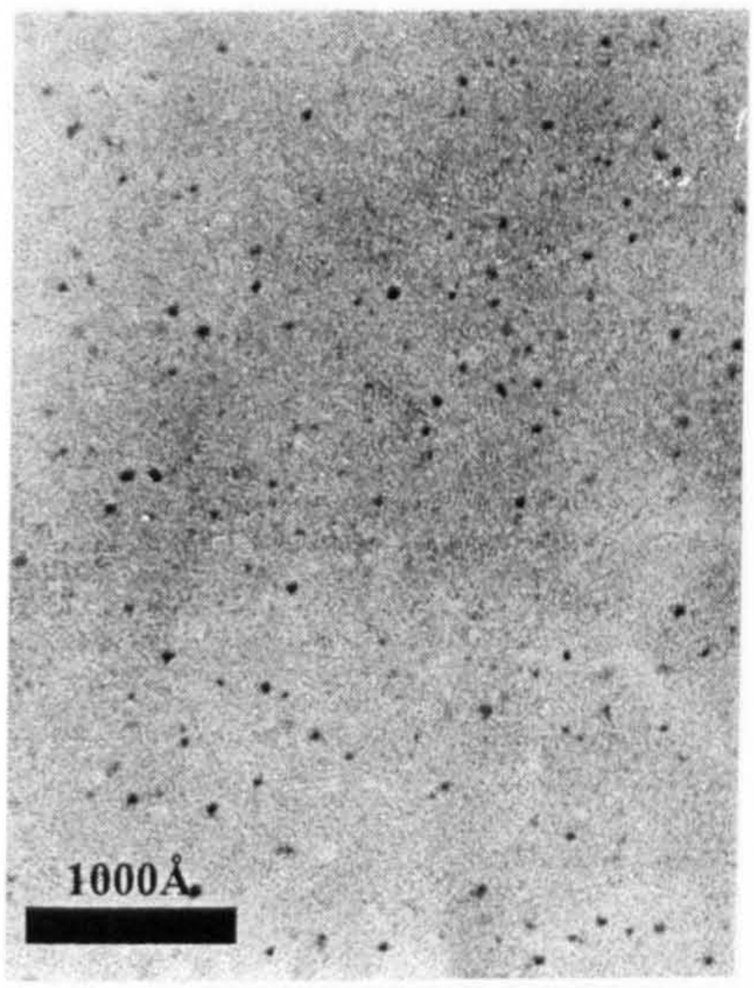

c)

Figure 5.12) Dark field image of a) inner and b) outer rings of vi4(8Å FeTi/ 30 seconds N) and c) the bright field image of the same area as in a) and b).

These images showed no difference in grain size; so the sample is either a single phase or the two considered phases have the same grain size. The evidence is inconclusive whether one or two phases is present. The bright field image in 5.12c is shown for consistency.

5.4 Hysteresis Loops

The loops shown here were measured in the in-plane configuration with data points taken every 5 to 10 Oe. It was determined that saturation magnetization values were quotable to within ±5% just as for the Fe/FeN hysteresis loops. As expected the addition of 15 at% Ti reduced the M_s of the starting material as compared to elemental Fe as shown in figure 5.13 below.

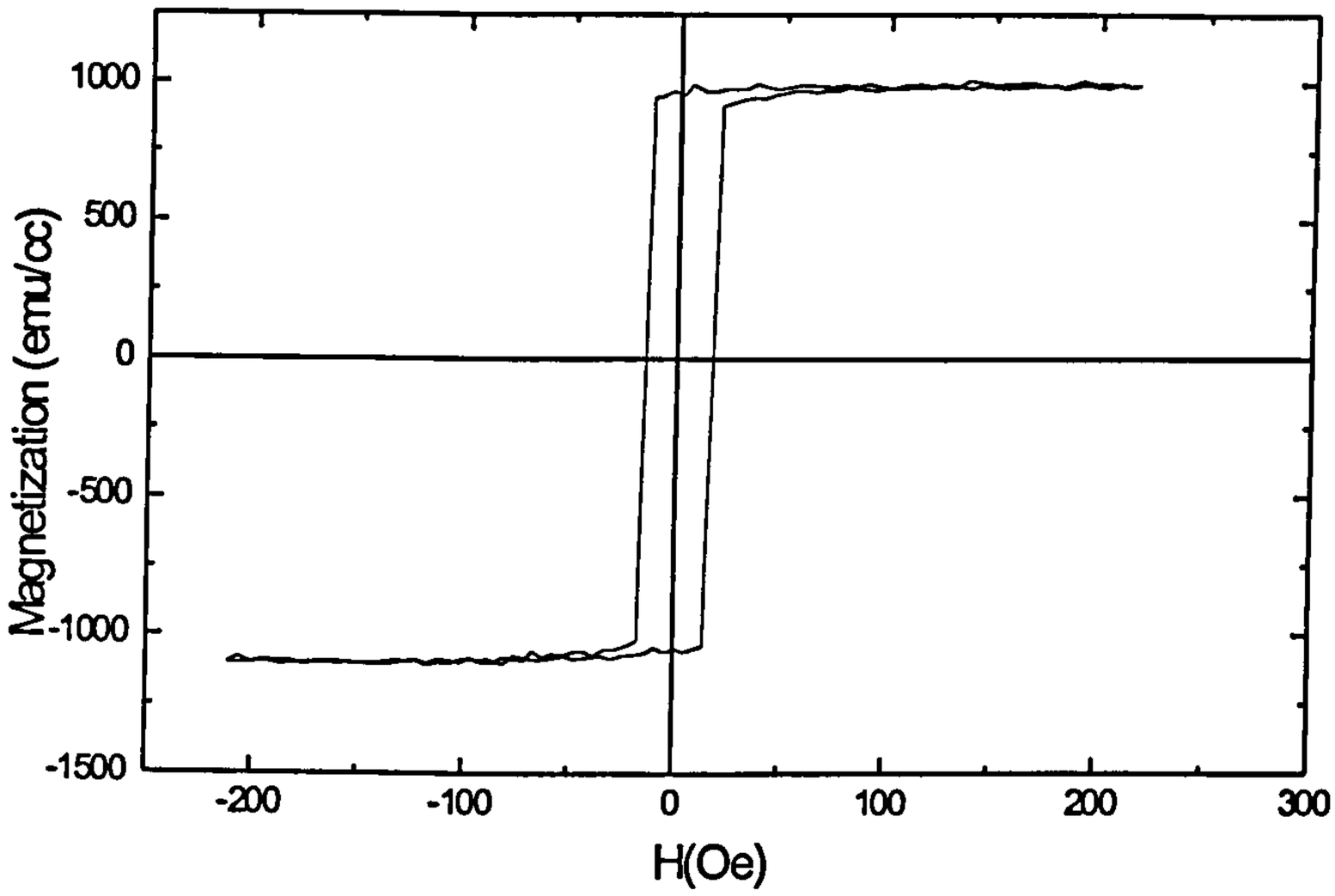

Figure 5.13) VSM hysteresis loop of the FeTi alloy film that was not exposed to the N beam.

The M_s for the alloy determined from the loop was 1046 emu/cm^3 while the coercivity was 16 Oe. The loop was very square characteristic of in-plane uniaxial magnetization. The effect of utilizing an effective bilayer of 96Å FeTi and 30 seconds nitrogen exposure on the magnetic response of the material is shown in figure 5.14.

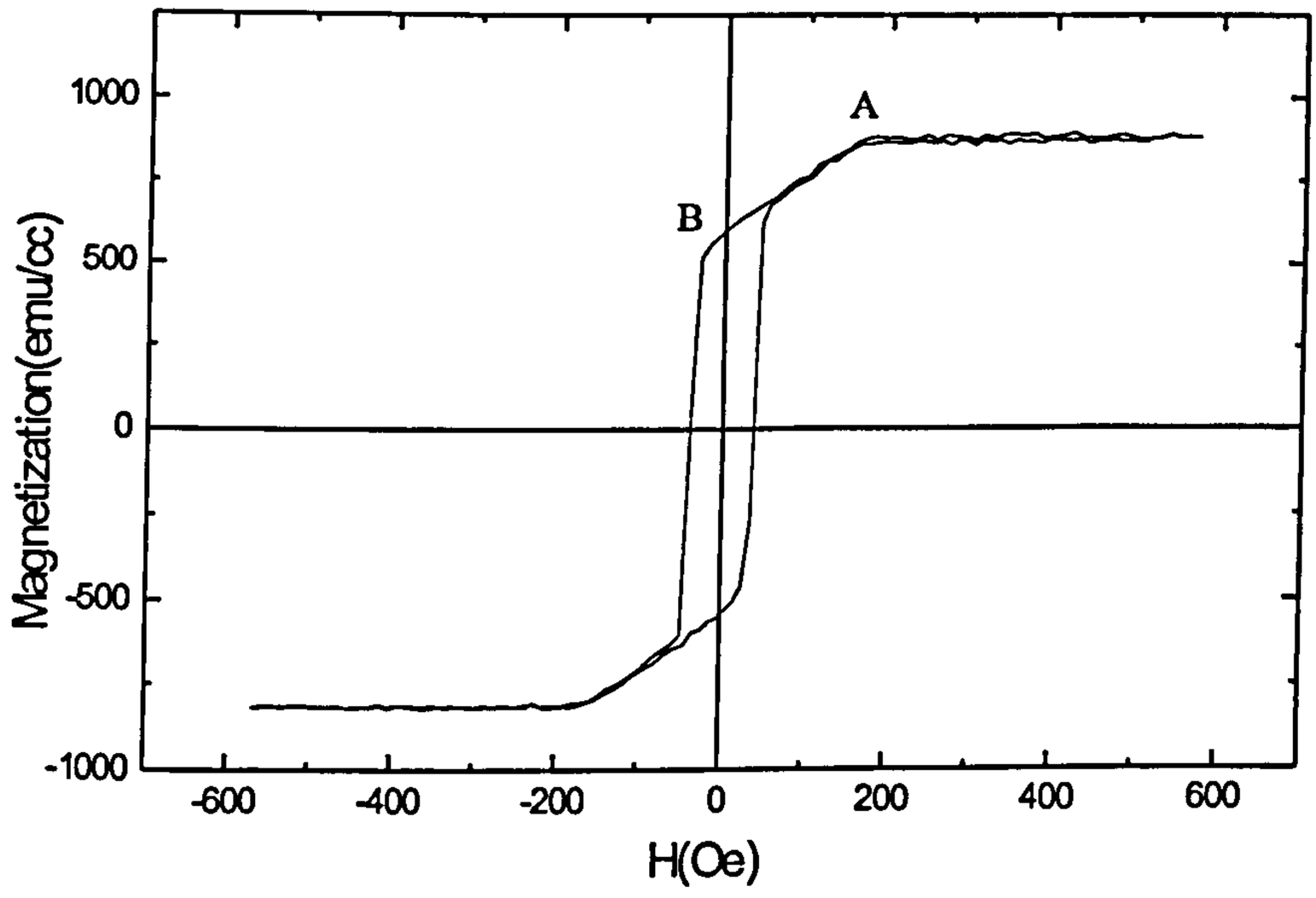

Figure 5.14) VSM hysteresis loop of vi6(96Å FeTi/30 seconds N).

The saturation magnetization was reduced by about 20% to about 848±5% emu/cm^3. The H_c has doubled to 38 Oe when compared to the unexposed alloy. The loop was fundamentally different. There seem to be two magnetization reversal mechanisms present. In the region between saturation, A, where the saturation field was about 176 Oe and the coercive field, B, there is a loop shape consistent with rotation of magnetization while the loop was very square at the coercive field. Hence the magnetization rotates until it reaches a field for which domain wall motion occurred. As initially discussed in chapter 4 the loop in figure 5.14 is characteristic of a material with stripe domains. Reducing the initial FeTi thickness to 48Å gave the hysteresis loop in figure 5.15.

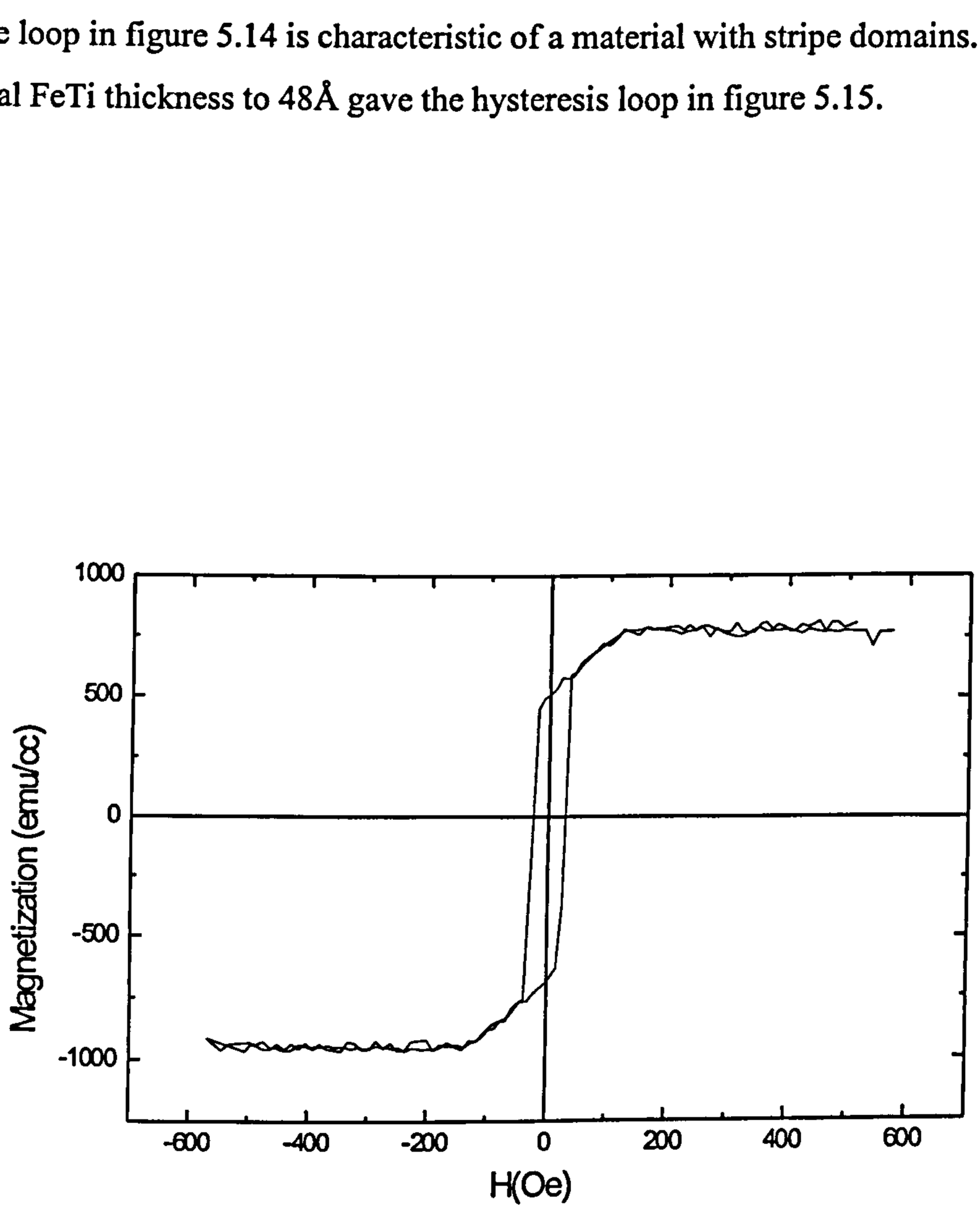

Figure 5.15) VSM hysteresis loop of vi3(48Å FeTi/30 seconds N).

Again the loop is characteristic of stripe domains. The M_s measured from the loop was 862±5% emu/cm^3. Here the saturation field (H_s) was about 130 Oe and the H_c was measured as 27 Oe.

Further reduction of the initial FeTi layer brought about a very different loop as shown in figure 5.16.

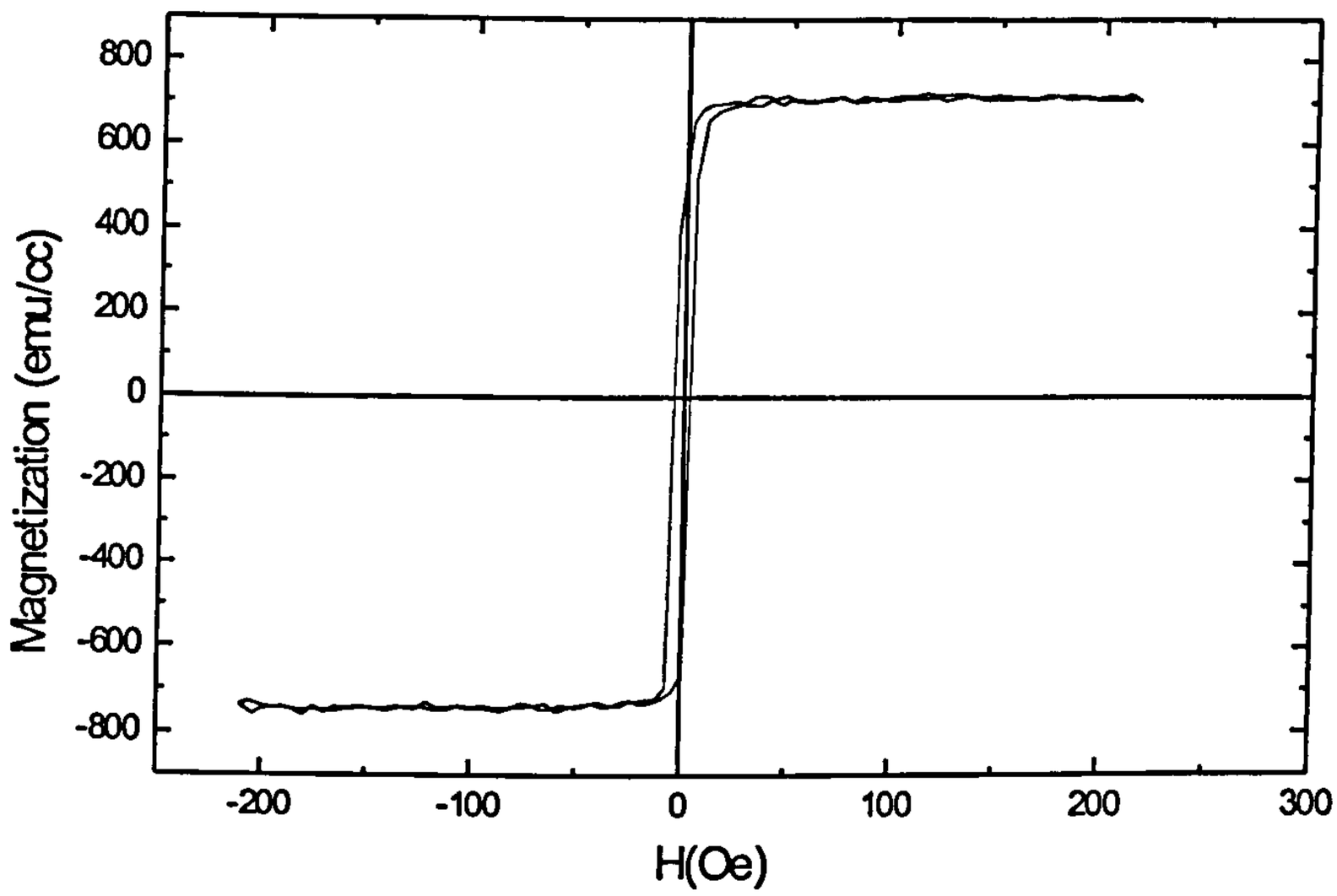

Figure 5.16) VSM hysteresis loop of vi5 (24Å FeTi/30 seconds N).

As seen in the Fe/FeN sample set, the hysteresis loop is very soft and square. The M_s was 726 ±5% emu/cm^3 and H_c=4 Oe. There was no phase change or grain growth in the FeTi/FeTiN that could be associated with the variation in the magnetic response as was the case in the Fe/FeN system, but it can be assumed that the relative amount of nitrogen present played a part in the transition. The loop for the sample with initial FeTi layer of 16Å is shown in figure 5.17.

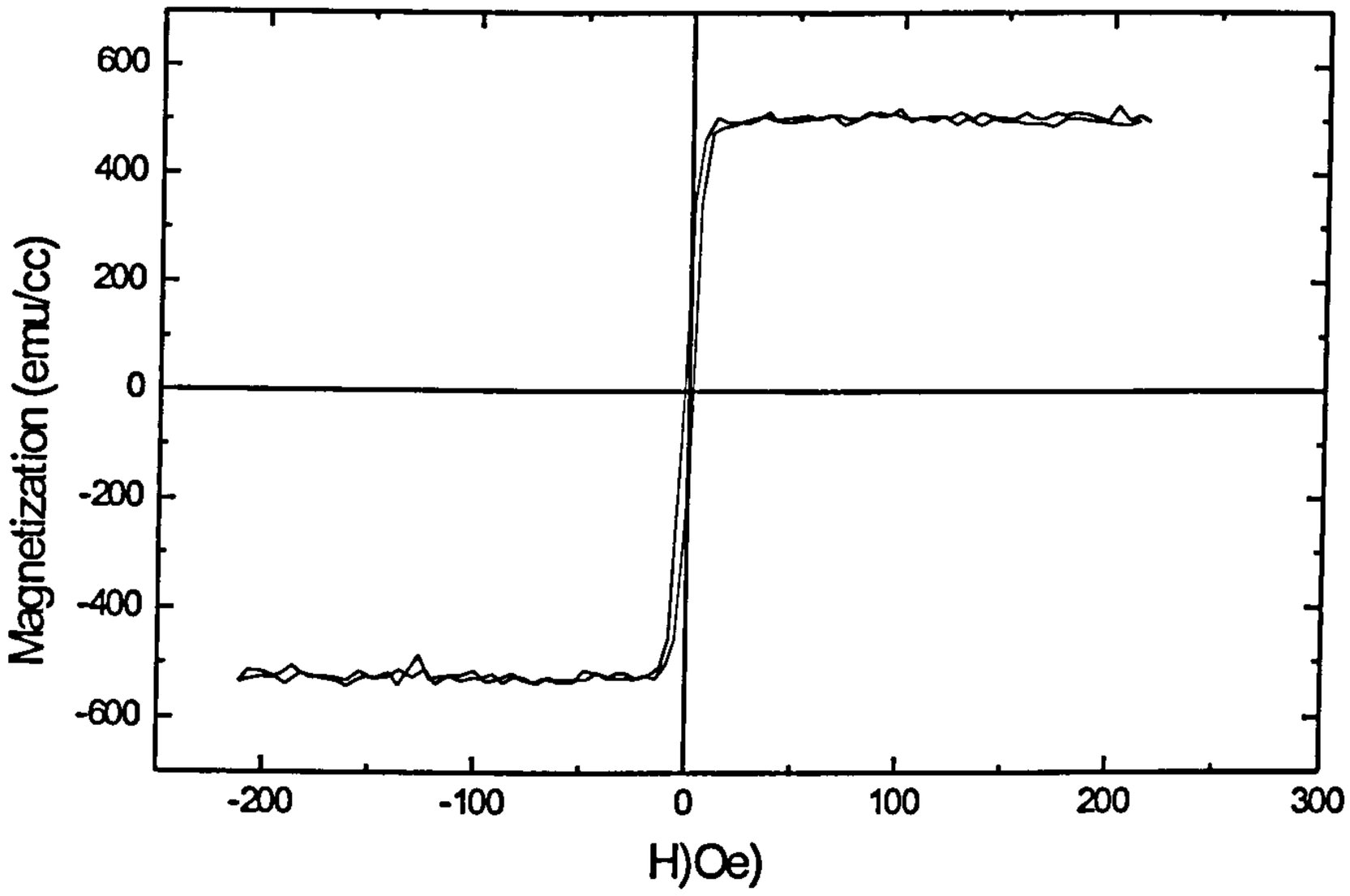

Figure 5.17) VSM hysteresis loop of vi7(16Å FeTi/30 seconds N).

As in the previous figure the loop is soft and square indicative of an in-plane magnetization. Here M_s=512.7±5% and H_c=2 Oe. As previously seen, this material is FCC.

When the initial FeTi layer was reduced to 8Å the sample became non-ferromagnetic. The hysteresis loop, obtain using the AGFM, is shown in figure 5.18. There is a strong diamagnetic signal with a minute ferromagnetic signal. The ferromagnetic signal is evidenced by the presence of hysteresis. From this, the sample is not completely nitrided, however the volume fraction of remaining ferromagnetic material is small compared to the amount of diamagnetic material. From this it appears that it is not the phase transition, but the relative amount of nitrogen that determines the magnetism of the system, as both this sample and that of figure 5.17are FCC. Both have ferromagnetic signals but the amount of ferromagnetic material in the 8Å FeTi sample is far less.

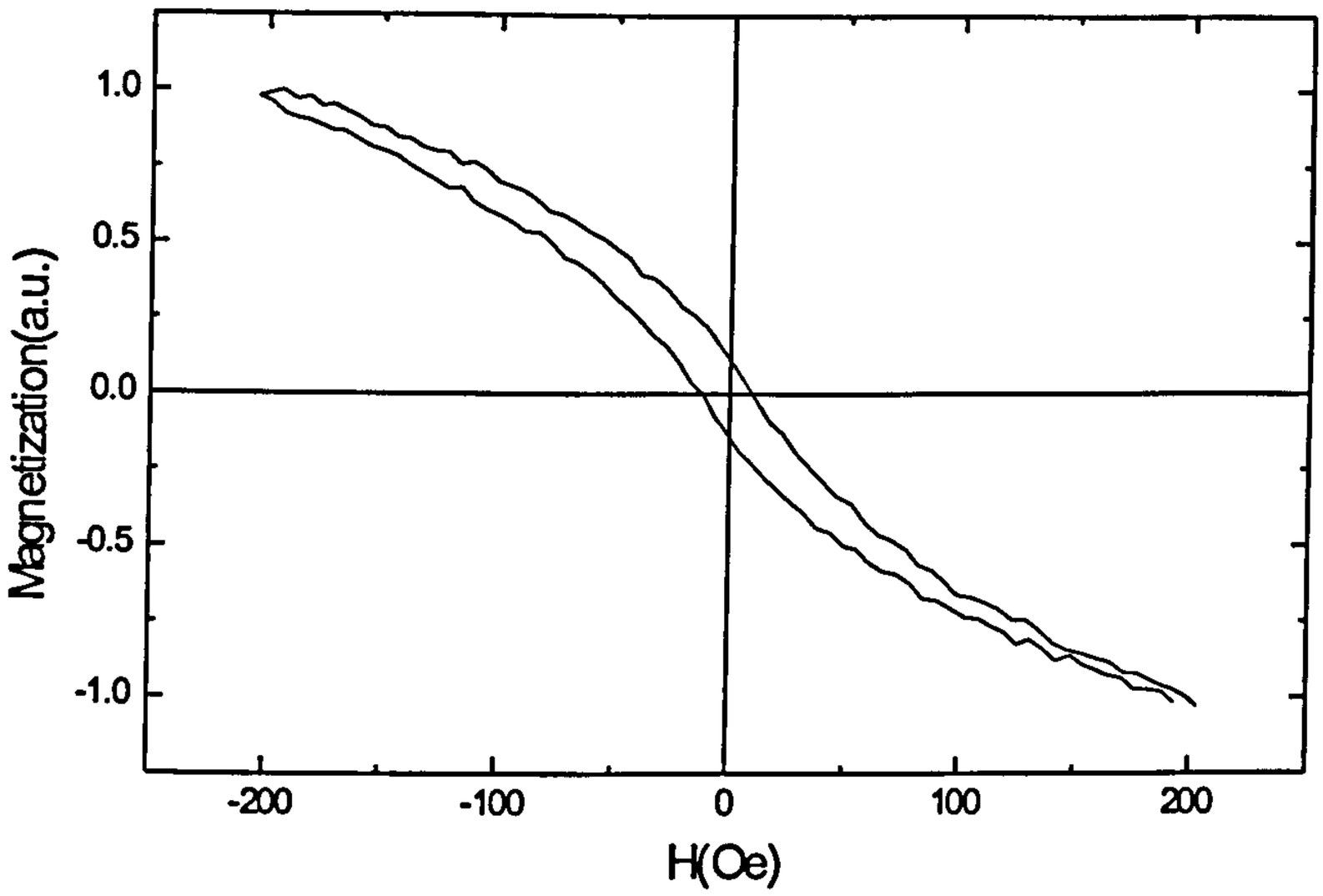

Figure 5.18) AGFM magnetization curve of vi4(8Å FeTi/30 seconds N).

For samples with effective bilayers consisting of 48Å FeTi layers and nitrogen exposure times of 5, 30 and 60 seconds the hysteresis loops each showed the characteristic stripe domain loop. Figure 5.19 shows the loop for the sample with nitrogen exposure time of 5 seconds. The coercivity is 54 Oe and M_s =722 emu/cm^3. The saturation field was considerably higher than the other samples in this series with H_s= 385 Oe. This was an indication that the magnetization was harder to rotate from its easy axis. The case for 30 seconds nitrogen exposure was previously discussed in figure 5.15. Figure 5.20 shows the hysteresis loop for 60 seconds nitrogen exposure. The values of M_s, H_c, and H_s were 771 ±5% emu/cm^3, 41 Oe, and 182 Oe respectively. The feature of importance here was the variation of the saturation field with increasing nitrogen exposure time, which decreased drastically.

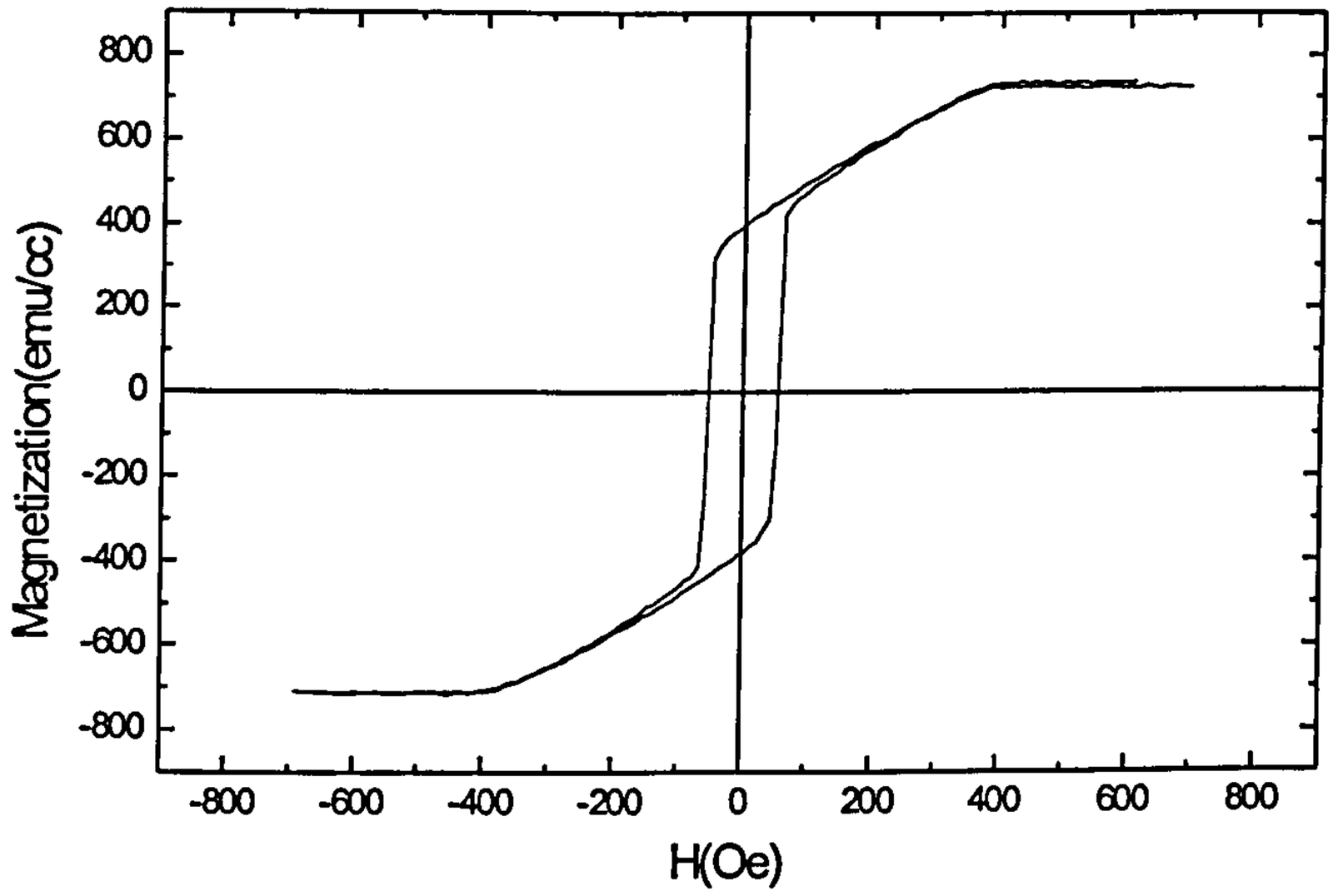

Figure 5.19) VSM hysteresis loop of vi8(48Å FeTi/5 seconds N).

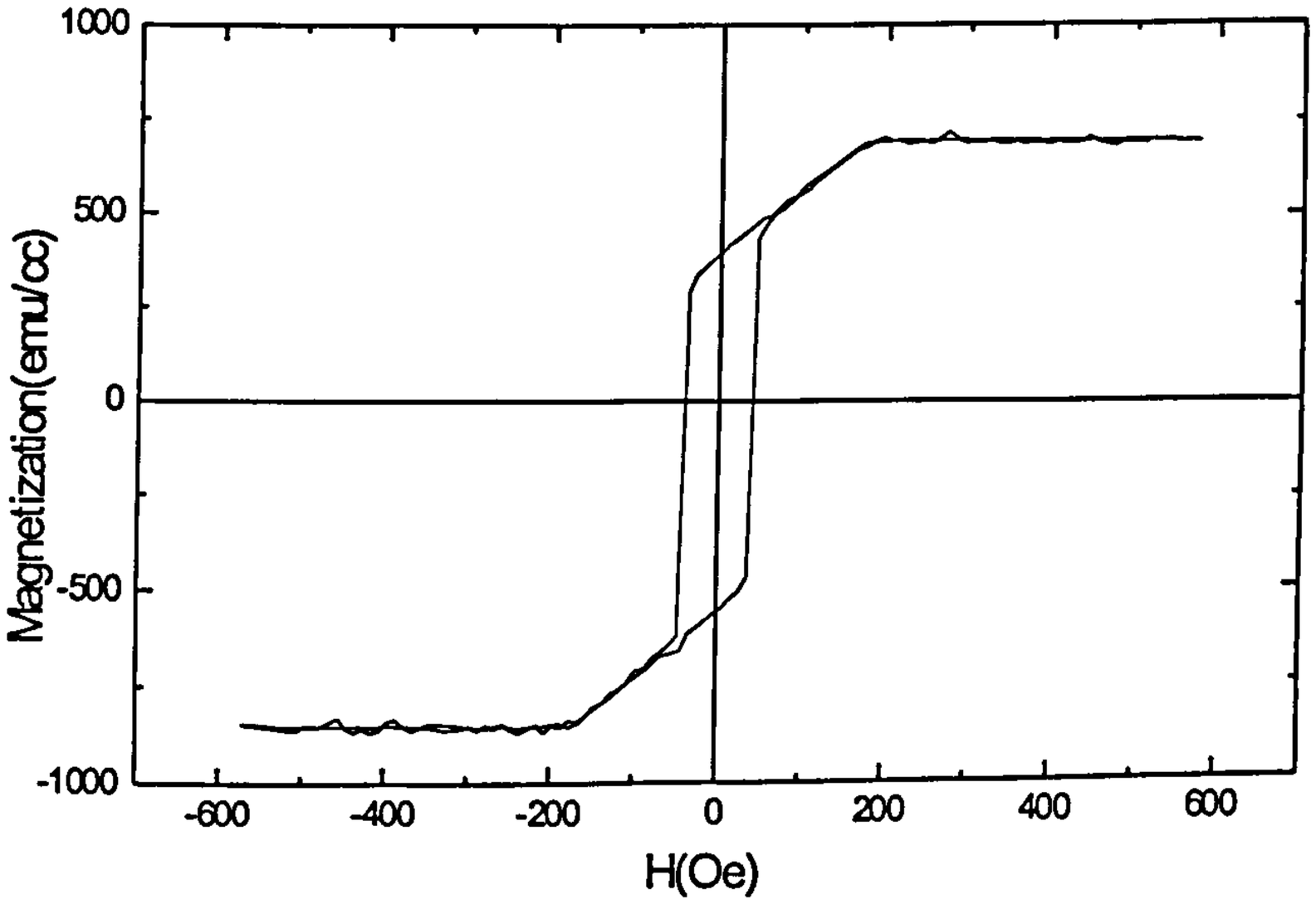

Figure 5.20) VSM hysteresis loop of vi9 (48Å FeTi/60 seconds N).

The reactively sputtered samples showed the same characteristics as the atom source samples. The sample deposited in the lowest nitrogen partial pressure shown in figure 5.21 was expected to contain stripe domains.

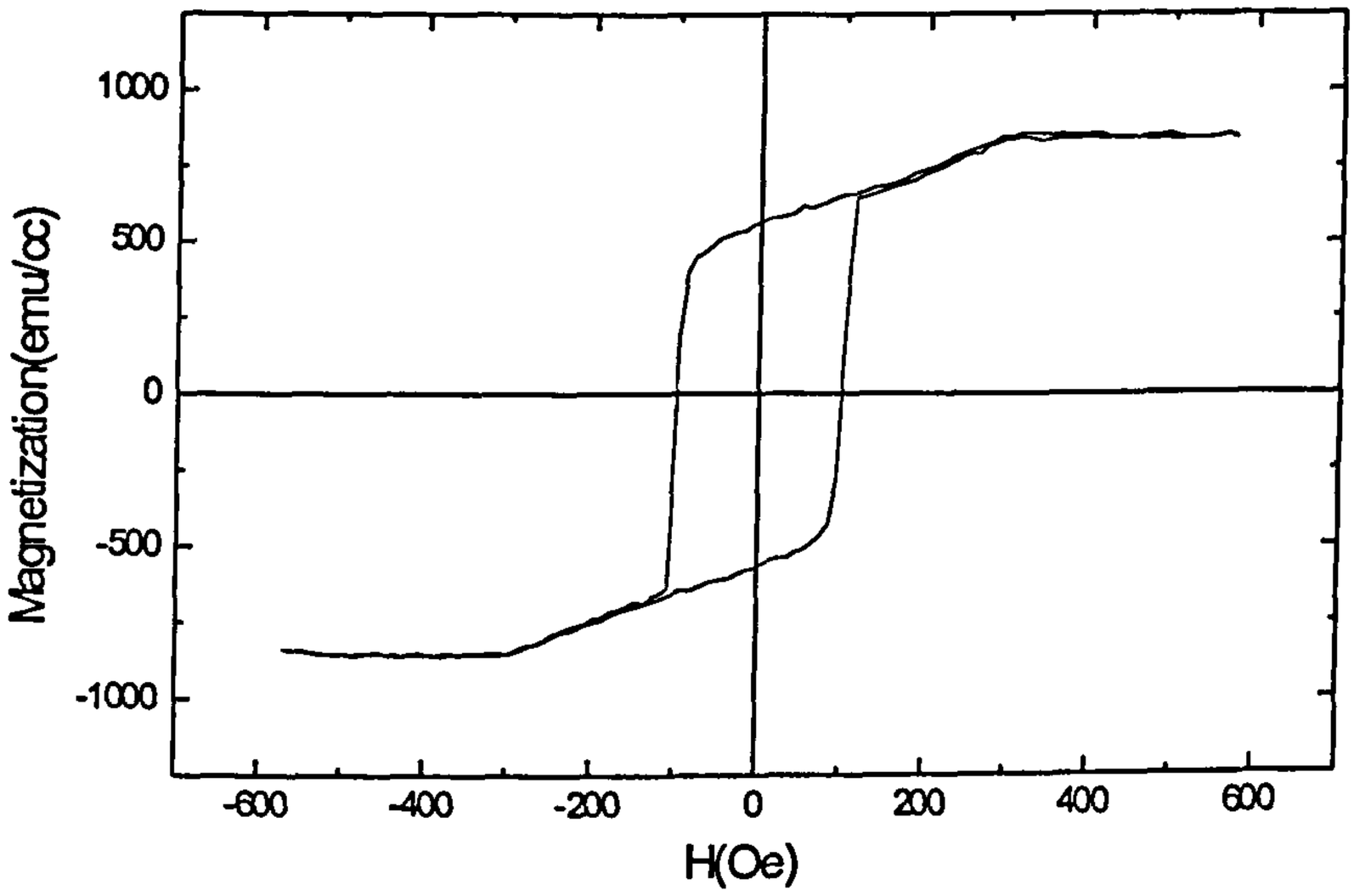

Figure 5.21) VSM hysteresis loop of vi11 (reactively sputtered sample with partial pressure ratio of 6%). The film has a thickness of 693Å.

The saturation magnetization was 849 emu/cm^3. The H_c and H_s were 98.4 and 314 Oe respectively. This sample was magnetically harder than the atom source samples. Increasing the partial pressure of nitrogen, the hysteresis loop measured for the sample was soft and square, reminiscent of decreasing the initial FeTi layer thickness as figure 5.22 shows.

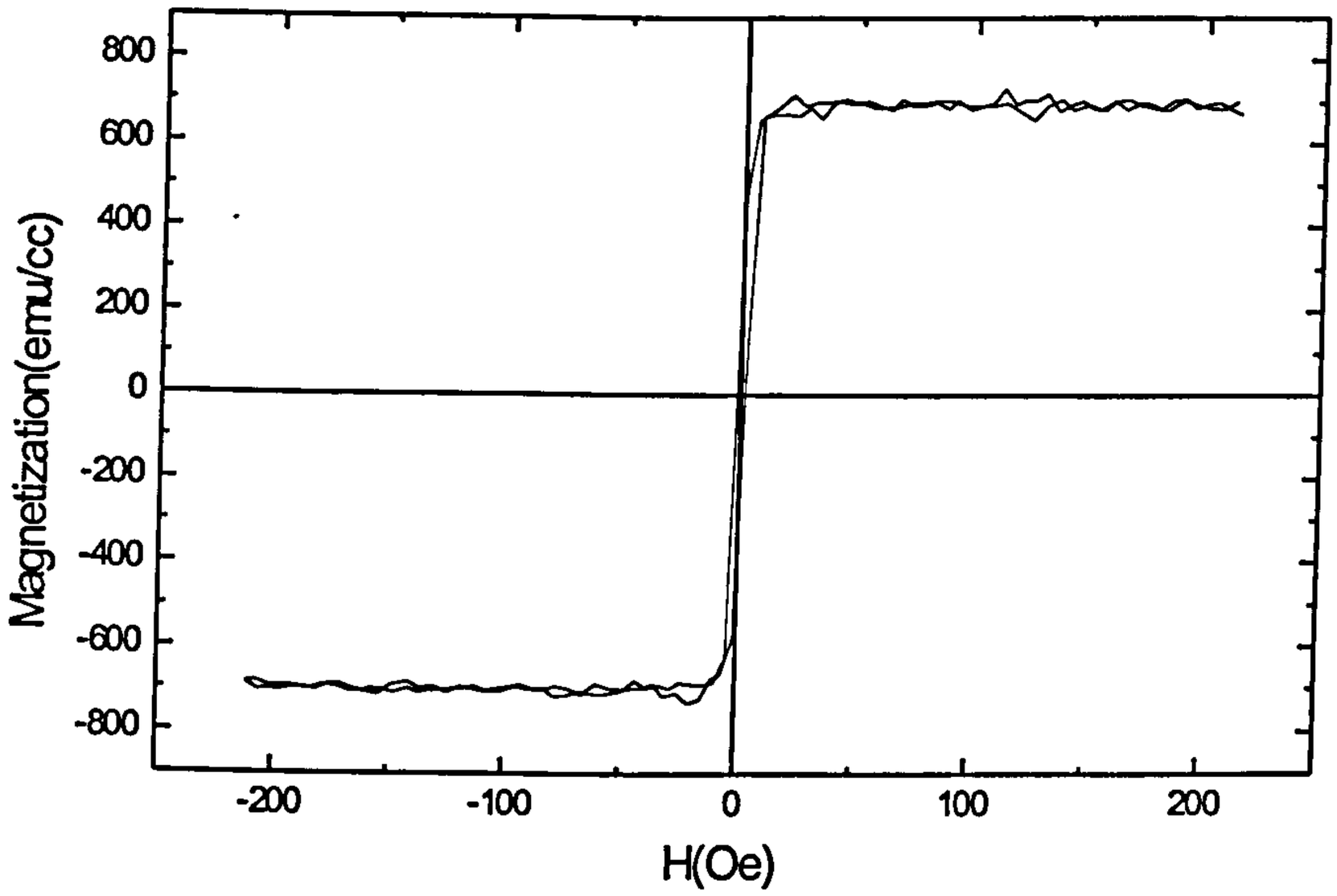

Figure 5.22) VSM hysteresis loop of vi12(reactively sputtered FeTiN sample with partial pressure ratio of 12%). The thickness is 455Å.

The M_s was 694 ±5% emu/cm^3 and the coercivity was 2 Oe. The sample deposited in the highest nitrogen partial pressure used in this sample set was not ferromagnetic as shown by the AGFM magnetization curve in figure 5.23.

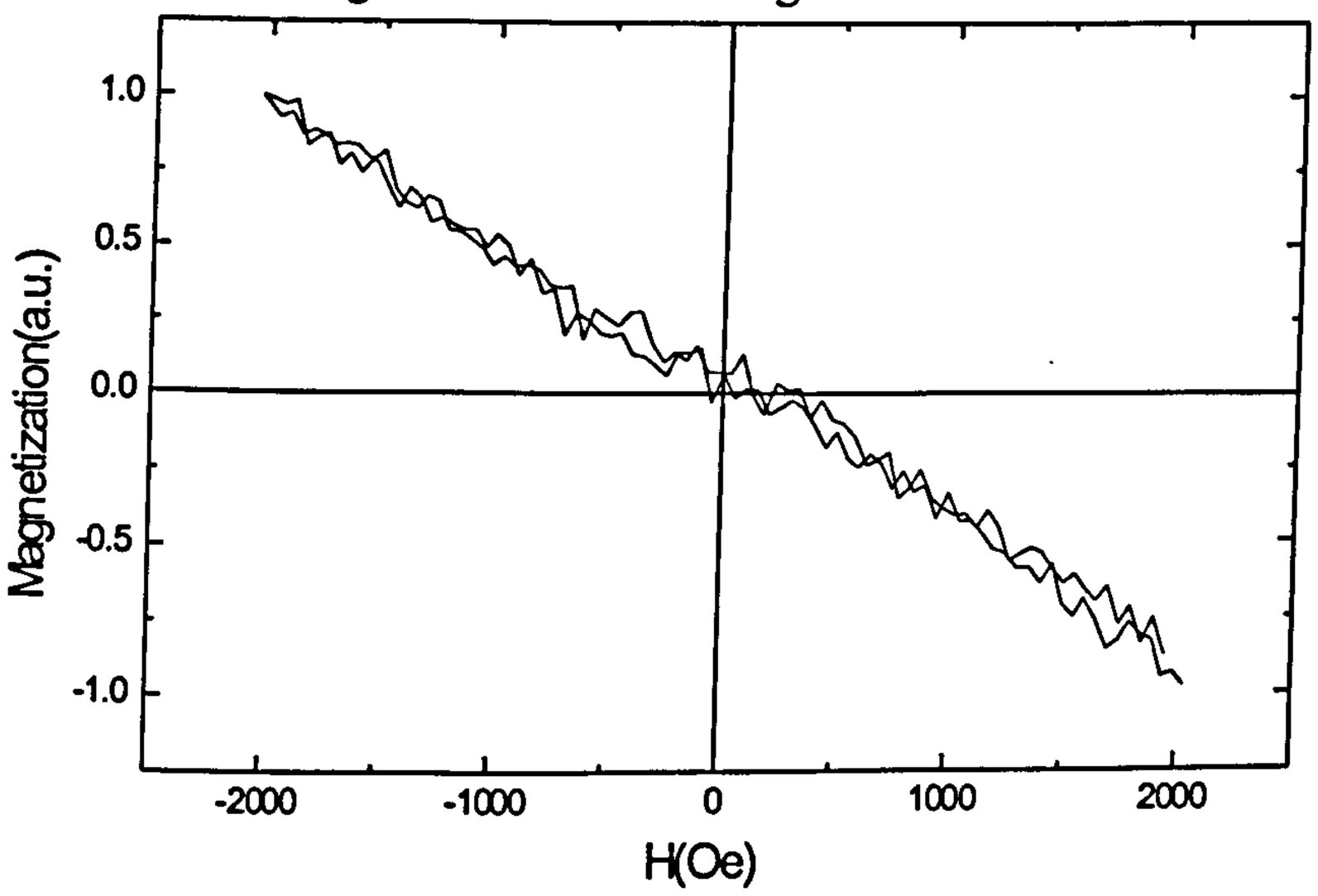

Figure 5.23) AGFM magnetization curve of vi13 (reactively sputtered FeTiN sample with partial pressure ratio of 26%). The film thickness is 308Å.

The sample gave a diamagnetic response as for the atom source sample deposited using 8Å FeTi layers, with a complete depletion of ferromagnetic material owing to charge transfer.

5.5 MFM

As was shown in the section on hysteresis loops above there were five samples in the FeTi/FeTiN sample set that have hysteresis loops indicating stripe domains. For the samples nitrided with the atom source there are no stripe domains for samples with an initial FeTi layer thickness of less than 48Å. Figure 5.24 shows the stripe domain patterns for this sample set taken with the sample in the remanent state.

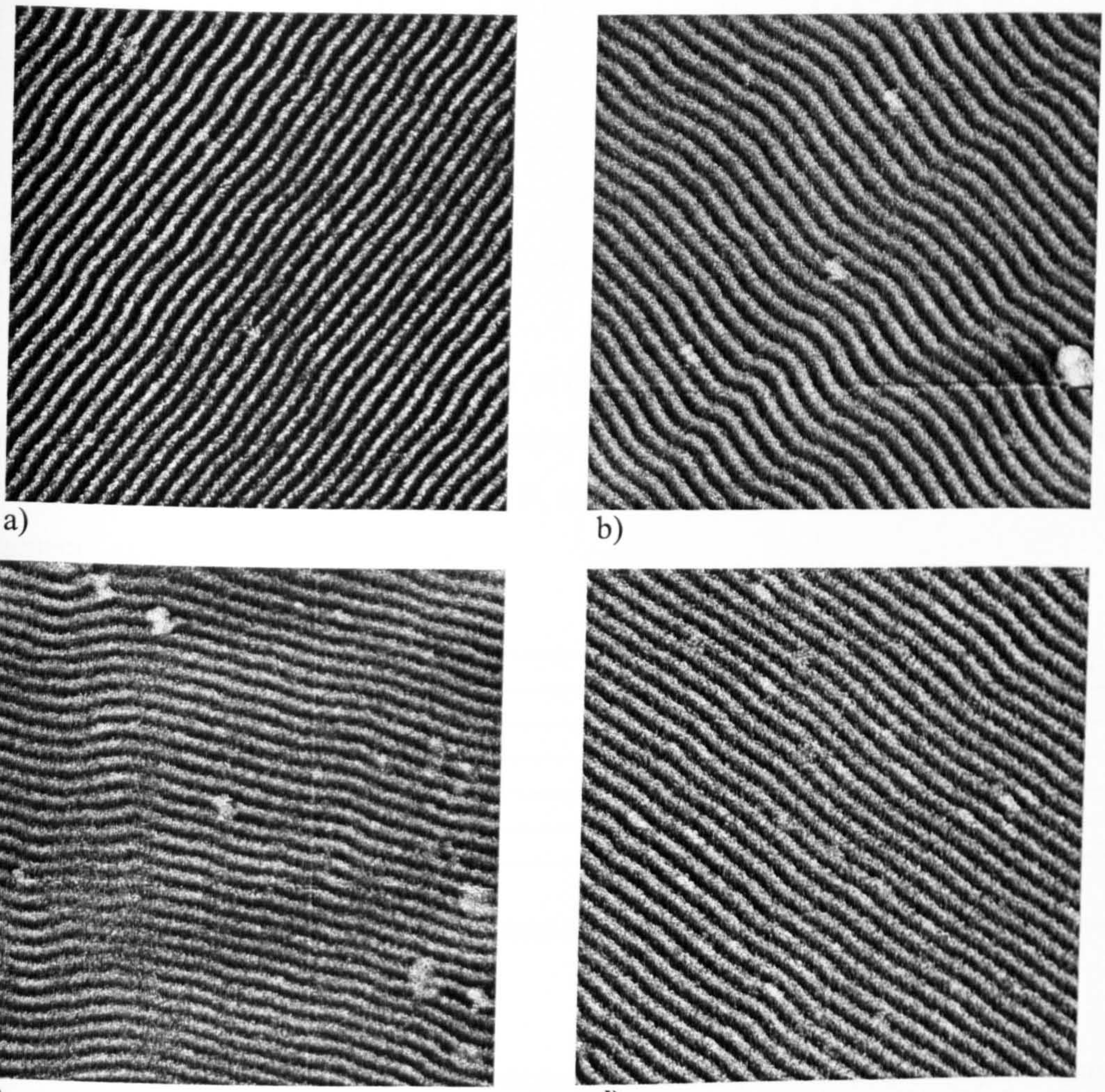

Figure 5.24) 5×5μm MFM images of a) vi6 (96Å FeTi/30 seconds N), b) vi3 (48Å FeTi/30 seconds N), c) vi8 (48Å FeTi/5 seconds N) and d) vi9 (48Å FeTi/60 seconds N) each in the remanent state.

The samples are identified in the caption in terms of the effective bilayers. Table 5.1 lists the values of H_c, H_s, and domain width. The domain width was determined from intensity plots for which a typical example is shown in figure 5.25.

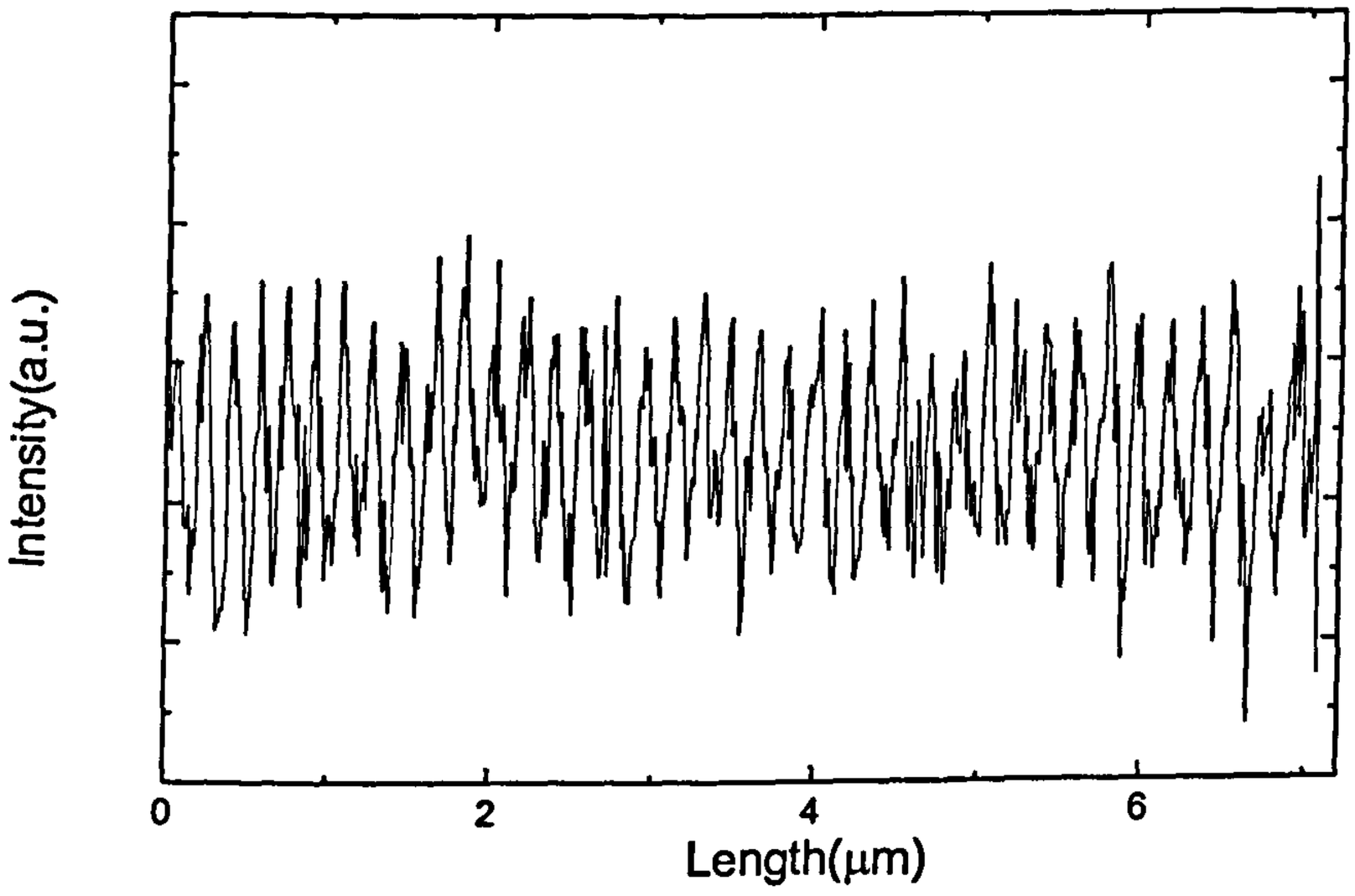

Figure 5.25) Intensity plot of the stripe domains of sample vi9(48Å FeTi/60 seconds N).

The intensity plot was intensity of image vs. distance. The number of peaks in the plot was equal to half the number of stripe domains given that peaks referred to bright stripes and troughs to dark stripes. As H_s increased the domain width decreased, in general, as seen in

table 5.1.

sample	coercivity(Oe)	saturation field(Oe)	stripe domain width(Å)
vi3(48Å FeTi/30 sec N)	26.8	123	907
vi6(96Å FeTi/30 sec N)	38.2	163	842
vi8(48Å FeTi/5 sec N)	54.2	376	781
vi9(48Å FeTi/60 sec N)	40.8	182	884
Vi11(reactive, ppr=6%)	98.4	291	691

Table 5.1) List of the coercivity, saturation field and stripe domain width for the samples showing stripe domains in the FeTi series.

The sample with an effective bilayer of 48Å FeTi 30 seconds nitrogen exposure shows a strong tendency for the magnetization to meander. The MFM images appear to be wavy. This occurs due to regions for which the in-plane components in adjacent regions

were oriented at different angles with respect to adjacent regions. The effect can be analogous to ripple on a much larger scale.

5.5.1 Variable Field MFM

As a magnetic field was applied to the sample with the strong long-range ripple the MFM images progressed as shown in figure 5.26. As can be seen, the stripes appear below the saturation field and are aligned with the saturating field. The meandering of the stripes was absent until the field was reduced sufficiently. When a field was applied at 90 degrees to the saturating field the stripes rotated by 45 degrees with a more prominent appearance of a meandering magnetization. Qualitatively there was no change in the domain width as the field was reduced from saturation to a remanent state.

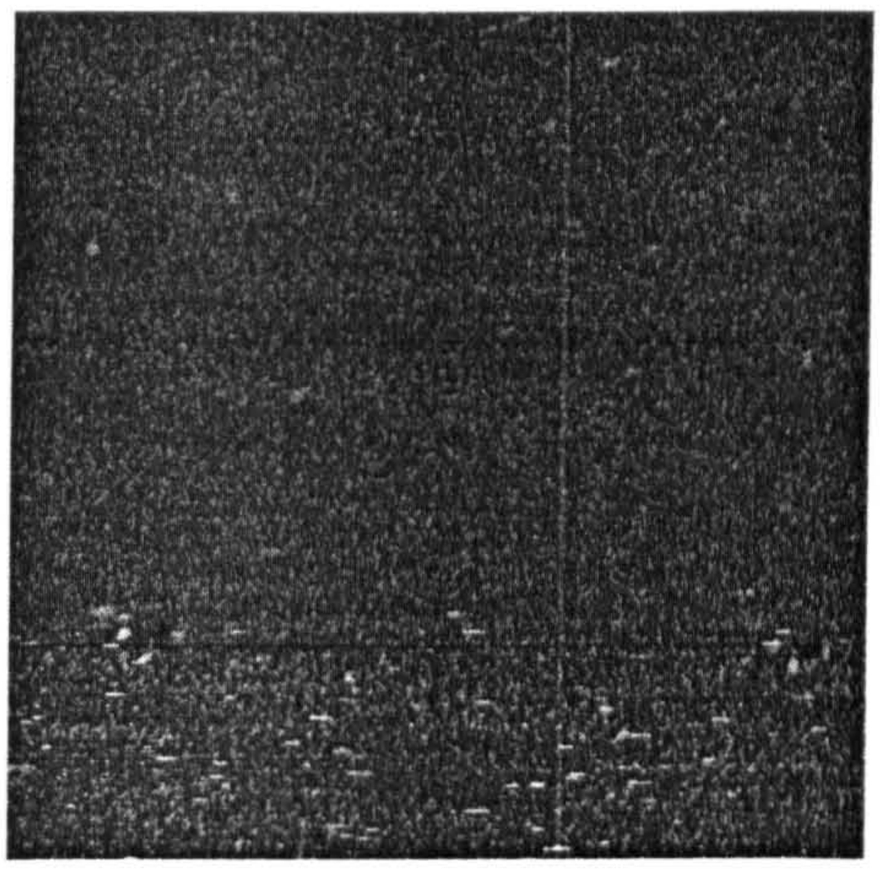

a)

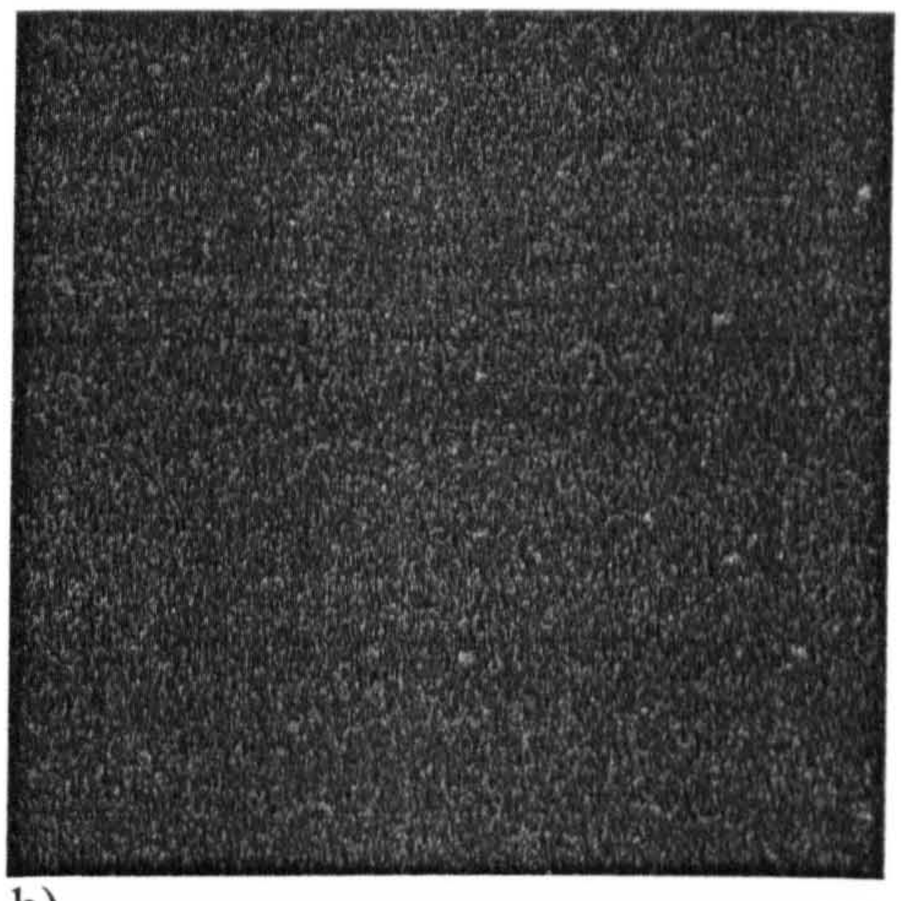

b)

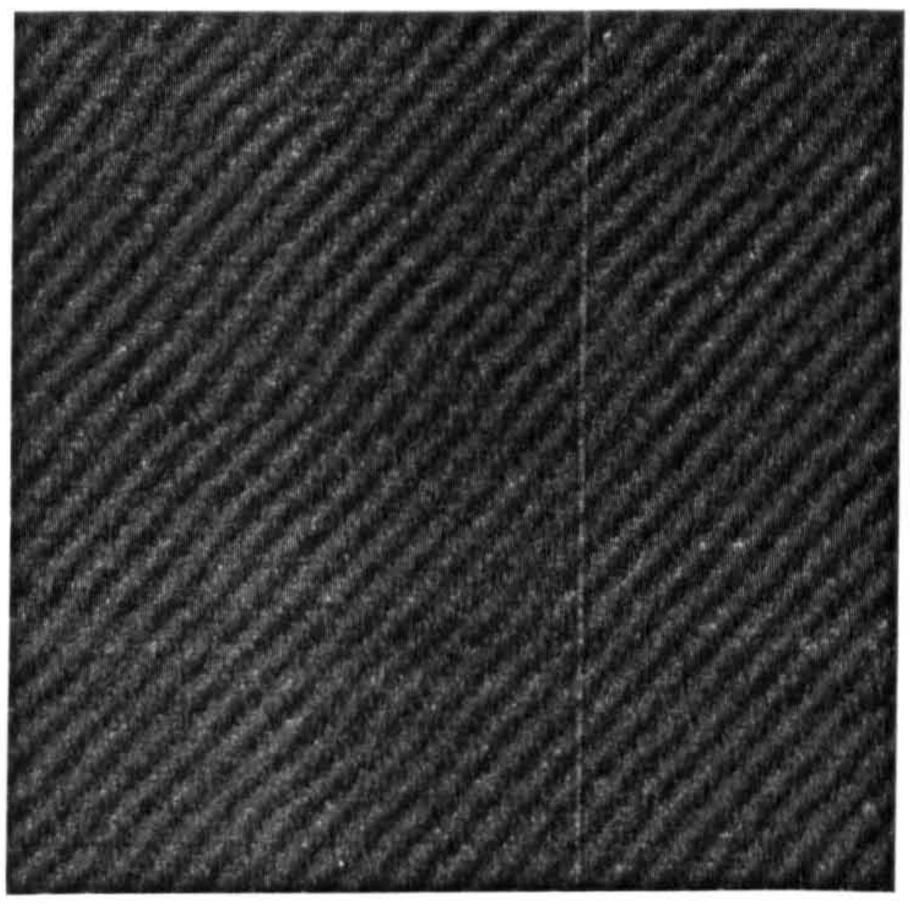

c)

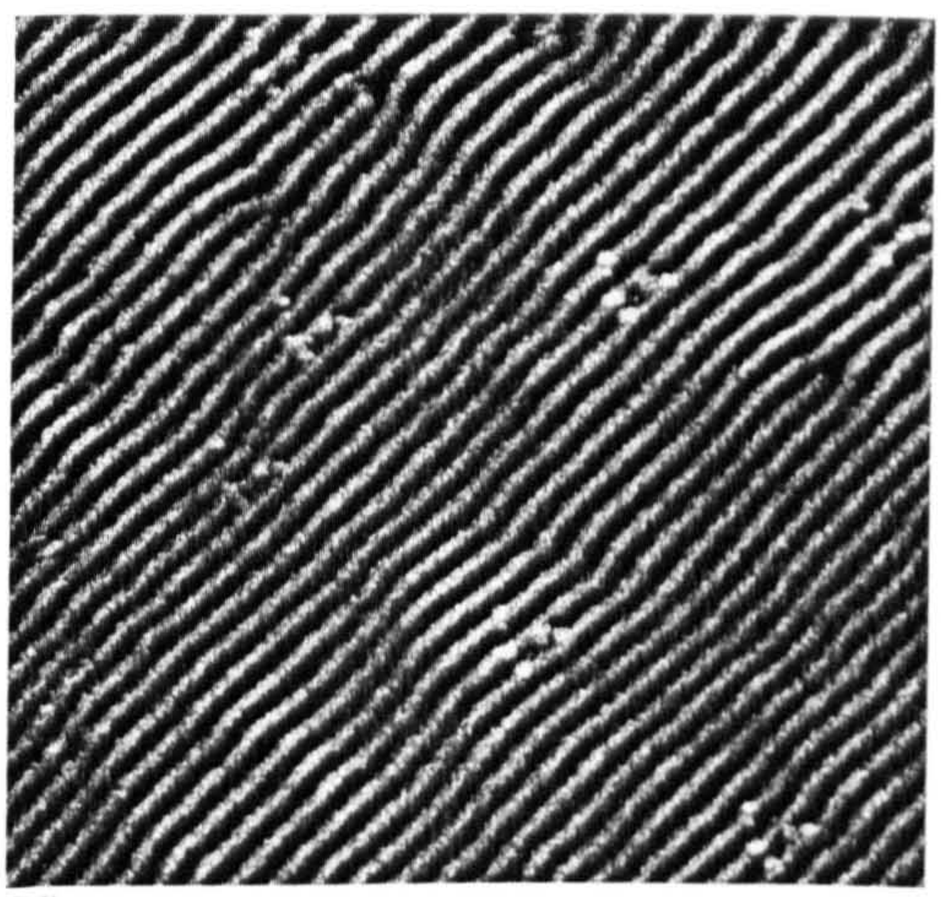

d)

Figure 5.26a-d)

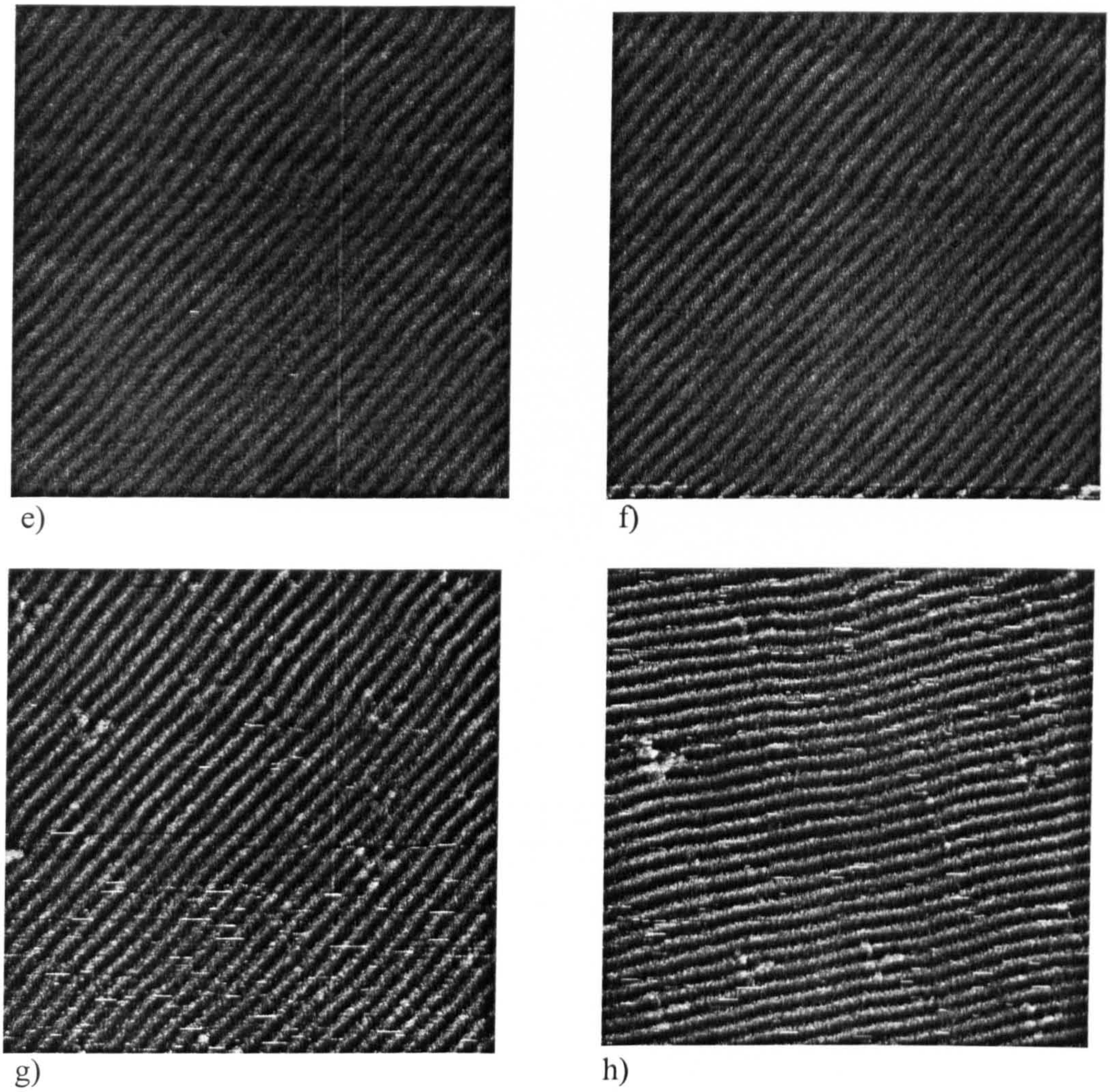

e) f)

g) h)

Figure 5.26) MFM images of vi3(48Å FeTi/30 seconds N) taken in the presence of applied fields of a)262 Oe, b) 123 Oe, c) 85 Oe, d) 71 Oe, e) 57 Oe, f) 46 Oe, g) 39 Oe. Figure h) was acquired with an additional field applied perpendicular to the one applied in (g). The applied field was along the stripe direction for images prior to g.

Such scans were similarly obtained for the sample with effective bilayer of 96Å FeTi 30 seconds nitrogen exposure, for which there was no predominant long range ripple. The hysteresis loop was displayed in figure 5.14. In accord with Hara[69] the applied field images are direct evidence for the weak type of stripe domain. Figure 5.28 shows the MFM results from the test.

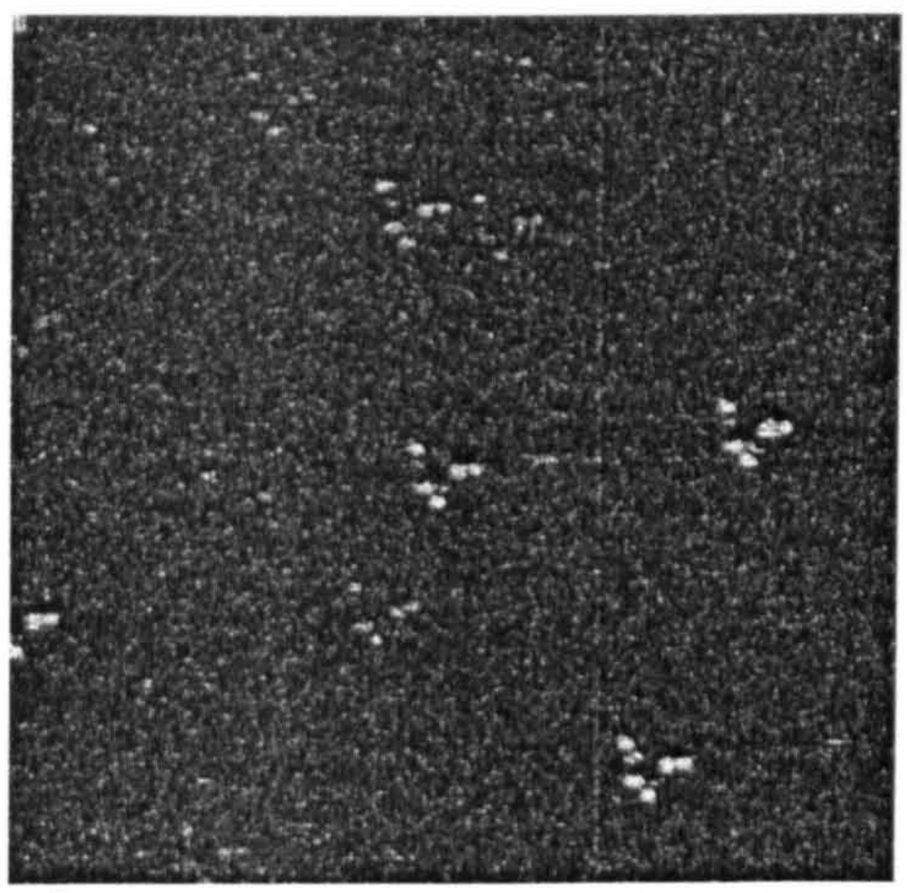

a)

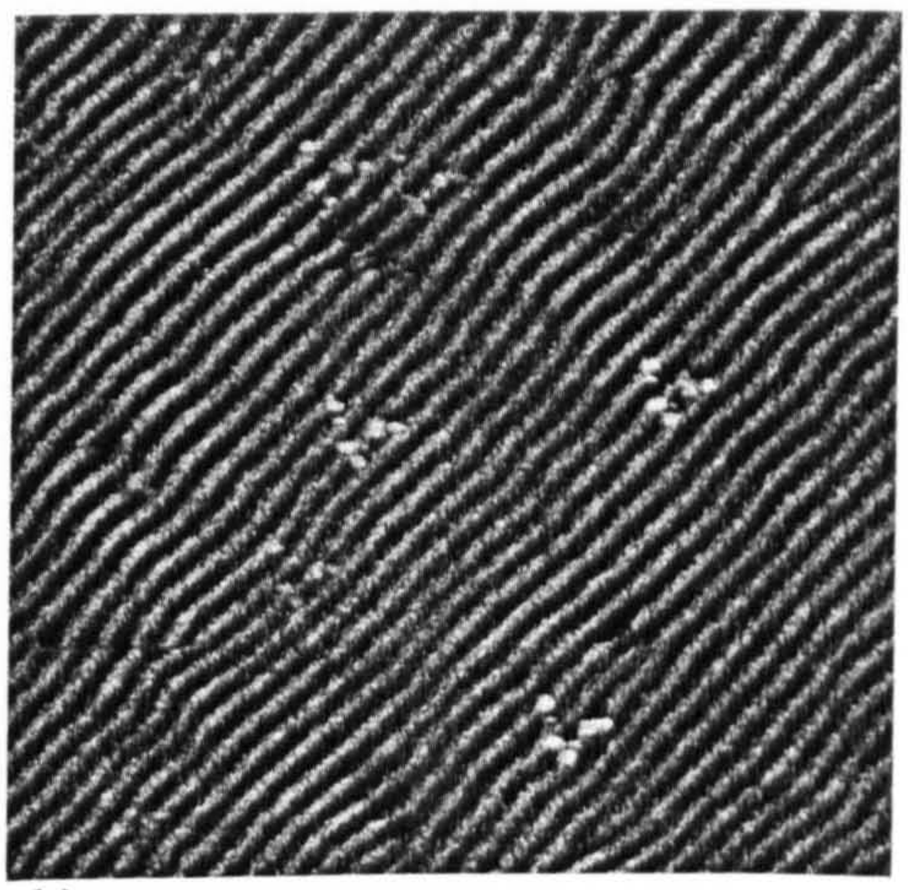

b)

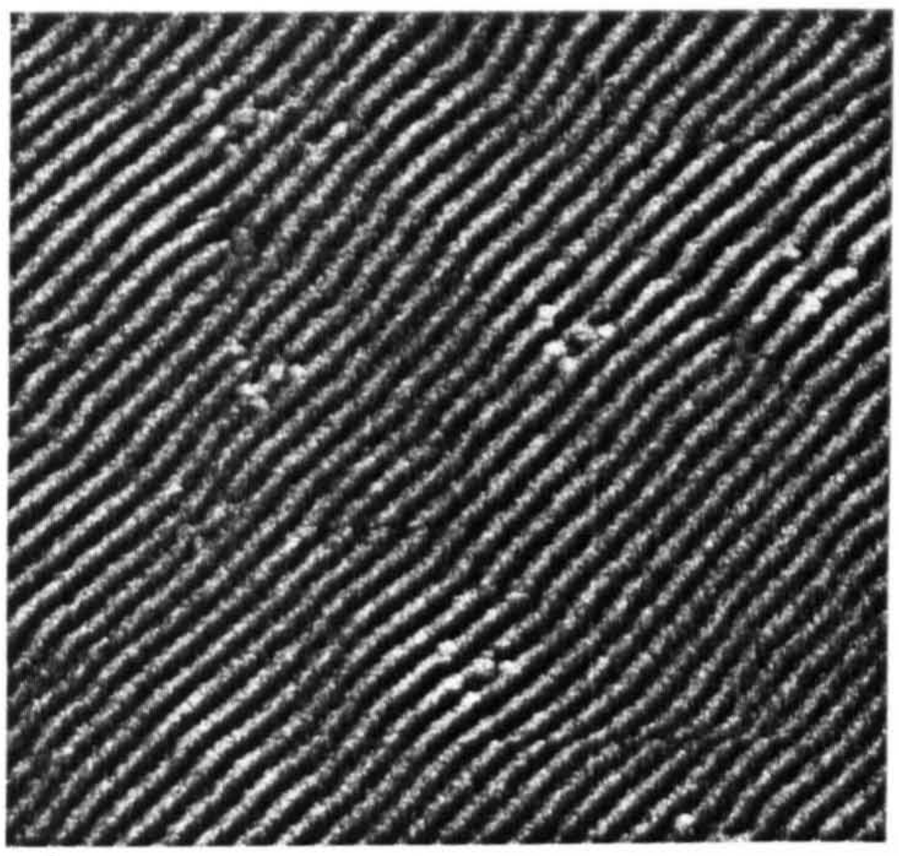

c)

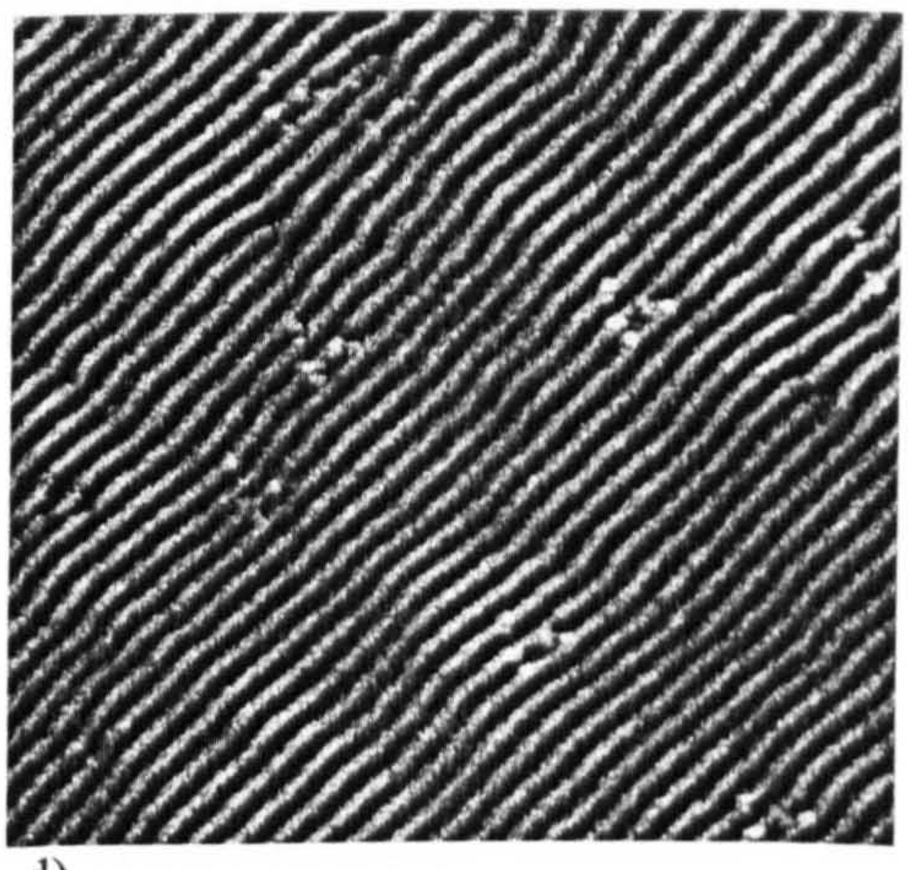

d)

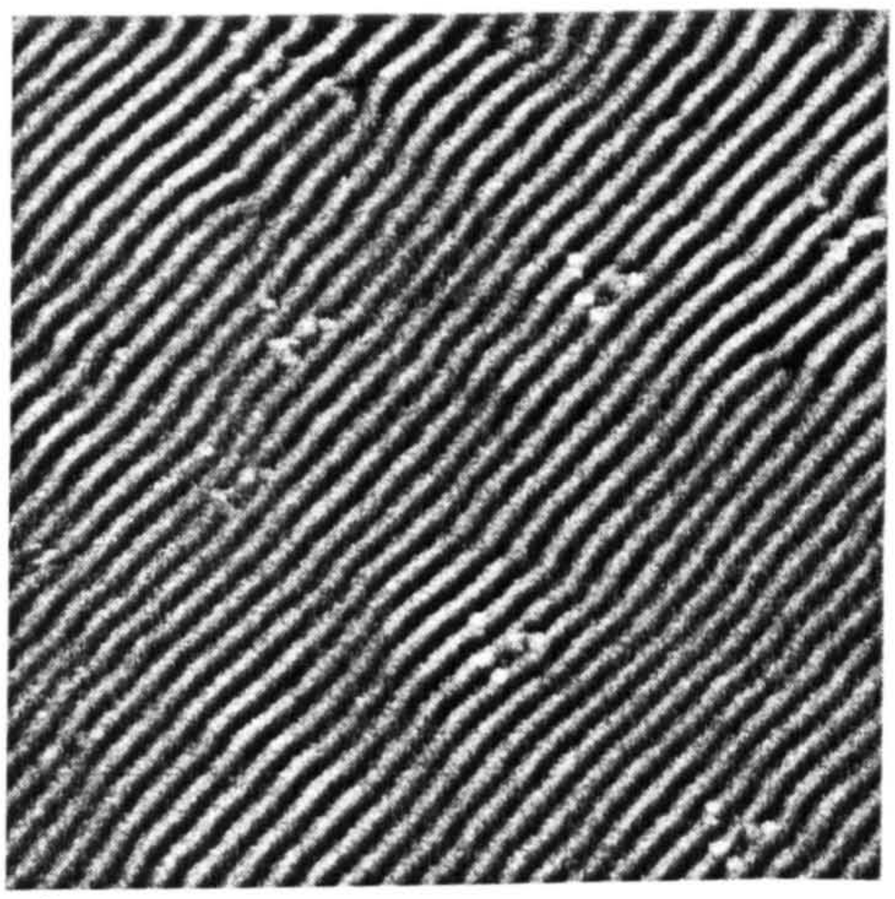

e)

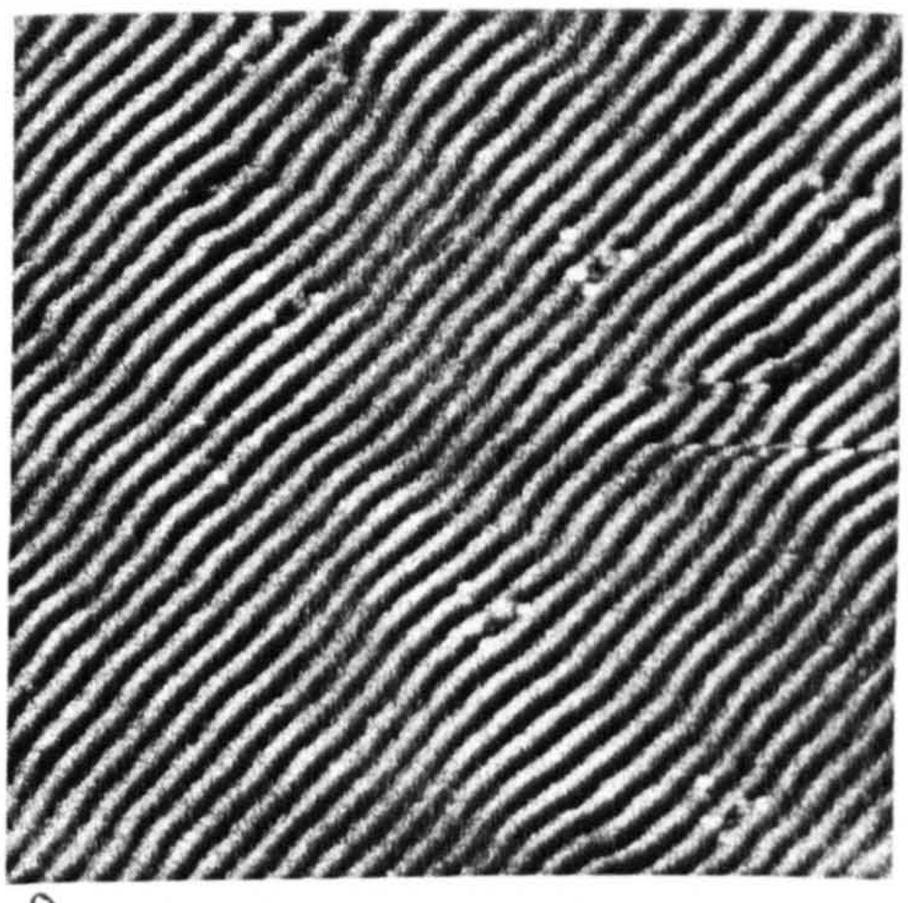

f)

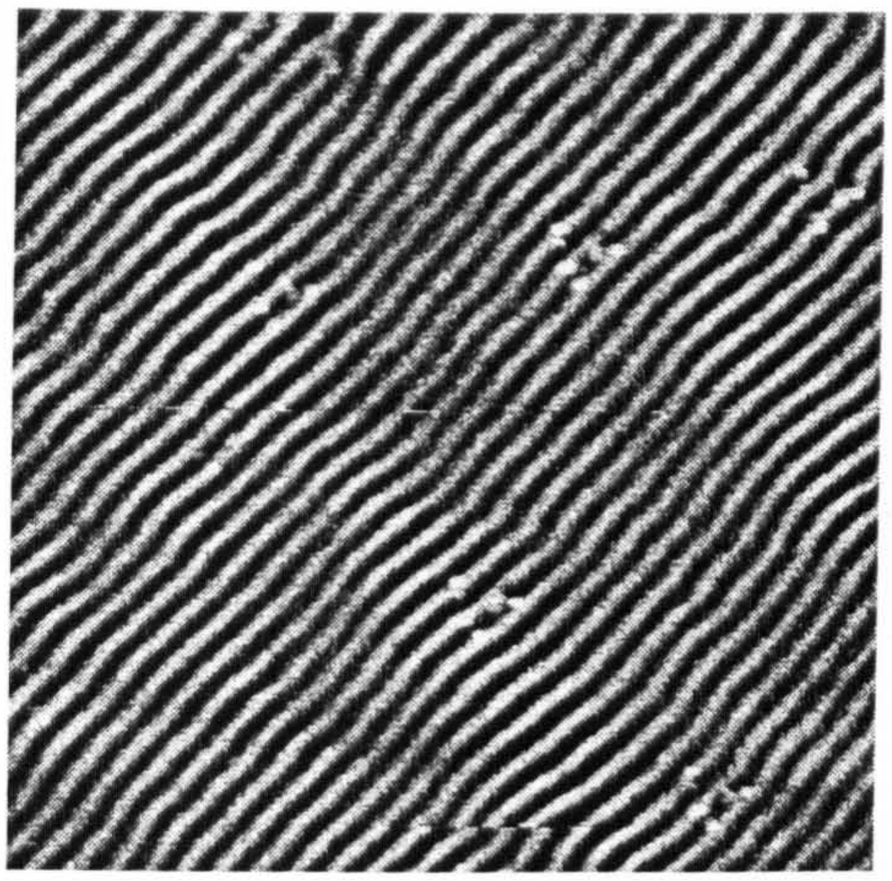

g)

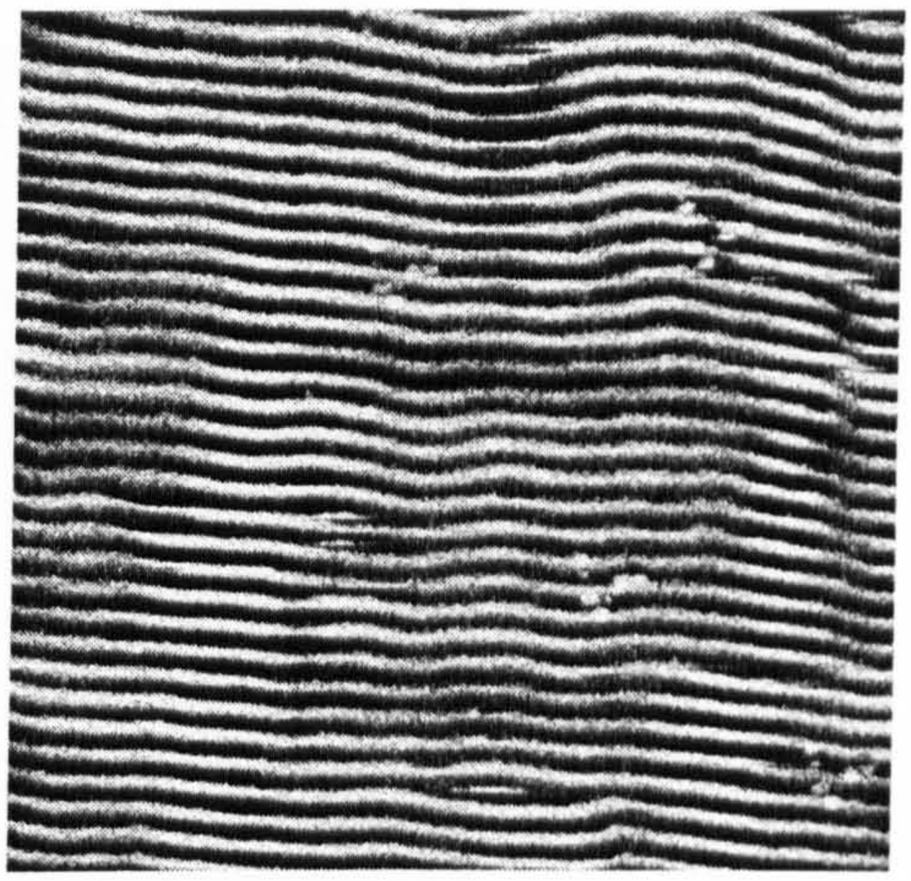

h)

Figure 5.27) MFM images of vi6(96Å FeTi/30 seconds N) taken in applied fields of a) 262 Oe, b) 123 Oe, c) 85 Oe, d) 71 Oe, e) 57 Oe, f) 46 Oe, g) 39 Oe and h) in addition to the field applied in (g) a perpendicular field greater than the saturation field of the sample. The initial applied field direction is along the stripe direction prior to (h).

Saito et al. investigated homogeneous single layer films, predicting a critical thickness below which the stripe domains are absent. The atom source samples seem to have such a critical behaviour. It would seem that the critical thickness was around 900Å. However when the reactive sample was imaged the stripe domain pattern in figure 5.28 was acquired. This sample was 693Å thick as determined by reflectivity. It was over 200Å thinner than the atom source samples with stripe domains. The reactive sample was much closer in principle to the situation considered by Saito and shows that such a critical thickness for stripe formation is below that of the atom source samples. The MFM image for the reactive sample also showed signs of meandering in-plane magnetization.

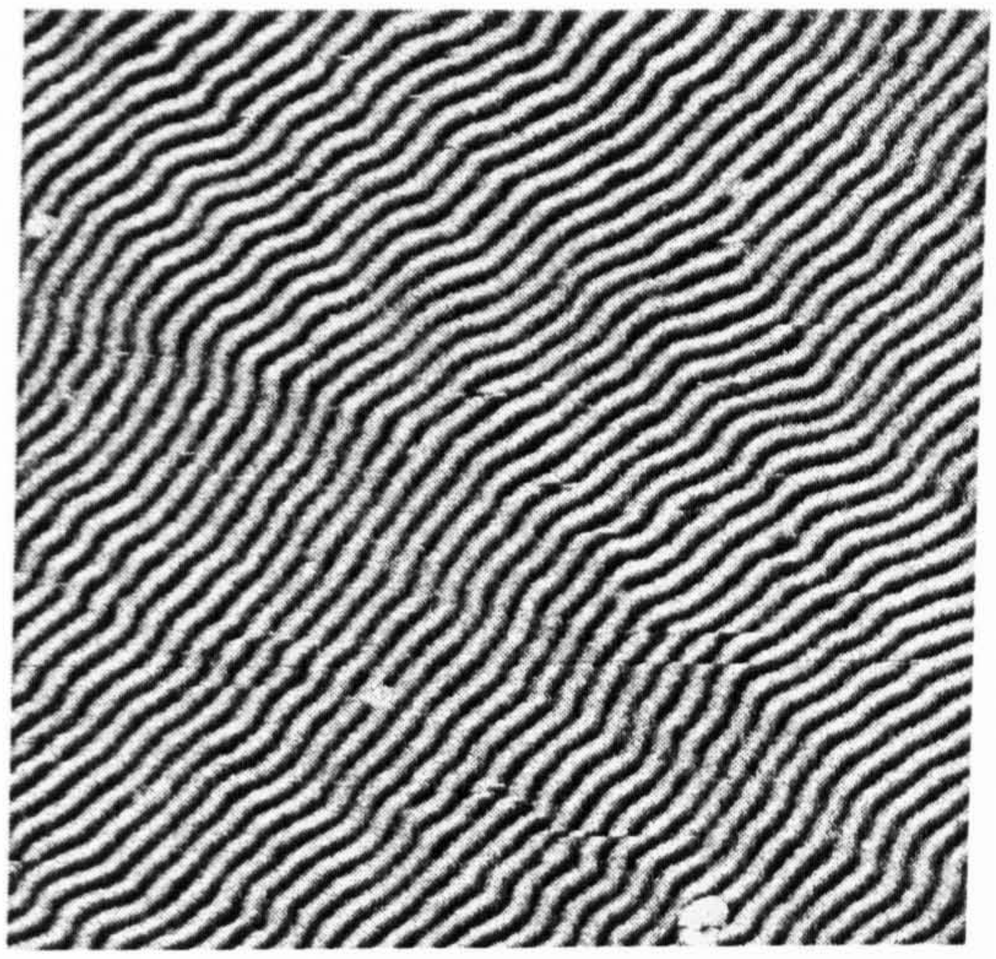

Figure 5.28) MFM image of vi11(reactive FeTiN deposited using a partial pressure ratio of 6%).

5.6 Lorentz Microscopy

As in chapter four the stripe domains were destroyed by specimen preparation for microscopy. Figure 5.29 shows a Lorentz image of the sample with an effective bilayer of 48Å FeTi 60 seconds nitrogen exposure.

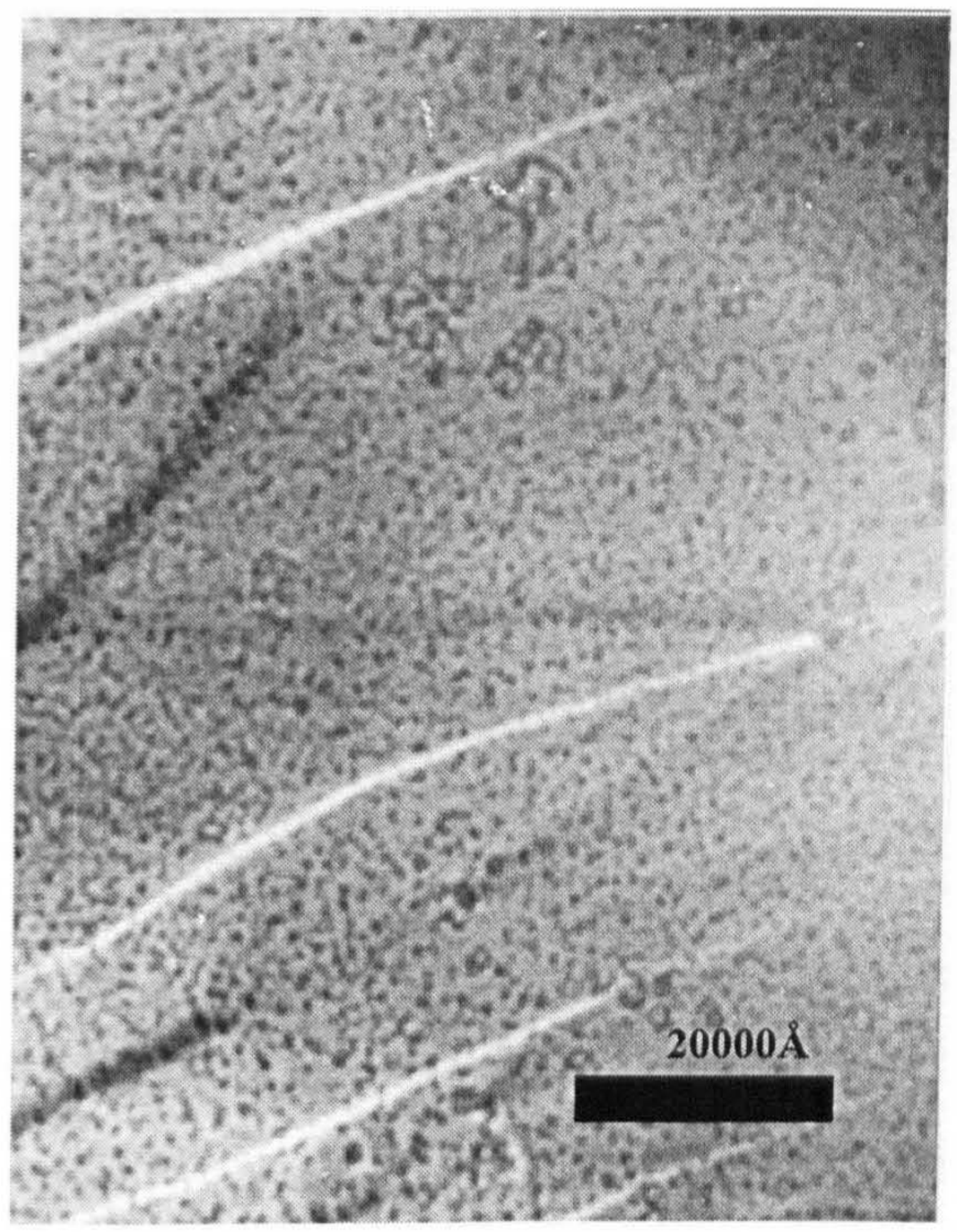

Figure 5.29) Lorentz microscopy image of vi9(48Å FeTi/60 seconds N).

Domain walls from in-plane domains are shown with in-plane closure domains near the hole of the specimen near the bottom left of the micrograph of figure 5.29. Hence the perpendicular anisotropy seems to be stress induced by the presence of the substrate. Such an effect has also been seen in single films with stripe domains, by Spain[72]. From this it appears that the stripe domains are the result of stress in the films that was relieved upon thinning the sample.

5.7 Discussion

The FeTi/FeTiN sample set was considerably less complex structurally as compared to the Fe/FeN system. It appears that the Ti has facilitated two things. It has impeded the formation of the different FeN phases and blocked grain growth. The two systems show similar trends in the magnetic properties with the presence of stripe domains

maintained over a larger range of deposition conditions in the FeTi/FeTiN system. With decreasing layer thickness the magnetic behaviour of the samples progresses from a weakly perpendicular anisotropy to soft in -plane magnetization and finally attains a non-ferromagnetic state. The hysteresis loops of the samples prepared by reactive sputtering followed the same magnetic and structural trends with increased nitrogen content. The stripe domains in both the Fe/FeN and FeTi/FeTiN samples consisted of weak stripes. The stripes are maintained over a wider range of sample conditions when Ti was added. This may be attributed to the fact that thin films with a composition of FeTi alloy used here have been shown to possess perpendicular anisotropy[79].

When the M_s was considered with respect to a varying initial layer thickness an asymptotic approach to the unexposed FeTi value was found as shown in figure 5.30. The plot also shows the trend for the Fe/FeN samples. Both approach the M_s of the unexposed material with the FeTi/FeTiN samples doing so more quickly. This may be a result of the Ti reducing the charge transfer to the Fe.

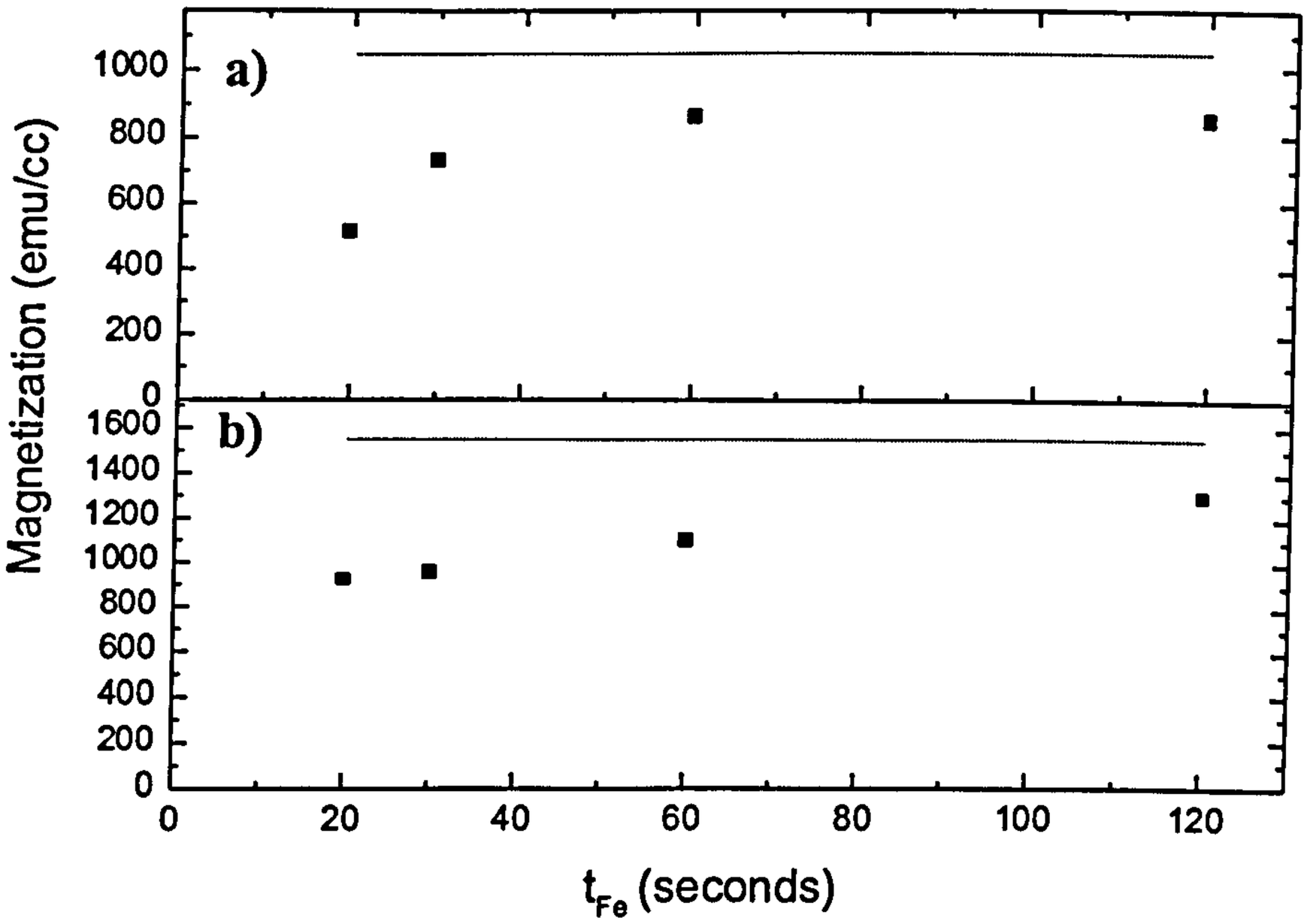

Figure 5.30) M_s vs. deposition times between nitrogen exposure for a) FeTi and b) Fe, where the lines in each figure represent the unexposed level of magnetization measured on the VSM for 500Å thick films which corresponds to deposition times of 700 and 600 seconds respectively for Fe and FeTi.

The addition of Ti into Fe has had a striking effect. The crystallography of the system is the most obvious. The structure has been simplified and the grain growth inhibited. The magnetic properties are the same with respect to the magnetization reversal and anisotropy. The anisotropy is maintained over a larger parameter space, while the magnetization is reduced with respect to the commensurate Fe/FeN samples. Though the moments found by Wang[50] were not reproduced here, it seems plausible that with subsequent heat treatments they may be possible as the nonmagnetic samples in this chapter may be considered as high, nitrogen contentγ-N austenite with Ti substitutions. Jack[14] has proposed that quenching γ-N austenite would produce a larger volume fraction of α″ in the material. This might lead to a high moment write-head stable to temperatures exceeding 500°C. Further work should prove useful.

Chapter 6 Conclusions and Future Work

6.1 Conclusions

Several conclusions can be drawn from the preceding chapters. The reflectivity showed the progression from single layer films to multilayers with sharp good quality interfaces in both the Fe/FeN and FeTi/FeTiN sample sets. The atom source nitrided samples follow a logical progression of phase formation consistent with the FeN phase diagram. The addition of 15 at% Ti restricted the reactivity of the Fe in the alloy as evidenced by the FeTi/FeTiN sample set remaining BCC for all but the two thinnest initial FeTi layer which were FCC. The grain structures were very different with grain sizes ranging from 100-1000Å in the FeFeN samples while no marked grain growth occurred in the FeTi/FeTiN set. The Ti appears to be inhibiting grain growth remaining nanocrystalline, in part possibly due to reducing the reactivity of the nitrogen with the Fe. The magnetization curves of both sets went from non-ferromagnetic to ferromagnetic with increasing bilayer thickness. Stripe domains appear in both systems for certain deposition conditions. The stripe domains are weak stripes in both cases, with stripes present over an extended range of deposition parameters in the FeTi/FeTiN samples. Lorentz microscopy showed no evidence of stripe domain structure in either of the two types of samples looked at here, pointing to stress in the film as the mechanism that established the stripe domains. And finally the samples showing stripes are quite different than those considered by Saito due to the multilayer structure requiring a more appropriate model. As always, the data presented here if subjected to further scrutiny might produce alternate interpretations that could be equally valid. To be closed-minded would be unscientific.

The nitriding of Fe and FeTi alloy via a nitrogen atom source provides a unique and effective means of altering the magnetic and structural properties of the systems presented in this thesis.

6.2 Future Work

The work presented here has been preliminary in nature. It establishes a baseline for the use of an atom source in forming iron nitride thin films. The Fe/FeN sample set established that the phases present can be manipulated by varying the initial Fe thickness. Further measures can be taken to accomplish this; the parameter space has not been exhausted. The atom source provides for variation of the nitrogen flow rate, power of the RF supply, and variation of the aperture through which the nitrogen effuses. Decreasing the nitrogen flow introduced into the atom source decreases the amount of nitrogen available. The present samples have in excess of 20 at% N in the respective layers given that Fe_4N was formed, while the α'' phase only contains 11 at% N. Varying the power of the atom source will vary the ratio of $N:N_2$ within the beam as the atom source would be operating at less than maximum efficiency. This would alter the reactivity of the nitrogen in that the molecular nitrogen would have to dissociate at the Fe surface prior to diffusing. An accurate quantification of the amount of nitrogen exuding from the atom source is still necessary. Prior work on oxygen incorporation in thin films has been studied using a sensitive micro-balance[80]. There was evidence of oxide formation ex situ, in the present study, and any determination of nitrogen incorporation would require an ultra sensitive in situ quartz crystal oscillator. The fact that there was no evidence of nitriding for an Fe film not directly exposed to the atomic beam points to variation of the local pressure of nitrogen as a means of varying the phases present. Using an aperture with fewer openings could accomplish this for a given nitrogen partial pressure. This would alter the ease with which the nitrogen could effuse toward the substrate.

As mentioned in chapter 1, a variety of substrates and substrate conditions have been used. Of particular interest are the substrate temperature and the use of a silver underlayer in producing the α'' phase. $Fe_{16}N_2$ is a metastable phase meaning one cannot simply mix Fe and N into a pot and get out the α'' phase. The atom source samples provide a unique opportunity. It is expected that annealing high nitrogen content nitrogen austenite will produce higher volume fractions of the α'' phase. The FeTi/FeTiN sample

synthesized with the thinnest initial layer was a single FCC layer. It is effectively a high nitrogen concentration austenite with Ti substitutions. Annealing this sample could prove fruitful. Annealing experiments would require in situ phase determination as oxide formation would convolute analysis. The α'' phase sits in the region of $Fe_4N+\alpha$-Fe. Annealing the appropriate samples using an in situ heating stage in the TEM will help to further understand the efficacy of the atom source nitriding technique and holds promise for forming the α'' phase. The use of a Ag underlayer may have served two purposes. The lattice spacing of Ag is very near that of one of the α'' reflections, hence providing an epitaxial relationship that would be favourable for formation of the α'' phase. Part of the idea behind alloying Fe with another transition metal was to alter the nitrogen affinity of the Fe[14]. Silver forms an azide of the form AgN_3 that is the only apparent nitride of silver. This sets up a scenario for which nitrogen could be absorbed by the silver from the Fe in a way as to regulate the reactivity and amount of nitrogen in the Fe as occurred when Ti was used. From this an FeAgN alloy film is conceivable. Noble metals are well known for forming a small moment when in Fe/NM multilayers. This could also work to the advantage of the proposed alloy as presently the alloyed metal detracts from the Fe moment. The FeTi alloy used in this thesis is nonmagnetic in the $FeTi_2$ form and the consequences of this were seen in the magnetization value of the unexposed alloy as compared to the Fe thin film. It is evident that a further search for an alloying element is necessary and there seems to be a wealth of possibilities.

The work on stripe domains can be pushed further. The models from the literature applied to the multilayers here was not wholly appropriate though a good first approximation. The samples showing stripe domain patterns were much more complex. The Stoner-Wohlfarth model posited above considers the presence of two different species. However, the formalism requires non-interacting layers. This approximation deviates from the actual scenario quite substantially. Further work is necessary to develop a model of stripe domains for bilayers of two ferromagnetic layers that incorporates exchange energy and a more accurate representation of the influence of the nitrogen.

The effect of the presence of the nitrogen has not fully been determined. All present literature points to the system as an interstitial alloy and then points to charge

transfer as the origin of the high moment. An investigation of any bonding is required. Electron energy loss spectroscopy would show any chemical shift due to the nitrogen bonding. This technique however requires very thin single layer samples in order to reduce multiple scattering contributions to spectra. For this a series of samples with a single layer reflectivity profile each with a different nitride phase would be required to definitively probe the situation. This requires further tailoring of deposition conditions to produce such a sample set. Single layer samples were produced for thin initial metal layers, so this presents a possibility. The Stoner-Wohlfarth model presents a means for determining the angle of the magnetization in the stripe domain films. Torque magnetometry measurements would elucidate the relevance and validity of the model as well as aid in determining the angles of the magnetization in the film.

The FeN system alone poses a plethora of research opportunities. The recent development of spin tunnel junctions is an arena for which the atom source would be quite compatible. The present study produced samples with different magnetic characteristics depending on nitrogen exposure. This could be beneficial for the magnetoresistance effect integral in tunnel junctions. The two layers separated by a high resistance insulating layer need to have different switching fields. This scenario could readily be set up in conjunction with a high resistance, metal nitride layer if they were thin enough. Increasing the relative amount of nitrogen improved the softness of the Fe. Hence by setting up the appropriate nitrogen concentration gradient each of the layers would have a different coercivity, which is vital to setting up the antiparallel high resistance state.

Nitrogen is not the only possible source gas. Hydrogen and oxygen are also possibilities. Hydrogen could be used as a means of removing the surface oxide without drastically altering the surface as is the case in ion beam etching of substrates. The hydrogen would react with the surface oxide to form water which would be pumped away. This avenue would lead to a means of forming better epitaxy with the substrate. The oxidizing of Al using the atom source has potential for use in spin tunnel-junction barrier layers.

Further improvements in measurements of the data presented here would also be beneficial. The X-Ray diffractometer used Cu K_α radiation, which is above the absorption

edge. This has contributed to a large background, which may obscure any weaker peaks. Use of a different radiation source target or synchrotron radiation would help elucidate the structure of the system. Synchrotron radiation would further improve knowledge of the structure given the improved intensity and more finely collimated incident beam that is possible using a synchrotron source. Alignment of the sample is crucial for reflectivity measurements. There is a significant reduction in intensity of the signal if the sample is not aligned. Again alignment is much more precise using a synchrotron owing to an increased number of degrees of freedom of the sample.

The parameter space is vast and the potential has only begun to be explored.

Appendix

The Stoner-Wohlfarth calculations for the hysteresis loops displayed in figures 4.38-40 are detailed below.

Consider a single domain thin film with easy axis parallel to y and an applied field H along z. the energy of the system is a combination of the anisotropy, applied field and the demagnetizing field energies, E_K, E_H and E_D:

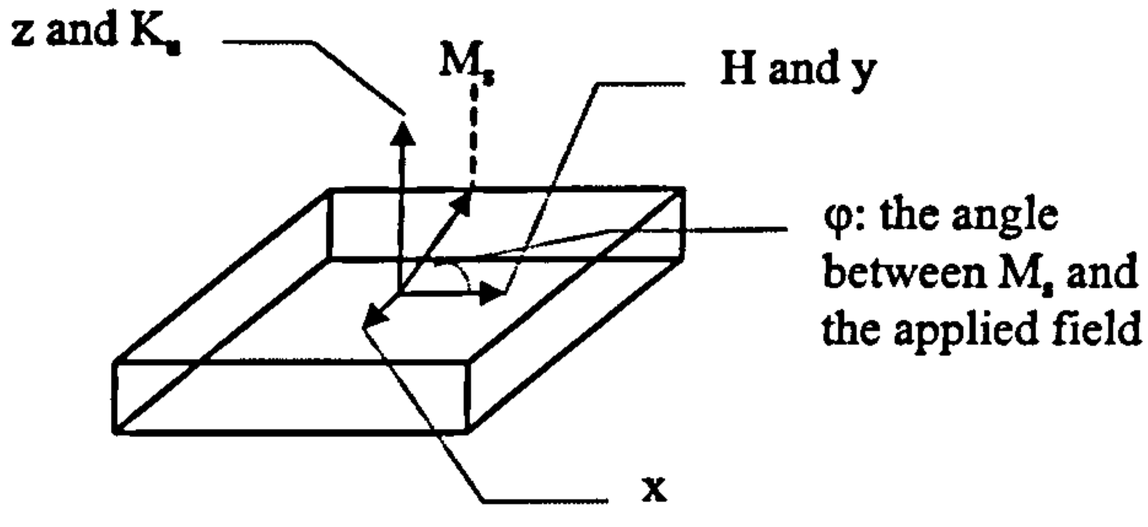

$$E_{tot} = E_K + E_H + E_D \quad (A.1)$$

where

$$E_K = K_u \cos^2\varphi \quad (A.2)$$

$$E_H = -M_s \bullet H = -M_s H \cos\varphi \quad (A.4)$$

and

$$E_D = -\frac{1}{2} M \bullet H_D \quad (A.5)$$

where

$$H_D = -N_D M \quad (A.6)$$

where N_D is the demagnetizing factor,
for a thin film $N_x = N_y = 0$ and $N_z = 4\pi$

Hence, constricting rotation to the y-zplane.

$$E_D = -\frac{1}{2}(4\pi M_z^2) \quad (A.7)$$

where

$$M_z = M_s \sin\varphi \quad (A.8)$$

hence,

$$E_{tot} = K_u \cos^2\varphi - M_s H \cos\varphi - 2\pi M_s^2 \sin^2\varphi \quad (A.9)$$

since

$$\sin^2\varphi + \cos^2\varphi = 1$$
$$\Rightarrow \sin^2\varphi = 1-\cos^2\varphi$$

$$\Rightarrow E_{tot} = (K_u + 2\pi M_s^2)\cos^2\varphi + - M_s H \cos\varphi - 2\pi M_s^2 \quad (A.10)$$

let

$$K_u + 2\pi M_s^2 \equiv K_{eff} \quad (A.11)$$

s.t.

$$E_{tot} = K_{eff}\cos^2\varphi - M_s H\cos\varphi - 2\pi M_s^2 \equiv E \quad (A.12)$$

at saturation E is a minimum since M and H are aligned

hence,

$$\frac{\partial E}{\partial \varphi} = 0 \quad (A.13)$$

differentiating wrt φ gives

$$\frac{\partial E}{\partial \varphi} = -2K_{eff}\cos\varphi\sin\varphi + M_s H\sin\varphi = 0 \quad (A.14)$$

$$\Rightarrow \cos\varphi = \frac{M_s H}{2K_{eff}} \text{ and } \sin\varphi=0 \text{ are extrema}$$

Then for a minimum

$$\frac{\partial^2 E}{\partial E^2} > 0 \quad (A.15)$$

$$\frac{\partial^2 E}{\partial E^2} = -2K_{eff}(\cos^2\varphi - \sin^2\varphi) + M_s H\cos\varphi \quad (A.16)$$

since

$$\sin^2\varphi = 1 - \cos^2\varphi$$

$$\frac{\partial^2 E}{\partial E^2} = -2K_{eff}(2\cos^2\varphi - 1) + M_s H\cos\varphi > 0 \qquad \text{(A.17)}$$

for $\sin\varphi = 0$ the solutions are $\varphi = 0$ or $n\pi$

substituting $\varphi = 0$ into $\frac{\partial^2 E}{\partial E^2}$ gives

$$-2K_{eff} + M_s H > 0 \qquad \text{(A.18)}$$

$$H > \frac{2K_{eff}}{M_s} \qquad \text{(A.19)}$$

for $\varphi = \pi$

$$\frac{\partial^2 E}{\partial E^2} = -2K_{eff} - M_s H > 0 \qquad \text{(A.20)}$$

$$\Rightarrow H < \frac{-2K_{eff}}{M_s} \qquad \text{(A.21)}$$

for $\cos\varphi = \frac{M_s H}{2K_{eff}}$

substituting $M_s H = 2K_{eff}\cos\varphi$ into $\frac{\partial^2 E}{\partial E^2}$ gives

$$2K_{eff}\cos^2\varphi - 2K_{eff}(\cos^2\varphi - \sin^2\varphi) > 0 \qquad \text{(A.22)}$$

$$\Rightarrow 2K_{eff}\sin^2\varphi > 0 \qquad \text{(A.23)}$$

which holds everywhere except for $\varphi = 0$ and π

then for the condition

$$\cos\varphi = \frac{M_s H}{2K_{eff}}$$

gives, multilplying by M_s

$$M_z = \frac{M_s^2 H}{2K_{eff}} \qquad \text{(A.24)}$$

where $M_z = M_s\cos\varphi$

this is a straight line with slope of

$\frac{M_s^2}{2K_{eff}}$ and y intercept = 0

therefore the magnetization curve between $\varphi = 0$ and π is a straight line of slope $\frac{M_s^2}{2K_{eff}}$

when $M_z = M_s$ i.e. when the magnetization has aligned with the field or is saturated (at $\varphi = 0$ and π)

$H = \pm\frac{2K_{eff}}{M_s}$ is the saturation field.

Thus giving the magnetization curve shown in figure 4.39.

QED

If one considers a thin film with easy axis along y and an applied field along y as well, the total energy is:

$$E_{tot} = E_K + E_H + E_D \tag{A.25}$$

where

$$E_K = K_u \sin^2\varphi \tag{A.26}$$

$$E_H = M_s H \cos\varphi \tag{A.27}$$

and

$$E_D = \frac{1}{2} M \cdot H_D \tag{A.28}$$

where

$$H_D = -NM \tag{A.29}$$

for the situation considered here N_x, N_y, and $M_z = 0$ since the magnetization is restricted to the x-y plane and the demagnetizing factors for the field applied in the plane of the field are nil.

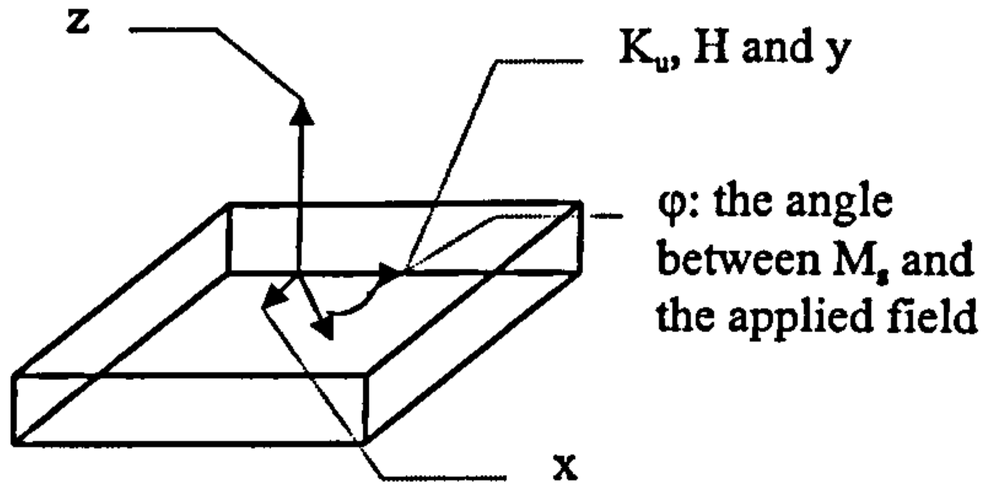

$$\Rightarrow \quad E_{tot} = K_u \sin^2\varphi - M_s H \cos\varphi \equiv E \tag{A.30}$$

or

$$\frac{\partial E}{\partial \varphi} = 0 \tag{A.31}$$

$$\frac{\partial E}{\partial \varphi} = 2K_u \sin\varphi\cos\varphi + M_s H \sin\varphi = 0 \tag{A.32}$$

the solutions include $\sin\varphi = 0$ which is a minimum for $\varphi = 0$ or $n\pi$

and

$$2K_u\cos\varphi = -M_sH \tag{A.33}$$

for a minimum $\frac{\partial^2 E}{\partial E^2} > 0$ (A.34)

$$\frac{\partial^2 E}{\partial E^2} = 2K_u(\cos^2\varphi - \sin^2\varphi) + M_sH\cos\varphi > 0 \tag{A.35}$$

again

$$\sin^2\varphi = 1 - \cos^2\varphi$$

$$\Rightarrow 2K_u(2\cos^2\varphi - 1) + M_sH\cos\varphi > 0 \tag{A.36}$$

looking at solutions for $\sin\varphi = 0$ i.e. $\varphi = 0, \pi$

for $\varphi = 0$

$$\frac{\partial^2 E}{\partial E^2} > 0 \tag{A.37}$$

gives

$$H > -\frac{2K_u}{M_s} \tag{A.38}$$

for $\varphi = \pi$

$$H < \frac{2K_u}{M_s} \tag{A.39}$$

for the solution $\cos\varphi = -\frac{M_sH}{2K_u}$

$$\frac{\partial^2 E}{\partial E^2} = 2K_u\cos^2\varphi - 2K_u > 0 \qquad \text{(A.40)}$$

$$\Rightarrow 2K_u(\cos^2\varphi - 1) > 0 \qquad \text{(A.41)}$$

and

$$-2K_u\sin^2\varphi > 0 \qquad \text{(A.42)}$$

This statement never holds and hence the solution is an unstable one. So only the two previous solutions are stable and the result is a square hysteresis loop as was given in figure 4.38. The stripe domain loop is produced by the addition of the two loops as in figure 4.40.

References

1.) K.H. Jack, Proc. Roy. Soc. London A. 208, 216, (1951).
2.) Kim and Takahashi, Appl. Phys. Lett. 20, 492, (1972).
3.) Y. Sugita, K. Mitsuoka, M. Komuro, H. Hoshiya, Y. Kozono, M. Hanazono, J. Appl. Phys. 70(10), 5977, (1991).
4.) M. Takahashi and H. Shoji, J. Mag. Mag. Mater. 208, 145, (2000).
5.) H. Shoji, H. H. Nashi, K. Eguchi, M. Takahashi, J. Mag. Mag. Mater. 162, 202, (1996).
6.) H. Takahashi, H. Shoji, M. Takahashi, J. Mag. Mag. Mater. 174, 57, (1997).
7.) M. Takahashi, H. Shoji, H. Takahashi, H. Nashi, T. Wakiyama, M. Doi, M. Matsui, J. Appl. Phys. 76(10) pt 2., 6642, (1994).
8.) S. Okamoto, O. Kitakami, Y. Shimada, J. Mag. Mag. Mater.208, 102, (2000).
9.) Y. Takahashi, H. Shoji, M. Takahashi, J. Mag. Mag. Mater. 210, 333, (2000).
10.) M.A. Brewer, C.J. Echer, K.M. Krishnan, T. Kobayashi, A. Nakanishi, J. Appl. Phys. 81(8), 4128, (1997).
11.) Y. Sugita, H. Takahashi, M. Komuro, and M. Igarashi, J. Appl. Phys. 79(8), 5576, (1996).
12.) H. Takahashi, M. Komuro, M. Hiratani, M. Igarashi, Y. Sugita, J. Appl. Phys. 84(3), 1493, (1998).
13.) S. Okamoto, O. Kitakami, Y. Shimada, J. Appl. Phys. 85(8), 4952, (1999).
14.) K.H. Jack J. Appl. Phys. 76(10), 6620, (1994).
15.) J.M.D. Coey, J. Appl. Phys. 76(10), 6632, (1994).
16.) H.Y. Wang, E.Y. Jiang, Z.W. Ma, Y.J. He, H.S. Huang, J. Phys. Con. Mater. 11, 989, (1999).
17.) E.Y. Jiang, H.Y. Wang, Z.W. Ma, J. Appl. Phys. 85(8), 4488, (1999).
18.) R.M. Metzger, X. Bao, M. Carbucicchio, J. Appl. Phys. 76(10), 6626, (1994).
19.) J.M.D. Coey, P.A.I. Smith, J. Mag.. Mag. Mater. 200, 405, (1999).
20.) K.M. Krishnan, M.A. Brewer, T. Kobayashi, A. Nakanishi, A. Young, "Magnetic Hysteresis in Novel Magnetic Materials", G.C. Hadjipanayis(ed.) p. 561Kluwer Academic Publishers, Netherlands, 1997.
21.) A. Sakuma, J. Appl. Phys. 79(8), 5570, (1996).
22.) J.A. Brug, T.C. Anthony, J.H. Nickel, MRS Bull. 23, Sept. (1996).
23.) D. Weller, A. Moser, L. Folks, M.E. Best, W. Lee, M.F. Toney, M. Schwickert, J.U. Thiele, M.F. Doerner, IEEE Trans. Mag. 36(1), 10, (2000).
24.) X. Shi, P.V. Koeppe, M.H. Kryder, IEEE Trans. Mag.27(6), 4942, (1991).
25.) X. Shi, and M.H. Kryder, J. Appl. Phys. 73(10), 5989, (1993).
26.) W.P. Jayasekara, J.A. Bain, M.H. Kryder, IEEE Trans. Mag. 34(4), 1438, (1998).
27.) R.W. Chantrell and J.D. Hannay, Physics World, Oct., 22, (1999).
28.) K.H. Jack, Proc. Roy. Soc. London, 205, 200, (1951).

29.) K.H. Jack, Proc. Roy. Soc. London, 195, 34, (1948).
30.) Cullity, "Introduction to Magnetic Materials", Addison-Wesley, 1972.
31.) E. Camps, S. Muhl, O. Alvarez-Fregoso, J.A. Juarez-Islas, O. Olea, S. Romero, J. Vac. Sci. Tech. A 17(4), 2007, (1999).
32.) H. Yumoto, M. Suzuki, S.J. Li, T. Tsuchiya, Jpn. J. Appl. Phys. 39, 207, (2000).
33.) S. Iwatsubo and M. Naoe, J. Appl. Phys. 87(9), 5245, (2000).
34.) T. Yoshitake, and M. Ohkoshi, IEEE Trans. Mag. 31(6), 3850, (1995).
35.) M.H. Kryder, S. Wang, K. Rook, J. Appl. Phys. 73(10), 6212, (1993).
36.) K.A. McNeill, A.M. Bell, W.J.O'Kane, T.K. McLaughlin, J. Appl. Phys. 87(9), 5837, (2000).
37.) Y. Hoshi and M. Naoe, IEEE Trans. Mag. 26(5), 2344, (1990).
38.) S. Wang, E. Obermeyer, M.H. Kryder, IEEE Trans. Mag. 27(6), 4879, (1991).
39.) S. Wang and M.H. Kryder, J. Appl. Phys. 69(8), 5625, (1991).
40.) M.A. Russak, C.V. Jahnes, E. Klokholm, J.W. Lee, M.E. Re, B.C. Webb, J. Appl. Phys. 70(10), 6427, (1991).
41.) J. Hong, K. Sin, L. Nguyentran, S.X. Wang, IEEE Trans. Mag. 33(5), 2845, (1997).
42.) A. Chakraborty, K.R. Mountfield, G.H. Bellesis, D.N. Lambeth, M.H. Kryder, J.Appl. Phys. 80(2), 1012, (1996).
43.) J.S. Baek, S.C. Yu, W.Y. Lim, C.S. Kim, T.S. Kim, C.O. Kim, J. Appl. Phys. 83(11), 6646, (1998).
44.) W.P. Jayasekara, S. Khizroev, M.H. Kryder, IEEE Trans. Mag. 35(2), 613, (1999).
45.) A. Chakraborty, G.H. Bellesis, K.R. Mountfield, D.N. Lambeth, M.H. Kryder, J. Appl. Phys. 79(8), 5011, (1996).
46.) B. Viala, V.R. Inturi, J.A. Barnard, J. Appl. Phys. 81(8), 4498, (1997).
47.) C.H. Lee, D.H. Shin, D.H. Ahn, S.E. Nam, H.J. Kim, J. Appl. Phys. 85(8), 4898, (1999).
48.) V.R. Inturi and J.A. Barnard, J. Appl. Phys. 79(8), 5904, (1996).
49.) M.K. Minor, B. Viala, J.A. Barnard, J. Appl. Phys. 79(8), 5005, (1996).
50.) H.Y. Wang, Y.J. He, Z.W. Ma, E.Y. Jiang, H.S. Huang, W.H. Mao, J. Appl. Phys. 85(7), 3745, (1999).
51.) H.Y. Wang and E.Y. Jiang, J. Phys. Con. Mater. 9, 2739, (1997).
52.) T.J. Klemmer, V.R. Inturi, J.A. Barnard, J. Vac. Sci. Tech. A, 15(3), 1190, (1997).
53.) L. Varga, H. Jiang, T.J. Klemmer, W.D. Doyle, E.A. Payzant, J. Appl. Phys. 83(11), 5955, (1998).
54.) B. Viala, M.K. Minor, J.A. Barnard, J. Appl. Phys. 80(7), 3941, (1996).
55.) J.F. Bobo, M.J. Casanove, L. Hennet, E. Snoeck, M. Piecuch, J. Mag. Mag. Mater. 164, 61, (1996).
56.) H. Ono, M. Fujinaga, T. Yonemoto, T. Miyagawa, Y. Kitano, J. Mag. Mag. Mater. 118, 352, (1993).
57.) P.J. Flanders and C.D. Graham Jr., Rep. Prog. Phys. 56, 431, (1993).
58.) K.K. Shih, M.E. Re, D.B. Dove, Appl. Phys. Lett. 57(4), 412, (1990).

59.) E.C. Stoner and E.P. Wohlfarth, Proc. Roy. Soc. London, 240, 74, (1948).
60.) Sir Peter Hirsch, "Eledctron Microscopy of Thin Crystals", Krieger Publishing, 1977.
61.) R.M. Bozorth, "Ferromagnetism", IEEE Press, 1993 reissue.
62.) C. Kittel, Phys. Rev. (70(11 and 12), 965, (1946).
63.) C. Kooy and U. Enz, Philips Res. Reps. 15, 7, (1960).
64.) J.R. Barnes, S.J. O'Shea, M.E. Welland, J.Y. Kim, J.E. Evetts, R.E. Somekh, J. Appl. Phys. 76(5), 2974, (1994).
65.) Y.J. Chen, T. Suzuki, S.P. Wong, H. Sang, J. Appl. Phys. 85(8), 5048, (1999).
66.) M. Labrune, J. Miltat, IEEE Trans. Mag. 26, 1521, (1990).
67.) I.B. Puchalska, A. Hubert, S. Winkler, B. Mirecki, IEEE Trans. Mag. 24(2), 1787, (1988).
68.) E.E. Huber Jr. And D.O. Smith, J. Appl. Phys. 30(4), 267S, (1959).
69.) K. Hara, J. Sci. Hiroshima Univ. ser. A-II, 34(2), 139, (1970).
70.) L.M. Alvarez-Prado, G.T. Perez, R. Morales, F.H. Salas, J.M.Alameda, Phys. Rev. B 56(6), 3306, (1997).
71.) N. Saito, H. Fuhiwara, Y. Sugita, J. Phys. Soc. Japan, 19(7), 1116, (1964).
72.) R.J. Spain, Appl. Phys. Lett. 3(11), 208, (1963).
73.) H. Fujiwara, Y. Sugita, N. Saito, Appl. Phys. Lett. 4(12), 199, (1964).
74.) H. Aitlamine, L. Abelmann, I.B. Puchalska, J. Appl. Phys. 71(1), 353(1992).
75.) A. Asenjo, J.M. Garcia, C. Prados, M.Vazquez, Phys. Rev. B 62(10), 6538, (2000).
76.) S. Foss, C. Merton, R. Proksch, G. Skidmore, J. Schmidt, E.D. Dahlberg, T. Pokhil, Y.T. Cheng, J. Mag. Mag. Mater. 190, 60, (1998).
77.) N. Sulitano, J. Mag. Mag. Mater. 214, 176, (2000).
78.) W.Win, E.J. Yun, R.M. Walser, J. Appl. Phys. 79(8), 4933, (1996).
79.) H. Tamai and K. Tagami, IEEE Trans. Mag. 23(5), 2737, (1987).
80.) N. Cabrera and N.F. Mott, Reps. Prog. Phys., 12, 163, (1949).
81.) B.K. Tanner and J.M. Hudson, IEEE Trans. Mag. 28(5), 2736, (1992).
82.) K.O'Grady, R.L. White, P.J. Grundy, J. Mag. Mag. Mater. 177-181, 886, (1998).
83.) P.J. Grundy and R.S. Tebble, Adv. in Phys. 17(66), 153, (1968).
84.) P.J. Grundy and B. Johnson, Brit. J. Appl. Phys(J. Phys. D) ser. 2, 2, 1279, (1969).
85.) M. Kohler, T. Schweinbock, T. Schmidt, J. Zweck, G. Bayreuther, P. Fischer, G. Schutz, T. Eimuller, P. Guttmann, G. Scgmahl, J. Appl. Phys. 87(9), 6481, (2000).
86.) J. Drabecki and J. Zbroszcyk, J. Mag. Mag. Mater. 24, 29, (1981).
87.) L. Belliard, J. Miltat, V. Kottler, V. Mathet, C. Chappert, and T. Valet, J. Appl. Phys. 81(8), 5315, (1997).
88.) Chikazumi, S., "The Physics of Ferromagnetism" 2nd edition, Clarendon Press, 1997.
89.) D.J. Craik and R.S. Tebble, Ferromagnetism and Ferromagnetic Domains, North Hollan Publishing, 1965.
90.) O.F. Bakkaloglu, M.F. Thomas, R.J. Pollard, and P.J. Grundy, J. Mag. Mag. Mater. 126, 261, (1993).
91.) P.J. Grundy, D. Greig, and E.W. Hill, Endeavour, 17(4), 154, (1993).

92.) L.M. Falicov, D.T. Pierce, S.D. Bader, R. Gronsky, K.B. Hathaway, H.J. Hopster, D.N. Lambeth, S.S.P. Parkin, G. Prinz, M. Salamon, I.K. Schuller, R.H. Victora, J. Mater. Res., 5(6), 1299, (1990).

93.) M.N. Baibich, J.M. Broto, A. Fert, F. Nguyen Van Dau, F. Petroff, P. Eitenne, G. Creuzet, A. Friederich, J. Chazelas, Phys. Rev. Lett., 61(21), 472, (1988).

94.) D.J. Sellmyer and Z.S. Shan, Nato Advanced Study Institute, Mykonos Greece, July 1st-12th, (1996).

95.) C. Hammond, "Basics of Crystallography and Diffraction", Oxford Press, 1997.

96.) E. Chason and T.M. Msyer, Crit. Revs. Sol Stat. Mat. Sci.22(1), 1, (1997).

97.) I.K. Schuller, S. Kim, C. Leighton, J. Mag. Mag. Mater. 200, 571, (1999).

98.) U. Gradmann, J. Mag. Mag. Mater. 54-57, 733,(1986).

99.) P. Bruno, G. Bayreuther, P. Beauvillain, C. Chappert, G. Lugert, D. Renard, J.P.Renard, J. Seiden, J. Appl. Phys. 68(11), 5759, (1990).

100.) Y Matsuda, Y Yahisa, J, Inagaki, E, Fujita, A Ishikawa, Y Hosoe, J. Appl. Phys.79(8), 5351, (1996).